

# **A Viability Study of Gamma Emission Tomography for Spent Fuel Verification: JNT 1955 Phase I Technical Report**

L. Eric Smith  
Vladimir Mozin  
Erin Miller  
Nikhil Deshmukh  
Rick Wittman  
Sophie Grape  
Stefano Vaccaro  
Tapani Honkamaa

Staffan Jacobsson-Svärd  
Peter Jansson  
Tim White  
Holly Trelue  
Anna Davour  
Peter Andersson  
Scott Holcombe

**October 2016**



This page intentionally blank

## DISCLAIMER

This report was prepared as an account of work sponsored by an agency of the United States Government. Neither the United States Government nor any agency thereof, nor Battelle Memorial Institute, nor any of their employees, makes **any warranty, express or implied, or assumes any legal liability or responsibility for the accuracy, completeness, or usefulness of any information, apparatus, product, or process disclosed, or represents that its use would not infringe privately owned rights.** Reference herein to any specific commercial product, process, or service by trade name, trademark, manufacturer, or otherwise does not necessarily constitute or imply its endorsement, recommendation, or favoring by the United States Government or any agency thereof, or Battelle Memorial Institute. The views and opinions of authors expressed herein do not necessarily state or reflect those of the United States Government or any agency thereof.

PACIFIC NORTHWEST NATIONAL LABORATORY

*operated by*

BATTELLE

*for the*

UNITED STATES DEPARTMENT OF ENERGY

*under Contract DE-AC05-76RL01830*

Printed in the United States of America

Available to DOE and DOE contractors from the  
Office of Scientific and Technical Information,  
P.O. Box 62, Oak Ridge, TN 37831-0062;  
ph: (865) 576-8401  
fax: (865) 576-5728  
email: [reports@adonis.osti.gov](mailto:reports@adonis.osti.gov)

Available to the public from the National Technical Information Service,  
U.S. Department of Commerce, 5285 Port Royal Rd., Springfield, VA 22161  
ph: (800) 553-6847  
fax: (703) 605-6900  
email: [orders@ntis.fedworld.gov](mailto:orders@ntis.fedworld.gov)  
online ordering: <http://www.ntis.gov/ordering.htm>



This document was printed on recycled paper.

(9/2003)

# **A Viability Study of Gamma Emission Tomography for Spent Fuel Verification: JNT 1955 Phase I Technical Report**

Pacific Northwest National Laboratory

L. Eric Smith, Erin Miller, Nikhil Deshmukh, Rick Wittman

Uppsala University

Staffan Jacobsson-Svärd, Peter Jansson, Sophie Grape, Anna Davour,  
Peter Andersson, Scott Holcombe

Lawrence Livermore National Laboratory

Vladimir Mozin

Los Alamos National Laboratory

Holly Trelue

STUK

Tapani Honkamaa

International Atomic Energy Agency

Tim White

Directorate Euratom Safeguards of the Directorate General for Energy of  
the European Commission

Stefano Vaccaro

October 2016



## Abstract

The potential for gamma emission tomography (GET) to detect partial defects within a spent nuclear fuel assembly is being assessed through a collaboration of Support Programs to the International Atomic Energy Agency (IAEA). In the first phase of this study, two safeguards verification objectives have been identified. The first is the independent determination of the number of active pins that are present in the assembly, in the absence of *a priori* information about the assembly. The second objective is to provide quantitative assay of pin-by-pin properties, for example the activity of key isotopes or pin attributes such as cooling time and relative burnup, under the assumption that basic fuel parameters (e.g., assembly type and nominal fuel composition) are known. The efficacy of GET to meet these two verification objectives has been evaluated across a range of fuel types, burnups, and cooling times, and with a target total interrogation time of less than 60 minutes. This evaluation of GET viability for safeguards applications was founded on a modelling and analysis framework applied to existing and emerging GET instrument designs. Monte Carlo models of different fuel types were used to produce simulated tomographer responses to large populations of “virtual” fuel assemblies. Instrument response data were processed using a variety of tomographic-reconstruction and image-processing methods, and scoring metrics specific to each of the verification objectives were used to predict performance. This report describes the analysis framework and metrics used to predict tomographer performance, the design of a “universal” GET (UGET) instrument intended to support the full range of verification scenarios envisioned by the IAEA, and a comparison of predicted performance for the notional UGET design and an optimized variant of an existing IAEA instrument.

## Executive Summary

The accurate verification of spent-fuel declarations is central to the International Atomic Energy Agency's (IAEA) safeguards approaches at facilities handling and storing irradiated fuel. Safeguards approaches at such facilities could include fuel verification by on-site inspectors using attended methods, or alternatively, using permanently installed, unattended instrumentation. At present, IAEA's authorized instruments for attended partial defect detection have limitations in terms of independence, defect sensitivity, and implementation flexibility. The IAEA has no authorized instrument for unattended partial defect detection in spent fuel. The IAEA states the need for "more sensitive and less intrusive alternatives to existing NDA (nondestructive assay) instruments" for partial-defect detection in its Long-Term R&D Plan (IAEA 2013).

Passive gamma-ray emission tomography is attractive for addressing partial defect detection and verifying the integrity of the fuel assembly because it has the potential to directly image the spatial distribution of the active material in the fuel pins and the relative locations of the pins in the assembly structure, without the need for any operator-declared information. The gamma-ray signatures, particularly in younger fuels, can be strongly correlated to irradiation parameters such as final (integral) burnup and cooling time, thereby achieving more specificity than other methods. Further, tomography has the potential to directly image the interior of the assembly, at multiple axial locations along the assembly length so that pin-level assay (as opposed to volume-integrating assay) can be achieved. Finally, gamma tomography is potentially viable in both wet and dry measurement environs, and in either unattended or attended modes, characteristics that afford significant operational flexibility.

Through prior work in modeling and measurements, a substantial body of knowledge has been assembled on the viability of gamma-ray tomography. For example, a project undertaken by the IAEA (2003 to present under JNT 1510) designed, fabricated, and field-tested a transportable, underwater version of a gamma-ray emission tomographer. This work has provided invaluable information on instrument design and field applicability. Past and current projects in Sweden and Norway, funded by reactor operators primarily for purposes of code validation, add to the experience available on equipment design, tomographic reconstruction techniques and analysis methods. The Swedish experience includes the construction of a laboratory mockup and a heavy, stationary type of underwater test platform, which was used in measurements at a commercial boiling water reactor (BWR). The Norwegian experience includes a tomographic device aiming at measuring power, burnup and fission gas distributions in research fuel.

While the prior gamma emission tomography (GET) work has been informative and encouraging, a number of technical and viability questions needed to be addressed in the context of IAEA's evolving fuel verification needs, for example: What is the potential for GET-based verification over a wide range of fuel types, including fuel with very dense pin spacing (e.g. VVER and PWR) and very long cooling times (e.g., at 40 years where  $^{137}\text{Cs}$  may provide the only viable signature)? Can a single instrument design achieve that potential, while being suitably robust, cost-effective and maintainable for long-term operation? Addressing such questions was the primary motivation for commissioning the viability study described in this report, a study performed under the auspices of several Support Programs to the IAEA: United States, Sweden, Finland, and the European Commission. In the first phase of this study, two safeguards verification objectives have been identified. The first is the independent determination of the number of active pins that are present in the assembly, in the absence of *a priori* information about the assembly. The second objective is to provide quantitative assay of pin-by-pin properties, for example the activity of key isotopes or pin attributes such as cooling time and relative burnup, under the assumption that basic fuel parameters (e.g., assembly type and nominal fuel composition) are known.

Toward the goal of reducing potential confusion about the terminology adopted in this report, a few definitions may be helpful. The acronym GET is used to refer to the topic of gamma-emission tomography generally—it is not specific to a particular instrument design. Because this viability study involves multiple tomographer designs, GET is often used to describe the project and the project team. In this report, the acronym UGET refers specifically to the Universal GET instrument design (i.e., UGETv1) and should not be confused with the use of the same acronym for *unattended* GET. While unattended implementation scenarios were a key motivator for JNT 1955 and “unattended” is even part of the task title, the viability analysis presented in this report is largely agnostic to implementation mode and therefore, the distinction between unattended and attended operation is not emphasized.

## Verification Objectives and Study Parameters

Additional description of the verification objectives adopted in Phase I, and an overview of the implementation scenarios defined by the IAEA and the GET study team, are provided here.

*Objective 1 - Independent pin counting for verification of item integrity.* Verification is performed in a manner completely independent of operator-declared information (e.g., fuel assembly type, initial enrichment, burnup, and cooling time). The assembly is treated as an unknown sample and emitted gamma rays at one or more energies are used to directly calculate the spatial distribution of the emitting material. The primary performance question is whether missing or substituted pins can be confidently detected. The evaluation metrics for Objective 1 recognize the inherent tradeoffs between the probability of detection and probability of false alarm. Objective 1 is consistent with existing IAEA criteria for detection of partial defects in spent fuel, as described for example, in IAEA documents regarding verification criteria for fuel transferred to dry storage and difficult-to-access storage.

*Objective 2 - Pin-by-pin characterization for detection of anomalies.* Isotopic concentrations (e.g.,  $^{137}\text{Cs}$ ,  $^{154}\text{Eu}$ , or  $^{144}\text{Pr}$ ) in each pin in an assembly, and derived characteristics such as burnup and cooling time, are used to detect pin-tampering scenarios. This might include, for example, a scenario where one or a few pins are replaced between reactor cycles to produce weapons-grade instead of reactor-grade plutonium. For this verification objective, operator-declared information could be incorporated (e.g., fuel assembly type and geometry in order to correct for self-attenuation), but it is not necessarily required (i.e., a nominal fuel geometry information could be inferred from the tomographic analysis itself). The evaluation metric for Objective 2 focuses on the achievable accuracy and precision of pin-wise characteristics (e.g., isotopic concentration, burnup, cooling time), as compared to a known ground truth (assumed to be available) for each pin. Current IAEA fuel verification criteria do not require verification of pin-by-pin characteristics but Objective 2 analysis was included in this study to inform the IAEA and stakeholders about its viability and potential.

The matrix of implementation scenarios, cooling times, deployment constraints, and target measurement times, for all three fuel types considered in this study (i.e., boiling water reactor [BWR], pressurized water reactor [PWR] and water-water energetic reactor [VVER]), is summarized in Table ES.1. These parameters were defined at the inception of Phase I by the project team and stakeholders. The Phase I analysis and findings presented in this report departed from the original recommendations in several ways. First, verification of the contents of atypical items, for example cans containing fuel pins extracted from other assemblies, was not addressed. Second, a nominal assay time of 60 minutes or less was assumed for all implementation scenarios. Third, only underwater assay was considered. Fuel burnup values from 10 to 40 gigawatt-days per metric ton of uranium (GWd/MTU) were analyzed.

With the verification objectives and implementation scenarios as guidance, the key outcomes of the JNT 1955 Phase I were defined to be:

- Development of a modeling and analysis framework that has the flexibility, efficiency, and fidelity to support quantitative GET performance studies that accurately reflect field performance.
- Definition of a nominal universal GET design (UGETv1) that is capable of spanning all of the verification objectives and implementation scenarios assumed in this study. The design should use commercially available hardware and to the extent possible, nonproprietary data acquisition and analysis software. It should also be capable of supporting both attended and unattended applications. A lifecycle cost estimate for UGETv1 should be provided.
- Quantitative assessment of predicted performance for Objective 1, independent pin counting for verification of item integrity. Performance should be predicted and compared for the UGETv1 design and the passive gamma emission tomographer (PGET) developed under JNT 1510.
- Preliminary viability assessment of gamma-ray tomography for Objective 2, verification of pin-by-pin characteristics, and detection of anomalies. UGETv1 and PGET performance should be compared using different assumptions and methods for the reconstruction of isotopic activities, integral burnup, and cooling time in each pin of an assembly.

**Table ES.1.** Description of implementation scenarios as originally defined for JNT 1955 Phase I.

<b>Implementation Scenario</b>	<b>Cooling time (years)</b>	<b>Deployment Constraints</b>	<b>Target Measurement Time (minutes)</b>
Routine verification of old fuel being transferred to a geologic repository	40	Attended or unattended; dry or water	30
Routine verification of fuel being transferred to dry storage	5	Attended or unattended; water	30
Random verification of in-pool inventory	1	Attended; water	30
Anomaly resolution of specific assemblies or atypical items	1 to 40	Attended; water	60

## Modeling and Analysis Framework

A large portion of the effort in JNT 1955 Phase I was devoted to the development of a modeling and analysis framework that can support the verification objectives and implementation scenarios described above. Such a framework must incorporate fuel models, burnup and cooling-time calculations to predict isotopic inventories, efficient and flexible Monte Carlo radiation-transport and detector-response methods, adaptable tomographic reconstruction algorithms, and performance metrics appropriate to the two distinct verification objectives. The GET modeling and analysis framework depicted in Figure ES.1 was designed in a modular fashion so that candidate analysis methods (e.g., different image-processing algorithms) could be inserted and evaluated concurrently.

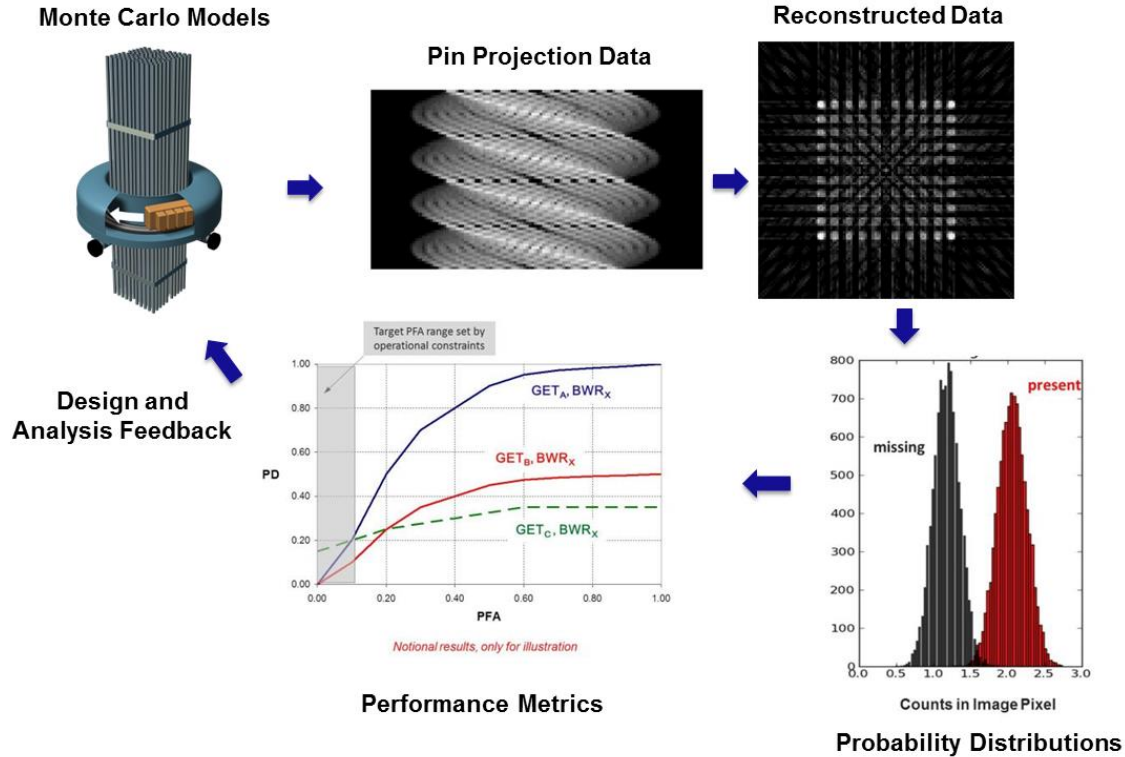


**Figure ES.1.** Illustration of GET analysis and evaluation framework, from Monte Carlo modeling of emitted signatures through performance evaluation.

A novel and particularly important aspect of the GET framework is the concept of the single-pin sinogram. The single-pin sinogram is the detector response for a virtual assembly in which all but one of the pins are inert (they attenuate but do not emit radiation). The summation of single-pin sinograms for each active pin position in the assembly is equivalent to the sinogram from the full assembly. This single-pin sinogram modeling approach allows the characteristics of each emitting pin to be varied (e.g., relative burnup) while the attenuation characteristics of the surrounding pins are unchanged. Poisson noise is then added to the projection data, for an assumed projection data collection time. The net result is that a large population of simulated spent fuel assemblies, each with a distinctive and inhomogeneous pin-to-pin burnup, and statistical noise commensurate with the desired measurement time, can be created from a single transport calculation. For this study, a uniform pin-to-pin variation of  $\pm 20\%$  was assumed for all scenarios and all fuel types. This level of burnup variation is at the extreme end of likely burnup variations even for BWR fuels (less variation is expected for PWR fuels), but within bounds indicated by discussions with operators. Validation examples for the Monte Carlo N particle-based radiation transport approach used in the GET study are shown in Figure ES.2. These results provide confidence that the simulated tomographer responses are a sufficiently accurate reflection of measured responses to support performance viability assessments.

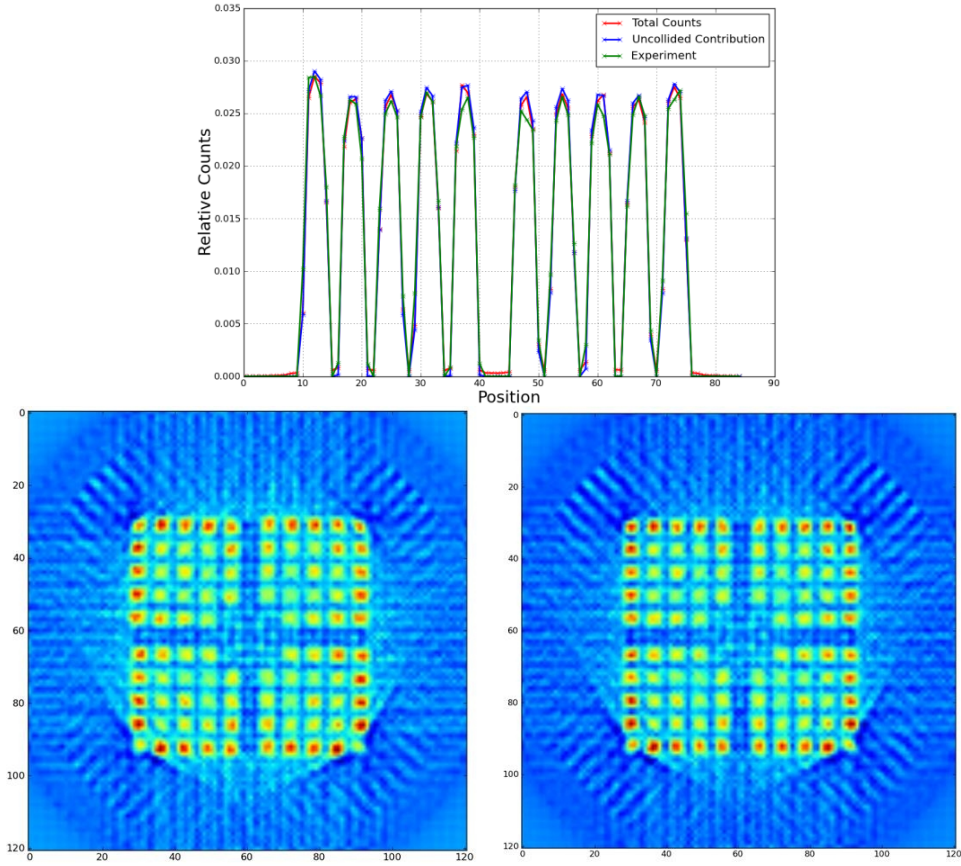


**Figure ES.2.** Example of empirical validation performed for GET modeling and analysis framework. (Top) Measured and simulated projection data (count rate versus position for a single detector of the instrument) from a Swedish tomographer. (Bottom) Measured (left) and simulated (right) image reconstructions for assay of  $^{140}\text{Ba}$  concentration in BWR assemblies using the same tomographer, and filtered backprojection without attenuation correction.

## Universal GET Design

A universal tomographer design, capable of supporting both verification objectives and all expected implementation scenarios, was defined for this study. While it is recognized that a universal tomographer design may not be the correct implementation approach (i.e., ultimately, more than one tomographer design may prove more practical and effective), the challenge posed to the JNT 1955 team was universality in a single design.

In general, the GET design parameter space reduces to spatial resolution (Can individual pins be distinguished?), energy resolution (How well can isotopic lines be distinguished?), and collection efficiency (Are total count rates manageable? Is there sufficient collection of key emission lines to ensure reasonable total assay times?). The collimator parameters (bore length, width, and height) are the principal determinants of the spatial resolution and collection efficiency, and also define the data-collection geometry (number of samples per projection and angular sampling). Energy resolution and to a lesser extent, the collection efficiency, are coupled through the choice of detector material. Total data-collection time will depend on each of these parameters, as well as other engineering and cost considerations (e.g., acquisition time could be decreased by the use of multiple detector assemblies, increasing cost, and mechanical complexity).

Prior work informed the development of UGETv1 design; two tomographers represented extremes in the design space. The first device, IAEA's existing PGET instrument is a transportable, underwater device designed to assay relatively long-cooled fuels (>5 years) where the intensity of emissions, and the proportion of those emissions at energies greater than 1500 keV, are relatively low. PGET was specifically designed to deliver on Objective 1 (pin counting); Objective 2 (pin-by-pin burnup quantification) was not explicitly considered in the original PGET user requirements. Each PGET detector head has a dense array of cadmium telluride (CdTe) detectors with very limited spectroscopic capability (i.e., broad regions of interest [ROIs]) and relatively light collimation (10-cm depth). The second device, called PLUTO, was built by Uppsala University to validate the codes of reactor operators. This large, underwater device was designed to measure commercial BWR fuel shortly after removal from the reactor (few weeks) where the total emission intensity is high and the proportion of high-energy emissions is high compared to longer-cooled fuels. Because individual isotopes were to be assayed, spectroscopic detectors (i.e., bismuth germanate [BGO] scintillators) were required. This system used a sparsely populated detector array with very heavy collimation (30-cm depth).

Informed by this prior work as well as original simulations and analysis, the JNT 1955 team defined the nominal UGETv1 design depicted in Figure ES.3. The design uses commercially available LaBr<sub>3</sub> scintillators (3.8 x 3.8 cm) with sufficiently high full-energy efficiency and energy resolution to efficiently collect and resolve key isotopic signatures from <sup>137</sup>Cs, <sup>134</sup>Cs, and <sup>154</sup>Eu. The collimator geometry (1.5 mm wide, 1.0 cm tall, and 20 cm deep) has a field of view narrow enough to meet spatial-resolution requirements for single-pin detection, yet large enough for sufficient absolute collection efficiency of key signatures for longer-cooled, lower-activity fuels. In-collimator filtration could be used to mitigate the high count rates associated with lower-energy emissions, particularly at short cooling times. To collect projection data, each detector head scans laterally on a translate stage, and each translate stage is mounted on a common rotate stage. While only a single detector head is required for full data collection, multiple heads shorten the total collection time. The fixed interior radius of the device is large enough to assay even VVER-1000 fuels (not analyzed in this study) with appropriate mechanical clearance.

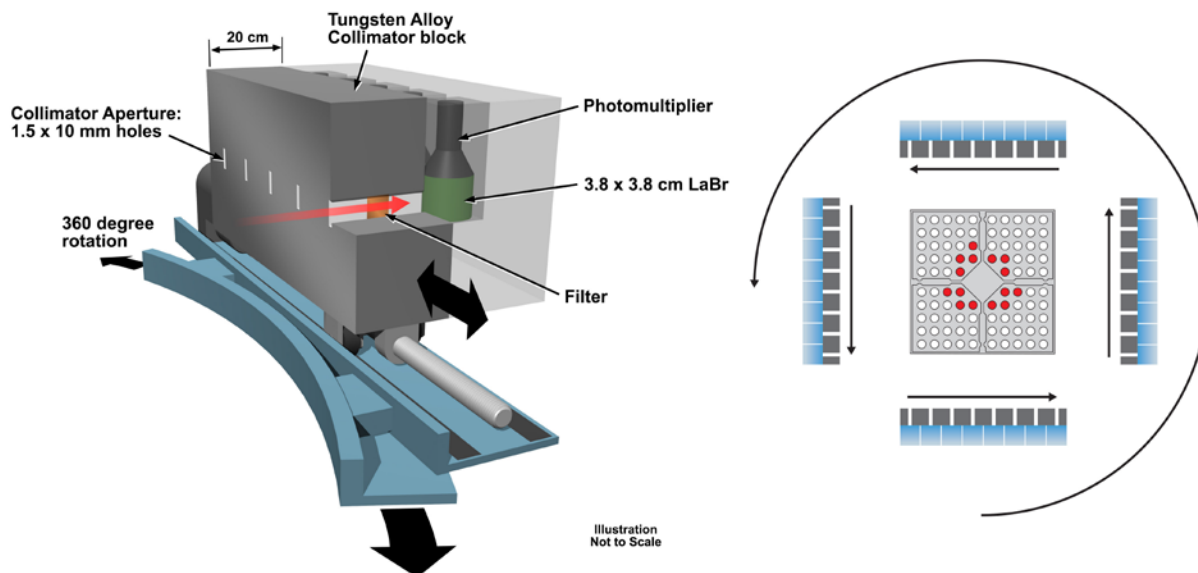


**Figure ES.3.** Diagram of a single detector head of the nominal universal GET design (UGETv1) defined in Phase I (left). The full instrument would include four heads, eight detectors each, and a translate-rotate geometry (right).

## Objective 1: Methods and Results

As described previously, Objective 1 analysis is performed in a manner completely independent of operator-declared information. Simulated sinogram data are mathematically inverted to form an image of the cross section of the fuel assembly using either a purely analytic filtered backprojection (FBP) approach or an algebraic approach. For the U.S. Support Program to the IAEA (USSP) analysis in Phase I, the FBP algorithm employed a simple ramp filter without any form of attenuation correction. The Swedish Support Program to the IAEA (SWESP) analyses was executed using both the analytic and the algebraic approach, assuming either no attenuation or a nominal uniform attenuation correction.

The reconstructed images for each assembly must then be processed to locate the assembly in the image, define the pin locations in the assembly, and calculate the average gray level for each reconstructed pin. USSP image analysis assumed that the assembly location and orientation can be readily and accurately determined—no analysis tools were developed or applied to perform those tasks for this study. SWESP analysis included algorithms to identify fuel rods in the reconstructed images and extract pin-wise data, fully independent of prior information. The algorithms were developed in previous tomographic studies, and allow for identification of fuel type and determination of assembly location and orientation. For both the USSP and SWESP analyses, the image intensity data were reconstructed on a regular pixel grid and the aggregated intensity of multiple pixels in a “neighborhood” centered on each pin location (known beforehand or obtained from image analysis) was calculated. These aggregated pin-region intensity values are referred to as the pin scores.

Figure ES.4 illustrates key steps in the analysis process leading up to pin scores, based on SWESP algorithms and empirical data from previous measurement campaigns using the PLUTO instrument on BWR fuel. The reconstructed image on the left and pin-search algorithm results in the center assume no *a priori* information about the fuel assembly. The histogram of pin scores on the right illustrates how fuel pins are clearly separated from background, which enables the identification of fuel type and assembly position and orientation. Similar results were obtained for experimental PGET data.



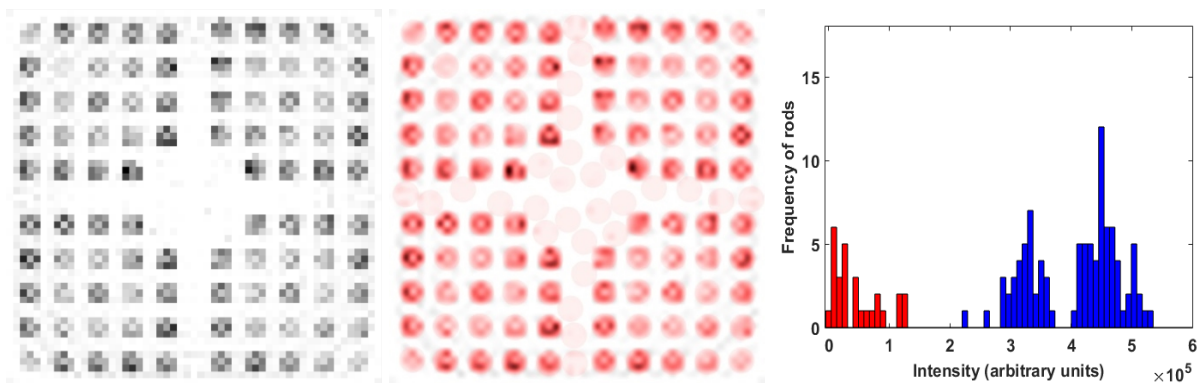


**Figure ES.4.** Algebraically reconstructed image of the  $^{140}\text{Ba/La}$  distribution in a SVEA-96 BWR assembly measured using the PLUTO device (left). The results of automated rod search in the reconstructed image, continuing until the whole image area is filled. Identified positions are overlaid in red over the reconstructed image (middle). A histogram of the pin scores extracted in the automated image analysis. The positions that correspond to actual fuel rods are marked with blue bars and non-rod positions are marked with red bars in the histogram (right).

In the Objective 1 analysis performed by USSP and SWESP on simulated assemblies, missing pins were simulated by omitting certain single-pin sinograms when creating each virtual assembly. While two types of partial defects are possible—missing or substituted pins—the focus in this study was on missing pins because it was shown to be the more difficult detection case for Objective 1. The variability of these pin scores for a population of virtual fuel assemblies can be visualized by examination of the score as a function of the pin position from the center of the assembly to the edge. Example pin-score summaries produced from USSP and SWESP analyses are shown in Figure ES.5 for assay of PWR assemblies, using the UGETv1 instrument and the 1275-keV emission line from  $^{154}\text{Eu}$ .

The scores for missing pins near the periphery of the assembly (right side of the plots) are well-separated from present-pin scores, but toward the center of the assembly the separation of the missing and present distributions decreases—consistent with intuition that it is generally more difficult to detect a missing pin in the interior of an assembly due to a greater degree of self-attenuation. Note that the USSP pin-score example incorporates a higher degree of realism in terms of the virtual assembly population (100 assemblies with  $\pm 20\%$  pin-wise burnup variation) but lower-fidelity image reconstruction algorithms (no attenuation correction and ideal response function of the detection system in the FBP). SWESP pin-score results are based on 10 virtual assemblies with no pin-wise burnup variation and the analyses were executed with algebraic reconstruction, including correction for attenuation and modeling of the detection system's intrinsic response function. Furthermore, SWESP used image analysis to identify fuel rods and extract pin scores.

The SWESP investigations of the performance of various reconstruction methods for BWR fuel show that larger separation between rod and non-rod regions may be obtained by taking uniform attenuation into account in the reconstructions, and that the capability to model the detection system's intrinsic response function can give additional improvements for algebraic methods, as compared to FBP. The separation between the distributions of present and missing pins in Figure ES.5 appears to be greater for the SWESP results than for the USSP results because of the different reconstruction methods employed, and because the SWESP results do not include pin-to-pin burn-up variations.

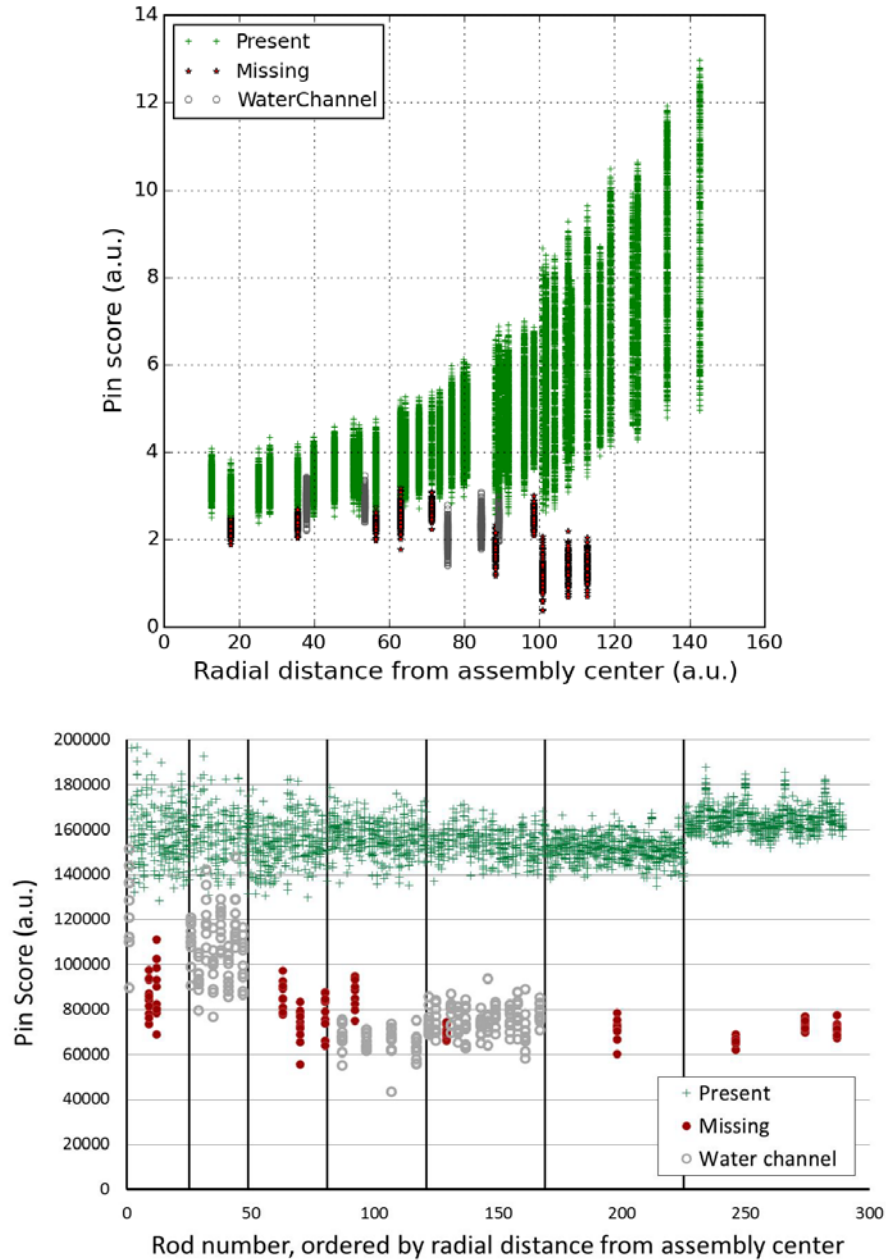


**Figure ES.5.** Example pin-score plots for present and missing pins, assuming UGET assay of PWR assemblies (40 GWd/MTU, 1-year cooling) using the 1275 keV emission from  $^{154}\text{Eu}$ . USSP calculations assume significant pin-wise burnup variation and simple FBP reconstruction algorithms (top). SWESP calculations assume no pin-wise burnup variation, nominal attenuation correction, and inclusion of the detection system’s response function in an algebraic reconstruction process (bottom).

In the Objective 1 performance predictions, a receiver-operator characteristic (ROC) method has been used on the USSP data to quantify the trade-off between probability of detection (PD) and probability of false alarm (PFA) based on pin-score histograms for present and missing pins at each pin location. This process is repeated for each pin location in the assembly or more practically, by groups of pins with the same radial distance from the center of the assembly. In this study, that grouping is termed a “ring.” Once the ring-specific PD and PFA values have been calculated, they need to be translated to a fuel assembly-

level PD and PFA that reflects how the IAEA is expected to make verification decisions in the field. In this study, the assembly-level performance predictions were formulated based on the following question: For a given PD value at any missing-pin location, what is the assembly-level PFA?

In the comparative performance analyses presented in this report, it is assumed that both the PGET and UGETv1 instruments have perfect efficiency and energy calibration. Neither of these can be achieved using the pulse processing electronics in the PGET device that underwent field-testing through 2015. The IAEA is currently refurbishing the PGET instrument to improve its capabilities in this regard, and the performance predictions in this report assume full success in that undertaking. To reflect the difference between the as-fielded instrument of the past, and the potential of the future as analyzed here, the simulated device is often labeled “Ideal PGET.” Where that labeling is not present, it should be assumed. No additional labeling regarding these idealized assumptions is applied to UGETv1 since it is a notional (not actual) instrument design.

USSP’s Objective 1 performance predictions for UGET and Ideal PGET were calculated for all three fuel types (BWR, VVER, and PWR) and fuel characteristics consistent with the three implementation scenarios described previously: 40 GWd/MTU, 1 yr cooling; 20 GWd/MTU, 5 yr cooling; and 10 GWd/MTU, 40 yr cooling. Results for the latter two implementation scenarios are given in Figure ES.6 for virtual assembly populations numbering 1000, and  $\pm 20\%$  pin-wise burnup variation.

These findings indicate that the probability of detecting a single missing pin, at any location in the assembly (even inner pins) is greater than 0.80 with both Ideal PGET and UGETv1, for VVER and BWR fuels, regardless of burnup and age. This is true assuming false alarm rates of approximately 0.05 (1 alarm per 20 assemblies assayed) are operationally tolerable. However, Figure ES.6 also illustrates that the single-missing-pin performance for Ideal PGET and UGET is low for PWR fuel due to its large physical dimension and relatively tight fuel-pin spacing.

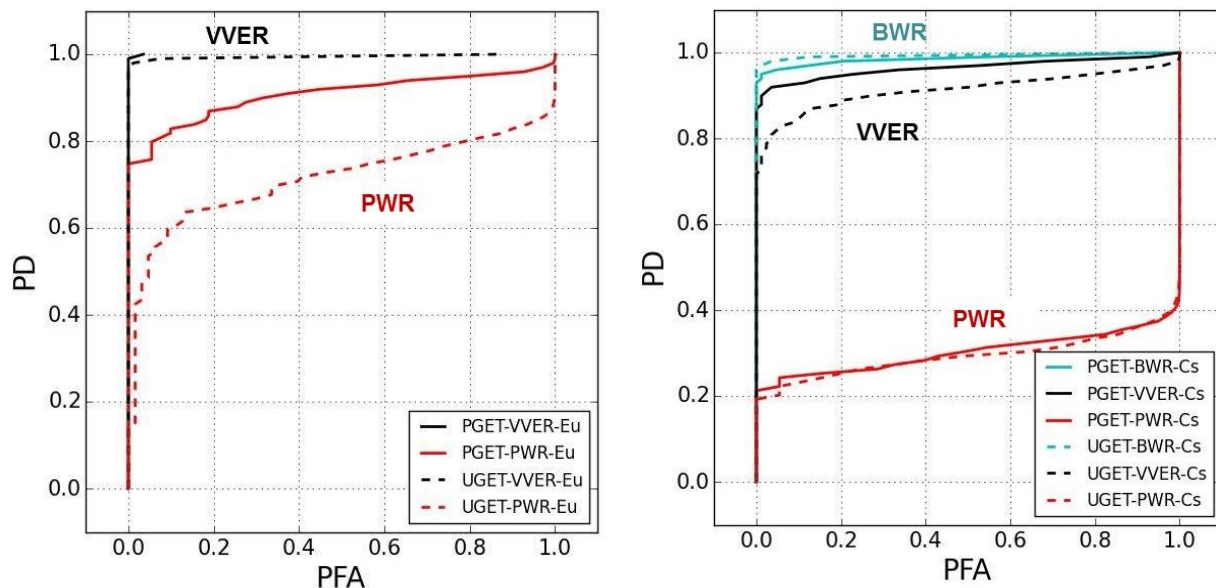


**Figure ES.6.** Predicted sensitivity for detection of a single missing pin (i.e., bias defect) for Ideal PGET and UGET for BWR, VVER and PWR fuels. Nominal burnup of 20 GWd/MTU and 5-year cooling time with assay based on  $^{154}\text{Eu}$  (left); BWR performance is even higher than for VVER and therefore, not shown. Nominal burnup of 10 GWd/MTU and 40-year cooling time with assay based on  $^{137}\text{Cs}$  (right).

A summary of the USSP Objective 1 findings is provided in Table ES.2: the probability of detecting a single missing pin in any of the prescribed locations dispersed in the assembly, at an assembly-level false alarm rate of 0.10. PD values are high for BWR and VVER fuel for all three burnup/cooling time combinations, for both UGET and Ideal PGET. PD values for a single missing pin at the prescribed locations in PWR assemblies are significantly lower, due to the large physical dimension and high degree of self-attenuation in those assemblies.

**Table ES.2.** Summary of the USSP Objective 1 findings: probability of detecting a single missing pin in any location of an assembly, for an assembly-level false alarm rate of 0.10. Key assumptions: 1000 assemblies per population and  $\pm 20\%$  pin-wise burnup variation; total assay times of less than 60 minutes; perfect energy and efficiency calibration; FBP image reconstruction algorithms without any form of attenuation correction. Note that Ideal PGET is not capable of assay high burnup, short-cooled fuels due to count-rate limitations (denoted with X). Red PD values indicate scenarios where detection probabilities for a single missing inner pin are in the range of IAEA’s low detection probability.

	40 GWd/MTU, 1 yr		20 GWd/MTU, 5 yr		10 GWd/MTU, 40 yr	
	PGET	UGET	PGET	UGET	PGET	UGET
PWR	X	>0.95	0.82	0.60	0.25	0.20
VVER-440	X	>0.95	>0.95	>0.95	0.90	0.85
BWR	X	>0.95	>0.95	>0.95	>0.95	>0.95

It is important to note that the summary results presented in Figure ES.6 and Table ES.2 are based on a very conservative assembly-level PFA formulation that aggregates the sensitivities at all radial distances. Under the method for calculating the assembly-level PFA described earlier, it is the inner rings that dominate the assembly-level PFA. This means that even for PWR assemblies, single-missing pins are quite detectable for many regions of the assembly.

No ROC curves have been produced based on data analysis using the SWESP procedure with algebraic reconstruction assuming uniform attenuation in the image area and including the system’s response function followed by automated image analysis (compare the upper and lower part of Figure ES.5), since only a limited set of cases have been analyzed using this procedure. Accordingly, the ROC analyses are limited to FBP reconstruction with no inclusion of attenuation. As indicated by the results presented in Figure ES.5, ROC curves may improve by applying alternative reconstruction methods.

Additional interpretation and observations on the Objective 1 results are given here:

- Ideal PGET performance assumes perfect efficiency and energy calibration, neither of which can be achieved using the current design of the PGET pulse processing electronics. Similar assumptions are made for the notional UGETv1 design. See the Conclusions for more discussion.
- A very strict verification criterion was assumed: detection of a single missing pin without a false alarm at any of the pin locations in the assembly. For PWR, detection of a single missing pin is bias-defect detection (<0.5% of total mass), a level of sensitivity far higher than IAEA’s partial-defect expectations of today (i.e., ~50% mass defect). Additional analysis could be performed to calculate ROC curves for higher defect levels (e.g., 5% or 10% of the pins); it is expected that performance levels would be significantly higher than those tabulated above.
- For the data in Table ES.2 produced by the USSP, no attenuation correction was included in the FBP image reconstruction algorithm. Case studies performed by SWESP have indicated that incorporation of even a nominal, uniform attenuation assumption over the fuel region (no operator-provided information required) could improve performance, and algebraic modelling of the measurement

system's response function may lead to additional improvement. Further analysis (of existing simulated assembly populations) is needed to more definitively quantify potential performance improvements using alternative reconstruction algorithms.

- The UGETv1 collimator design is likely over-conservative, based on additional inquiry into count rates that can be managed by commercially available pulse-processing electronics. A UGET collimator design with a larger field of view (e.g., in vertical direction) would increase sensitivity and produce incremental improvement to the performance reported here.

## Objective 2 Methods and Results

The Objective 2 viability analysis assumes that the geometry of the fuel assembly, pin locations, and pin composition are known. This geometric information may be provided by the operator, or deduced without operator input (e.g., using image analysis on reconstructed images from Objective 1). Regardless of origin, that fuel-geometry information is incorporated into a system response function that inverts the measured sinogram data to calculate the isotopic concentrations (e.g.,  $^{137}\text{Cs}$  or  $^{154}\text{Eu}$ ) in each pin. These isotopic concentrations themselves could be considered verification parameters by the IAEA, but they can also be used to derive burnup and cooling time on a pin level. The performance metric for Objective 2 is the achievable accuracy and precision of pin-wise parameter determination, as compared to a known ground truth for each pin. *This assumes that the operator can provide this high-fidelity ground truth, for example pin-by-pin isotopic and burnup values. It should be noted that such data are not typically provided to the IAEA today in spent fuel declarations.*

Both SWESP and USSP analyses employed iterative algebraic tomographic reconstruction techniques that allow a system response matrix (i.e., detailed information about the imaging system and object) to be incorporated in the inversion, making them well-suited for quantitative determination of pin-wise characteristics. Critical to the accuracy of these algebraic techniques is the fidelity of the system response function to the physics prescribed in either simulated tomographer responses (the primary data source in this study) or actual field measurements. The system matrix methods used by SWESP for Verification Objective 2 have their origin in the deterministic ray-tracing methods developed for analysis of data from prior work for facility operators, implemented in the TOMOPACK software. USSP primarily employed a hybrid deterministic-Monte Carlo transport approach developed previously by PNNL in the Radiation Detection Scenario Analysis Toolbox (RADSAT).

Example Objective 2 results from USSP and SWESP analyses are shown in Figure ES.7 for assay of  $^{154}\text{Eu}$  and  $^{137}\text{Cs}$  concentrations, using the UGETv1 instrument. The fractional error in isotopic concentration is the difference between the calculated and true value (assumed here to be provided by the operator), normalized by the true value. SWESP analyzed PWR assemblies with no pin-wise burnup variation using Uppsala University's algebraic reconstruction algorithms; USSP analyzed VVER assemblies with  $\pm 20\%$  pin-wise burnup variation using PNNL's algebraic reconstruction algorithms. Consistent with intuition and the trends observed in Objective 1, the fidelity of the tomographic assay degrades for interior pin locations. However, the relatively low systematic bias and uncertainties, even for interior pins, are quite encouraging. For example, the one-sigma uncertainty (as indicated by the error bars) for both SWESP and USSP calculations is less than approximately 5% for all pin locations, indicating that detection of pins with burnup levels 20% lower than declared could be detected with a PD greater than 0.95 and PFA less than 0.05 (a PD/PFA combination that requires an approximate four-sigma contrast). For the USSP data, blue markers represent substituted pins with an isotopic concentration half that of the assembly mean. Consistent with intuition, the uncertainty for calculation of concentration in these pins is higher, and a positive systematic bias (perhaps due to cross-talk from nearest neighbors) is evident.

Example Objective 2 results from USSP for Ideal PGET are shown in Figure ES.8 for assay of  $^{154}\text{Eu}$  and  $^{137}\text{Cs}$  concentrations in VVER fuels. Due to the limited spectroscopic capability of the Ideal PGET instrument, the degrading effects of scatter produce larger biases and overall uncertainties than was the case for UGET. It is more difficult to faithfully capture the granularity of scatter effects in realistic assembly populations with significant pin-wise burnup variation, in a system response function using wide energy windows. The systematic bias and uncertainties, especially for interior pins, indicate that it may be possible to detect pins with isotopic concentrations of 40 to 50% lower than declared, assuming a PD greater than 0.95 and PFA less than 0.05. As discussed later, more study is needed on the calculation of PGET system response matrices in order to more fully understand and characterize its Objective 2 potential when using wide energy windows.

In addition to assessment of pin-wise isotopic content, the work on Verification Objective 2 also included studies on the tomographic determination of pin-wise fuel burnup and cooling time. Here, previously established relations between the fuel's contents of key isotopes and these fuel parameters were applied to assess achievable precision in the estimation of individual fuel rod properties. It was shown that for short-cooled fuel, a combination of pin-wise  $^{137}\text{Cs}$ ,  $^{134}\text{Cs}$ , and  $^{154}\text{Eu}$  obtained from tomographic measurements may be used to assess both burnup and cooling time, while for long-cooled fuel the absence of the latter two may limit the assessment to burnup only. In this context, one should note that the achievable precision in estimated burnup and cooling time will be higher in peripheral rod positions than in central positions, as a direct consequence of the measurement precision being a function of the rods' position in the assembly. Accordingly, the achievable precision for central rods will also generally be higher in fuel with smaller dimensions, such as BWR, due to reduced gamma-ray attenuation. The SWESP analyses of the UGET design using detailed algebraic reconstruction techniques concluded that the statistics obtained in a 40-min tomographic assay on 1-year cooled PWR fuel would allow for the burnup to be determined with between <1 percent (peripheral rods) and 6-10 percent (central rods) precision ( $1\sigma$ ), where the use of gamma rays of higher energy from the short-lived isotopes would yield the best results. For 40-year cooled PWR fuel, the studies showed that a total assay time of about two hours would be required to collect  $^{137}\text{Cs}$  data with enough statistics for assessing the burnup in the most central pins with about 10 percent precision ( $1\sigma$ ), while shortening the measurement time with a factor of four would about double that number.



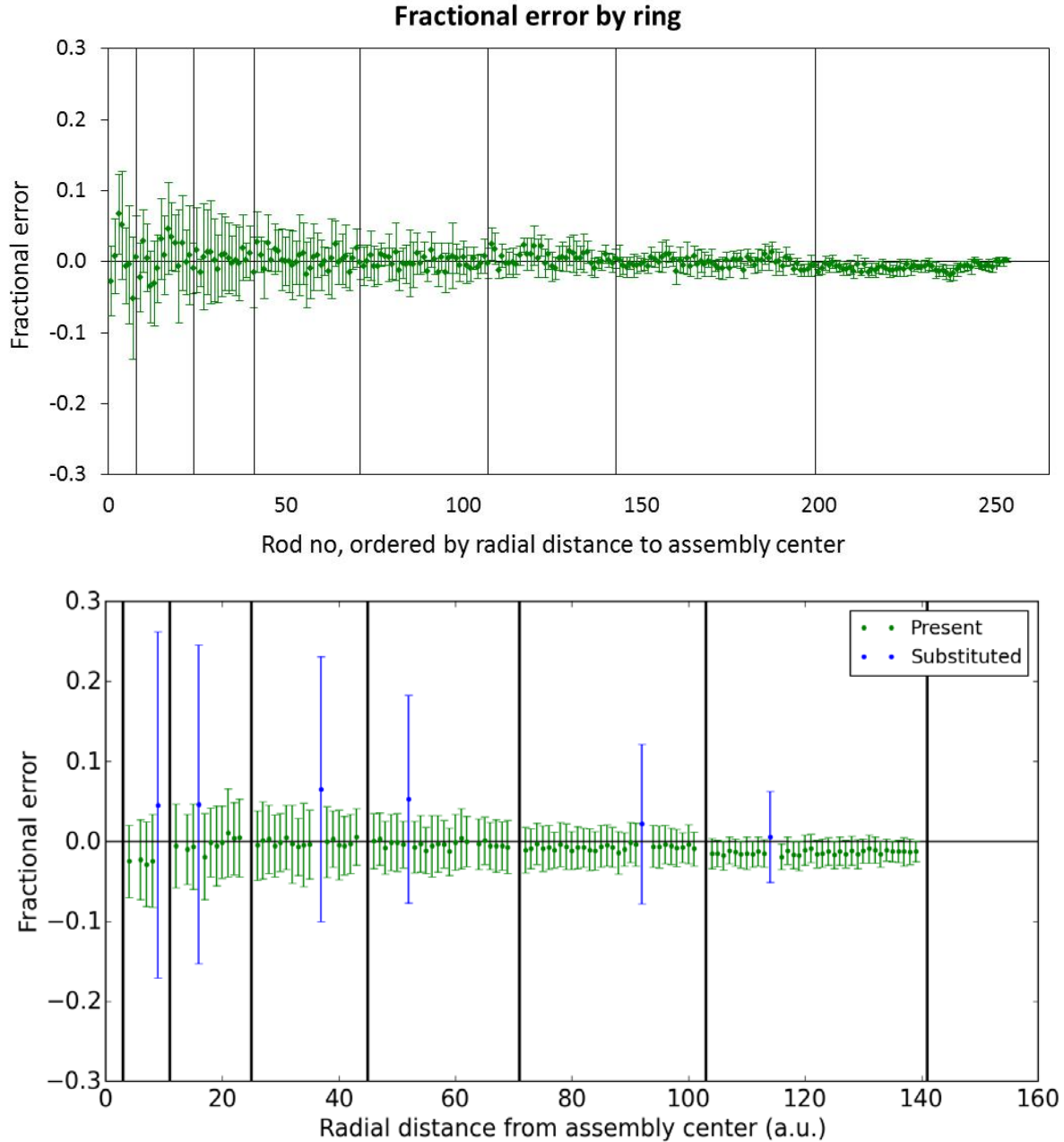


**Figure ES.7.** Example results for the pin-by-pin quantification of isotopic concentration using UGETv1 and a total assay time of less than 60 minutes. Fractional error is the relative difference between calculated and true isotopic concentrations. SWESP calculations of  $^{154}\text{Eu}$  (based on only the 1275 keV emission) assuming no pin-wise burnup variation and 10 PWR assemblies, nominally 40 GWd/MTU and 1-year cooling (top). USSP calculations of  $^{137}\text{Cs}$  (based on 662 keV emission) assuming  $\pm 20\%$  pin-wise burnup variation and 1000 VVER assemblies, nominally 20 GWd/MTU and 5-year cooling (bottom). Tampered pins (blue), have a nominal activity half that of the present pins (green).

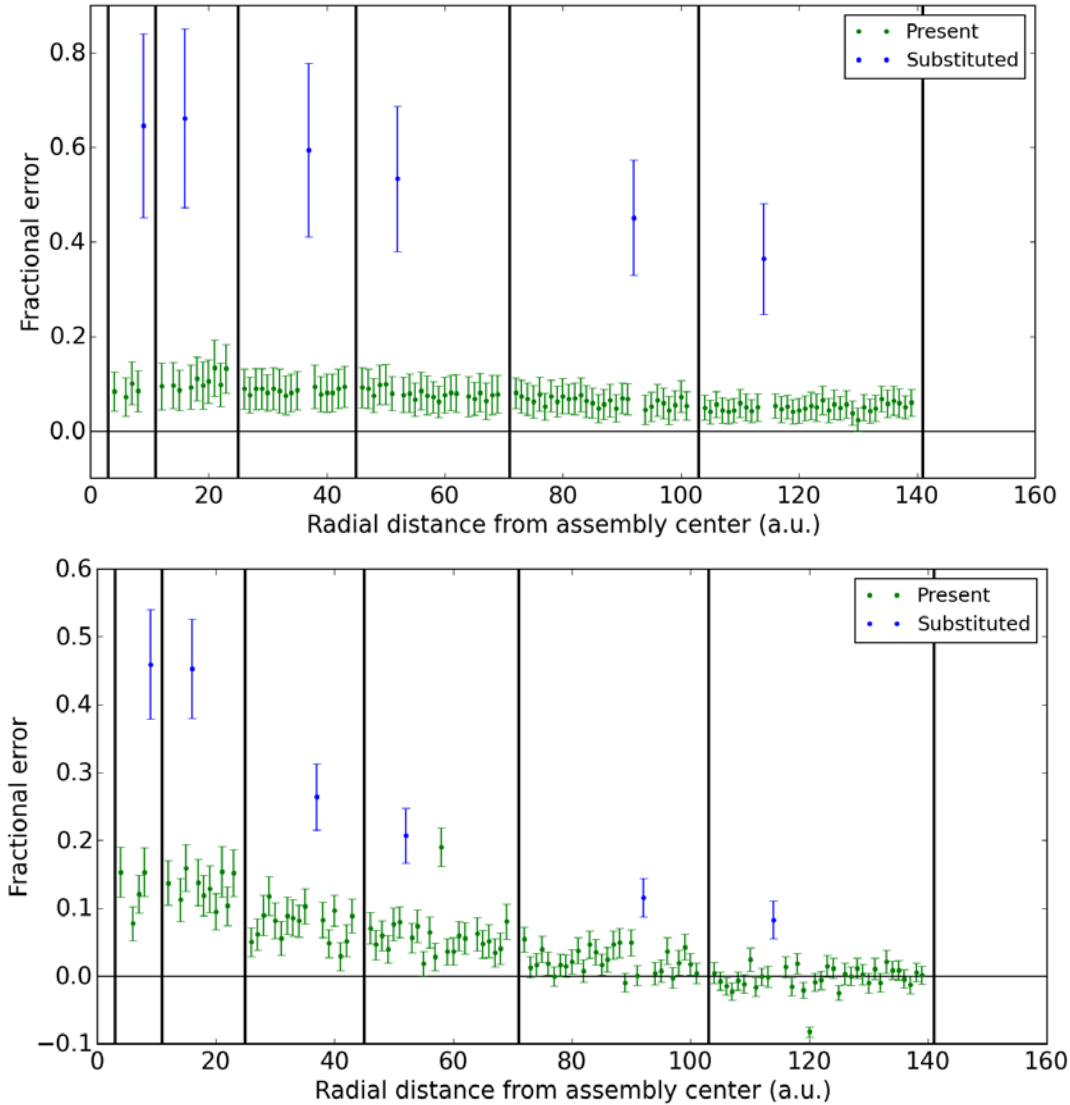


**Figure ES.8.** Fractional error of Ideal PGET-assayed isotopic concentrations in VVER fuels.  $^{154}\text{Eu}$  for nominal burnup of 20 GWd/MTU and 5-year cooling time (top).  $^{137}\text{Cs}$  for nominal burnup of 10 GWd/MTU and 40-year cooling time. In both cases, 100 virtual assemblies,  $\pm 20\%$  pin-wise burnup variation, and 60-minute assay times were assumed (bottom). Tampered pins (blue), have a nominal activity half that of the present pins (green).

A tabular summary of the Objective 2 findings is provided in Table ES.3: the estimated detectable burnup discrepancy, relative to a perfectly known ground truth, that could be detected in inner pins when requiring  $\text{PD} = 0.95$  and assembly-level  $\text{PFA} = 0.05$  in a  $< 60$ -minute assay. The results show that for UGET assay of VVER fuel and younger PWR fuels, burnup deviations of approximately 20% can be confidently detected, which is encouraging since it indicates a possibility to detect substation scenarios in which specific pins are irradiated for only two or three of the typical four-cycle span in a light-water reactor. The detectable discrepancy for Ideal PGET is somewhat higher due to the challenge of accurately compensating for highly variable object scatter in the system response function. This indicates that it may be difficult to detect single-cycle tampering scenarios with PGET, but more investigation of data acquisition and activity analysis algorithms are needed for PGET in order to understand its full potential.



Additional interpretation and observations on the Objective 2 results are presented as follows.

- Ideal PGET performance assumes perfect efficiency and energy calibration, neither of which can be achieved using the current design of the PGET pulse-processing electronics.
- Predicted performance is highly dependent on the fidelity of the system response function used in the reconstruction of isotopic activities. Further refinement of the system response functions used by SWESP and USSP are likely to improve the predicted performance.
- It remains to be seen how well simulated tomographer responses replicate some of the degrading real-world effects in measured responses. Prior empirical work by Upsalla University [UU] on BWR fuels provides semi-quantitative support for the performance predictions for UGET, but many open questions remain about realistic Objective 2 performance for PGET.

**Table ES.3.** Summary of Objective 2 findings: Estimated detectable burnup discrepancy, compared to ground truth, for interior pins, for PD of 0.95 and assembly-level false alarm rate of 0.10 for the PGET and UGET device designs. Key assumptions: Total assay time less than 60 minutes; “perfect” PGET energy and efficiency calibration. Note that Ideal PGET is not capable of assay high burnup, short-cooled fuel due to count-rate limitations, and that Ideal PGET performance for PWR has not been analyzed. Neither was UGET analyzed for the 20 GWd/MTU PWR case.

	40 GWd/MTU 1 yr		20 GWd/MTU 5 yr		10 GWd/MTU 40 yr	
	PGET	UGET	PGET	UGET	PGET	UGET
<b>PWR</b>	X	~20%	--	--	--	~40%
<b>VVER-440</b>	X	<20%	~40%	~20%	~40%	~20%

## Conclusions

GET has the potential to provide *bias-defect* sensitivity in most fuel verification scenarios, a significant improvement over IAEA’s current partial-defect capabilities using a Fork-based system or digital Cerenkov viewing device.

The “Ideal PGET” analyzed in this study assumes perfect absolute efficiency and energy calibration across all 208 CdTe detectors. The current design of the PGET pulse processing electronics cannot support this kind of high-fidelity calibration but a current project to refurbish and improve PGET’s data acquisition system is expected to close the gap between the actual instrument and the idealized response simulated in this study. Further study, using measured responses from the refurbished PGET, could illuminate on the realistic performance of the device.

A “Universal” GET design is capable of supporting the full range of fuel characteristics considered in this study, but that versatility comes at a price in terms of both assay time and instrument lifecycle cost. The lifecycle cost of the first four-head UGETv1 analyzed in this study is estimated at about 800k€ of which ~380k€ is for purchase of components, ~220k€ is for engineering and fabrication, and 200k€ is for software development. Subsequent units are estimated to cost approximately 550k€ due to reduced engineering and software development costs. A UGET variant design only for longer-cooled (i.e., greater than a few years) fuel could be significantly lighter and lower cost. It is also possible that UGETv1 performance could be improved via methods that were outside the scope of this project, for example alternative data collection geometries (i.e., irregular angular sampling) intended to extract more information from interior pins.

Efforts were made to assess the performance of various reconstruction techniques for the UGETv1 design. Among the conclusions drawn were that algebraic reconstruction including modeling of system's intrinsic response function and uniform "black-box" attenuation gave the most promising results in terms of separation between fuel rods and background. Prior work by UU has also indicated that image analysis and algebraic reconstruction methods offer the potential robustness to issues such as misalignment of assemblies, bowing of individual fuel rods, non-functioning detector elements, irregular measurement positions etc.

Despite their very different designs, Ideal PGET and UGETv1 exhibit, in general, comparable performance for the detection of missing pins (Objective 1), and PGET achieves that sensitivity in shorter assay times. That said, the higher collection efficiency of PGET elevates its performance over UGET for cases where the signal coming from interior pins is particularly weak (e.g., PWR assemblies), while UGET achieves high performance for the shortest-cooled fuels that cannot be measured by PGET. (PGET count rates would be well beyond the limits of even the most capable pulse-processing electronics for room-temperature semiconductors.) These comparative findings are based on an analytic FBP reconstruction; as indicated by Figure ES.5, results may vary with other reconstruction methods.

Predicted performance for Ideal PGET is lower than for UGETv1 for pin-by-pin isotopic quantification (Objective 2), primarily because significant object-scatter contributions in PGET's wide energy windows perturb a relatively small full-energy peak signal. Smaller energy windows might offer improvements in Objective 2 performance for PGET, but more study is needed to quantify this potential.

The modeling and analysis framework developed for Phase I provides end-to-end capability to assess tomographer performance for nuclear fuel assay, and could be considered a new, standing capability for the international safeguards community. For example, the simulated and measured tomographic data sets produced in this project could be used to support continued study of GET for other implementation scenarios or of alternative reconstruction and analysis algorithms. Because much of the framework was developed in a modular fashion, portions of it (e.g., specific image analysis and image reconstruction algorithms) can be extracted for specific purposes. It should be noted, however, that there has been no effort to integrate, harden, and interface the software components. Additional development work would be needed to support field application by safeguards inspectors.

Finally, work was done to suggest and investigate possible inspection procedures for GET. The envisioned inspection procedure, identified and refined as part of this project can be outlined according to the following:

- Objective 1: Baseline inspection procedure
  1. Tomographic measurement
  2. Online image reconstruction
  3. Online image analysis
  4. On-site initial integrity statement
- If undeclared removal/replacement is suspected: Detailed rod-activity reconstruction based on current fuel type and position in device. (No additional measurement required.)

The last step reflects the functionality of Verification Objective 2, at least if operator-declared information is used for the detailed modeling. However, it may also be envisaged that geometric information is extracted directly from reconstructed images in step 2, without any need for operator-declared data. The project team and stakeholders have discussed the potential for such a procedure ("Verification Objective 1.5"), but analysis of this approach was beyond the scope of this study.

## Acknowledgments

U.S. participation in this UGET project has been funded by the U.S. Support Program to the International Atomic Energy Agency (IAEA) and the National Nuclear Security Administration's Office of Nonproliferation and Arms Control. Uppsala University's contributions were funded by the Swedish Radiation Safety Authority (SSM) via the Swedish Support Program to the IAEA under contracts SSM2013-85-9, SSM2014-94, SSM2015-99, SSM2016-130, and activity number 3060152-08. The computations performed by Uppsala University were partially performed on resources provided by Swedish National Infrastructure for Computing (SNIC) through Uppsala Multidisciplinary Center for Advanced Computational Science (UPPMAX) under projects p2013091, snic2013-1-296, snic2014-1-203, and snic2014-1-392. Finnish participation was supported by the Finnish Support Program to the IAEA, financed by Finnish Foreign Ministry. The contribution by the European Commission was financed through the regular European Commission budget.

The authors appreciate the guidance of IAEA's James Ely, Misha Mayorov, and Alain Lebrun on the GET viability study.

## Acronyms and Abbreviations

ASIC	application-specific integrated circuit
ASIRT	Additive Simultaneous Iterative Reconstruction Technique
BGO	bismuth germinate scintillation material
BWR	boiling water reactor
Cps	counts per second
DOE	U.S. Department of Energy
Euratom	European Atomic Energy Community
ECSP	European Commission Cooperative Support Programme
Euratom safeguards	Directorate Nuclear Safeguards of the Directorate General for Energy of the European Commission
FBP	filtered backprojection
FOV	field of view
GET	gamma emission tomography
GWd/MTU	gigawatt-day per metric ton of uranium
GWd/t	gigawatt-day per tonne
HPGe	high-purity germanium
IAEA	International Atomic Energy Agency
IFT	inverse Fourier transform
LANL	Los Alamos National Laboratory
LEU	low enriched uranium
LLNL	Lawrence Livermore National Laboratory
LSF	line spread function
MCNP	Monte Carlo N-Particle
MOX	mixed oxide
NDA	nondestructive assay
NGSI	Next Generation Safeguards Initiative
NNLS	non-negative least squares
PD	probability of detection
PFA	probability of false alarm
PGET	passive gamma emission tomographer
PNNL	Pacific Northwest National Laboratory
PWR	pressurized water reactor
RADSAT	RAdiation Detection Scenario Analysis Toolbox
RCC	right circular cylinder
ROC	receiver-operator characteristic
ROI	region of interest
SKB AB	Swedish Nuclear Fuel and Waste Management Company
SNIC	Swedish National Infrastructure for Computing
SSM	Swedish Radiation Safety Authority
STUK	Finnish Radiation and Nuclear Safety Authority
SWESP	Swedish Support Program to the IAEA
UGET	universal gamma emission tomographer
UPPMAX	Uppsala Multidisciplinary Center for Advanced Computational Science

USSP	U.S. Support Program to the IAEA
UU	Uppsala University
VVER	water-water energetic reactor (Vodo-Vodyanoi Energetichesky Reaktor, Russian nuclear reactor design)

# Contents

Abstract .....	iii
Executive Summary .....	iv
Acknowledgments.....	xxi
Acronyms and Abbreviations .....	xxii
Contents .....	xxiv
Figures .....	xxvii
Tables.....	xxxvi
1.0 Introduction .....	1
2.0 Overview of Prior Work .....	5
2.1 IAEA MSSP JNT 1510: Tomography for Safeguards Applications.....	5
2.1.1 Field Trials and Key Findings .....	6
2.1.2 Next Steps .....	8
2.2 Additional Experimental Experience of Emission Tomography on Nuclear Fuel.....	9
3.0 Study Parameters .....	11
3.1 Verification Objectives .....	11
3.1.1 Objective 1: Independent Pin Counting for Verification of Item Integrity .....	11
3.1.2 Objective 2: Pin-by-pin Characterization for Detection of Anomalies .....	11
3.2 Implementation Scenarios and Fuel Parameters .....	11
3.2.1 Account for a Range of Complexity in Tomographic Measurement .....	12
3.2.2 Account for a Range of Possible IAEA Implementation Scenarios.....	12
3.2.3 Consider Available Resources and Schedule .....	12
3.3 Key Outcomes from Phase I.....	13
4.0 Modeling and Analysis Framework: Overview.....	15
5.0 GET Simulated Spent Fuel Library .....	16
5.1 Relevant Prior Work.....	16
5.2 GET Fuel Library Definition.....	16
5.3 Definition of Pin-Diversion Scenarios .....	19
6.0 Experimental Studies of Single-Pixel Detectors.....	21
6.1 Measurement Campaign Overview .....	21
6.2 Evaluation of Collected Gamma-ray Spectra.....	24
6.3 Summary Findings from Single-Pixel Measurements.....	25
7.0 Defining a Universal GET .....	27
8.0 Simulating Fuel Assembly Populations.....	33
8.1 Generation of Source Terms .....	33
8.2 Radiation Transport to Produce Flux Sinograms .....	33
8.3 Detector-response Sinograms.....	36

8.4	Creating Realistic Virtual Assembly Populations .....	38
8.4.1	Pin-to-pin Burnup Variation.....	38
8.4.2	Statistical Noise.....	39
8.5	Verification and Validation of Simulated Tomographer Responses .....	40
8.5.1	Process Validation: Source Term to Detector Response .....	40
8.5.2	Validating MCNP simulations using data from the PLUTO Device .....	42
8.5.3	Validating Models of the JNT 1510 Device.....	44
8.5.4	Cross-verification: MCNP and Geant4 UGET Models.....	48
9.0	Tomographic Reconstruction Algorithms .....	57
9.1	Overview of Available Reconstruction and Analysis Methods .....	57
9.1.1	Analytic Reconstruction Algorithms.....	57
9.1.2	Algebraic Reconstruction Algorithms.....	59
9.1.3	Image Analysis Methods.....	61
9.2	Reconstruction and Analysis Methods used for Verification Objective 1 .....	62
9.2.1	Methods Used by USSP .....	62
9.2.2	Methods Used by SWESP .....	63
9.3	Reconstruction Methods Used for Verification Objective 2 .....	68
9.3.1	Methods Used by SWESP.....	69
9.3.2	Methods Used by USSP .....	72
9.4	Conclusions for Reconstruction and Analysis Methods.....	76
10.0	Objective 1: Performance Metrics and Results .....	78
10.1	USSP Analyses.....	79
10.1.1	Performance Metrics .....	79
10.1.2	Results .....	80
10.2	SWESP Analyses .....	83
10.2.1	Demonstration of Analysis Methods Using Experimental Data .....	84
10.2.2	Analyses of UGET Device Performance.....	86
10.2.3	Conclusions and Suggested Inspection Procedure .....	91
11.0	Objective 2: Performance Metrics and Results .....	95
11.1	SWESP Analyses and Results.....	95
11.1.1	Assessing Rod-wise Isotopic Distributions .....	96
11.1.2	Determining Pin-wise Burnup and Cooling Time.....	100
11.1.3	Concluding Remarks on the SWESP Analyses for Verification Objective 2 .....	102
11.2	USSP Analyses and Results .....	103
11.2.1	Results: MCNP-based System Matrix for Methods Confirmation.....	103
11.2.2	Results: RADSAT-based System Matrix .....	105
12.0	Conclusions .....	111
13.0	References .....	115
Appendix A	.....Tabular Overview of Modeling and Analysis Framework	A.1

Appendix B Emission Intensity Values for Characteristic Gamma-ray Lines from GET Fuel Library	B.1
Appendix C ..... – TOMOPACK software for Objective 2 System Matrices	C.1
Appendix D ..... RADSAT for Objective 2 System Matrices	D.1
Appendix E ..... ROC Curves for Objective 1	E.1



# Figures

Figure ES.1. Illustration of GET analysis and evaluation framework, from Monte Carlo modeling of emitted signatures through performance evaluation.....	vii
Figure ES.2. Example of empirical validation performed for GET modeling and analysis framework. (Top) Measured and simulated projection data (count rate versus position for a single detector of the instrument) from a Swedish tomographer. (Bottom) Measured (left) and simulated (right) image reconstructions for assay of $^{140}\text{Ba}$ concentration in BWR assemblies using the same tomographer, and filtered backprojection without attenuation correction. ....	viii
Figure ES.3. Diagram of a single detector head of the nominal universal GET design (UGETv1) defined in Phase I (left). The full instrument would include four heads, eight detectors each, and a translate-rotate geometry (right).....	x
Figure ES.4. Algebraically reconstructed image of the $^{140}\text{Ba/La}$ distribution in a SVEA-96 BWR assembly measured using the PLUTO device (left). The results of automated rod search in the reconstructed image, continuing until the whole image area is filled. Identified positions are overlaid in red over the reconstructed image (middle). A histogram of the pin scores extracted in the automated image analysis. The positions that correspond to actual fuel rods are marked with blue bars and non-rod positions are marked with red bars in the histogram (right). ....	xi
Figure ES.5. Example pin-score plots for present and missing pins, assuming UGET assay of PWR assemblies (40 GWd/MTU, 1-year cooling) using the 1275 keV emission from $^{154}\text{Eu}$ . USSP calculations assume significant pin-wise burnup variation and simple FBP reconstruction algorithms (top). SWESP calculations assume no pin-wise burnup variation, nominal attenuation correction, and inclusion of the detection system's response function in an algebraic reconstruction process (bottom). ....	xii
Figure ES.6. Predicted sensitivity for detection of a single missing pin (i.e., bias defect) for Ideal PGET and UGET for BWR, VVER and PWR fuels. Nominal burnup of 20 GWd/MTU and 5-year cooling time with assay based on $^{154}\text{Eu}$ (left); BWR performance is even higher than for VVER and therefore, not shown. Nominal burnup of 10 GWd/MTU and 40-year cooling time with assay based on $^{137}\text{Cs}$ (right). ....	xiii
Figure ES.7. Example results for the pin-by-pin quantification of isotopic concentration using UGETv1 and a total assay time of less than 60 minutes. Fractional error is the relative difference between calculated and true isotopic concentrations. SWESP calculations of $^{154}\text{Eu}$ (based on only the 1275 keV emission) assuming no pin-wise burnup variation and 10 PWR assemblies, nominally 40 GWd/MTU and 1-year cooling (top). USSP calculations of $^{137}\text{Cs}$ (based on 662 keV emission) assuming $\pm 20\%$ pin-wise burnup variation and 1000 VVER assemblies, nominally 20 GWd/MTU and 5-year cooling (bottom). Tampered pins (blue), have a nominal activity half that of the present pins (green). ....	xvii
Figure ES.8. Fractional error of Ideal PGET-assayed isotopic concentrations in VVER fuels. $^{154}\text{Eu}$ for nominal burnup of 20 GWd/MTU and 5-year cooling time (top). $^{137}\text{Cs}$ for nominal burnup of 10 GWd/MTU and 40-year cooling time. In both cases, 100 virtual assemblies, $\pm 20\%$ pin-wise burnup variation, and 60-minute assay times were assumed (bottom). Tampered pins (blue), have a nominal activity half that of the present pins (green). ....	xviii
Figure 1. Schematic of the PGET detector heads (left); rendering of the PGET instrument design including the housing and fuel assembly in the interrogation chamber (right). ....	6

Figure 2. Example images from fuel-pin arrays measured during the Ispra 2012 tests, using the $^{137}\text{Cs}$ energy window.....	7
Figure 3. Example PGET images from BWR fuel assemblies measured during the Olkiluoto 2013 tests: 8x8 BWR with one water channel, 41 GWD/MTU, 27-year cooling time (left); 10x10 BWR with 3 x 3 pin water-channel section, 38 GWD/MTU, 10-year cooling (right). Both were assayed using the 700-1100-keV energy window corresponding to $^{154}\text{Eu}$ .....	7
Figure 4. Example PGET images from VVER-440 fuel assemblies measured during the Loviisa 2014 tests: 44 GWD/MTU, 12-year cooling time (left); assembly with 3 removed pins, 41 GWD/MTU, 12-year cooling time (right). Both were assayed using the 700-1100-keV energy window corresponding to $^{154}\text{Eu}$ . ....	8
Figure 5. Flowchart describing the modeling and analysis framework for the GET viability study.	15
Figure 6. Measured gamma-ray spectra (left column, logarithmic scales) and spectra normalized so that maximum is one (right column, linear scales). Peak positions for $^{134}\text{Cs}$ (605 and 796 keV), $^{137}\text{Cs}$ (662 keV) and $^{154}\text{Eu}$ (1274 keV) are marked with 34, 37, and 54, respectively. ....	23
Figure 7. Comparison of two fuel tomographer designs used to inform the UGETv1 design: PGET, based on two large arrays of small, non-spectroscopic CdTe detectors in a rotate-only geometry (left), and PLUTO, based on a few large spectroscopic BGO scintillators in a translate-rotate geometry (right). ....	27
Figure 8. Detector response functions for NaI and LaBr <sub>3</sub> for simulated projection data.....	29
Figure 9. Total count rate as a function of the collimator design, assuming a 3.8x3.8 cm LaBr <sub>3</sub> scintillator. ....	30
Figure 10. Peak count rate for the 1275 keV line from $^{154}\text{Eu}$ as a function of collimator and scintillator size. The target count rate, which reflects the count rate needed to provide sufficient statistical precision in reasonable count times, is shown. A PWR fuel with burnup of 20 GWD/MTU and 5-year cooling time was assumed in this calculation. ....	30
Figure 11. Diagram of a single detector head of the nominal Universal GET design defined in Phase I (left), the full instrument would include four heads, 8 detectors each, and a translate-rotate geometry (right). ....	31
Figure 12. Overview of modular process for creating simulated fuel assemblies. ....	33
Figure 13. Illustration of how simulations of single-pin flux sinograms for a single energy region are used to assemble a full BWR assembly flux sinogram in that energy region. ....	36
Figure 14. Depiction of charge-carrier trapping effects (i.e., tailing) on CdTe detector response functions, in the context of a PGET energy window spanning 400-700 keV. For this study, 50 percent tailing was assumed.....	37
Figure 15. Comparison of simulated detector response functions for LaBr <sub>3</sub> (3.8-cm RCC) and CdTe (wafer with edge facing incident flux and 1.5 cm <sup>3</sup> cube). Tailing effects of 50 percent were assumed for the CdTe. Labels on the peaks are the peak-to-total efficiency for each detector type.....	38
Figure 16. Example tomographic images of a VVER assembly reconstructed based on sinograms with varying levels of pin-to-pin burnup variation. A uniform distribution over the variation extents is assumed.....	39
Figure 17. Example PGET images of a VVER assembly obtained in reconstructions based on sinograms created by adding different levels of statistical noise, corresponding to different integration times. ....	39

Figure 18. Benchmarking comparison between experimental and calculated HPGe spectra for a 17x17 PWR spent nuclear fuel assembly with 16-year cooling time measured at the Clab facility in Sweden. The table compares measured and calculated peak areas for nine characteristic photopeaks in the spectrum. ....	41
Figure 19. Benchmarking comparison between experimental and calculated HPGe spectra for a 17x17 PWR spent fuel assembly with 7-year cooling time measured at the Clab facility in Sweden. The table compares measured and calculated peak areas for 12 characteristic photopeaks in the spectrum.....	42
Figure 20. Overlay of the measured and calculated projection data profiles at two arbitrary angular orientations for the SVEA-96S spent fuel assembly in the PLUTO instrument at Forsmark nuclear power plant. All data are normalized by the total area. Two sets of calculated data are depicted: total gamma-ray flux with scattering contribution and the direct transmission from the source location. ....	43
Figure 21. Comparison of reconstructed images from the measured and calculated projection data for the PLUTO experiment with the SVEA-96S BWR assembly at the Forsmark nuclear power plant, providing an experimental benchmark for the adopted simulation procedure.....	44
Figure 22. Overlay of the measured and calculated projection data profiles at two arbitrary orientations from PGET instrument test measurements with a VVER-440 assembly at Loviisa nuclear power plant in 2014 [Levai 2014]. Datasets are normalized by the total area. Calculated results demonstrate a good agreement in the contrast region as well as in the gamma-ray scattering contribution. The right side of the measured profile in the 180-degree projection demonstrates higher pixel count rates due to electronics effects at the time of the experiment. ....	45
Figure 23. Reconstructed images (filtered back projection method) of measured and calculated projection data from PGET instrument test with a VVER-440 spent fuel assembly with three missing pins at Loviisa nuclear power plant in 2014. Ring artefacts and smearing in the measured image are likely due to effects of electronics instabilities. ....	46
Figure 24. The JNT 1510 model used in Geant4. ....	47
Figure 25. Calculated counts above three energy thresholds (400 and 700 keV) for two different rotational angles of the JNT 1510 device. The calculated counts (c) have been normalized to the corresponding average measured count (m). ....	47
Figure 26. MCNPX geometry used the 45-degree rotation (and -23 mm lateral position) in case 1. The photon current through the surfaces at the back of the square detector surfaces were sampled, i.e. using the F1 tally. ....	49
Figure 27. The investigated rod positions (left), the contribution of each rod to all detector positions in the 0 degree rotation of case 1 (center), the corresponding contributions in the 45-degree rotation of case 1 (right).....	49
Figure 28. Schematics showing the Geant4 model of the UGET device. The left part illustrates the coordinate system that defines the lateral position and rotation of the device relative to a fuel assembly indicated by the blue square in the center. The rotation is given by angle phi. The lateral position is given by the y' position of the collimator head (i.e. the distance between the center of the head and the x' axis). The right part indicates a view from above for case 2 with 0 degree rotation and -23 mm lateral position (i.e., with detector number 5 pointing towards the central rod in the assembly). ....	50
Figure 29. The number of counts in the full energy peak, per emitted source photon for the energies 662 keV (left column) and 1274 keV (right column), for detector numbers 3 (bottom), 5 and 7 (top) in the 0-degree rotation of case 1. ....	51

Figure 30. The number of counts in the full energy peak, per emitted source photon for the energies 662 keV (left column) and 1274 keV (right column), for detector numbers 3 (bottom), 5 and 7 (top) in the 45-degree rotation of case 1.....	52
Figure 31. Comparison between Geant4 and MCNP calculations of the 1274-keV source in case 1. The left pane shows the 0-degree rotation and the right pane shows the 45-degree rotation. The correlation coefficient for a linear model is given by the parameter $r$ , where a value close to 1 indicates linearity. ....	53
Figure 32. The projections for 0-degree (top) and 45-degree (bottom) rotation using a 1274-keV source distributed homogenously over the fuel rods, calculated with the MCNP and Geant4 models. The horizontal line indicates an arbitrarily selected threshold for removing counts originating outside the field of view. ....	54
Figure 33. The relative difference between MCNP and Geant4 calculations as a function of MCNP calculated full energy peak counts. The vertical lines indicate the position of the threshold set in Figure 32.....	55
Figure 34. The frequency distribution of the relative differences between MCNP and Geant4 calculations, where all calculations are above the threshold set in Figure 34. The solid lines indicate a Gaussian fit to the calculated data. ....	56
Figure 35. Schematic relations in Fourier reconstructions.....	58
Figure 36. Schematic illustration of the filtered backprojection technique (BP=backprojection). ....	58
Figure 37. Tomographic reconstruction methods for Objective 1 translate sinogram data into images of gamma-ray emission intensity. These images are further analyzed to deduce pin-wise data. ....	62
Figure 38. Example reconstructed image of a VVER-440 assembly from a virtual assembly population (left), pin-region average intensity values for that virtual assembly (right). ....	62
Figure 39. Pin scores from 100 VVER-440 assemblies assayed by the PGET, instrument assuming a total assay time of less than 10 minutes and an energy window of $>700$ keV. The assembly population has a nominal burnup of 20 GWd/MTU, cooling time of 5 years and pin-wise activity variation of $\pm 20$ percent.....	63
Figure 40. An example of an attenuation correction image obtained by simulating the response of a homogeneous distribution of fuel materials in the image area. The correction image is given by the inverse of the reconstruction results from these simulations, normalized to an average of one. Here, dark areas correspond to large correction factors and bright areas to small. For a homogeneous object of BWR fuel size, the ratio between the highest and lowest correction factor was 2.16. As expected, the correction matrix is rotationally symmetric. In this case, the corners are given high correction factors, which is a result of limitations in the width of each projection in the simulated data set used here.....	64
Figure 41. The modeled response function (a.u. on the $z$ axis) of the UGET device for 1274 keV gamma rays (top figure), taking into account the physical properties of the measurement system (e.g., in terms of finite collimator slit width and gamma-ray transmission through the collimator material). These effects give rise to significant contributions from penumbra and umbra regions. The origin ( $X,Y=0$ ) of the response function is centered at the front of the slit opening, and only positive $Y$ s are presented (bottom figure). ....	65
Figure 42. The 55x55 quadratic pixel pattern used for SWESP reconstructions of BWR fuel, overlaid over the SVEA-96 fuel geometry (left); an illustration of the gamma-ray attenuation model used in SWESP algebraic image reconstructions for Verification Objective 1 (right) (Jacobsson Svärd et al. 2015a).....	66

Figure 43. The cross section of the SVEA-96 fuel assembly (left), an example of a reconstructed image (middle), and the mask applied on the reconstructed images for deducing the position of the assembly in the measuring device (right). .....	67
Figure 44. The reconstructed image from Figure 44 (left); a mask applied for identifying individual fuel rods in the image (right) (from Troeng 2004). .....	67
Figure 45. Histograms of rod activities, deduced using image analysis routines applied on images reconstructed from simulated $^{137}\text{Cs}$ data (662 keV) of a BWR assembly with equal activity contents in all fuel rods. Activities are presented in arbitrary units on the x axis and the frequency of fuel rods on the y axis. The search for fuel rods have continued until the whole image was filled. Identified objects corresponding to fuel rods are marked in blue, whereas regions in the background are marked in red. ....	68
Figure 46. Graphical depiction of the Objective 2 reconstruction process. ....	69
Figure 47. For Verification Objective 2, one may use a priori information to improve the algebraic reconstructions. Left: The pixel pattern can be adapted to fit the regions containing gamma-ray emitting materials. In the SWESP reconstructions in this work, a pattern with 5 pixels covering each fuel rod has been used, here illustrated for a SVEA-96 assembly. No pixels are assigned to other regions in the assembly. Right: The gamma ray attenuation in the fuel area is taken into account in detail by introducing exact estimates of the travel distances $d_i$ through different materials in the fuel. In particular, the uranium dioxide of the fuel pellets, illustrated in grey shade, attenuates the gamma rays significantly. ....	71
Figure 48. Overview of how PNNL's RADSAT hybrid transport is used to generate the system matrix, $W$ for a tomographer. ....	73
Figure 49. Zero angle flux projections for RADSAT (red) and MCNP (black) for the flux in a 1-keV energy bin covering the 662-keV emission from $^{137}\text{Cs}$ . ....	74
Figure 50. Reconstructions for 1-keV sinogram data (see Figure 50) generated by MCNP (left) and RADSAT (right) radiation transport. ....	74
Figure 51. RADSAT single-pin projection data, including the object-scatter contributions below the peak energy of 662 keV. ....	75
Figure 52. Full-assembly down-scatter as a function of energy and detector pixel, assuming an ideal PGET design, for a projection angle of 0 degrees: MCNP (left) and RADSAT (right). .	75
Figure 53. Map of the missing pin locations (in red) in the three assembly types: five for BWR (left), six for VVER (middle) and 11 for PWR (right). ....	78
Figure 54. Example of how pin-score distributions for missing and present pins (left pane) can be used to calculate the probably of detection (PD) and probability of false alarm (PFA) as a function of threshold, $T$ . The result is a ROC curve for a specific pin location (right pane)....	79
Figure 55. Example ROC curves as a function of pin location in a population of PWR assemblies with nominal burnup of 20 GWd/MTU, cooling time of 5 years and pin-wise burnup variation of +/-20%, and assay using the PGET device and an energy window >700 keV. Ring 1 is composed of the 8 pins that form a square closest to the center of the assembly, Ring 2 is formed from the pins in the next square region, and the rest of the rings are aggregated similarly. Scores from the water channels are not included in the ROC analysis. Rings 6-8 have identical performance; only Ring 6 is shown. ....	80
Figure 56. Predicted sensitivity for detection of a single missing pin (i.e., bias defect) for UGET, assuming VVER and PWR fuel with nominal burnup of 40 GWd/MTU and 1 year cooling time. BWR performance is even higher than for VVER and therefore, not shown. No results are shown for PGET because the count rates for this high-burnup, short-cooled fuel are too high for that instrument. ....	81

Figure 57. Predicted sensitivity for detection of a single missing pin (i.e., bias defect) for PGET and UGET, assuming VVER and PWR fuel with nominal burnup of 20 GWd/MTU and 5-year cooling time. BWR performance is even higher than for VVER and therefore, not shown. ....	82
Figure 58. Predicted sensitivity for detection of a single missing pin (i.e., bias defect) for PGET and UGET, assuming BWR, VVER, and PWR fuel with nominal burnup of 10 GWd/MTU and 40-year cooling time. ....	82
Figure 59. Ring-level ROC curves (left) and pin-score summary (right) for PWR fuel with nominal burnup of 10 GWd/MTU and 40-year cooling time. Note the overlap in pin scores between present and missing pins (and water channels) for much of the inner portion of the assemblies. ....	83
Figure 60. Reconstructed image of the $^{140}\text{Ba}/\text{La}$ distribution in the SVEA-96 fuel assembly that was measured using the PLUTO device in the Forsmark NPP in 2002 (left)(Jacobsson Svård et al. 2005). The results of automated rod search in the reconstructed image, continuing until the whole image area is filled. Identified positions are overlaid in red over the reconstructed image (middle). A histogram of the rod activities extracted in the automated image analysis (right). The positions that correspond to actual fuel rods are marked with blue bars and non-rod positions are marked with red bars in the histogram. ....	85
Figure 61. Initial reconstructed image based on PGET data collected on a BWR 8x8 assembly in Olkiluoto, showing assembly misalignment and a severe artifact in the device's center due to poor energy calibration of the detector elements (left). The frame illustrates the nominal fuel position in the device. The results of assembly positioning, a new image reconstruction and automated rod search in the new image (steps 2-4 above). Here, the 64 identified highest-activity positions are overlaid in red over the reconstructed image (middle). (NB: This fuel type contains 63 rods and one central water channel, but the central artifact destroys the possibility to analyze the fuel's centre.) A histogram of the rod activities obtained in the automated image analysis, when continuing to search for possible rods until the whole image area is filled (left). The 64 positions illustrated in the middle image are marked with blue bars in the histogram and the additional regions are marked with red bars. ....	85
Figure 62. A reconstructed grey-scale image of a VVER-440 assembly in the PGET Loviisa measurements, including a representation (red) of a nominal VVER assembly geometry, centered in the device. (Figure from Davour et al. 2016.) Image analysis shows that the fuel assembly (in grey-scale) is dislocated by as much as +29.9 mm in x (horizontal in this image) and +10.2 mm in y (vertical in this image). ....	86
Figure 63. A reconstructed image (left), obtained in algebraic reconstruction including modeling of the UGET device's response function and uniform attenuation in the image area. Results of automated image analysis for identifying possible fuel rods in the image and quantifying their activity contents (right). A discriminator level is indicated in the figure, offering complete separation of fuel rods (blue) from water channels (white) and empty fuel-rod positions (red), indicating a perfect ROC curve. ....	88
Figure 64. Rod scores obtained when analyzing a set of 10 sinograms from 1-year cooled PWR 17x17 fuel using algebraic image reconstruction and automated image analysis to extract reconstructed rod-by-rod activities. Rods are ordered in "rings" (quadratic) according to radial distance from the assembly center. The two innermost rings are not separated here. All empty fuel-rod positions are clearly separated from the distribution of fuel rods. However, for as yet unknown reasons, the five most central water channels do not offer the same level of separation, albeit still scoring lower than all fuel rod positions in all 10 simulations. ....	89

Figure 65. Similar analysis as in Figure 65, but for data at a total assay time of 40 mins. All empty fuel-rod positions are still clearly separated from the distribution of fuel rods. However, the five most central water channels overlap somewhat with the distribution of fuel rods. ....	90
Figure 66. Rod scores obtained when analyzing a set of 10 sinograms from long-cooled, low-burnup PWR 17x17 fuel using algebraic image reconstruction and automated image analysis to extract reconstructed rod-by-rod activities. There are some overlaps between fuel rods and non-rod positions in the inner sections. However, for the dominant part of the fuel (the >70 percent that are situated in the four outermost rings), non-rod positions can be easily separated from fuel rods.....	91
Figure 67. Illustration of the Objective 2 analysis approach. The comparison of reconstructed rod-wise isotopic activities to a known ground truth is the key performance metric for this objective.....	95
Figure 68. Results obtained in tomographic reconstructions of simulated $^{137}\text{Cs}$ data from a SVEA-96 fuel assembly in the PLUTO device (data from Jacobsson Svård et al. 2015a). All rods were assigned equal $^{137}\text{Cs}$ contents in the simulations. A gray-scale 55x55-pixel tomographic image of the $^{137}\text{Cs}$ distribution in the assembly cross section (left). Relative pin-wise contents of $^{137}\text{Cs}$ obtained in a reconstruction using the methods described in Section 9.3.1 (right). The precision obtained was 0.87 percent ( $1\sigma$ ), indicating that relative pin-by-pin $^{137}\text{Cs}$ contents can be measured at the 1% level for this fuel type. ....	97
Figure 69. Results obtained in tomographic reconstructions of simulated sinograms for a short-cooled, high-burnup PWR 17x17 fuel assembly in the suggested UGET device design, presented as mean values of fractional error in reconstructed rod-by-rod isotopic contents obtained in analyses of 10 datasets, including error bars corresponding to $\pm 1\sigma$ confidence intervals. All rods were assigned equal isotopic contents in the simulations. The analyses were made based on full-energy gamma peaks at 662 keV ( $^{137}\text{Cs}$ ), 796 keV ( $^{134}\text{Cs}$ ) respectively 1274 keV ( $^{154}\text{Eu}$ ).....	98
Figure 70. Results obtained in tomographic reconstructions of simulated sinograms for a long-cooled, low-burnup PWR 17x17 fuel assembly in the suggested UGET device design, presented as mean values of fractional error in reconstructed rod-by-rod isotopic contents of $^{137}\text{Cs}$ obtained in analyses of 10 datasets, including error bars corresponding to $\pm 1\sigma$ confidence intervals. All rods were assigned equal isotopic contents in the simulations. ....	99
Figure 71. Fractional error, relative to true values, for pin-by-pin isotopic activity determination using UGET, PNNL's algebraic reconstruction method, and MCNP-based system response function. The top pane shows results for $^{137}\text{Cs}$ , and the bottom pane shows results for $^{154}\text{Eu}$ . The 100-assembly population assumed VVER fuel with nominal burnup of 20 GWd/MTU, 5-year cooling time, and $\pm 20$ percent pin-wise burnup variation. Tampered pins (blue), have a nominal activity half that of the present pins (green).....	105
Figure 72. Fractional error, relative to true values, for pin-by-pin $^{154}\text{Eu}$ activity determination using UGET, PNNL's algebraic reconstruction method, and RADSAT-based system response function. The 100-assembly population assumed VVER fuel with nominal burnup of 40 GWd/MTU, 1-year cooling time, and $\pm 20$ percent pin-wise burnup variation. Tampered (substituted) pins (blue), have a nominal activity half that of the present pins (green). No results are shown for PGET because the count rates for this high-burnup, short-cooled fuel are too high for that instrument. ....	106

Figure 73. Fractional error, relative to true values, for pin-by-pin $^{154}\text{Eu}$ activity determination using UGET (top panel) and PGET (bottom panel) using PNNL's algebraic reconstruction method and RADSAT-based system response function. The 100-assembly population assumed VVER fuel with nominal burnup of 20 GWd/MTU, 5-year cooling time, and $\pm 20$ percent pin-wise burnup variation. Tampered pins (blue), have a nominal activity half that of the present pins (green).....	107
Figure 74. Fractional error, relative to true values, for pin-by-pin $^{137}\text{Cs}$ activity determination using UGET (top panel) and PGET (bottom panel) using PNNL's algebraic reconstruction method and RADSAT-based system response function. The 100-assembly population assumed VVER fuel with nominal burnup of 10 GWd/MTU, 40-year cooling time, and $\pm 20$ percent pin-wise burnup variation. Tampered pins (blue), have a nominal activity half that of the present pins (green).....	108
Figure APX C.1. Illustration of some possible geometries of the CIRCLE_PART object..	C.4
Figure APX C.2. Overview over the TOMOPACK software implementation of geometry modules.....	C.5
Figure APX C.3. Illustration of the COLLIMATOR object.....	C.6
Figure APX C.4. Illustration of the FUEL object, here with data for a GE12S fuel assembly. In this case, small-diameter RINGS are fuel rods and large-diameter RINGS are water rods.....	C.7
Figure APX C.5. Overview over the TOMOPACK software implementation of tomography modules.....	C.8
Figure APX D.1. Predefined tetrahedral mesh showing fuel and clad regions.....	D.1
Figure APX D.2. Treatment of JNT 1510 collimator with two sets of angles showing aperture field of view angles (red) and penetrating angles (blue) for down-scatter energy groups (left) and peak energy groups (center); and (right) treatment of the UGET-v1 collimator with unattenuated aperture field of view angles (red) and penetrating angles (blue). .....	D.2
Figure APX D.3. Coordinate system to define angular quadrature for modeling the collimators..	D.3
Figure APX D.4. Angular sensitivities of the PGET (left) and UGET (right) collimators.....	D.4
Figure APX D.5. Reconstructions from 661-662 keV sinograms from MCNP (left) and RADSAT (right) based models for a VVER-440 assembly. ....	D.4
Figure APX D.6. Reconstructions from 661-662 keV sinograms from MCNP (left) and RADSAT (right) based models for a PWR assembly.....	D.5
Figure APX D.7. Zero angle projections for all downscattered energy bins from (40-661 keV) from MCNP (upper-left), MCNP "smoothed" (upper-right) and RADSAT (lower) based models.....	D.5
Figure APX D.8. Reconstructions from 200-210 keV sinograms from MCNP (left), MCNP "smoothed" (center) and RADSAT (right) based models. ....	D.6
Figure APX D.9. Reconstructions from 400-661 keV sinograms from MCNP (left), MCNP "smoothed" (center) and RADSAT (right) based models. ....	D.7
Figure APX E.1. Probability of detection (PD) for a single missing pin in each ring of an assembly, versus the ring-level PFA (i.e., not assembly-level PFA) for PGET (left) and UGET (right). Fuel is BWR nominal burnup of 10 GWd/MTU and 40-year cooling.....	E.1
Figure APX E.2. PD for a single missing pin in each ring of an assembly, versus the ring-level PFA (i.e., not assembly-level PFA) for PGET and UGET, assuming VVER-440 fuels: 40 GWd/MTU, 1-year cooling (top); 20 GWd/MTU, 5-year cooling (middle); 10 GWd/MTU, 40-year cooling (middle).....	E.2



Figure APX E.3. PD for a single missing pin in each ring of an assembly, versus the ring-level PFA (i.e., not assembly-level PFA) for PGET and UGET, assuming PWR fuels: 40 GWd/MTU, 1-year cooling (top), 20 GWd/MTU, 5-year cooling (middle), 10 GWd/MTU, 40-year cooling (bottom). ..... E.3

# Tables

Table ES.1. Description of implementation scenarios as originally defined for JNT 1955 Phase I. .vi	
Table ES.2. Summary of the USSP Objective 1 findings: probability of detecting a single missing pin in any location of an assembly, for an assembly-level false alarm rate of 0.10. Key assumptions: 1000 assemblies per population and $\pm 20\%$ pin-wise burnup variation; total assay times of less than 60 minutes; perfect energy and efficiency calibration; FBP image reconstruction algorithms without any form of attenuation correction. Note that Ideal PGET is not capable of assay high burnup, short-cooled fuels due to count-rate limitations (denoted with X). Red PD values indicate scenarios where detection probabilities for a single missing inner pin are in the range of IAEA's low detection probability.....xiv	
Table ES.3. Summary of Objective 2 findings: Estimated detectable burnup discrepancy, compared to ground truth, for interior pins, for PD of 0.95 and assembly-level false alarm rate of 0.10 for the PGET and UGET device designs. Key assumptions: Total assay time less than 60 minutes; "perfect" PGET energy and efficiency calibration. Note that Ideal PGET is not capable of assay high burnup, short-cooled fuel due to count-rate limitations, and that Ideal PGET performance for PWR has not been analyzed. Neither was UGET analyzed for the 20 GWd/MTU PWR case. ....xix	
Table 1. Summary of support program roles in JNT 1955 Phase I. The total effort associated with each task is represented by four boxes; the relative contributions of each organization are denoted by the number of boxes. ....2	
Table 2. Some pros and cons of GET instrumentation including detectors with high full-energy-peak gamma-detection efficiency in the context of safeguards and fuel integrity verification.10	
Table 3. Description of implementation scenarios considered in JNT 1955 Phase I.....13	
Table 4. Summary of spent fuel assembly models in the GET library. ....17	
Table 5. Characteristic fission products and associated gamma-ray emissions from spent fuel in 0.4 and 2.5 MeV energy region. ....18	
Table 6. Parameters for the digital data acquisition system and data on the used detectors, as supplied by the manufacturers. The amount of given detector specifications varies between manufacturers. The energy resolution for BGO was estimated using measured data.....22	
Table 7. Parameters of the used nuclear fuel assemblies measured.....22	
Table 8. Evaluated data on peaks identified in the measured energy spectra as given by the data acquisition software used. Intensities (I) are given in counts per second with one sigma uncertainty. The energy resolution (R) is given as full width half maximum (FWHM) relative to the peak position, in percent. No data on energy resolution are presented for cases where the data acquisition software reported data that were obviously incorrect, e.g., less than 0.01 percent for the LaBr detector. ....24	
Table 9. Parameters of the UGETv1 design. ....31	
Table 10. Summary of selected cases for a code-to-code benchmark of the models used in the UGET simulations, covering the gamma-ray flux from a PWR 17x17 fuel assembly. In all cases, two source energies (662 keV and 1274 keV) and two rotations of the device (0 and 45 degrees) were used.....48	
Table 11. Pros and cons of analytic FBP reconstruction techniques for use on nuclear fuel assemblies. ....59	
Table 12. Pros and cons of algebraic reconstruction techniques for use on nuclear fuel assemblies.61	

Table 13. The alternative approaches taken in this work in the modeling of the system matrix W used in algebraic reconstructions for Verification Objective 2.....	77
Table 14. The set of fuel parameters and total assay times analyzed using the SWESP reconstruction and analysis toolbox. All cases were simulated for PWR 17x17 fuel, and each case comprised a set of 10 sinograms. The simulated data were provided by USSP. The total assay times given include time for positioning of the detectors as well as time for data collection, an were estimated by USSP. ....	87
Table 15. Ring-by-ring precision and systematic deviations of reconstructed isotopic contents from true values, obtained in analyses of simulated sinograms for a 1-year-cooled high-burnup PWR 17x17 assembly in the UGET device design. The statistics in the simulated data corresponds to a total assay time of 40 minutes. ....	99
Table 16. Ring-by-ring precision and systematic deviations of reconstructed $^{137}\text{Cs}$ contents from true values, obtained in analyses of simulated sinograms for a 40-year-cooled low-burnup PWR 17x17 assembly in the suggested UGET device design. The statistics in the data corresponds to varying total assay times, as accounted for in the table.....	100
Table 17. Isotopes typically used for determining fuel burnup and cooling time in gamma-scanning measurements, given with half-lives ( $T_{1/2} = \ln(2)/\lambda$ ), gamma-ray energies ( $E_\gamma$ ) and burnup dependence $\kappa$ (from Jansson 2002). ....	101
Table 18. Estimation of achievable uncertainties in the tomographic determination of pin-wise burnup and cooling time for 1-year cooled high-burnup PWR17x17 fuel based on the effect from counting statistics, given for fuel rods at various distances from the assembly center. The estimations for each combination of isotopes were deduced from the analyses of 10 simulated datasets (sinograms) for the suggested UGET device design, with counting statistics corresponding to a total assay time of 40 minutes. ....	102
Table APX A.1. Overview of Modeling and Analysis Framework. ....	A.1
Table APX B.1. Characteristic Gamma-ray Emission Intensities for GET Assemblies at 1 Year Cooling Time. ....	B.2
Table APX B.2. Characteristic Gamma-ray Emission Intensities for GET Assemblies at 5 Years Cooling Time. ....	B.7
Table APX B.3. Characteristic Gamma-ray Emission Intensities for GET Assemblies at 40 Yrs. Cooling Time. ....	B.12
Table APX D.1. Transport parameters and typical runtimes. ....	D.6

# 1.0 Introduction

The accurate verification of declarations about the fissile content of spent fuel is central to the International Atomic Energy Agency's (IAEA) safeguards approaches at facilities handling and storing irradiated fuel. Generally speaking, IAEA safeguards approaches call for verification of spent fuel using a partial defect or best-available method, for fuels that are being transferred to difficult-to-access storage and that have a design allowing disassembly (IAEA 2006, IAEA 2009, IAEA 2010). Safeguards approaches at various facilities could include spent fuel verification by on-site inspectors using attended methods or alternatively, could be performed by permanently installed, unattended instrumentation. At present, IAEA's authorized instruments for attended partial defect detection have limitations in terms of independence, defect sensitivity, and implementation flexibility. The IAEA has no authorized instrument for unattended partial defect detection in spent fuel. The IAEA states the need for "more sensitive and less intrusive alternatives to existing NDA instruments" for partial-defect detection in its Long-Term R&D Plan (IAEA 2013).

Passive gamma-ray emission tomography (GET) is attractive for addressing partial defect detection and verifying the completeness of the fuel assembly because it has the potential to directly image the spatial distribution of the active fuel material in the fuel pins and the relative locations of the pins in the assembly structure without the need for any operator-declared information. The gamma-ray signatures, particularly in younger fuels, can be strongly correlated to irradiation parameters such as final (integral) burnup and cooling time, thereby achieving more specificity than other methods. Further, tomography has the potential to directly image the interior of the assembly at multiple axial locations along the assembly length so that pin-level assay (as opposed to volume-integrating assay) can be achieved. Finally, gamma tomography is viable in both wet and dry measurement environs, and in either unattended or attended modes, characteristics that afford significant operational flexibility.

A substantial body of knowledge has been assembled, both through modeling and measurements, regarding the viability of gamma-ray tomography. For example, a project undertaken by the IAEA (2003 to present) has designed, fabricated, and field-tested a transportable, underwater version of a gamma-ray emission tomographer. This work has provided invaluable information regarding instrument design and field applicability (Levai et al. 2002, Honkamäa et al. 2014). Past and current projects in Sweden and Norway, funded by reactor operators primarily for purposes of code validation, add to the experience available on equipment design, tomographic reconstruction techniques, and analysis methods. The Swedish experience includes the construction of a laboratory mockup (Jansson et al. 2013) and a heavy, stationary type of underwater test platform, which was used in measurements at a commercial boiling water reactor (BWR) (Jansson et al. 2006). The Norwegian experience includes a tomographic device aiming at measuring power, burnup, and fission gas distributions in research fuel (Holcombe et al. 2015).

Toward the goal of reducing potential confusion about the terminology adopted in this report, a few definitions may be helpful. The acronym GET is used to refer to the topic of gamma-emission tomography generally—it is not specific to a particular instrument design. Because this viability study involves multiple tomographer designs, GET is often used to describe the project and the project team. In this report, the acronym UGET refers specifically to the Universal GET instrument design (i.e., UGETv1) and should not be confused with the use of the same acronym for *unattended* GET. While unattended implementation scenarios were a key motivator for JNT 1955 and "unattended" is even part of the task title, the viability analysis presented in this report is largely agnostic to implementation mode and therefore, the distinction between unattended and attended operation is not emphasized.

While the prior gamma emission tomography work has been informative and encouraging, a number of technical and viability questions need to be addressed in the context of IAEA’s evolving fuel verification needs, for example: What is the potential for GET-based verification over a wide range of fuel types, including fuel with very dense pin spacing (e.g. VVER and PWR) and very long cooling times (e.g., at 40 years where  $^{137}\text{Cs}$  may provide the only viable signature)? Can a single instrument design achieve that potential, while being suitably robust, cost-effective and maintainable for long-term operation? Addressing these questions is the primary motivation for the viability study described in this paper, a study performed under the auspices of several Support Programs to the IAEA: United States, Sweden, Finland, and the European Commission. Participating organizations include:

- United States. Pacific Northwest National Laboratory (PNNL), Lawrence Livermore National Laboratory (LLNL), and Los Alamos National Laboratory (LANL)
- Sweden. Strålsäkerhetsmyndigheten (SSM, Swedish Radiation Safety Authority), Uppsala University (UU)
- Finland: Säteilyturvakeskus (STUK, Finnish Radiation and Nuclear Safety Authority)
- European Commission: Directorate Euratom Safeguards of the Directorate General for Energy of the European Commission. in the framework of the European Commission Support Program.

The roles of the various support programs are summarized in Table 1.

**Table 1.** Summary of support program roles in JNT 1955 Phase I. The total effort associated with each task is represented by four boxes; the relative contributions of each organization are denoted by the number of boxes.

Task	SWESP	USSP	FINSP	EC
Summarize, collect data from prior work	■		■ ■	■
Define “Universal” GET design	■	■ ■ ■		
Define, validate Monte Carlo models	■	■ ■ ■		
Develop simulated projection library		■ ■ ■ ■		
Objective 1 analysis	■	■ ■ ■		
Objective 2 analysis	■ ■	■ ■		
Technical and programmatic review	■	■	■	■

This technical report documents the methods and findings from JNT 1955 Phase I. The organization of this report is presented as follows and reflects the scope of Phase I, as derived from the original project work plan (May 2013).

- Definition of high-priority IAEA fuel verification objectives and high-priority implementation scenarios that can then be used to guide and constrain the scope and evaluation metrics of the viability analysis
- Development of a candidate “Universal GET” (UGETv1) design that uses state-of-the-art options in detector and pulse-processing electronics, and is capable of assaying the wide range of fuel types and implementation scenarios relevant to safeguards verification

- Monte Carlo modeling of GET responses over a wide range of fuel types encountered in IAEA applications, and including difficult-case fuels (e.g., pressurized water reactor [PWR], 10 GWd/t, 40-year cooling)
- Verification of modeled responses using code-to-code verification and validation using available field measurements
- Implementation and evaluation of candidate tomographic reconstruction algorithms capable of incorporating a range of *a priori* information about the object model used in the reconstruction. Emphasis was placed on non-proprietary algorithms that facilitate long-term maintenance and enhancement by the IAEA
- Defect sensitivity analysis using metrics specific to the needs of safeguards verification of assembly/item integrity
- Interpretation of results and discussion of caveats and their potential impact on the findings of the study.



## 2.0 Overview of Prior Work

JNT 1955 Phase I has built on the successes and lessons learned from previous and ongoing studies of GET on irradiated nuclear fuel assemblies. This body of prior work presents an opportunity to share subject matter expertise, instrumentation, methods, data, and experimental testing locations. An overview of that prior work and relevance to JNT 1955 is provided below in this section.

### 2.1 IAEA MSSP JNT 1510: Tomography for Safeguards Applications

As early as the 1980s, the IAEA began exploring passive gamma-ray tomography via the Member State Support Programs (Levai et al. 1993). Under JNT A 01201, small-scale systems (e.g., less than 10 detectors) were developed and tested in multiple field campaigns on BWR and PWR fuel items (Levai et al. 2002). Building on that project, JNT A 1510 began in 2003 and was completed in late 2015. Under JNT 1510, a full-scale, transportable tomography system based on IAEA's user requirements for underwater application was designed, fabricated, and field-tested. Key requirements included:

- Ability to detect missing pins or replaced pins from PWR spent fuel assemblies with minimum burnup of 15 MWd/tU and cooling time up to 40 years. Minimum cooling time and maximum burnup was not defined
- Ability to measure a horizontal section of the assembly at any axial position along the full length of an assembly
- Transportable and adaptable to various fuel types and fuel-pond designs
- Total assay times less than 30 minutes for a given axial slice of the assembly
- Attended operation but automated analysis
- Field implementation by inspectors with no particular tomography expertise (i.e., non-experts)

Based on these requirements, the JNT 1510 team proposed a passive gamma emission tomographer (PGET) design in which two detector arrays, each with 104 detectors, rotate (step by step) around the assembly (Figure 1, left). At each step, data is collected from all detectors in both arrays. Each array measures a full 360 degree scan with 4-mm sampling, and the positions of the two arrays are offset by 2 mm so that the merging of the datasets from the two heads produces 2-mm, 360-degree sampling. Each PGET detector head consists of a multi-slit collimator made of tungsten and 104 cadmium telluride (CdTe) detectors measuring 10 x 5 x 2 mm, with the 2x5 mm face oriented toward the collimator slit.

Full-energy peak efficiency of each CdTe detector is very low (see Section 8.2) due to the small detector size, therefore the gamma-ray signals of interest are collected in broad regions of interest (ROIs). For the  $^{137}\text{Cs}$  line, the typical ROI is 400-700 keV. For the  $^{154}\text{Eu}$  1274-keV peak, the ROI is generally 700-1100 keV. The system has three freely adjustable ROIs, which apply to all detectors. The pulse-processing electronics and calibration process are described in more detail by Sokolov et al. (2008).

The detector heads, pulse-processing electronics, power supplies and rotational stage are contained in a sealed housing (Figure 1, right), a torus with a central hole for the fuel assembly. A circular rail inside the toroidal housing allows rotation of the two detector banks from -10 to +370 degrees in steps of 1 degree, controlled by a stepping motor. The fuel-assembly chamber has a 450-mm height and a 325-mm inner diameter, large enough to assay PWR 17x17 fuel (but not VVER-1000 fuels). The outer diameter of the torus is 955 mm and the entire PGET instrument weighs 520 kg.



The current PGET software package consists of two separate modules, acquisition control and data processing. The interface between the modules is a raw data file. Automated acquisition and analysis is launched through a user interface.

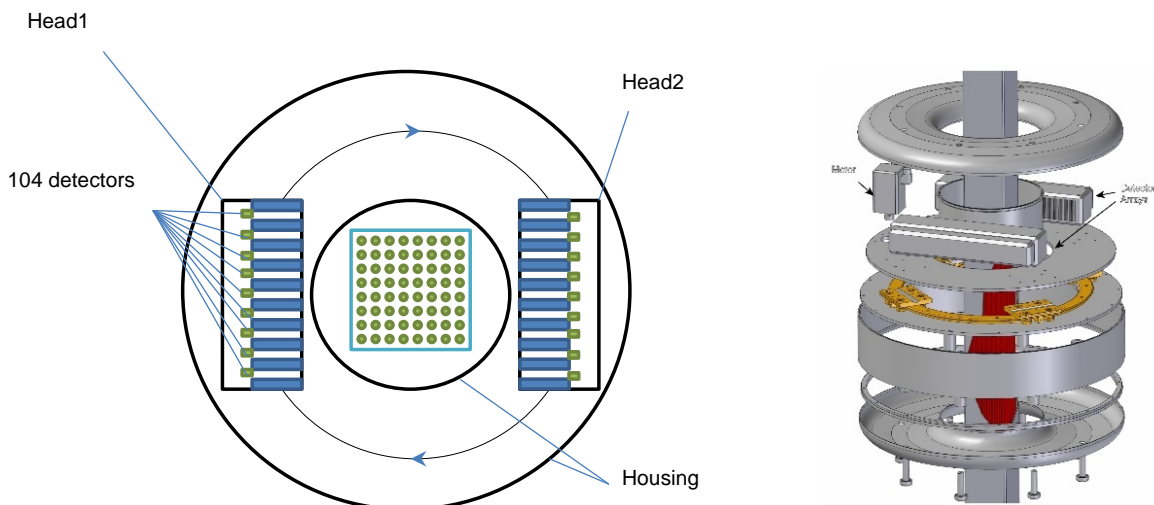


**Figure 1.** Schematic of the PGET detector heads (left); rendering of the PGET instrument design including the housing and fuel assembly in the interrogation chamber (right).

### 2.1.1 Field Trials and Key Findings

During Task JNT 1510, four test campaigns were conducted: Ringhals, Sweden in 2009, Ispra, Italy in 2012, Olkiluoto, Finland in 2013, and Loviisa, Finland in 2014. Each campaign is described briefly in this section, along with key findings and lessons learned that have and will inform continuing IAEA investigation of tomography for spent fuel.

The Ringhals test in 2009 failed to collect any measurement data due to a hardware error in the measurement electronics. The detector arrays were sent to the manufacturer for repair and recalibration. According to the manufacturer, high ripple in the power supply unit and electrical disturbances were responsible for the failure. While the data acquisition aspects of this test were not successful, the test did demonstrate the suitability of the PGET design for field deployments, including in the fuel pond of an operating power reactor.

The Ispra test in 2012 allowed more flexibility for measurement planning and execution because the Ispra ESSOR research reactor was awaiting decommissioning. Three fuel-pin arrays (i.e., not full fuel assemblies) containing six, eight, and 12 irradiated fuel rods, were measured. Burnup varied from 4 to 30 GWd/MTU; cooling times for the pins were 40-50 years. Subsequent to the field measurements, it was discovered that one of the detector heads was not fully functional and therefore, the data from only one head was used in the post-processing for item images (examples in Figure 2). While the irradiated fuel items measured at Ispra were relatively limited and not fully representative of fuel assemblies targeted by the IAEA for PGET assay, the test successfully demonstrated in-pool data acquisition in realistic geometries, over many days of continuous operation. Subsequent analysis produced encouraging images of the fuel-pin arrays. The findings from the Ispra tests informed the continuing development of calibration and analysis methods for the PGET device (Berndt et al. 2012).

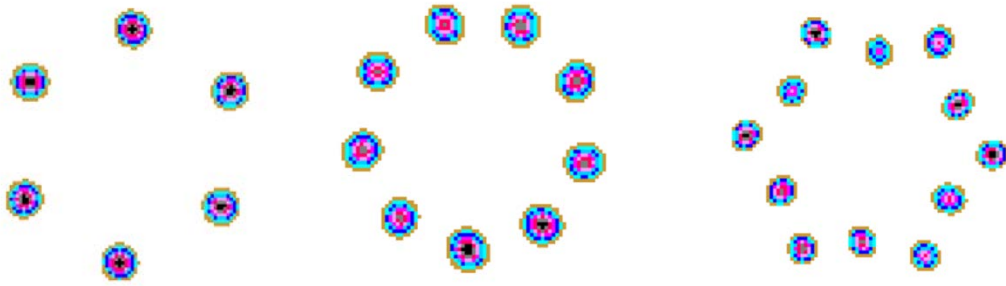


**Figure 2.** Example images from fuel-pin arrays measured during the Ispra 2012 tests, using the  $^{137}\text{Cs}$  energy window.

The Olkiluoto test in 2013 proved to be the first successful campaign for PGET on full fuel assemblies in the fuel pond of an operating reactor. During the 2.5-day campaign, four BWR assemblies were measured, some of them several times with different total collection times to allow investigation of the impact of statistical noise on the final images. Imaging was done primarily based on  $^{154}\text{Eu}$  photons for assemblies with cooling times larger than three years, but a short-cooled assembly was also imaged using  $^{144}\text{Pr}$  photons. Hardware-related issues arose during the test, including the intermittent failure of one detector head and variations in efficiency and noise levels between the arrays. A number of individual detectors failed, creating issues during the data analysis stage. Despite the difficulties, the system was capable of creating cross-sectional images in which nearly all pins and water channels were clearly distinguished (particularly for the more sparse 8x8 BWR fuel). Example images from the Olkiluoto test are shown in Figure 3. For these BWR fuels, which have a relatively sparse rectangular lattice and small overall dimension (and therefore, lower self-attenuation), the potential to accurately image individual fuel pins using PGET was demonstrated.

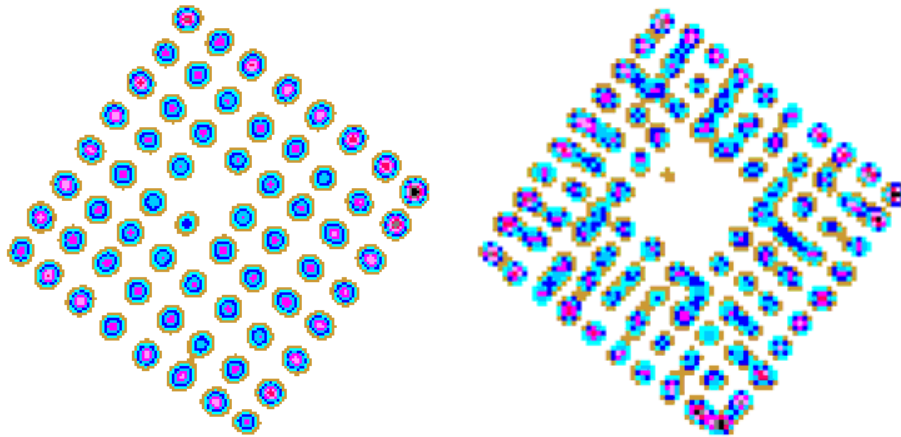


**Figure 3.** Example PGET images from BWR fuel assemblies measured during the Olkiluoto 2013 tests: 8x8 BWR with one water channel, 41 GWd/MTU, 27-year cooling time (left); 10x10 BWR with 3 x 3 pin water-channel section, 38 GWd/MTU, 10-year cooling (right). Both were assayed using the 700-1100-keV energy window corresponding to  $^{154}\text{Eu}$ .

Prior to the measurements at Loviisa in 2014, the detector arrays were both checked for their functionality, faulty detectors were moved to peripheral positions, and both arrays were re-calibrated. A total of five VVER-440 assemblies were measured during the campaign lasting 2.5 days. Burnup levels ranged from 36 to 46 GWd/MTU; cooling times varied from 10 years to 34 years. One assembly, having

three missing rods, was measured twice. Other assemblies had no missing rods, only water channels in the middle position (a normal feature of this fuel type). Application-specific integrated circuit (ASIC) issues caused noisy data for some scans that required special treatment in post-processing, and a problem with the stepping motor meant that the full 360-degree scan was not completed (and not understood until the data analysis stage). The automated analysis software functioned as expected: it was able to generate images within a few seconds, without human intervention. Example images are shown in Figure 4. For these VVER fuels where the pin array is somewhat denser than BWR, present pins are generally distinguishable and water channels (center) and missing pins (right image) are evident. Artifacts that preclude clear resolution of some pins are likely because of hardware issues during the measurements and degradation of some detector channels.

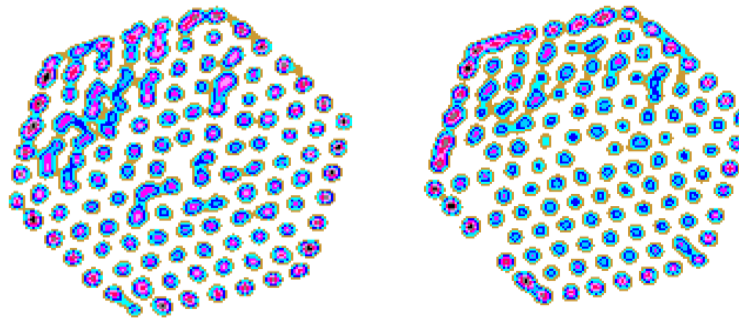


**Figure 4.** Example PGET images from VVER-440 fuel assemblies measured during the Loviisa 2014 tests: 44 GWD/MTU, 12-year cooling time (left); assembly with 3 removed pins, 41 GWd/MTU, 12-year cooling time (right). Both were assayed using the 700-1100-keV energy window corresponding to  $^{154}\text{Eu}$ .

### 2.1.2 Next Steps

JNT 1510 demonstrated the potential of tomography for the verification of BWR and VVER fuels and the detection of missing pins, but that potential has been only partially realized with the device used in the field trials described above (Honkamaa et al. 2014). In those trials, the majority of the issues with PGET have been due to unreliable operation of the detector heads, pulse-processing electronics, and the electronic noise introduced by the high current of the stepping motor. Difficulties with accurate and reproducible calibration of energy and absolute collection efficiency were also problematic. A significant flaw in the pulse-processing electronics design (and contrary to the original requirements) was the serial, rather than parallel, readout of the 208 detectors that made it impossible to complete scans in the required 30-minute time frame, even though the actual data collection time was significantly shorter than 30 minutes.

Toward the goal of more fully realizing the potential of the PGET design for IAEA verification challenges, PGET is being refurbished under a Finnish Support Program project, FIN 1997, entitled “Implementation support for PGET”. IAEA has contracted a full upgrade of the acquisition electronics of the device including parallel readout of all 104 detectors in each head, sequential spectrum acquisition, and analog-to-digital conversion that can support higher-fidelity energy and efficiency calibration. The upgraded system is anticipated to be dry-tested and calibrated in Finland in early fall 2016. The first test campaigns have been initially scheduled in November 2016 in Loviisa and spring 2017 in Olkiluoto.

## 2.2 Additional Experimental Experience of Emission Tomography on Nuclear Fuel

Gamma emission tomography measurements on individual irradiated fuel rods have been executed for fuel characterization purposes during several decades (Sawicka and Palmer 1988, Niculae and Craciunescu 1996, Caruso 2007), and methods and equipment are still developed and applied for this purpose. (Caruso and Jatuff 2014). Albeit knowledge can be gained from tomography instrumentation and methods selected for application on individual rods, one should also acknowledge that the application of emission tomography on complete fuel assemblies differs from that on individual rods in terms of equipment as well as analysis methods. Because this report focuses on tomography on complete assemblies, previous experience covered here is limited to that type of object, as further described below.

The first studies of emission tomography for measurements on complete fuel assemblies; initially started with the safeguards application (Levai et al. 1993, Jacobsson 1996, Jacobsson et al. 1998). The studies presented by Levai et al. (2002) led to the IAEA support program project JNT 1510, as described in Section 2.1 above. In parallel with this development, a request from Swedish nuclear power plant operators to use tomography for validating their core simulators for pin-power distributions led to a Swedish project including the construction and use of a heavy (30-metric tons) device for tomographic measurements of the  $^{140}\text{Ba/La}$  distribution in 2-4-week-cooled BWR fuel assemblies (Jacobsson Svård et al. 2005). Furthermore, a laboratory mockup was constructed within this project (Jansson et al. 2013), which allowed not only for development and testing of methods for pin-power measurements but also for exchange of active fuel rods with empty or nonactive fuel rods, which proved highly useful for investigating the safeguards aspects of the tomographic technique. As a consequence, there were also a number of Swedish studies on the safeguards aspects of this technique (Jacobsson et al. 2000, Jacobsson et al. 2001a, Jacobsson et al. 2001b, Jacobsson Svård et al. 2006 and Lundqvist et al. 2007).

During recent years, international nuclear research institutes have also gained interest in the application of the tomographic technique on complete fuel assemblies, because of its capability to assess individual fuel rods without the need for hazardous and time-consuming disassembly of the fuel bundles (Holcombe et al. 2012 and Baird 2013). Adding to the experience from previous projects, accounted for above, a relatively large pool of knowledge and expertise is now available on tomography, upon which further development of the technique can be based.

In the current project, information was readily available on four developed instrument designs for pin-wise fuel characterization by means of tomography on complete assemblies: 1) the PLUTO device used in Sweden (Jansson et al. 2006), 2) a further development of the PLUTO design (Lundqvist et al. 2010), 3) the laboratory mockup used in the Swedish project Jansson et al. 2013), and 4) the instrument recently brought into use within the OECD-Halden Reactor Project (Holcombe et al. 2015). Some general differences can be noted among these designs and the safeguards device brought forward within the JNT 1510 project, presented in Section 2.1:

- For the purpose of fuel characterization, high-fidelity data on pin-wise isotopic contents is requested.
- As a consequence, the devices designed for this purpose include relatively large gamma-ray detectors, which offer high full-energy peak detection efficiency.
- These detectors must be shielded with heavy collimators in order to limit counting rates, in particular when measuring short-cooled fuel.
- Using data-acquisition systems that allow for collection of gamma-ray spectra, data on full-energy peaks can be extracted by means of spectroscopic peak analysis with background subtraction.

One can identify some benefits and drawbacks of this type of instrument design for the safeguards purpose, as accounted for in Table 2.

**Table 2.** Some pros and cons of GET instrumentation including detectors with high full-energy-peak gamma-detection efficiency in the context of safeguards and fuel integrity verification.

Benefits	Drawbacks
<ul style="list-style-type: none"> <li>• Enables exclusion of gamma rays that have scattered into the detectors, thus enabling reduced background levels in reconstructed images, which in turn is beneficial for distinguishing between fuel rods and background.</li> <li>• Enables the analysis of one or several characteristic gamma-ray energies, which can be used for deducing pin-wise fuel properties such as BU and CT.</li> <li>• Enables simple and accurate modeling of gamma-ray transport, which is beneficial for the tomographic analyses.</li> </ul>	<ul style="list-style-type: none"> <li>• Requires heavy detector collimation, thus leading to a relatively bulky instrument, which may complicate transportability in case of inspection use.</li> <li>• Detector elements cannot be closely packed together, thus making lateral translation of detector head(s) necessary to cover a whole projection, increasing mechanical complexity.</li> <li>• Detector size implies that a relatively small number of detector elements fit into each detector head. For a fixed assay time, this type of system may collect data at a lower level of statistics compared to a multidetector system with smaller detector elements.</li> </ul>

The tomography device brought into use within the OECD-Halden Reactor Project includes one high-purity germanium (HPGe) detector, which is mounted in dry conditions outside the fuel vessel (Holcombe et al. 2015). This type of detector requires cooling with liquid nitrogen, which makes it impractical for submersible use in fuel storage pools. Furthermore, the use of only one detector element implies relatively long total assay times for this setup. However, the exquisite energy resolving capability of this detector type enables the analyses of numerous isotopes, demonstrating the capabilities to deduce a variety of pin-wise fuel properties when allowing for peak analysis. At Halden, this device will be used for measuring power, burnup, and fission gas distributions in fuels being subjected to test irradiations in the Halden research reactor.

In the current project, JNT 1955, data from measurements using the PLUTO device on SVEA-96 BWR fuel with about 4 weeks cooling time (Jacobsson Svärd et al. 2005) collected at the commercial nuclear power plant at Forsmark, Sweden, were made available for benchmarking and evaluation purposes. For these data, operator-declared data on the measured  $^{140}\text{Ba}/\text{La}$  distributions were also available, which were calculated using the operator's core simulator with a stated accuracy in pin-wise isotopic content of 4% ( $1\sigma$ ). These data thus offered a unique opportunity for benchmarking of simulation codes as well as of reconstruction and analysis methods. A short comparison between the PLUTO device and the JNT 1510 PGET device is presented later in this report. For a more thorough description of the PLUTO device, see Jansson et al. 2006.

Finally, it can be noted that the computer codes that were developed for analysis of tomographic data from the PLUTO device were available to this project, and they have been used in the analyses performed by SWESP. Accordingly, these reconstruction and analyses methods are products of previous work, while their use on data from this project is novel. However, as part of this project, the methods and their applicability have also been documented in scientific journals (Jacobsson Svärd et al. 2015 a), (Davour et al. 2016).

## 3.0 Study Parameters

Verification objectives and representative implementation scenarios were defined to focus the scope of the viability study and ensure that the study's results are immediately relevant to IAEA's decisions about viability. The guiding parameters for the study, as defined by the IAEA and the JNT 1955 collaboration, are summarized below.

### 3.1 Verification Objectives

#### 3.1.1 Objective 1: Independent Pin Counting for Verification of Item Integrity

For this objective, verification of the spent fuel assembly integrity is performed in a manner completely independent of operator-declared information (e.g., fuel assembly type, initial enrichment, burnup, and cooling time). The assembly is treated as an unknown sample and emitted gamma rays at one or more energies are used to directly calculate the spatial distribution of the emitting material. This spatial distribution is then used to determine the geometric pattern of the pins (e.g., sparse and rectangular for BWR, dense and hexagonal for VVER) and to count the number of pins composing that array. Two types of partial defects are considered: 1) diverted pins that are not replaced with any material, leaving an empty water or air channel, and 2) diverted pins that are substituted with depleted uranium oxide pins. Pins are removed or substituted in various locations of the simulated assemblies to provide insight into the impact of partial-defect location. The evaluation metrics for Objective 1 recognize the inherent tradeoffs between PD and PFA. Objective 1 is consistent with existing IAEA criteria for detection of partial defects in spent fuel.

#### 3.1.2 Objective 2: Pin-by-pin Characterization for Detection of Anomalies

Though pin-level partial defect detection is the primary need that could be addressed by gamma emission tomography, it is also possible to quantify isotopic concentrations (e.g.,  $^{137}\text{Cs}$  or  $^{154}\text{Eu}$ ) in each pin of an assembly. These isotopic concentrations can also be used to determine the burnup and cooling time on a pin level. Assaying these pin-by-pin characteristics could help reveal, for example, diversion scenarios where one or a few pins are replaced between reactor cycles. For this verification objective, operator-declared information could be incorporated (e.g., fuel assembly type and geometry in order to correct for self-attenuation), but it is not necessarily required since the geometry may be deduced by applying image analysis techniques on reconstructed images from Objective 1-type analyses. Pin tampering at various levels of burnup and in various locations in the assembly should be considered. The evaluation metric for Objective 2 should focus on the achievable accuracy and precision of pin-wise burnup determination, as compared to a known ground truth for each pin. The level of statistical confidence achievable for varying levels of burnup in the tampered pins should also be considered. Current IAEA fuel verification criteria do not require verification of pin-by-pin characteristics but Objective 2 analysis was included in this study to inform the IAEA and stakeholders about its viability and potential.

### 3.2 Implementation Scenarios and Fuel Parameters

The GET project team and stakeholders collaborated to define the set of implementations scenarios and fuel characteristics appropriate for UGET Phase I. The matrix of scenarios and fuel parameters struck a balance between the wide range of possible combinations, and project management constraints (e.g., schedule, computational complexity, available funding at the participating institutions). Criteria for selection of the scenarios and fuel parameters are described here.

### **3.2.1 Account for a Range of Complexity in Tomographic Measurement**

From general considerations, the effectiveness of gamma-ray tomographic measurement is expected to decrease as the amount of self-attenuation increases, the energy of characteristic gamma-ray emission lines decreases, and the total emission intensity of characteristic gamma-ray emissions decreases. Therefore, assembly geometry (outer dimensions and pin spacing) can be a primary consideration for GET instrument design and performance. For example, PWR and VVER fuels would have a higher degree of self-attenuation than BWR fuels, and thus be more challenging cases for tomographic devices (all other variables being equivalent). Also significant are the energy and relative intensity of the detectable gamma-ray emissions, which vary with respect to assembly burnup and cooling time. In this context, variable burnup accumulated by individual pins may be important for the performance of the image reconstruction methods and to the metrics used to evaluate the sensitivity to pin-diversion sensitivity. This effect may be captured in burnup/depletion calculations by assuming a permanently inserted control rod or peculiar shuffling patterns. Factors such as initial fuel loading and type (low enriched uranium [LEU] or mixed oxide [MOX]), and the operational parameters of a reactor are expected to weakly affect the typical shape of detectable gamma-ray spectra; investigation of these effects was not included in UGET Phase I. Based on the logic above, JNT 1955 Phase I emphasized the evaluation of several common assembly configurations (PWR, BWR, and VVER-440 types) coupled with burnup and cooling time variations.

### **3.2.2 Account for a Range of Possible IAEA Implementation Scenarios**

The range of potential spent fuel GET measurements by the IAEA may include attended and unattended implementations in several distinct scenarios. For example, verification of fuel assemblies transferred to a geologic repository will typically be performed at substantial cooling times (dozens of years) when assembly heat and gamma-ray emissions have substantially decreased. Routine assembly movement from a storage pool to a temporary dry storage may be performed only a few years after discharge, when characteristic fission products with comparable half-life are still contributing to the emission spectrum. A nonroutine resolution of anomalies in very recently discharged spent fuel is an extreme case when managing the total gamma-ray emission rate is the primary consideration. Therefore, over the span of the cooling time, the intensity and energy structure of the gamma-ray emissions from fuel change substantially and may require specific GET instrument configurations for different periods even for the same assembly type. To account for this variability, cooling times of 1, 5, and 40 years were assumed for JNT 1955 Phase I.

### **3.2.3 Consider Available Resources and Schedule**

The number of GET implementation scenarios with a variety of spent fuel assembly configurations, in combination with burnup and cooling time parameters selected for the computational effort, needed to be reasonably contained to ensure timely execution. Analysis of the GET assay performance requires modeling of gamma-ray spectroscopic responses in multiple projections for large detector arrays behind collimators with very low geometric collection efficiency. As the complexity of assembly definitions increases (e.g., asymmetric pin burnup or axial fuel composition dependence), the amount of processor time and memory necessary to obtain response spectra increases. With several possible GET instrument concepts, each with unique parameters (detector type, size, collimation, and standoff, etc.) and several diversion cases, the number of required projection data calculations for a single assembly can be considerable. Limiting the overall number of modeling scenarios to several representative cases was a critical decision at the initial stages of the project.

The matrix of recommended implementation scenarios, cooling times, deployment constraints and target measurement times, for all three fuel types considered in this study (i.e., BWR, PWR, and VVER), is summarized in Table 3. These parameters were defined at the inception of Phase I by the UGET team and stakeholders. The Phase I analysis and findings presented in this report departed from the original recommendations in several ways. First, verification of the contents of atypical item, for example cans containing fuel pins extracted from other assemblies, was not addressed. Second, a nominal assay time of 60 minutes or less was assumed for all implementation scenarios. Third, only underwater assay was considered. Fuel burnup values from 10 to 40 GWd/MTU were analyzed in order to span the typical range encountered in the commercial power industry.

**Table 3.** Description of implementation scenarios considered in JNT 1955 Phase I.

<b>Implementation Scenario</b>	<b>Cooling time (years)</b>	<b>Deployment constraints</b>	<b>Target Measurement Time (minutes)</b>
Routine verification of old fuel being transferred to a geologic repository	40	Attended or unattended; dry or water	30
Routine verification of fuel being transferred to dry storage	5	Attended or unattended; water	30
Random verification of in-pool inventory	1	Attended; water	30
Anomaly resolution of specific assemblies or atypical items	1 to 40	Attended; water	60

### 3.3 Key Outcomes from Phase I

The key outcomes of Phase I, as defined at the outset of the project, are listed as follows.

- Development of a modeling and analysis framework that has the flexibility, efficiency, and fidelity to support quantitative GET performance studies that accurately reflect field performance.
- Definition of a nominal Universal GET design that is capable of spanning all of the verification objectives and implementation scenarios assumed in this study. The design should use commercially available hardware and to the extent possible, nonproprietary data acquisition and analysis software. A lifecycle cost estimate for UGET should be provided.
- Identification and demonstration of a variety of tools and algorithms for analyses of tomographic data, such as tomographic reconstruction algorithms and tools for analysis of tomographic images.
- Quantitative assessment of predicted performance for Objective 1, independent pin counting for verification of item integrity. Performance should be predicted and compared for the nominal UGETv1 design defined in JNT 1955 and the PGET developed under JNT 1510.
- Preliminary viability assessment of gamma-ray tomography for Objective 2, verification of pin-by-pin characteristics and detection of anomalies. UGETv1 and PGET performance should be compared using different assumptions and methods for the reconstruction of isotopic activities, integral burnup and cooling time in each pin of an assembly.





## 4.0 Modeling and Analysis Framework: Overview

The GET viability study described in this paper is largely based on simulated instrument responses. Figure 5 presents an overview of the modeling and analysis framework developed and exercised for the simulated data. Note that the framework allows for the simultaneous evaluation of candidate approaches in each step, which will support comparative evaluations of different instrument designs, analysis algorithms, and performance metrics under the different verification objectives discussed earlier.

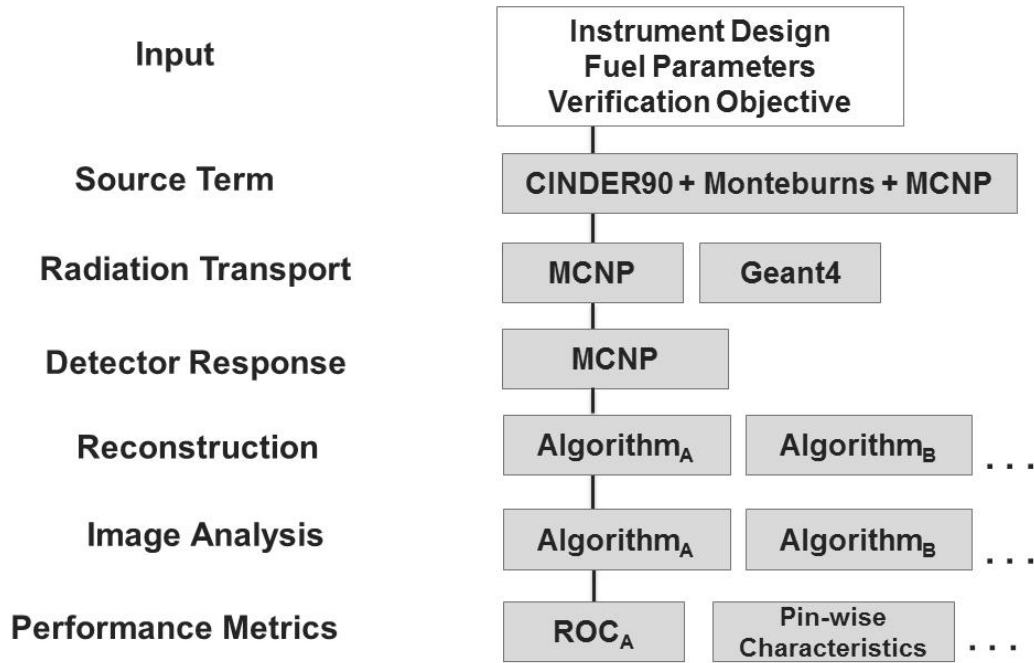


**Figure 5.** Flowchart describing the modeling and analysis framework for the GET viability study.

The input to each case study includes a model of the instrument (e.g., collimator, detector type, or angular sampling), fuel configuration and parameters (e.g., initial enrichment, assembly-averaged burnup and cooling time), and the verification objective. Descriptions of each step in the framework, assuming that input, are given in the sections that follow. These descriptions reference various sets of projection data (simulated and measured), reconstruction algorithms and analysis methods used by the USSP and SWESP through the course of JNT 1955 Phase I. A tabular overview of products from the modeling and analysis framework (including fuel type, tomographer design, forward transport method, reconstruction technique and analysis technique) is provided in Appendix A.

## 5.0 GET Simulated Spent Fuel Library

To computationally evaluate the performance of candidate gamma-ray emission tomographers, a dedicated library of simulated spent nuclear fuel assemblies was defined. Experience and models from an earlier U.S. Department of Energy (DOE) Next Generation Safeguards Initiative (NGSI) project (Humphrey et al. 2012) was leveraged to generate isotopic activities for different fuel geometries, initial enrichments, burnup values, and cooling times. These calculations were validated by experimental measurements of gamma-ray spectra from spent fuel assemblies in a small number of cases. While the calculations reveal the presence of thousands of isotopes in the irradiated fuel inventory, there are four main isotopes that primarily define the energy structure of the gamma-ray flux important to tomography instruments, for the range of cooling times considered in this study (1 year to 40 years):  $^{137}\text{Cs}$  (30-year half-life),  $^{154}\text{Eu}$  (8.6-year half-life),  $^{134}\text{Cs}$  (2-year half-life), and  $^{144}\text{Pr}$  (284-day half-life). Characteristic gamma rays emitted by these isotopes determine spectroscopic and operational requirements (e.g., energy resolution and count rate) of the detectors in a GET instrument detector package.

### 5.1 Relevant Prior Work

An extensive modeling study of spent nuclear fuel inventories that was completed as a part of the NGSI project investigated a variety of fuel properties and parameters in the course of burnup/depletion calculations (Galloway et al. 2012). The resulting library of assembly inventory definitions accounts for a number of assumptions and effects, such as geometric detail and reactor operation conditions. Within each set, calculations varied with a range of initial  $^{235}\text{U}$  enrichment, integral burnup, and cooling time after discharge from a reactor. Detailed spent fuel material inventories were defined for several assembly types (PWR, BWR, and VVER) with time- and spatially dependent data for thousands of isotopes. The fidelity of some subsets of the NGSI library was informed by operator-provided reactor utilization parameters. The calculation methodology in this effort varied, but the most common approach was based on a combination of the Monte Carlo N-Particle (MCNP) transport code (Pelowitz et al. 2008) and the isotope generation/decay implemented by the Monteburns code (Trellue et al. 2011).

Spent fuel assembly definitions and calculation methodology developed in earlier NGSI work provided a sufficient level of detail for the GET viability study, and were used as the foundation for the GET simulated fuel library.

### 5.2 GET Fuel Library Definition

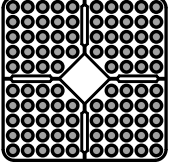
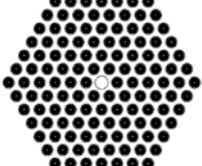
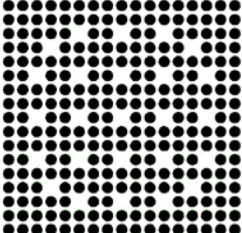
Preparation of the GET fuel library was informed by the requirements and parameters of the implementation scenarios described in Section 3.2. Initial assembly definitions were drawn directly from NGSI library sets that offer the highest fidelity in terms of individual pin material inventory. A series of additional inventory calculations was completed in order to provide the GET project with data on specific assembly types and parameters and to support the benchmarking effort. Fuel models used in the course of the GET simulations were defined in the form of the MCNP input files with position-dependent individual pin material compositions. For transport calculations, these fuel definitions were later coupled with the MCNP models of tomographic instruments and separately calculated pin-specific discrete gamma-ray source terms.

Fuel compositions for all GET assemblies were determined for a range of burnup values. Fuel assemblies with the integral burnup of approximately 40 GWd/MTU were assumed as the typical IAEA integrity verification case. A subset of low-burnup fuel models was used to simulate unusual measurement scenarios such as an early discharge or individual pin substitutions between reactor cycles. Additional

consideration was given to the availability of empirical data that can be used for benchmarking response calculations for specific fuel types. A number of assembly models were created in order to replicate the characteristics of fuels assayed in field measurements for high-fidelity GET response modeling.

In its final form, the GET fuel library contained three assembly types: 1) SVEA-96 BWR with 96 pins, 2) VVER-440 with 126 pins, and 3) 17x17 Westinghouse PWR with 264 pins. All three selected fuel types represent common modifications of commercial assemblies and had associated experimental data available for validation. BWR and VVER-440 fuels were previously measured with tomographic instruments, and single-pixel gamma-ray spectroscopy data were available for BWR and 17x17 PWR cases. A VVER-1000 assembly type with 312 pins, which can be considered the most difficult case because of tight pin packing and linear dimensions, was not included in the Phase I analysis. A summary of the GET fuel library is provided in Table 4.

**Table 4.** Summary of spent fuel assembly models in the GET library.

Assembly type	SVEA 96 BWR 	VVER-440 	17x17 Westinghouse PWR 
Number of fuel pins	96	126	264
Number of water channels	4	1	25
Bundle configuration	4x(5x5) four subassemblies, rectangular	Hexagonal	Rectangular
Shroud	Enclosed in shroud	Enclosed in shroud	No shroud
Burnup range	~5.0 – 41.0 GWd/MTU	~5.0 – 40.0 GWd/MTU	~4.5 – 40.0 GWd/MTU
Cooling time	Arbitrary		

As discussed in Section 6.0 of this report, the spent fuel spectroscopic response a few months after discharge is dominated by gamma-ray emissions from four primary fission products:  $^{137}\text{Cs}$  (30-year half-life),  $^{154}\text{Eu}$  (8.6-year half-life),  $^{134}\text{Cs}$  (2-year half-life), and  $^{144}\text{Pr}$  (284-day half-life). The nine individual gamma-ray lines produced by these isotopes and shown in Table 5 define the energy structure and are proportional to the total rate of gamma-ray emissions in the energy region between 0.4 and 2.5 MeV, important for tomographic measurement. The relative importance of the four isotopes varies with the fuel burnup and cooling time and can be explicitly calculated.

**Table 5.** Characteristic fission products and associated gamma-ray emissions from spent fuel in 0.4 and 2.5 MeV energy region.

Isotope	Energy, MeV	Half-life	Relevant Cooling Time Range
$^{137}\text{Cs}$	0.662	~30 y	more than 50 y
$^{134}\text{Cs}$	0.605	2.1 y	up to 10 y
	0.796		
$^{154}\text{Eu}$	0.723	8.5 y	up to 25–30 y
	0.873		
	0.996		
	1.005		
	1.274		
$^{144}\text{Pr}$ ( $^{144}\text{Ce}$ )	2.186	285 d	up to 5 y

For tomographic projection data calculations in this study, it was assumed that the calculated response of a tomographic instrument can be effectively emulated by approximating the emission source term from the fuel assembly pins with only the nine lines from Table 5. Adopting the nine-line emission source approximation permitted more efficient modeling and analysis of tomographic instrument configurations, burnup asymmetry and cooling time effects, object-scatter contributions to the projection data, as well as energy resolution, efficiency, and count-rate limits of the detector package. The nine-line simplification is intuitively appropriate for high cooling times (30–40 years after discharge) when the lines from fission products with long half-lives dominate the entire gamma-ray response. It becomes less accurate at shorter cooling times when a large variety of emitting isotopes is still present in the spent fuel. However, even after about a year of storage, the overall shape of the gamma-ray spectrum detected from a fuel assembly is defined primarily by these nine lines. The other emissions are important for the total count rate and continuum around key peaks, and also for the high-energy region above two MeV. These short cooling time effects cannot be dismissed, but can be accommodated by applying scaling factors as necessary (e.g., in calculating total count rates). For example, according to the detailed fuel inventory calculations completed in the course of this project, for a typical assembly with about 40 GWd/MTU integral burnup, the summed emission rate from the nine lines corresponds to about 65% of the total emission rate at 1-year cooling time, about 85% at 5 years, about 95% at 10 years, and about 99% at 15 years.

For each assembly type in the GET fuel library, detection efficiency for each of the nine characteristic lines was determined in a three-dimensional (3D) transport calculation for a tomographic instrument configuration. These results were normalized using an absolute emission-line intensity assigned to each individual pin according to the desired burnup map. Individual intensities of nine gamma-ray lines were determined using pre-calculated “lookup tables” for a range of burnup values and arbitrary cooling time periods. Examples of such tables for BWR, VVER-440, and 17x17 PWR assemblies are provided in Appendix B.

In a subset of modeling calculations, the gamma-ray emission source assumption deviated from the nine line approximation. For example, for benchmarking calculations against PLUTO experiment data, the source term was approximated by a single gamma-ray line at 1.596 MeV from  $^{140}\text{Ba}/^{140}\text{La}$  chain. Fuel assemblies in this experiment had a very short cooling time of 4-5 weeks and the tomographic instrument provided a spectroscopic response analysis capability. Outcomes of this benchmark are illustrated in Section 8.5.3. Also, for a series of single-pixel response modeling studies, a detailed material definition with thousands of isotopes and emission lines was used for high-fidelity gamma-ray spectrum modeling (Section 8.5.1).

### 5.3 Definition of Pin-Diversion Scenarios

To investigate the capability of GET assay to detect missing pins in an assembly, several pin-diversion scenarios were defined for the assemblies identified in Table 4. For each assembly type, a specific pattern of pin locations was selected to contain partial defects. These pin diversion maps supported the analysis of single pin diversion sensitivity depending on the position in the assembly from the center to the periphery and factored in adjacent water channels. The number of substituted pins amounted approximately to 5 percent of the total number of active fuel pins in the original assembly (five pins in BWR, six pins in VVER-440, and 11 pins in 17x17 PWR), see Figure 53.

Three partial defect scenarios were considered, though results from only the first and last are presented in this report as discussed later:

- Pin removal with water replacing extracted pins without any substituting materials
- Pin replacement with depleted uranium-filled pins in Zircaloy cladding (replicates high-density substitute)
- Pin replacement with fuel rods of the same construction but lower burnup (replicates material diversion between reactor cycles).



## 6.0 Experimental Studies of Single-Pixel Detectors

JNT 1955 Phase I involved modeling and analyses of the single-pixel detector responses, i.e., to study the response of individual detector elements in a GET device, see ref (JNT 1955 2013). Experimental energy spectra from collimated high and medium resolution gamma-ray detectors, collected on spent nuclear fuel assemblies were used to support decisions about the detectors to be proposed for a universal GET design, and to validate fuel and detector models.

In August 2013, under support from a collaboration among Euratom, the Swedish Nuclear Fuel and Waste management company (SKB), and the US Department of Energy (and completely separate from the JNT 1955 project), gamma-ray energy spectra were collected from three PWR fuel assemblies in the pool of the Swedish interim storage for spent nuclear fuel, Clab. Four types of gamma-ray detectors were used: three scintillator detectors (lanthanum bromide [LaBr], sodium iodide [NaI], and bismuth germanate [BGO]) with medium to low energy resolution and one HPGe detector with high-energy resolution.

The objectives of these measurements, relevant to of the way they were leveraged for JNT 1955, were three-fold:

- Validate simulated isotopic inventories calculated for the JNT 1955 study, using data from the HPGe detector
- Measure gamma-ray energy spectra from used fuel with the different detectors so that the measurement data can be used as a basis for evaluating the fidelity of JNT 1955 modeling
- Evaluate the capability of different detector types to measure pin-wise fuel properties related to UGET Verification Objective 2, such as burnup and cooling time.

Further information about the campaign and its key findings can be found in Vaccaro et al. (2016). The focus in this section is on the interpretation of the Clab data in support of defining a preferred detector type for the universal GET design. The key consideration was the extent to which different candidate GET detector materials are able to resolve several peaks of interest. The peak-resolving capability is particularly important for the determination of burnup and cooling time simultaneously, as discussed below.

### 6.1 Measurement Campaign Overview

The Clab facility is situated in Oskarshamn, Sweden, and it is managed by the Swedish Nuclear Fuel and Waste Management Company (SKB AB). In Clab, all used fuel generated from the nuclear power plants in Sweden are stored, awaiting future encapsulation and storage in a geological facility. Measurements were performed using the gamma scanning equipment and collimator system that is available at Clab (Jansson 2002, Jansson et al. 2014, Jacobsson et al. 1998).

To measure the gamma radiation from the different kinds of detectors under investigation, two data acquisition systems were used. The HPGe measurements were performed using the Lynx<sup>1</sup> system and the Genie-2000<sup>2</sup> software from Canberra Inc. The LaBr, NaI and BGO measurements were performed using the DSPEC-50<sup>3</sup> system and the MAESTRO<sup>4</sup> software from ORTEC Inc. Both systems are based on

---

<sup>1</sup> [http://www.canberra.com/products/radiochemistry\\_lab/pdf/Lynx-SS-C38658.pdf](http://www.canberra.com/products/radiochemistry_lab/pdf/Lynx-SS-C38658.pdf)

<sup>2</sup> [http://www.canberra.com/products/radiochemistry\\_lab/genie-2000-software.asp](http://www.canberra.com/products/radiochemistry_lab/genie-2000-software.asp)

<sup>3</sup> <http://www.ortec-online.com/download/dspec-50.pdf>

<sup>4</sup> <http://www.ortec-online.com/Products-Solutions/Applications-Software-MAESTRO.aspx>



digital signal analysis of the measured pulses from the detectors using trapezoidal shaping that allows for good energy resolution over a wide range of counting rates. The parameters used in the digital acquisition systems and properties of the used detectors can be found in Table 6. More details can be found in Jansson et al. 2014.

Three PWR 17x17 spent fuel assemblies were measured in this study with parameters as presented in Table 7. They represent a relatively large span of parameters of the PWR assemblies currently stored in Clab. An axial position near the maximum of the axial  $^{137}\text{Cs}$  distribution (i.e., burnup), situated in between two adjacent spacers, was measured for each assembly.

**Table 6.** Parameters for the digital data acquisition system and data on the used detectors, as supplied by the manufacturers. The amount of given detector specifications varies between manufacturers. The energy resolution for BGO was estimated using measured data.

Detector	Parameter	Value
HPGe	Type	Coaxial N-type
	Relative efficiency @ 1332 keV	44 %
	Energy resolution @ 1332 keV	0.15 %
	Trapezoidal rise time / flat top [ $\mu\text{s}$ ]	3.0 / 0.6
LaBr	Size (diameter x length) [mm]	25.4 x 50.8
	Energy resolution @ 662 keV	2.6 %
	Trapezoidal rise time / flat top [ $\mu\text{s}$ ]	0.8 / 0.3
BGO	Size (X x Y x Z) [cm]	2 x 3 x 5
	Energy resolution @ 662 keV	$\sim 30$ % <sup>†</sup>
	Trapezoidal rise time / flat top [ $\mu\text{s}$ ]	0.8 / 0.3
NaI	Size (diameter x length) [mm]	50.8 x 50.8
	Energy resolution @ 662 keV	7.2 %
	Trapezoidal rise time / flat top [ $\mu\text{s}$ ]	0.8 / 0.3

<sup>†</sup> Estimated using measured data.

**Table 7.** Parameters of the used nuclear fuel assemblies measured.

Assembly Id	Type	Burnup [MWd/tU]	Cooling time [years]	Initial enrichment of $^{235}\text{U}$ [%]
PWR 5	17x17	46866	5.2	3.94
PWR 19	15x15	35027	28.3	3.20
PWR 24	17x17	23151	18.2	2.10

Gamma-ray energy spectra from the measurements are presented in Figure 6, left column. To allow for easier comparison, Figure 6, right column, also displays the measured spectra, normalized so that the maximum count in any channel for each of the spectra is one. As can be seen in Figure 6, the spectra are dominated by the  $^{137}\text{Cs}$  peak at 662 keV, especially for the two assemblies with cooling times at or beyond 18 years. For the assembly with a cooling time of about 5 years, the spectrum also shows strong  $^{134}\text{Cs}$  peaks at 605 keV and 796 keV and a  $^{154}\text{Eu}$  peak at 1274 keV. As expected, the HPGe detector delivers the best energy resolution and the worst resolution is obtained from the BGO detector.

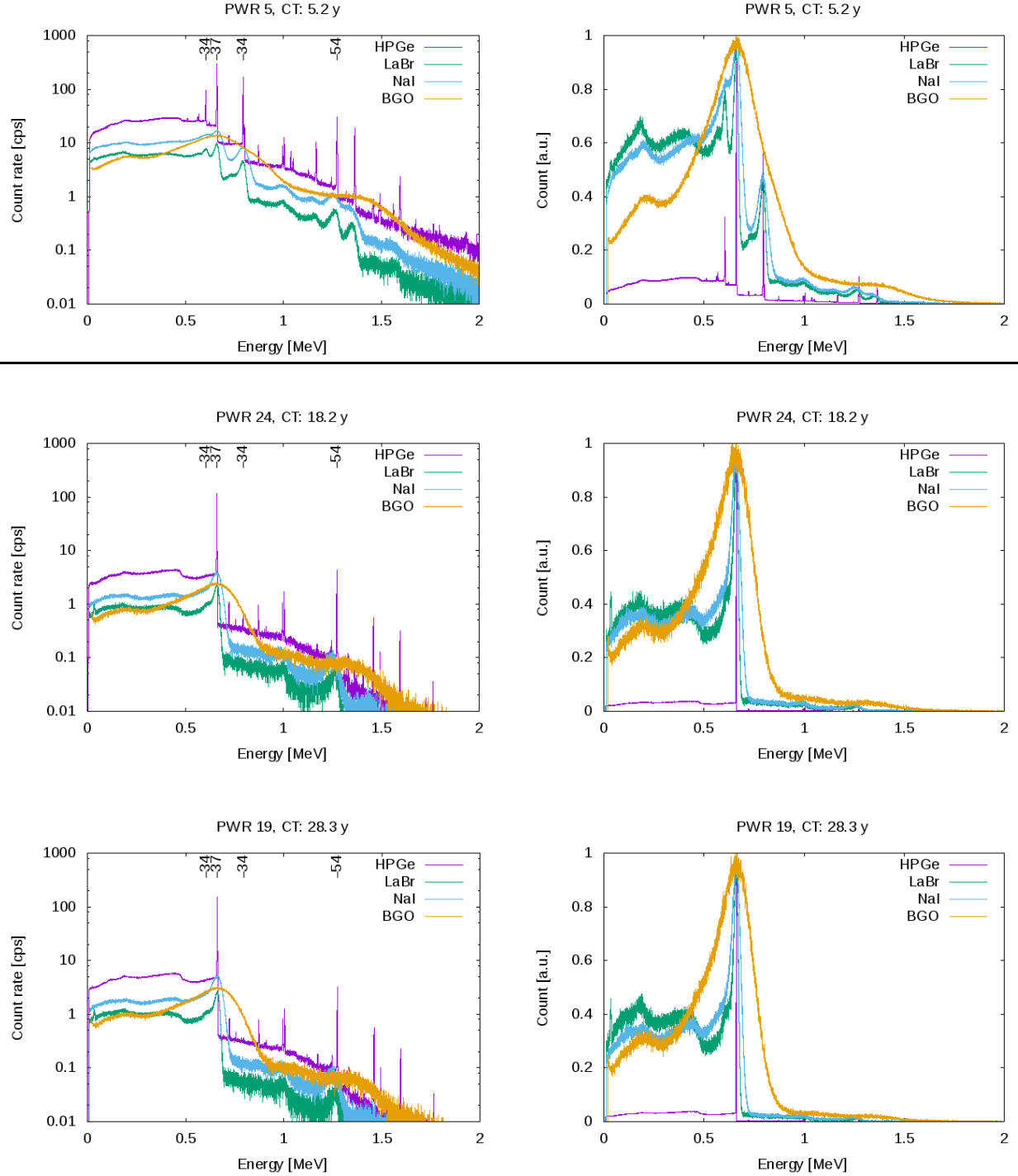


**Figure 6.** Measured gamma-ray spectra (left column, logarithmic scales) and spectra normalized so that maximum is one (right column, linear scales). Peak positions for  $^{134}\text{Cs}$  (605 and 796 keV),  $^{137}\text{Cs}$  (662 keV) and  $^{154}\text{Eu}$  (1274 keV) are marked with 34, 37, and 54, respectively.

## 6.2 Evaluation of Collected Gamma-ray Spectra

Table 8 shows data on some identifiable peaks in the measured energy spectra. They were quantified using the built-in basic peak-analysis routines of the MAESTRO software (from ORTEC Inc, for all but the HPGe detector) and the Genie-2000 software (from Canberra Inc, for the HPGe detector).

**Table 8.** Evaluated data on peaks identified in the measured energy spectra as given by the data acquisition software used. Peak intensities (I) are given in counts per second with one sigma uncertainty. The energy resolution (R) is given as full width half maximum (FWHM) relative to the peak position, in percent. No data on energy resolution are presented for cases where the data acquisition software reported data that were obviously incorrect, e.g., less than 0.01 percent for the LaBr detector. Note that the burnup for the assembly with CT of 18 years is somewhat lower than the other two assemblies (Table 7).

CT [y]	Detector	<sup>134</sup> Cs 605 keV		<sup>137</sup> Cs 662 keV		<sup>134</sup> Cs 796 keV		<sup>154</sup> Eu 1274 keV	
		I	R	I	R	I	R	I	R
		[cps]	[%]	[cps]	[%]	[cps]	[%]	[cps]	[%]
5	HPGe	695 ± 3	0.40	2755 ± 4	0.37	1548 ± 3	0.31	321 ± 2	0.21
18	HPGe			817 ± 2	0.27			40 ± 1	0.17
28	HPGe			1112 ± 1	0.28			29 ± 1	0.18
5	LaBr	184 ± 10	2.8	838 ± 11	3.5	464 ± 8	3.3	81 ± 5	2.4
18	LaBr			292 ± 5	3.6			11 ± 2	
28	LaBr			332 ± 6	3.7			6 ± 2	
18	NaI			1474 ± 20	8.3			27 ± 4	
28	NaI			2000 ± 23	8.5			23 ± 3	
18	BGO			1699 ± 23	31			5 ± 4	
28	BGO			2143 ± 26	30			6 ± 3	

The four peaks in Table 8 are all well resolved for the HPGe and the LaBr detectors for all cooling times in the measured set of assemblies. For the scintillator detectors, only peaks that are distinct enough to be analyzed with the basic routines in MAESTRO are given in the table (i.e., only for fuel assemblies with cooling times of 18 and 28 years). No data for the <sup>134</sup>Cs peaks are given for the 18- and 28-year cooling times because they have decayed and the peaks are no longer analyzable in the spectrum, see Figure 6.

At a cooling time of about five years, for the NaI detector, the <sup>134</sup>Cs peak at 605 keV interferes severely with the <sup>137</sup>Cs peak at 662 keV and for the BGO detector, the energy resolution is not enough to resolve individual peaks. Here, the basic peak analysis routines provided by the data acquisition software are not suited for evaluating such overlapping peaks and further analysis was not performed for five years cooling time.

One may consider a more elaborate peak-analysis for the NaI detector, e.g. using fitting to multiple gaussian functions. Hypothetically, the <sup>134</sup>Cs peak at 605 keV may then be resolved from the <sup>137</sup>Cs, albeit with larger uncertainty compared to a case where a single peak is evaluated. However, for the BGO detector, the energy resolution is considered to be too poor for such a procedure to yield useful precision.

## 6.3 Summary Findings from Single-Pixel Measurements

The key findings from the Clab measurements and analysis, with respect to detector type and the determination of burnup and cooling time are given here:

- LaBr - As can be seen in Table 8,  $^{134}\text{Cs}$ ,  $^{137}\text{Cs}$  and  $^{154}\text{Eu}$  can be readily resolved at short cooling times (about 5 years) by the LaBr detector. It is concluded that LaBr can be used for tomographic measurements of used fuel, with its energy resolution of about 3 percent full width half maximum (FWHM) being good enough to resolve the most dominant gamma peaks in the energy spectrum even at short cooling times (in the order of 5 years). Here, basic routines for peak evaluation have been used, whereas more advanced routines may be considered in a real measurement situation.
- NaI - At longer cooling times, after 18 years, NaI can be used to resolve the  $^{137}\text{Cs}$  peak because most of  $^{134}\text{Cs}$  has decayed. It may also be used for measuring the count rate in the  $^{154}\text{Eu}$  peak at 1274 keV, though this peak may become too weak after a few decades' cooling time. Further investigations are needed before conclusions are drawn on the applicability of NaI at relatively short cooling times.
- BGO - For long cooling times, even BGO detectors can be used to evaluate the intensity of the dominant  $^{137}\text{Cs}$  peak at 662 keV. According to the data measured in this study, they are usable for cooling times at 18 years and beyond. Further studies are needed to determine at which cooling times (earlier than 18 years) that BGO detectors become a usable option for tomographic measurements.
- Short cooling time - Based on the capability to measure count rate in individual gamma peaks, it is concluded that for short cooling times, the pin-by-pin burn up and cooling time may be determined independently in tomographic measurements using HPGe or LaBr by studying a combination of two of the peaks from  $^{134}\text{Cs}$ ,  $^{137}\text{Cs}$  or  $^{154}\text{Eu}$ . Relative pin-by-pin burnup values within a set of measurements can be obtained using only the  $^{137}\text{Cs}$  peak intensities.
- Long cooling time - The ability to use two isotopes for determining burnup and cooling time independently decreases with cooling time since the relative  $^{137}\text{Cs}$  contribution to the energy spectrum grows with time while the other isotopes decrease. At a cooling time of about 28 years, good counting statistics (i.e., long enough measurement times) are needed to be able to measure also the  $^{154}\text{Eu}$  peak and thus to be able to determine both burnup and cooling time pin by pin by means of tomography. The ability to use only the  $^{137}\text{Cs}$  peak for determination of relative pin-by-pin burnup grows with time, correspondingly.

Considering that peak analysis including subtraction of spectral background is beneficial for reducing scattered components in measured tomographic data, and thus to reduce background levels in measured Objective 1 images, attention was paid here to the possibility to perform such peak analysis on collected spectra. In addition, one should acknowledge that the capability to execute accurate isotopic analysis is crucial for Objective 2-type assessment. Furthermore, high peak efficiency and high energy resolution enable higher precision in the subtraction of spectral background and thus higher precision in the analysis of isotopic data.

For the JNT 1955 project and the definition of a nominal UGET design, it was assumed that commercially available peak-analysis routines are preferred for easy and transparent implementation. Based on the analysis presented here and the experience of others, NaI is unlikely to provide the peak-resolving performance desired for a UGET, especially for Objective 2 where determination of burnup and cooling time on a pin-wise basis is desired. This finding informed the decision to use LaBr, a suitable combination of energy resolution and full-energy peak efficiency, in the design of the UGET, as described in Section 7.0.



## 7.0 Defining a Universal GET

Examination of prior tomographic applications to spent nuclear fuel is informative for the development of a universal tomographer design for safeguards that can cover both verification objectives and all expected implementation scenarios. Two prior and/or ongoing projects represent the extremes of the design space (Figure 7), and have informed the definition of UGETv1.

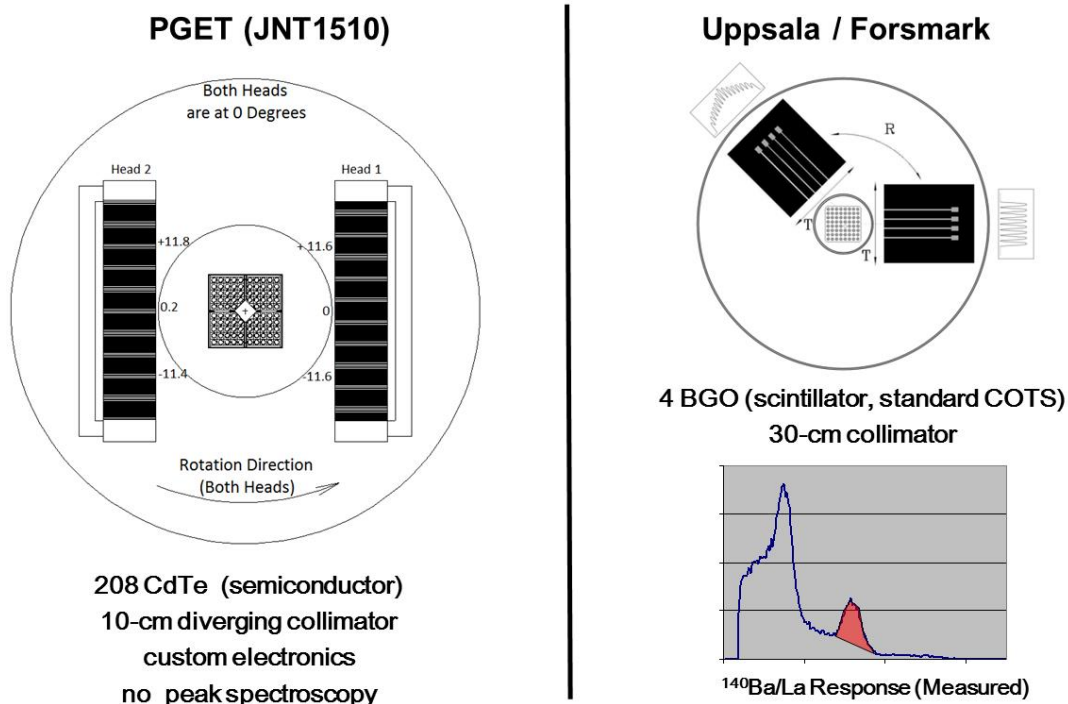


**Figure 7.** Comparison of two fuel tomographer designs used to inform the UGETv1 design: PGET, based on two large arrays of small, non-spectroscopic CdTe detectors in a rotate-only geometry (left), and PLUTO, based on a few large spectroscopic BGO scintillators in a translate-rotate geometry (right).

The first design is the PGET instrument, which was developed under IAEA's support program JNT 1510, see Section 2.1. PGET is a portable, underwater device designed to assay relatively long-cooled fuels (more than 5 years) where the intensity of emissions, and the proportion of those emissions that are at energies greater than 1500 keV, are relatively low. PGET was specifically designed to deliver on Objective 1 (pin counting) but not necessarily Objective 2 (pin-by-pin burnup quantification). Each PGET detector head has a dense array of CdTe detectors with very limited spectroscopic capability (i.e., broad ROIs) and relatively light collimation (10-cm depth). The detector array collects projection data and rotates through 360-degrees to collect a full sinogram. Two arrays are used to provide more inter-detector collimation. This approach can offer rapid data collection in a rotate-only geometry. This system has been field-tested and has shown promise for detecting missing pins with various fuel types and characteristics (Levai et al. 2002, Honkamaa et al. 2014).

The second example design was a tomographer called PLUTO built by Uppsala University in Sweden to validate the burnup codes of reactor operators, as discussed in Section 2.2. This large, underwater device was designed to measure commercial BWR fuel shortly after removal from the reactor (a few weeks) where the total emission intensity is high, the proportion of high-energy emissions is high compared to longer-cooled fuels, and the energy spectrum is dominated by the 1596 keV peak from  $^{140}\text{Ba/La}$  (Jansson

et al. 2006). In this case BGO scintillators were sufficient to resolve the single dominant peak while still enabling background subtraction needed for high-precision tomographic evaluation. This system used a sparsely populated detector array with very heavy collimation. The detector head required a translation step to adequately sample the projection data as well as rotate to collect complete sinogram data. The PLUTO system was developed for and demonstrated on BWR fuel at a nuclear power plant in Sweden (Jacobsson Svärd et al. 2005).

These two approaches were considered bounding cases for the detector-head design of a universal GET for safeguards.

- For PGET, there are sufficient detector pixels in the detector head to sample a single projection without movement and thus the only motion necessary to collect sinogram data is rotation of the detector head around the fuel assembly. Addition of the second detector head enables both reduced sampling time and finer sampling along a projection (because the detector arrays are offset by half of the detector pitch relative to each other). This approach is possible in part because the detector elements (2mm wide by 5mm tall by 10mm deep CdTe crystals) are small enough to allow the fine pitch. A problem with this geometry is the potential for crosstalk between collimator openings (septal penetration), which reduces the fidelity of the line integrals and thus the resolution of the reconstruction.
- The PLUTO approach used a sparser detector array (larger pixel pitch) and fewer total pixels in a detector array. The detector must be translated laterally in order to fill in the gaps between the widely spaced pixels. This design is required if the detector (scintillator) is larger than the pixel pitch, and has the advantage of not being a susceptible to septal penetration as a finer-pitch design (this may be an especially important feature for scenarios in which higher-energy photons must be detected).

In general, the tomographer design parameter space reduces to spatial resolution (Can individual pins be distinguished?), energy resolution (How well can isotopic lines be distinguished?), collection efficiency (Are total count rates manageable? Is there sufficient collection of key emission lines to ensure reasonable total assay times?). The collimator parameters (bore length, width, and height) are the principal determinants of the spatial resolution and collection efficiency, and also define the data-collection geometry (number of samples per projection and angular sampling). Energy resolution and to a lesser extent the collection efficiency, are coupled through the choice of detector material. Total data-collection time will depend on each of these parameters and other engineering and cost considerations (e.g., acquisition time could be decreased by the use of multiple detector assemblies, increasing cost and mechanical complexity).

Informed by prior work and simulations of the existing tomography instrument, it was determined that a collimator with a length-to-width aspect ratio of between 100:1.5 and 300:1 will be sufficient to provide spatial resolution on the order of a typical pin diameter or less, throughout the field of view. To meet Verification Objective 2 and identify gamma-ray signatures from specific isotopes, it is crucial to have a detector with spectroscopy capability. For calculating pin-wise burnup and cooling time values, it will be necessary to have a relatively high peak efficiency for key isotopic signatures lines, and be able to resolve the emission lines from key isotopes, primarily  $^{137}\text{Cs}$  (662 keV) and  $^{154}\text{Eu}$  (5 principal lines between 723 and 1264 keV). In addition, for cooling times less than a few years, it would be desirable to separate the response of  $^{134}\text{Cs}$  (605 and 796 keV) from the  $^{137}\text{Cs}$  lines. The need for a combination of relatively good energy resolution, high full-energy peak efficiency and cost-effectiveness drive the system design toward inorganic scintillators as the detection material and as described in Section 6.0, toward  $\text{LaBr}_3(\text{Ce})$ . A comparison of detector responses to simulated projection data for a single pixel for both  $\text{NaI}(\text{Tl})$  and  $\text{LaBr}_3$  are shown in Figure 8 while measured detector responses for these types of detectors are shown in Figure 6.  $\text{LaBr}_3$  was chosen as the scintillator for UGETv1 based on its combination of full-energy peak efficiency, energy resolution and high count-rate capabilities.

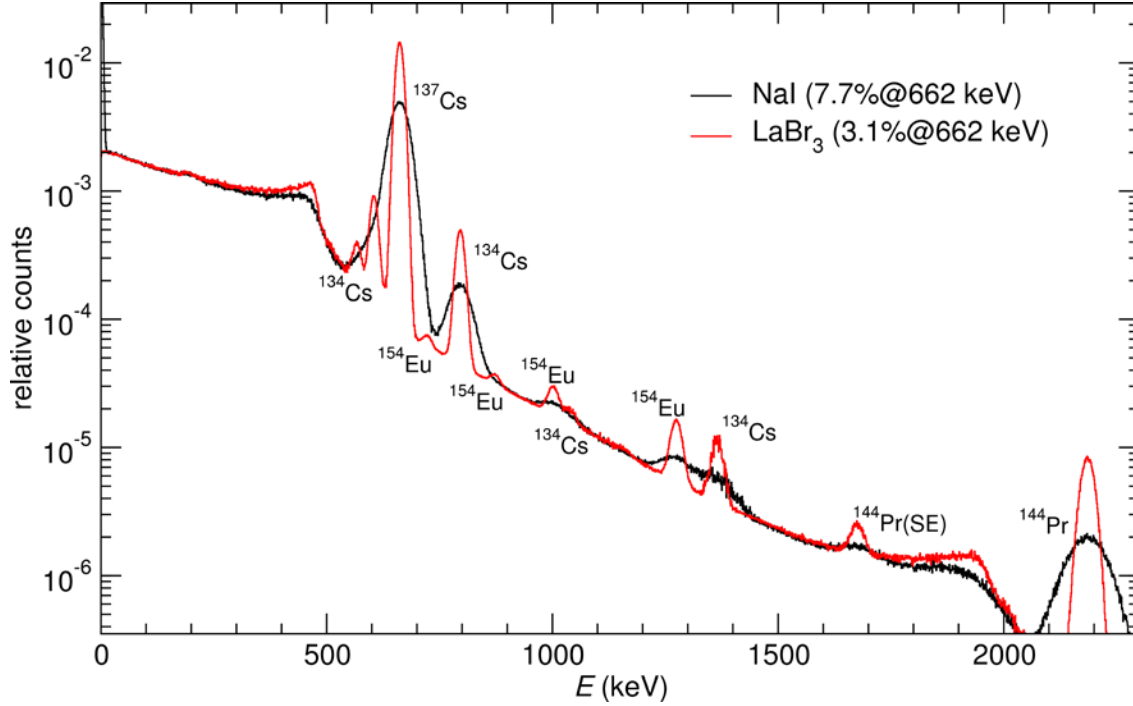


**Figure 8.** Detector response functions for NaI and LaBr<sub>3</sub> for simulated projection data.

Once noting that the spatial resolution is governed by the collimator field of view, and the energy resolution is defined by the detector material, the design challenge reduces to striking a balance between managing count rates across all implementation scenarios while ensuring sufficient imaging efficiency for challenging cases:

- **High-count rate.** For high burnup, short cooling time fuels, the total count rate at the detector needs to be less than about  $10^6$  counts per second (cps) in order to prevent excessive pileup in a LaBr<sub>3</sub> detector using commercially available pulse-processing electronics. For this study, the high-rate bounding fuel case was taken to be PWR, 40GWd/MTU, and 1-year cooling time.
- **Sufficient efficiency.** For medium-length cooling times (5-10 years), the system design must be efficient to the 1275-keV line from <sup>154</sup>Eu (for PWR), and for longer cooling times, efficient to the 662keV line from <sup>137</sup>Cs.

Detector-head design options were explored for two parallel-bore and one diverging-bore collimator, assuming a 3.8 cm right circular cylinder (RCC) LaBr<sub>3</sub> scintillator. Figure 9 shows that a collimator bore with dimensions 1.5 mm wide by 10 mm tall by 200 mm long is sufficient to ensure that count rates remain below  $10^6$  cps for even short-cooled, high burnup fuels.

The choice of scintillator size is driven mainly by the total and peak efficiency of the scintillator crystal (Figure 10), which translates directly into total assay time. Smaller detectors may be densely packed and thus require few lateral steps to collect a projection, but they also require longer total integration times as compared to larger detectors, which on the other hand require more steps per projection. Right circular cylinders are the standard commercially available geometry but an alternative is a slab detector that is thick in the direction parallel to the collimator bore, and narrow in the transverse direction. This allows a higher packing fraction (higher pixel pitch), fewer steps, and shorter overall data-collection time. This alternative design would drive up cost considerably since more and customized detector would be required, and therefore was not chosen for the UGETv1 design.



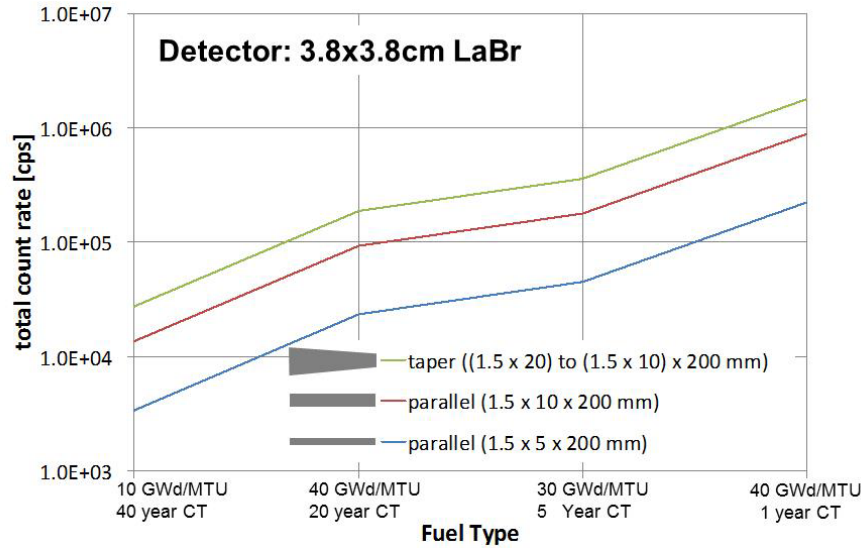


**Figure 9.** Total count rate as a function of the collimator design, assuming a 3.8x3.8 cm LaBr<sub>3</sub> scintillator.

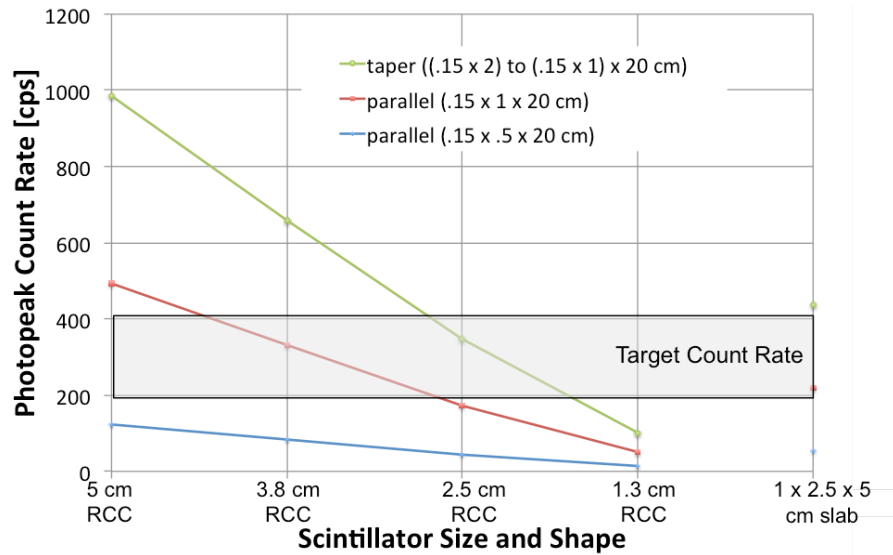


**Figure 10.** Peak count rate for the 1275 keV line from <sup>154</sup>Eu as a function of collimator and scintillator size. The target count rate, which reflects the count rate needed to provide sufficient statistical precision in reasonable count times, is shown. A PWR fuel with burnup of 20 GWd/MTU and 5-year cooling time was assumed in this calculation.

The analyses described above, along with additional calculations and the collective experience of the JNT 1955 team was used to arrive at a nominal UGETv1 design for this viability study. The UGETv1 design shown in Figure 11 is based on four detector heads with eight, 3.8-cm diameter scintillators behind a collimator with dimensions 1.5 mm wide by 1.0 cm tall by 20.0 cm deep. While only a single detector head is required for full data collection, multiple heads will decrease total collection time. To collect projection data, each head scans laterally on a translate stage, which in turn mounts on the rotate stage.

The interior radius of the device is large enough to assay even VVER-1000 fuels (not analyzed in this study) with appropriate mechanical clearance. Additional shielding is included in the design to protect the detectors in the high radiation fields and to manage count rates. UGET design parameters are shown in Table 9 and more discussion can be found in White et al. 2015.

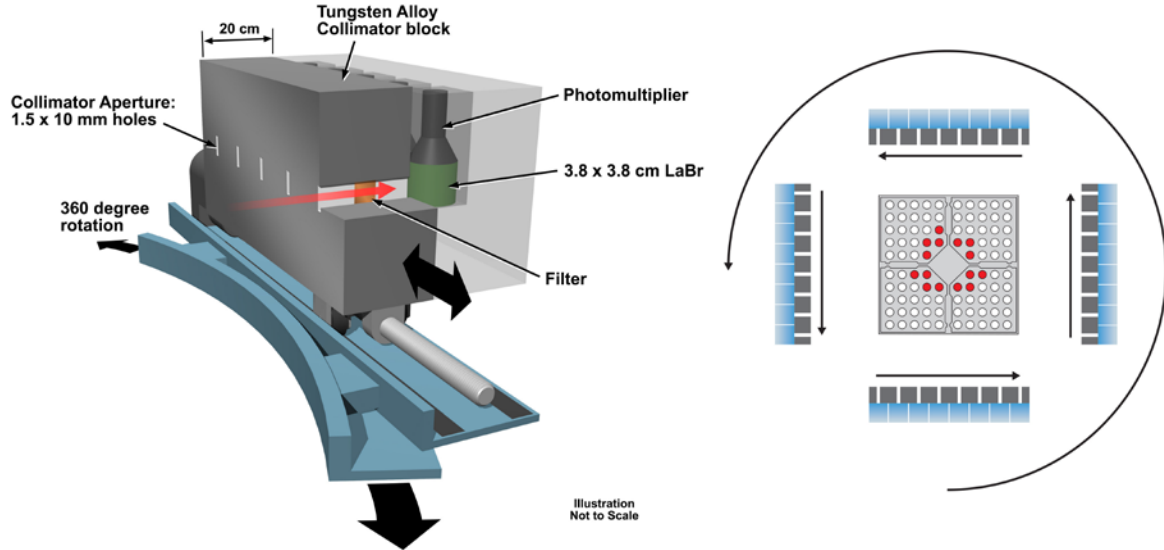


**Figure 11.** Diagram of a single detector head of the nominal Universal GET design defined in Phase I (left), the full instrument would include four heads, 8 detectors each, and a translate-rotate geometry (right).

**Table 9.** Parameters of the UGETv1 design.

Object and Scanner Parameters		
Maximum object diameter	37.5	cm
Scanner radius (object center to collimator face)	22.5	cm
Scintillator Parameters (LaBr)		
Diameter	3.8	cm
Length	3.8	cm
Collimator Parameters		
Material: Triamet-S18 (95% W, 3.5% Ni, 1.5% Cu)	18.0	g/cm <sup>3</sup>
Length	20.0	cm
Width	1.5	mm
Height	1.0	cm
Detector Head and Scan Parameters		
Number of detectors	8	
Collimator pitch	4.6	cm
Inter-scintillator gap	4.0	mm
Number of steps per projection for 2 mm sampling	23	
Number of angles	128	

A preliminary cost estimate for the UGETv1 design was calculated. For a four-head UGETv1 analyzed in this study is estimated at about 800k€, of which ~380k€ is for purchase of components, ~220k€ is for engineering and fabrication, and 200k€ is for software development. Subsequent units are estimated to cost approximately 550k€ due to reduced engineering and software development costs. Subsequent units of a two-head version are estimated to cost approximately 400k€.

## 8.0 Simulating Fuel Assembly Populations

A description of the process used to produce the populations of virtual fuel assemblies used in this study is provided in this section and can also be found in (White et al. 2014). The modeling framework is essentially a sequence of customized analytical solvers and Monte Carlo transport modules, as summarized in Figure 12. The primary advantage of this modular approach is the ability to split a complex calculation process into individual steps, and in particular to separate data-heavy spent fuel transmutation, the gamma-ray source definition, and the detector response reconstruction from the time-consuming 3D transport calculation.



**Figure 12.** Overview of modular process for creating simulated fuel assemblies.

### 8.1 Generation of Source Terms

The development of source terms for the virtual fuel assembly populations relies on detailed material definitions for each individual pin in the assembly at the time of discharge from the reactor (cooling time of zero years) calculated using MONTEBURNS (Trellue et al. 2011) or SCALE (SCALE 2009) burnup/depletion codes. Material inventory definitions can be provided in the form of binary CINDER 90 (Wilson et al. 2008) intermediate composition files, or in a human-readable format of MCNP input files. Each material file can contain an arbitrary number of isotopes, up to several thousand in some cases; isotopic inventory is controlled by the fidelity of the burnup calculation. Individual pin inventories are processed using a customized version of the CINDER 90 and DGSDEF (Mozin and Tobin 2010) codes. In this process, fuel composition is aged to an arbitrary cooling time using a quick and exact analytical calculation and data libraries. From the detailed material definitions at a specific cooling time, a discrete gamma-ray source term is reconstructed with absolute emission intensity determined for each line at the time of the measurement. Calculations are repeated for each individual pin, and as a result a volumetric source term for the complete assembly can be obtained. This volumetric source term then feeds the radiation transport step described next.

### 8.2 Radiation Transport to Produce Flux Sinograms

Transport of the gamma-ray flux from the fuel pins through the assembly and collimator to the detector locations creates a projection dataset that will be labeled a flux sinogram<sup>1</sup>. (Note that a flux sinogram is distinct from a detector response sinogram that includes the response of a particular detector to that incident flux.) A full-fidelity transport calculation of the fuel-imaging scenario would involve not only scatter and absorption of emitted gamma rays by the fuel assembly and surrounding material, but also the emission of secondary particles. It would include the modeling of imaging systems with on the order of 100 detector elements at each of 100 angular positions. In addition, the absolute collection efficiency of

---

<sup>1</sup> The sinogram can be visualized as a two-dimensional image in which one dimension is along the detector array and the other dimension is the angular position of the array relative to the object, and the collected intensity in each position is color-coded. A single point of activity (a delta function) in the object will form a sine curve in the sinogram. The sinogram is mathematically inverted to form a slice of the object in the reconstruction step.

the collimator is extremely low, allowed in practice because the emitted flux is so high. These factors conspire to make the radiation transport calculations computationally expensive. Further, thousands of virtual assemblies must be simulated in order to produce statistically valid estimates of performance where achieving low false alarm rates is important.

For these reasons, variance reduction tools were used to make the required simulations tractable within the constraints of the project schedule. Variance reduction methods applied to the GET study include:

- Gamma-ray source truncation. The complex gamma-ray emission source term defined for each pin can be simplified by accepting individual lines with highest contributions to the total emission intensity in the energy region of interest. As shown in Section 5.3, the modeling in this study assumed that the source term can be approximated by a subset of discrete lines from the several most important fission products ( $^{137}\text{Cs}$ ,  $^{134}\text{Cs}$ ,  $^{154}\text{Eu}$ ,  $^{144}\text{Pr}$ ). Relative line intensities can be adjusted to a specific combination of burnup and cooling time.
- Source axial extent limit. The gamma-ray source term for each assembly pin can be limited in the axial direction to the full or partial extent of the region subtended by the collimators. In case the source extent is truncated to a region shorter than the detector field of view, a normalization factor should be applied to the results. However, in this case some scattering and direct transport contributions can be lost in the response. In the PGET modeling presented here, a 1-cm axial extent was assumed; in the UGET modeling, 2.5 cm was assumed.
- Semi-deterministic transport. As a part of the regular Monte Carlo photon transport in the MCNP code package, the probability of the gamma-ray contributing to a point at the front face of the detector can be calculated analytically at each interaction or source point. This next-event estimator method is the primary way that low-efficiency transport geometries were sampled in this study.
- Gamma-ray population control-low energy cut-off. Gamma rays that were down-scattered below the energy region used for tomographic reconstruction can be terminated from the transport calculation.

The transport approach described above has been demonstrated to be accurate for a number of passive and active-interrogation experiments (Mozin 2012). A primary advantage of the method is that photons are tracked as a function of the pin from which they were emitted. This allows a parsing of the output data to provide flux sinograms from individual pins in an assembly. For example, 126 single-pin flux sinograms are generated and used to assemble the flux sinograms from a full VVER fuel assembly. Note that the flux sinogram from a single pin is attenuated by the rest of the pins in the assembly, but only the flux originating in that specific pin is recorded in the flux tally at the face of the detector. This parsing has several advantages. For example, by leaving one or more pins out of the sum, a sinogram from an assembly in which fuel pins have been replaced by inert (or less active) pins—fresh fuel or depleted material, for example—can be created. Also, the single-pin flux sinogram allows scaling of individual pin emissions before summing, thereby supporting the simulation of spatially inhomogeneous burnup, a key systematic uncertainty in tomographic performance estimation (see below). Spatial distribution of activity within the emitting pin was not considered in this work. The pin-by-pin flux sinogram data for each assembly also has a third dimension, energy, reported using the energy-bin structure used in the transport calculation. This energy structure can be dependent on the isotope of interest.

The statistical quality of the calculated single-pin sinograms is critically important for reducing subsequent creation of systematic effects in the large sets of derived virtual assemblies that were used to assess performance evaluation. For example, under-sampled sinogram data in the “base” assembly can lead to incorrect mean values used to add statistical noise for a population of assemblies derived from that original MCNP calculation. Single-pin data was calculated for the three assembly configurations (17x17 PWR, SVEA-96 BWR, and VVER-440), associated partial defects patterns, and the set of characteristic gamma-ray energies emanating from the key isotopes adopted in the analysis. For every case, extending

the base sinograms to a large population of reconstructed assemblies was accomplished by scaling individual pin data according to a burnup pattern (linear or nonlinear, depending on the isotope) and measurement time. In this process, any deficiencies present in the underlying result of a transport calculation will be extended to the entire set of virtual assemblies and will introduce systematic effects to the evaluation. Accordingly, rigorous criteria were developed to ensure convergence of the calculated single-pixel data, i.e. the summed counts from all fuel rods in one detector element position. The target relative uncertainty of <1% and the Pareto slope metric requirements were established for each individual detector pixel in every angular orientation. The transport calculation was extended until the convergence criteria were satisfied for all pixels that subtend assembly pins in the current projection.

A particular concern is the undersampling of pin contributions from the inner regions of the assembly where gamma-ray self-shielding and partial line-of-sight obstructions are important. However, the calculation scheme did not allow statistical analysis of individual single-pin sinograms. Instead, the implications of the underlying single-pin statistics on the results was investigated by comparing the tomographic reconstructions of two independent full-assembly sinograms: one from a full assembly calculation and another based on a compilation of single-pin sinogram data, which was obtained in separate calculations. Such formal comparison of two types of sinograms was performed for a “difficult case” of a 661 keV gamma-ray emission line in a 17x17 PWR assembly and a PGET instrument. Between two reconstructed images, the resulting aggregated pixel intensities for fuel pins in the assembly’s inner sections matched within 3%, providing a measure of statistical precision emanating from the base data. This evaluation provided an additional metric for the convergence of the modeled projection data. As a result, every single-pin sinogram calculated in the UGET project was supplemented by a full assembly sinogram and the two were routinely compared to ensure an absence of any significant discrepancies. Although one may not expect quantification of isotopic activities for fuel pins in the inner sections of an assembly at a higher level of precision than a few percent, one may still evaluate implications of variations in counting statistics, due to e.g. variations in detector count rate or measurement time, at a higher level of precision by investigating the statistical spread obtained when adding such variations to the base data.

The single-pin sinograms were also visually inspected. An example of single-pin flux sinograms, for a single energy bin, is shown in Figure 13. In those images, brighter pixels represent higher flux at the detector. In the upper left, a flux sinogram from a single corner pin is shown and in the upper right, the flux sinogram from an inner pin is shown. In the lower left, six pins have been added together to form a partial assembly (the inside pin is barely visible because of the high attenuation), and in the lower right a full assembly flux sinogram has been created.

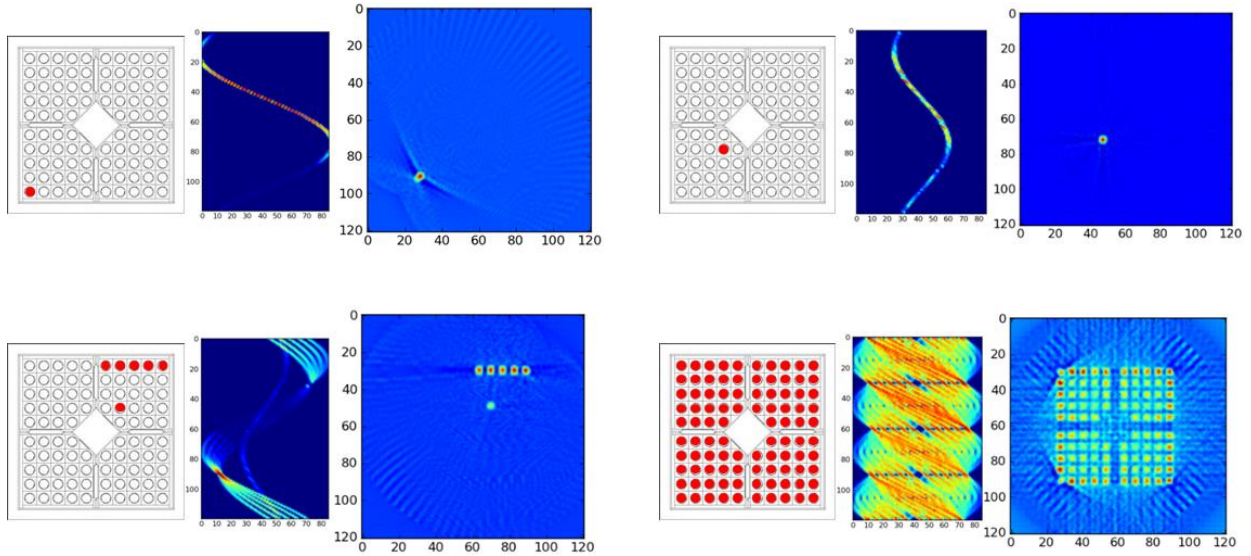


**Figure 13.** Illustration of how simulations of single-pin flux sinograms for a single energy region are used to assemble a full BWR assembly flux sinogram in that energy region.

### 8.3 Detector-response Sinograms

The radiation transport calculations described above provide the energy-dependent angular photon flux at the front face of each detector location, normalized per emitted particle in the MCNP calculations. This angular flux is then coupled to a separate Monte Carlo simulation of detector response. Such coupling relies on normalizing the per-particle angular flux data to an absolute count rate in the detector, which requires data specific to the assembly, pin and isotope of interest. Key scaling factors include the activity of each isotope (from the source-term step and any cooling calculation), detector efficiency, and the integration time.

This coupled simulation approach enables the study of various detector types (a relatively rapid calculation) separately from the full-field radiation-transport calculation for each virtual assembly (often a much lengthier calculation). This method has been used previously for other applications where the full-field transport of flux at specific locations in the problem is computationally expensive, and a variety of detector types are being considered to collect that flux (Smith et al. 2008, Shaver et al. 2009).

In this GET study, three different spectrometers were simulated to support the definition of UGETv1 and comparative analyses of UGETv1 and PGET: the inorganic scintillators  $\text{LaBr}_3(\text{Ce})$  and  $\text{NaI}(\text{Tl})$ , and cadmium telluride ( $\text{CdTe}$ ), a room-temperature semiconductor. The Monte-Carlo-based method for simulation of detector responses produces a gamma-ray spectrum spanning the entire energy range of interest, in narrow energy bins (typically 1-keV wide), and captures essential characteristics that include the full-energy peak efficiency and resolution, Compton continuum, and some of the secondary reaction effects (e.g., X-ray escape). One such vector, labeled a detector-response sinogram and representative of “infinite measurement time” in terms of statistical uncertainty, is produced for each energy-dependent flux sinogram.

Accurately translating incident flux into detector response is heavily dependent on assumptions for energy resolution. Arriving at reasonable assumptions was relatively straightforward for the  $\text{LaBr}_3$  and  $\text{NaI}$  because the scintillation characteristics of each material define the nominal energy resolution behavior—crystal size/orientation and charge-carrier readout methods have little effect on the energy resolution

relationship. The assumed energy resolution parameters for this study were 3.1% and 7.7% relative FWHM at 662 keV for  $\text{LaBr}_3$  and  $\text{NaI}$ , respectively (Hakimabad et al. 2007, Quarati et al. 2007). An energy dependence of  $1/\sqrt{E}$  was assumed. Example response functions for  $\text{LaBr}_3$  and  $\text{NaI}$  are shown in Figure 6 (measured) and Figure 8 (simulated).

The simulation of detector response for  $\text{CdTe}$  is significantly more uncertain, since it is dependent on several factors that are not always well-characterized by vendors, including the degree of charge-carrier trapping (defined in part by material quality), specifics of the electrode-readout configuration, and the noise levels in the front-end preamplifiers. None of this kind of information was available for the 208  $\text{CdTe}$  detectors in the PGET device, so assumptions were made based on published data deemed to be reasonably representative. As Figure 14 illustrates, the  $\text{CdTe}$  detector response was defined largely by a tailing parameter that aggregates several charge-collection effects into a single variable. The net effect of tailing is that counts are removed from the full-energy peak and shifted to the lower-energy continuum below the peak, thereby degrading the spectroscopic capabilities of the device. High-quality spectroscopy grade  $\text{CdTe}$  with readout electronics specifically designed for spectroscopic performance may have tailing levels less than 10% while counter-grade devices like those used in the PGET device are likely to have tailing levels greater than 50% (Richter and Siffert 1992, Sokolov et al. 2008).

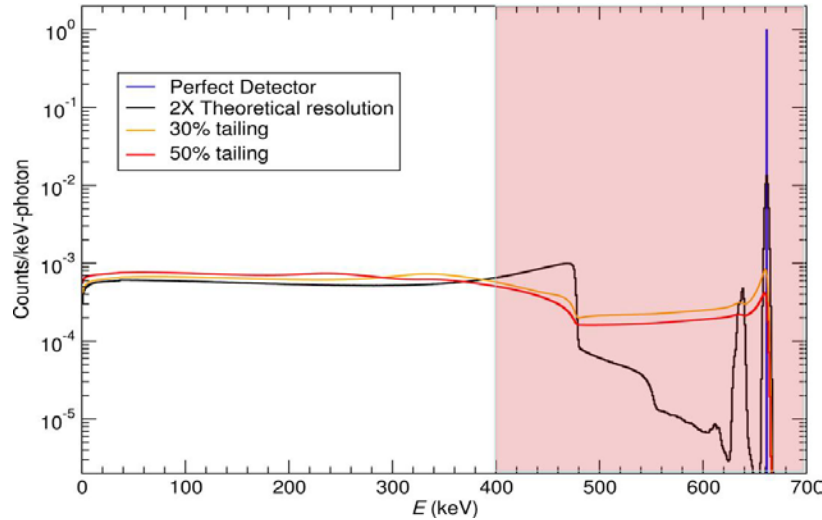


**Figure 14.** Depiction of charge-carrier trapping effects (i.e., tailing) on  $\text{CdTe}$  detector response functions, in the context of a PGET energy window spanning 400-700 keV. For this study, 50 percent tailing was assumed.

For the PGET simulated in this study, a tailing parameter of 50% was assumed. While efforts were made to reasonably represent the response of the  $\text{CdTe}$  sensors in the PGET instrument, the exact value of the tailing parameter will have little effect on simulated tomographer response for a PGET operated with the broad energy windows used to date. This is illustrated in Figure 14 where it is clear that the net count rate recorded in the 400-700 keV window is essentially unchanged under different tailing assumptions. Tailing assumptions would be more important for narrow energy windows, e.g., 600-700 keV that might be considered in future PGET analysis. In this study, the energy-dependent detector-response data for PGET is divided into three bins: 400-700 keV, 700-1100 keV, and greater than 1100 keV, consistent with the field settings of the PGET instrument.

A comparison of the peak-to-total ratios is given in Figure 15 for the 3.8-cm  $\text{LaBr}_3$  used in UGETv1, a small  $\text{CdTe}$  wafer similar to that used in the PGET device, and a larger 1.5-cm<sup>3</sup>  $\text{CdTe}$  representative of the larger devices available commercially today. This figure shows the benefit of a large, high-atomic



number detector, when peak spectroscopy is of interest (e.g., for Objective 2). Note that the LaBr<sub>3</sub> detector (scaled for display purposes) provides 20 times higher peak efficiency than the large CdTe.

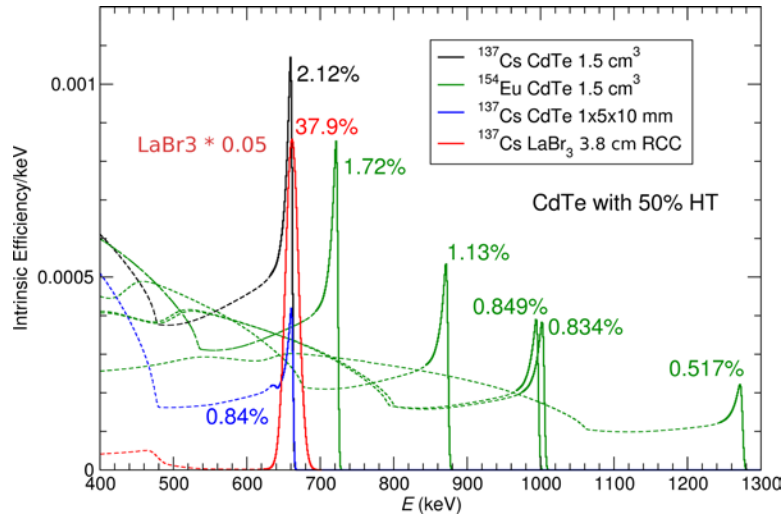


**Figure 15.** Comparison of simulated detector response functions for LaBr<sub>3</sub> (3.8-cm RCC) and CdTe (wafer with edge facing incident flux and 1.5 cm<sup>3</sup> cube). Tailing effects of 50 percent were assumed for the CdTe. Labels on the peaks are the peak-to-total efficiency for each detector type.

## 8.4 Creating Realistic Virtual Assembly Populations

Once a set of single-pin detector-response sinograms has been created at a nominal burnup level, that basis set can be used to generate a large population of simulated assemblies, each with a distinctive and inhomogeneous pin-to-pin burnup. A description of how single-pin detector-response sinogram data are used as the basis for creating virtual full-assembly sinogram data that includes appropriate levels of statistical noise and pin-to-pin burnup variation is provided in the following section.

### 8.4.1 Pin-to-pin Burnup Variation

A key source of systematic variation in the gamma-ray signatures emitted by fuel is the pin-to-pin burnup variation that is produced during irradiation in a reactor. To emulate this variation, the GET modeling framework includes an algorithm to apply a prescribed pin-wise burnup distribution to an assembly population. The algorithm is based on the scaling of individual single-pin sinograms with burnup-dependent weights. The weights applied to each single-pin sinogram are samples drawn from a user-defined probability distribution on pin-wise burnup; a collection of these single-pin sinograms forms one virtual fuel assembly.

In this study, a uniform distribution on pin-to-pin variation of  $\pm 20\%$  was assumed for all three fuel types, for simplicity and consistency in analysis. While it is recognized that pin-wise burnup variation can be very different in BWR, PWR, and VVER assemblies, limited information was available to apply greater fidelity to each fuel type. The assumed burnup variation may be at the extreme end of likely burnup variations even for BWR fuels (less variation is expected for PWR and VVER fuels), and therefore, represents a conservative assumption for viability questions where pin-wise burnup has a significant effect on performance (see discussions of pin scoring for Objective 1 analysis). Example images depicting how pin-wise burnup variation affects the images produced for each virtual fuel assembly are shown in Figure 16.

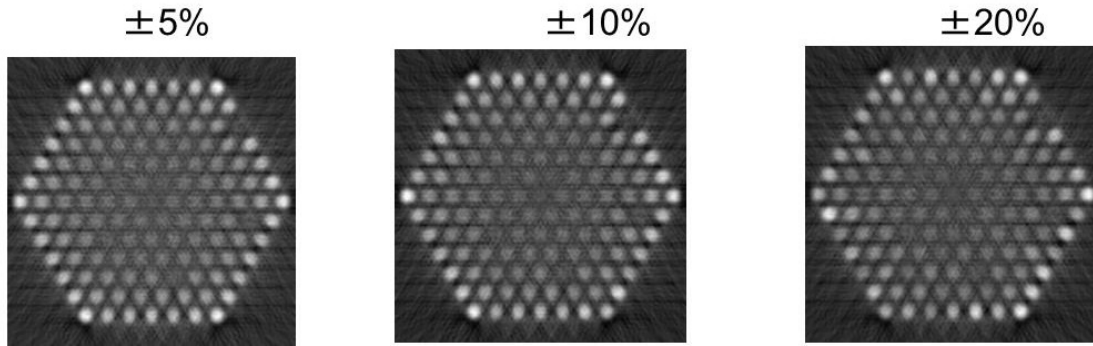


**Figure 16.** Example tomographic images of a VVER assembly reconstructed based on sinograms with varying levels of pin-to-pin burnup variation. A uniform distribution over the variation extents is assumed.

#### 8.4.2 Statistical Noise

Once burnup-variation weights have been applied to the single-pin sinograms, Poisson noise can be applied to obtain one realization of the measured energy-dependent tomographic response, for an assumed projection data collection time. Here, the addition of Poisson noise was applied based on the summed detector counts for each angular position (i.e., collected across all single-pin sinograms). This process was performed over all projections (all data points) in a virtual assembly. It could then be repeated many times to obtain sinograms for a population of virtual fuel assemblies with common initial loading, assembly-average burnup and cooling time, for a given detector type and total collection time. As discussed in Section 8.2, limitations in the statistics of the underlying base data from fuel pins in the assembly's inner section (single-pin sinograms) set the limit of achievable precision in the reconstructed pin-averaged pixel intensities for inner pins at about 3%. However, this procedure allows for the proper evaluation of additional pin-score variations inferred from counting statistics. Examples of reconstructed images obtained from sinograms corresponding to different projection collection times are given in Figure 17.

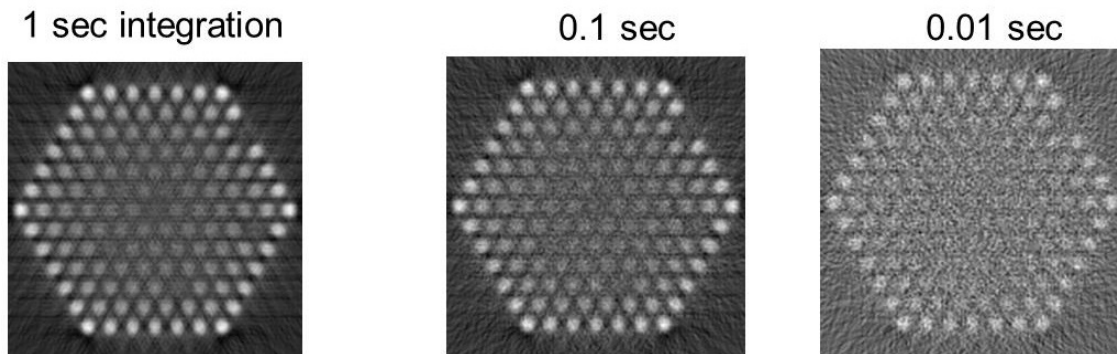


**Figure 17.** Example PGET images of a VVER assembly obtained in reconstructions based on sinograms created by adding different levels of statistical noise, corresponding to different integration times.

## 8.5 Verification and Validation of Simulated Tomographer Responses

The Monte Carlo modelling performed in this project was verified and validated in multiple ways, including inter-code comparisons and comparison to empirical data. Descriptions of several verification and validation activities are below.

### 8.5.1 Process Validation: Source Term to Detector Response

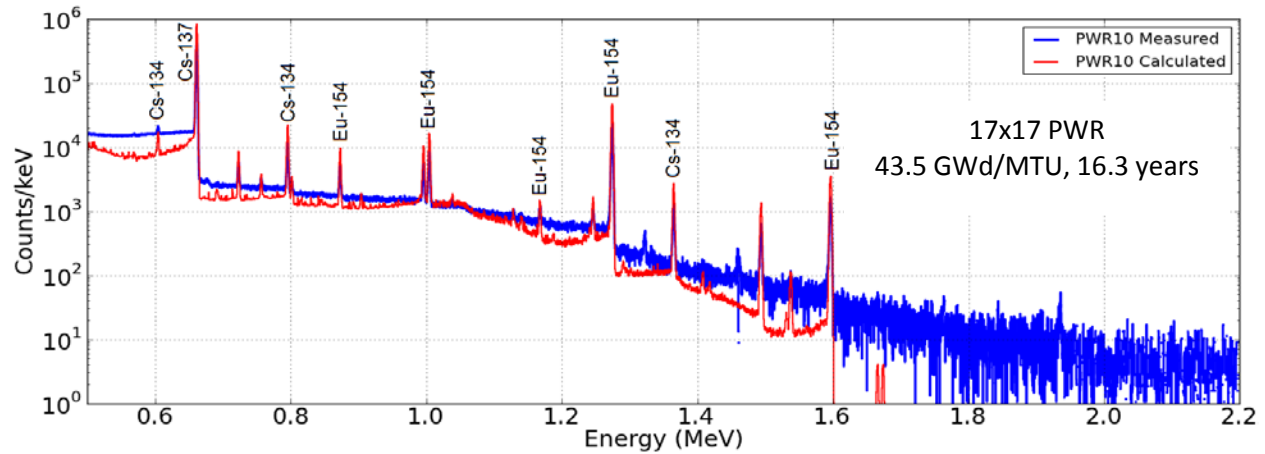
The sinogram modeling approach described above was validated against experimental measurements of real spent fuel assemblies in single-detector configurations and in full tomography setups. Benchmarking data were obtained from the single-pixel measurement effort conducted at the Clab facility in Sweden (Section 6.0), as well as from earlier deployments of prototypical tomographic instruments at reactor sites in Sweden and Finland. As a general consideration, the performance of the calculation technique in such benchmarks can be considered adequate if the calculated energy-dependent gamma-ray responses replicate the continuum shape, photo peak-to-continuum ratios, and overall count rate on the detector within a factor of few, when compared to experimentally measured results. Considering the multiple unknowns generally associated with spent fuel measured in the experiment and the assumptions implemented in modeling, highly precise agreement is generally not possible. However, significant departures between measured and simulated spectra in either the continua or net peak count rates can be used to indicate inaccuracies in the models or associated analysis. Discrepancies in the spectra shapes need to be analyzed and carefully extrapolated in the analysis of the tomographic instrument performance and the design process.

Validation of the assembly modeling process was completed using experimental data from spent fuel measurements at the Clab facility in Sweden described in Section 6.0. High-resolution HPGe response spectra measured in the course of this effort were replicated with high fidelity using the modeling approach described above. This benchmarking calculation was supported by the detailed burnup/depletion modeling of spent fuel material compositions using the SCALE code package and detailed fuel design and reactor data provided by the operator (Hu et al. 2016). For the calculation, extensive material compositions in the midsection of the assembly were generated for each pin and used as inputs to the modeling process. A full 3D model of the experimental setup was developed for transport calculations and accounted for the transmission of gamma rays from fuel pins, through the assembly, surrounding water medium and collimator, to the detector.

An example of the benchmarking comparison is shown in Figure 18 for a 17x17 PWR assembly with 43.5 GWd/MTU burnup and 16.3 years cooling time. The overall spectral shape in the region of interest is in general agreement, position and relative intensity of the major gamma peaks from  $^{134}\text{Cs}$ ,  $^{137}\text{Cs}$ , and  $^{154}\text{Eu}$  are correct, and the relative error on the peak areas of these isotopes is within approximately 35% percent on average. The offset between the measured and calculated continuum in the gamma-ray spectrum can be attributed to several factors: the level of detail in the modeled geometry, the assumed complexity of the source term, and the pulse processing electronic effects of the detector system. The uncertainties in these factors, as well as those in the burnup, source definition, transport, and detector response calculations are the likely cause of the discrepancy between the calculated and measured spectral continuum.

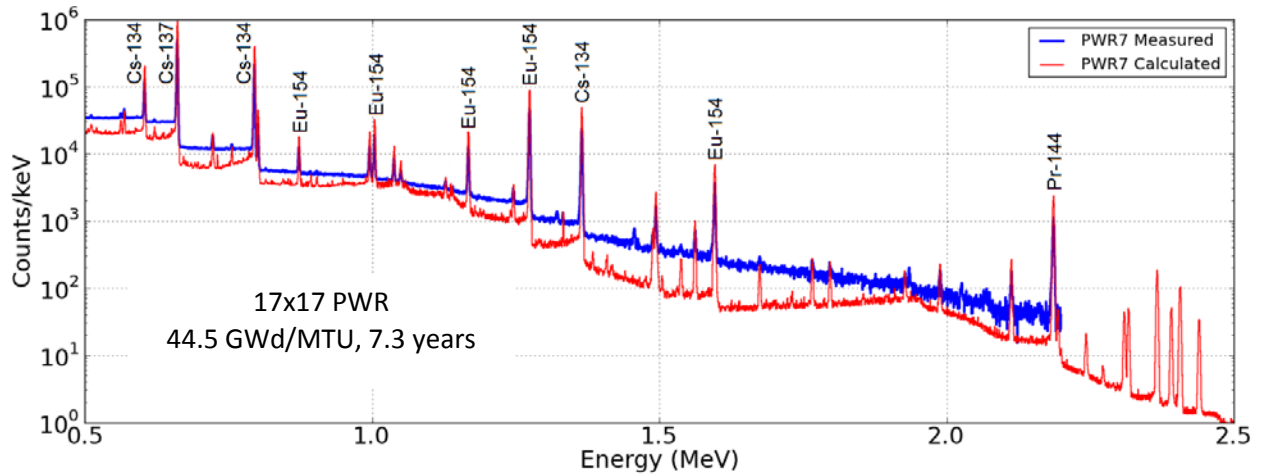
Benchmarking results for a more complicated case of a 17x17 PWR assembly with 44.5 GWd/MTU burnup and 7.3 years cooling time is shown in Figure 19. Considerably shorter cooling time in this case results in more extensive gamma-ray emission source term and complex spectroscopic response. Despite this, the measured and calculated spectra still demonstrate a relatively good agreement (approximately 22% for key photopeak areas). Although in some energy regions the calculated continuum departs from the experiment, the overall profile of the spectrum and peak parameters are adequately

replicated consistent with measured features. A number of benchmarking comparisons of this nature were performed for a range of assemblies measured at Clab, and in all cases a consistent reasonable agreement between the modeled and experimental spectra was observed. The exact fidelity of the calculation method used in this benchmarking was preserved for the tomographic projection data computations throughout the UGET effort.



Energy, MeV	Isotope	Peak Area, counts		Ratio (Calculated/ Measured)
		Measured	Calculated	
0.605	<sup>134</sup> Cs	10980 ± 374	15550 ± 259	1.416 ± 0.052
0.662	<sup>137</sup> Cs	1026079 ± 1074	1270147 ± 1278	1.238 ± 0.002
0.723	<sup>154</sup> Eu	8111 ± 175	11166 ± 155	1.377 ± 0.034
0.796	<sup>134</sup> Cs	25282 ± 212	33408 ± 231	1.321 ± 0.013
0.873	<sup>154</sup> Eu	8959 ± 398	12977 ± 292	1.448 ± 0.070
0.996		11328 ± 139	15115 ± 173	1.334 ± 0.023
1.005		19820 ± 181	26104 ± 206	1.317 ± 0.015
1.274		65708 ± 264	87762 ± 330	1.336 ± 0.007
1.596		5102 ± 75	6702 ± 91	1.314 ± 0.024

**Figure 18.** Benchmarking comparison between experimental and calculated HPGe spectra for a 17x17 PWR spent nuclear fuel assembly with 16-year cooling time measured at the Clab facility in Sweden. The table compares measured and calculated peak areas for nine characteristic photopeaks in the spectrum.



Energy, MeV	Isotope	Peak Area, counts		Ratio (Calculated/ Measured)
		Measured	Calculated	
0.605	Cs-134	232255 ± 719	270059 ± 674	1.163 ± 0.005
0.662	Cs-137	1183401 ± 1168	1384168 ± 1330	1.170 ± 0.002
0.723	Eu-154	16809 ± 529	20766 ± 392	1.235 ± 0.045
0.796	Cs-134	512315 ± 777	608321 ± 886	1.187 ± 0.002
0.873	Eu-154	19808 ± 261	25348 ± 237	1.280 ± 0.021
0.996		23124 ± 263	29346 ± 253	1.269 ± 0.018
1.005		41384 ± 288	50462 ± 297	1.219 ± 0.011
1.167	Cs-134	29620 ± 236	36317 ± 237	1.226 ± 0.013
1.274	Eu-154	135621 ± 389	166325 ± 455	1.226 ± 0.005
1.365	Cs-134	69716 ± 279	81582 ± 319	1.170 ± 0.007
1.596	Eu-154	10356 ± 116	12818 ± 127	1.238 ± 0.019
2.186	Pr-144	3714 ± 65	4562 ± 75	1.229 ± 0.029

**Figure 19.** Benchmarking comparison between experimental and calculated HPGe spectra for a 17x17 PWR spent fuel assembly with 7-year cooling time measured at the Clab facility in Sweden. The table compares measured and calculated peak areas for 12 characteristic photopeaks in the spectrum.

### 8.5.2 Validating MCNP simulations using data from the PLUTO Device

The procedures used for the MCNP simulations were benchmarked against experimental data collected with the PLUTO device (Jansson et al. 2006) on a SVEA-96S BWR fuel assembly at the Forsmark nuclear power plant in 2002. In the PLUTO measurements, spectroscopic evaluation of the area of the 1596 keV photo peak corresponding to  $^{140}\text{Ba}$  (a relatively short-lived isotope used for the specific objective of the Forsmark project, see Section 2.2) was performed. These data were reported to the UGET project to provide an experimental benchmark of the models used for simulating transport of full-energy gamma rays. Since a full energy absorption peak was evaluated, a mono-energetic source of 1596 keV gamma could be used in the MCNP simulations. The rod-by-rod distribution of the  $^{140}\text{Ba}$  gamma-ray emission intensity was provided from the operator-declared data and used for the benchmark.

The detailed 3D geometry of the PLUTO experiment as described by Jacobsson Svärd et al. (2005) was replicated for the gamma-ray transport in MCNP, including exact parameters of the SVEA-96S BWR assembly and the measured offset from the center of rotation. The  $^{140}\text{Ba}$  gamma-ray source term was distributed across assembly pins according to a map of the pin-wise content of this isotope, provided by the facility operator and based on computations. A total of 120 individual angular projections each with 85 individual pixel positions were calculated to replicate the data collected in the experiment. A comparison of measured and calculated projection shapes for two arbitrary angles is shown in Figure 20. The intrinsic efficiency of the BGO detectors used in the PLUTO instrument was not factored into the calculated response and the depicted results are normalized by the total area. Because of the extensive collimation and spectroscopic gamma-ray response processing in this device, the scattering contribution to the projection data is effectively rejected. Therefore, the PLUTO data contain only contrast information as opposed to the JNT 1510 (PGET) instrument data that provides a combination of contrast and scattering information. Figure 20 shows that the calculated PLUTO response effectively replicates most of the contrast features. In addition, the results confirm that the projection data are primarily populated by the direct transmission of the source photon to the detector.

Reconstructed images of the SVEA-96S BWR assembly were produced from the measured and calculated projection data using the same Filtered Back Projection method. As expected from the good agreement between the projection data profiles, the two reconstructed images shown in Figure 21 are practically indistinguishable. Reconstruction artefacts visible on the periphery of the assembly and between subassemblies are consistent between the two images. Apparent contrast and pin intensities are well replicated. Distorted pins at the bottom corners of the assembly originate from the incomplete lateral projection sampling at the maximum dimension (diagonal) assembly orientation. This effect is well captured by the modeling method.

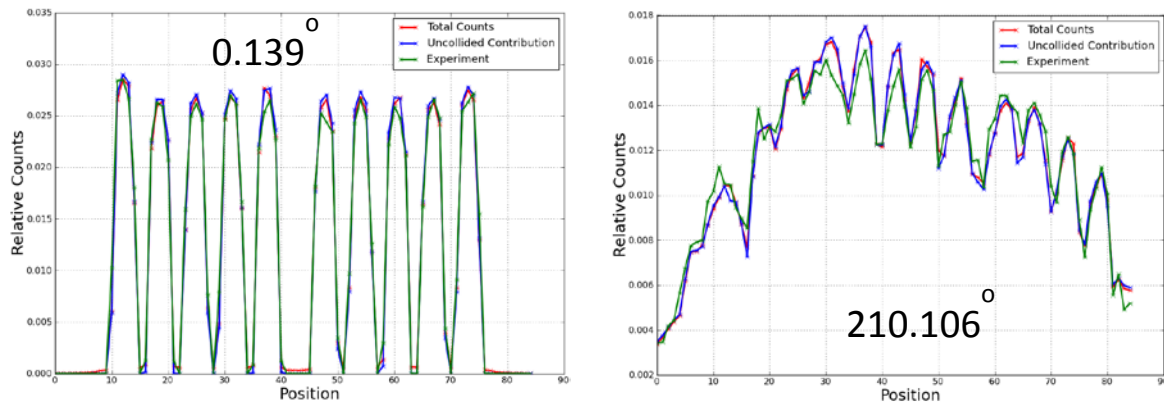


**Figure 20.** Overlay of the measured and calculated projection data profiles at two arbitrary angular orientations for the SVEA-96S spent fuel assembly in the PLUTO instrument at Forsmark nuclear power plant. All data are normalized by the total area. Two sets of calculated data are depicted: total gamma-ray flux with scattering contribution and the direct transmission from the source location.



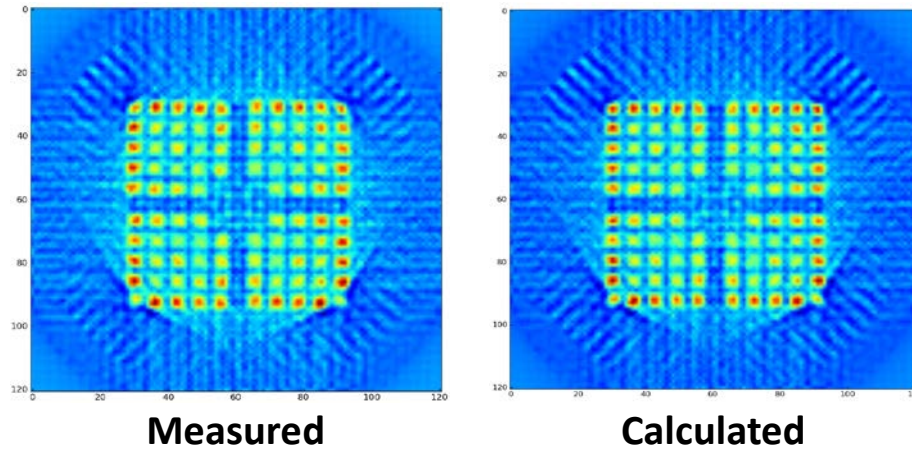


**Figure 21.** Comparison of reconstructed images from the measured and calculated projection data for the PLUTO experiment with the SVEA-96S BWR assembly at the Forsmark nuclear power plant, providing an experimental benchmark for the adopted simulation procedure.

### 8.5.3 Validating Models of the JNT 1510 Device

In addition to the PLUTO benchmark above, the capability of the modeling techniques to replicate tomographic data was also benchmarked using the experimental results from field tests of the JNT 1510 (PGET) instrument described in Section 2.1. Raw projection data and parameters of measured spent fuel assemblies were provided to the UGET effort to enable the comparisons. Two gamma-ray transport calculation techniques were implemented for this benchmark to allow for a later additional code-to-code comparison of the results for the proposed UGET device design, for which no experimental benchmark data are available (see Section 8.5.4). The first technique relied on the MCNP-based transport approach that was used to produce the main part of the data analyzed in this report, which had the full range of variance reduction and acceleration techniques enabled. The second technique used the alternative, yet also established, Geant4 simulation platform described in (Agostinelli et. al. 2003) and an analog gamma-ray transport calculation, with no variance reduction or acceleration techniques, to provide a proper benchmark.

#### 8.5.3.1 MCNP Benchmark

The MCNP-based projection data calculation benchmark was completed using the JNT 1510 (PGET) instrument test data with VVER-440 spent fuel assemblies measured at the Loviisa nuclear power plant in 2014. Projection data were provided for a VVER-440 assembly with 43.5 GWd/MTU burnup and 12 years cooling time with three missing pins as a number of counts at each pixel integrated above 400 keV. The exact position of the assembly in the measurement setup was established by reconstructing the image from the experimental data using the filtered back projection method. From this image, the offset of the assembly from the center of rotation and approximate assembly angular orientation inside the PGET instrument were determined and replicated in the detailed transport model of the measurement setup. Pin-specific fuel isotopic inventory at the time of discharge was calculated using the MONTEBURNS code and operator-provided cumulative pin burnup data assuming a typical three-cycle reactor utilization history. From these data, the gamma-ray emission source term for nine characteristic gamma-ray lines shown in Table 5 were calculated for each pin using the method described in Section 8.5.1. This source term was used to calculate projection data for a number of orientations of the JET 1510 instrument.

Reliability issues with PGET instrument data acquisition and positioning electronics during the field measurements introduced additional uncertainties and structure to the experimental results available for this benchmark. These effects were pixel-position dependent, and varied between subsequent measurements, preventing any attempts to introduce a systematic correction. As a result, only data from Head 1 of the PGET instrument measured in this experiment was deemed applicable for the benchmark comparison.

Figure 22 demonstrates a comparison between the measured and calculated projection data profiles at two arbitrary angular orientations as measured by Head 1 of the PGET instrument from the VVER-440 assembly. The exact intrinsic efficiency and gamma-ray energy discrimination threshold for PGET detector pixels were not determined, therefore only relative shape comparison is shown (area normalization). As in the experiment, the calculated photon flux at each pixel is integrated above 400 keV, which captures energy down-scatter and object scatter gamma-ray contributions. This scattering contribution is critically important to the performance of the tomographic instrument, and populates projection data underneath and on the periphery of the contrast region that is critical for the image reconstruction. The modeling technique accurately represents this effect both in relative magnitude and spatial distribution. The experimental projection data depicted in the 180 degrees orientation demonstrate one of the manifestations of the electronics issues with the PGET setup at the time of the experiment. The left side of the contrast region apparently registered with a lower count rate than the right side. This deficiency in the experimental data is discussed in the PGET report issued following the measurement (Levai et al. 2014). No artificial corrections were applied to the measured data, and they were depicted as acquired.

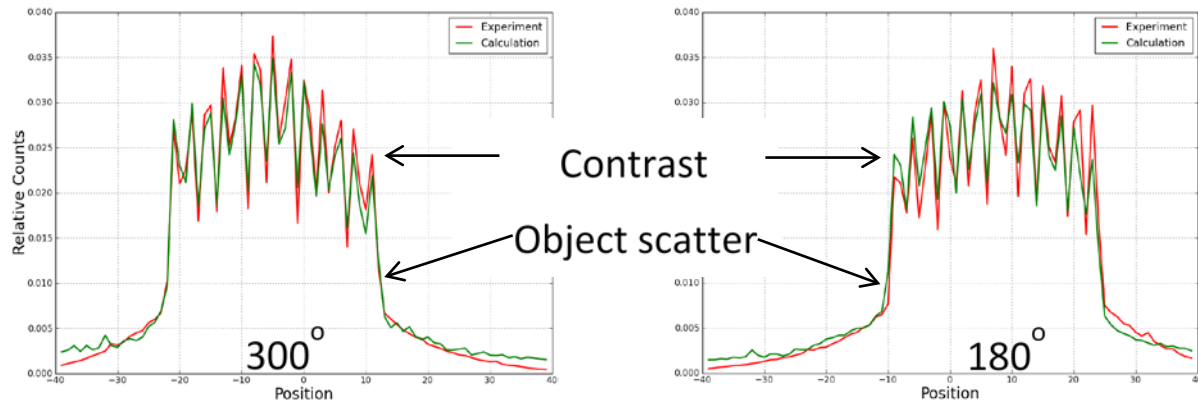


**Figure 222.** Overlay of the measured and calculated projection data profiles at two arbitrary orientations from PGET instrument test measurements with a VVER-440 assembly at Loviisa nuclear power plant in 2014 [Levai 2014]. Datasets are normalized by the total area. Calculated results demonstrate a good agreement in the contrast region as well as in the gamma-ray scattering contribution. The right side of the measured profile in the 180-degree projection demonstrates higher pixel count rates due to electronics effects at the time of the experiment.

To replicate the complete Head 1 sinogram measured in this experiment, the total of angular 120 projections equally spaced at 3-degree intervals were calculated. For a visual comparison, both measured and calculated projection datasets were reconstructed using the Filtered Back Projection method into images shown in Figure 23. The image reconstructed from the experimental data demonstrates further evidence of electronic instabilities in the PGET setup during measurement. Hot pixels lead to the appearance of bulls-eye and ring artifacts, and smearing of the pins in the left-bottom side suggest rotational positioning uncertainties. Still, the two images support a qualitative comparison, indicating that



the model adequately represents the contrast, scattering effects and even allows replication of characteristic reconstruction artefacts (rays on the periphery of the assembly).

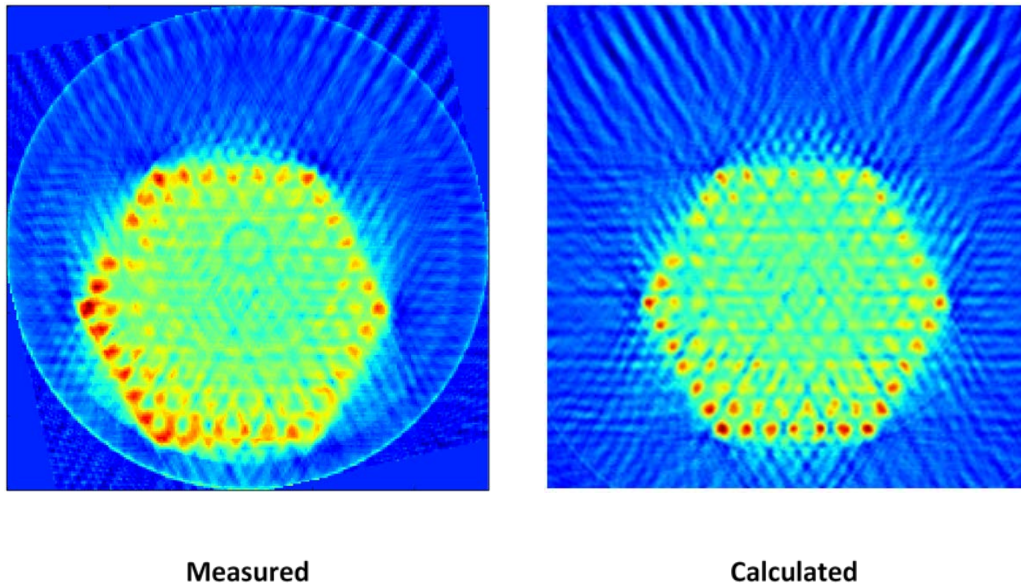


**Figure 233.** Reconstructed images (filtered back projection method) of measured and calculated projection data from PGET instrument test with a VVER-440 spent fuel assembly with three missing pins at Loviisa nuclear power plant in 2014. Ring artefacts and smearing in the measured image are likely due to effects of electronics instabilities.

### 8.5.3.2 Geant4 Benchmark

As described in Section 2.1, an ASEA Atom 8×8-1 BWR fuel assembly was measured in Olkiluoto, Finland, March 2013, using the PGET instrument, and experimental data from this campaign were used to provide an experimental benchmark for simulations using the Geant4 code. The homogeneous gamma-ray source spectrum from the fuel assembly was calculated using the same gamma-ray energies as for the MCNP benchmark. The geometry of the device was modeled in Geant4 using drawings provided to the UGET project, and a schematic of the model can be seen in Figure 24.

From the Geant4 models of the JNT 1510 device, the pulse count in each of the 204 detectors above three energy thresholds (200, 400 and 700 keV) was simulated for all rotational angles of the device. Figure 25 shows two examples of such counts for two different angles. The error bars in this figure represent the simulation uncertainty, as given by the Geant4 code, and an estimate of Poisson noise in the measured data.

As documented in Section 2.1, the measurement data contained erroneous data points, e.g. from faulty detectors or associated electronics, manifested as sharp dips in the projections (count vs detector number at some rotational angle). In the simulations, however, all detectors were assumed to be equal, thus not corresponding perfectly to the case in the measurement.

Compared to the measurement count, the simulations generally show relatively high counts in the outer detectors (around detector numbers 10-30 and 80-90), outside the fuel assembly, and also some edge effects with high counts in the outer detectors (around detector numbers 0-10 and 90-104). The relatively high count in the outer detectors (around 0-10 and 90-104) can be explained by scattered radiation

entering the detectors from the side of the device. (It was found after completion of the simulations that the simulated device included less side shielding than the actual PGET.)

The simulated projections of gamma radiation intensity from the JNT 1510 device show a shift between measured and calculated number of counts compared to the measurements, as shown in Figure 25. The likely reason for this discrepancy is that the fuel assembly was not completely centered in the measurement device during the measurements, while the simulations were based on a model where the fuel is perfectly centered in the device.

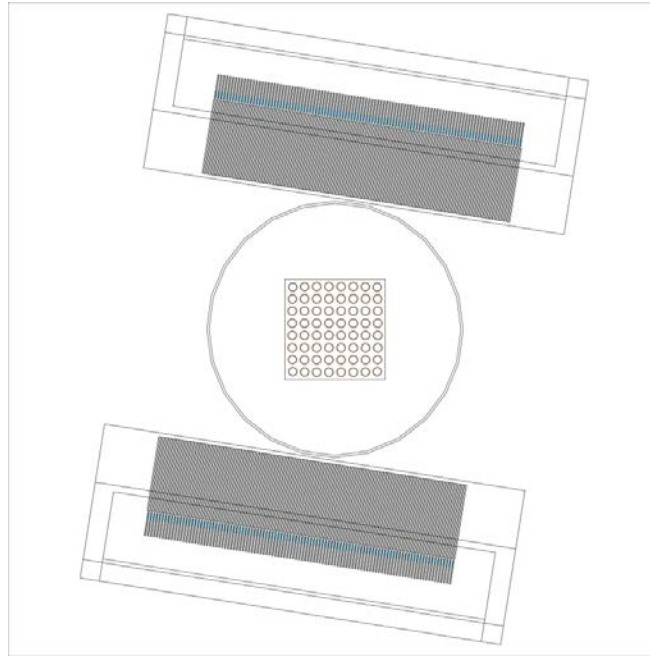


**Figure 244.** The JNT 1510 model used in Geant4.

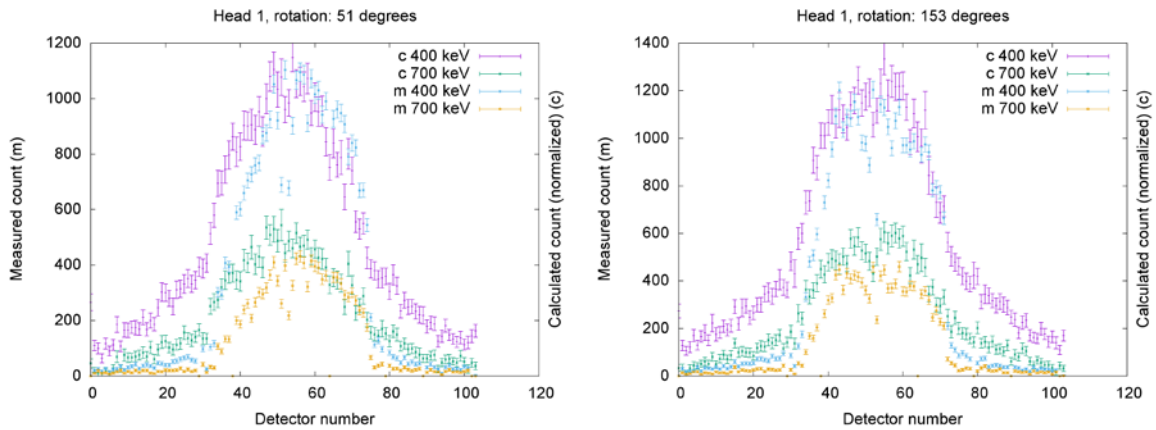


**Figure 255.** Calculated counts above three energy thresholds (400 and 700 keV) for two different rotational angles of the JNT 1510 device. The calculated counts (c) have been normalized to the corresponding average measured count (m).

#### 8.5.4 Cross-verification: MCNP and Geant4 UGET Models

As discussed in previous Sections, MCNP was used by the U.S. Support Program to the IAEA (USSP) to generate the large libraries of virtual fuel assemblies used in the Phase I viability study. While measured data were available for validation of the MCNP-simulated PGET response (Section 8.5.2.1), no such data were available for the proposed UGETv1 design. To build confidence in the fidelity of the MCNP simulations for the UGET instrument, cross-verification was performed for specific fuel cases, by comparing MCNP data to Geant4 simulation data, which were provided by SWESP. In this cross-verification task, two PWR cases were studied, one with no missing rods, and one with 11 missing rods

A drawing of a single UGETv1 detector head is shown in Figure 11 and a table of design parameters is shown in Table 9. Additional shielding is included in the design to protect the detectors in the high radiation fields and to manage count rates. In a full system, the head would sit on a rotating platform in a “donut” that would surround the fuel assembly at some vertical offset from the bottom of the assembly. Multiple heads could be included on the ring to decrease total data-collection time. For simulation purposes, only a single head was included in this code-to-code benchmark.

##### 8.5.4.1 Simulated Cases

The design of the UGET device was modeled in both frameworks (MCNP and Geant4) described in previous sections. The Geant4 model was used in this work only to validate the MCNP model. In Geant4, no techniques for variance reduction were used, which limited the number of cases to those that could be simulated in the available time frame. Therefore, only two selected cases for a PWR 17x17 fuel assembly were covered in this benchmark, as summarized in Table 10.

**Table 10.** Summary of selected cases for a code-to-code benchmark of the models used in the UGET simulations, covering the gamma-ray flux from a PWR 17x17 fuel assembly. In all cases, two source energies (662 keV and 1274 keV) and two rotations of the device (0 and 45 degrees) were used. Removed-rod locations are based on [0,0] at upper left of assembly.

Case Number:	1	2
Lateral positions of the device [mm]:	-23	-23, -21, -19, ..., 17, 19, 21 (one projection)
Pattern of removed rods:	None (complete assembly)	[-7,0], [-4,-4], [-4,3], [-4,8], [0,-8], [0,5], [1,-1], [2,2], [4,-2], [5,6], [8,-3]

##### 8.5.4.2 MCNP Simulations

Two sets of MCNP simulations were performed: first, using a model to specifically compare case 1 (with a complete fuel assembly) and second, using a model capable of calculating all combinations of device positions (lateral positions and rotations) and source energies in a reasonable time to specifically compare case 2 (with missing pins).

In the first MCNP model, MCNPX 2.5.0 was used to model the 1274 keV gamma transport in case 1 of Table 10. The MCNPX cell geometry used for the simulations is shown in Figure 26. It includes the fuel assembly with fuel rods and guide tubes, contained in a steel cylinder and a collimator with eight slits to the detector locations corresponding to the UGET design, as shown in Figure 27 and Figure 28.

The physical detectors have not been modeled. Instead, the photon current integrated over the detector end surface is estimated using the F1:P tally of MCNPX. Variance reduction was introduced by truncation of the axial source distribution and the angular emission distribution, where the axial emission is limited to the 42.5-mm height and the angular emission is limited to a 5-degree cone. In each simulation,  $10^{10}$  photon transports were simulated.

In each calculation, the contribution of each rod to each of the eight detector positions was investigated. Figure 27 shows the accumulated contribution of each rod in the two cases (i.e., the summed contribution of each rod to all detector positions).

The second model used a virtual geometry setup with a simultaneous calculation in all possible lateral positions at each rotation. For each angular orientation, all possible positions of the detector head pixels were separated by a perfect collimator impenetrable for gamma-rays. A sufficiently thick skin of collimating material was maintained between the individual pixels to allow for the shallow angle scattering effects. This approach was implemented to accelerate production of large projection data amounts for various assembly types and pin diversion cases.

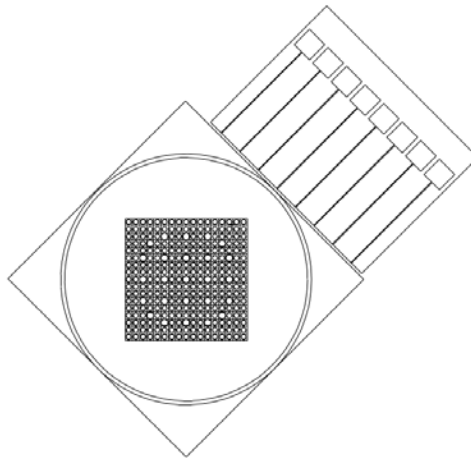


**Figure 26.** MCNPX geometry used the 45-degree rotation (and -23 mm lateral position) in case 1. The photon current through the surfaces at the back of the square detector surfaces were sampled, i.e. using the F1 tally.

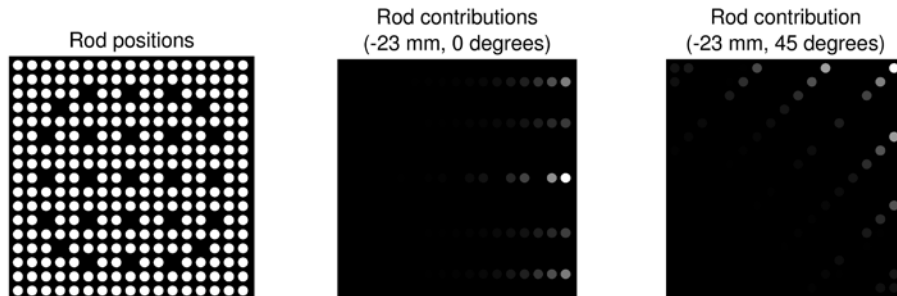


**Figure 27.** The investigated rod positions (left), the contribution of each rod to all detector positions in the 0 degree rotation of case 1 (center), the corresponding contributions in the 45-degree rotation of case 1 (right).

### 8.5.4.3 Geant4 Simulations

Geant4 simulations of the notional UGETv1 design were performed for the purposes of cross-verification and confidence-building with MCNP models used to support the analysis described in this report. Schematics of the Geant4 model of the UGET design is displayed in Figure 28. The coordinate system used, that defines the lateral position and the rotation of the device, is also shown in Figure 28. The reference physics list FTFP\_BERT was used in Geant4, implying that all standard electromagnetic interactions were modeled.

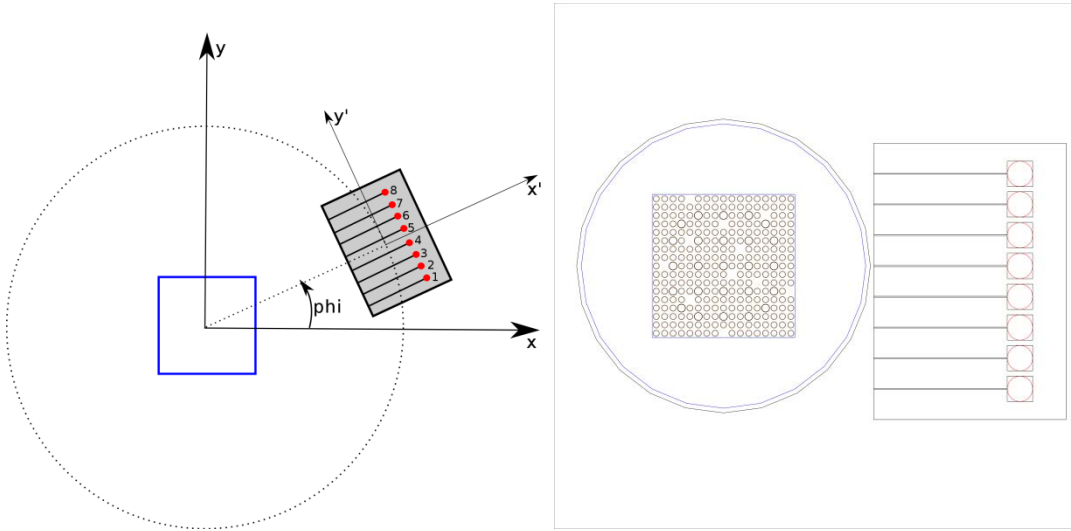


**Figure 28.** Schematics showing the Geant4 model of the UGET device. The left part illustrates the coordinate system that defines the lateral position and rotation of the device relative to a fuel assembly indicated by the blue square in the center. The rotation is given by angle  $\phi$ . The lateral position is given by the  $y'$  position of the collimator head (i.e. the distance between the center of the head and the  $x'$  axis). The right part indicates a view from above for case 2 with 0 degree rotation and -23 mm lateral position (i.e., with detector number 5 pointing towards the central rod in the assembly).

For each case, the spectra of energy depositions in the eight detectors of the collimator head were calculated for each pin in the fuel assembly. That is, the response in each detector to gamma rays emitted isotropically and homogeneously in a 42.5-mm high cylinder in each fuel pin, centered in front of the collimator opening.

Because of the large attenuation of gamma rays originating from fuel pins on the opposite side of the assembly, as seen from the detectors, the contribution to the response for these pins is relatively small. Figure 29 and Figure 31 show the response per fuel pin for case 1.

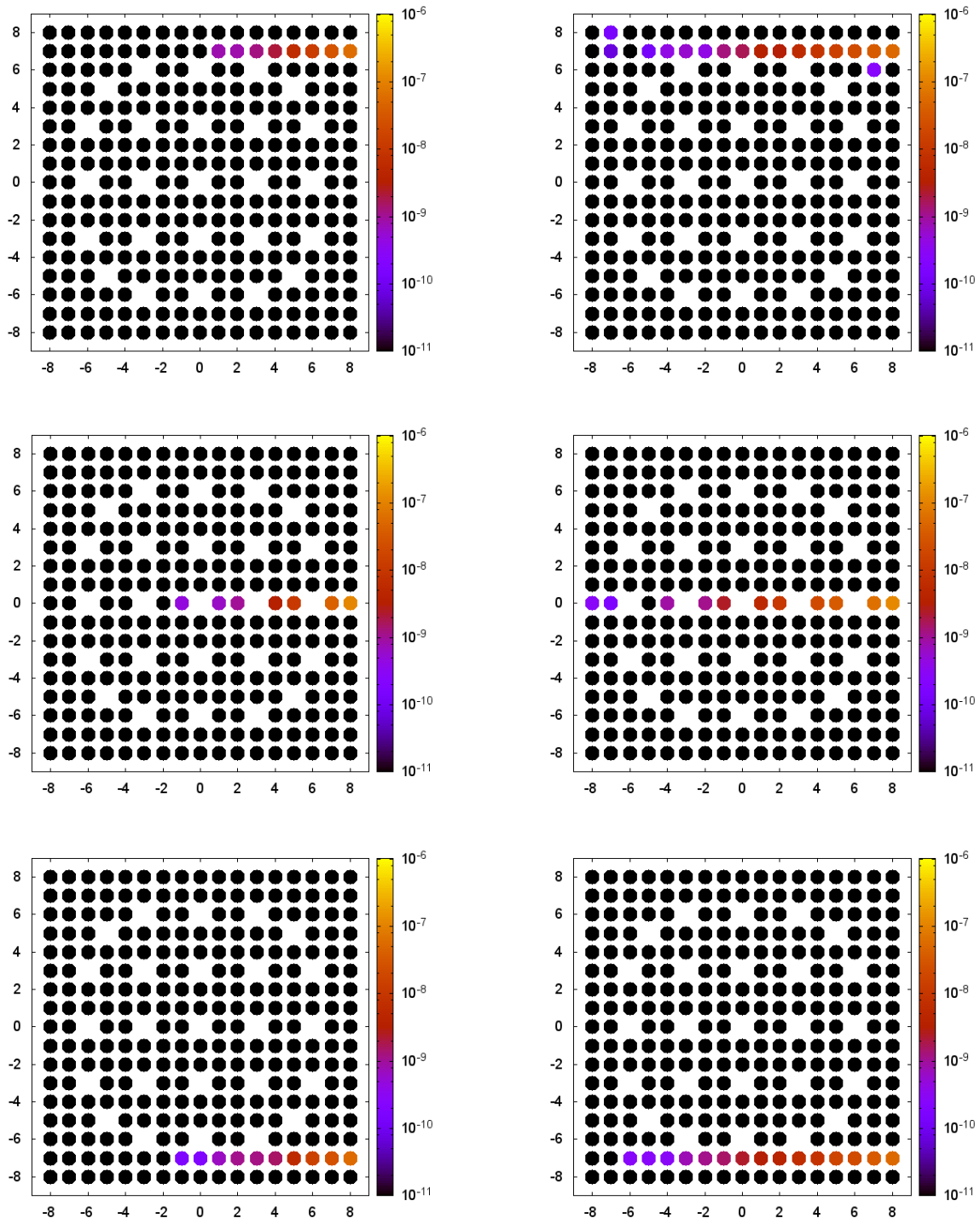


**Figure 29.** The number of counts in the full energy peak, per emitted source photon for the energies 662 keV (left column) and 1274 keV (right column), for detector numbers 3 (bottom), 5 and 7 (top) in the 0-degree rotation of case 1.

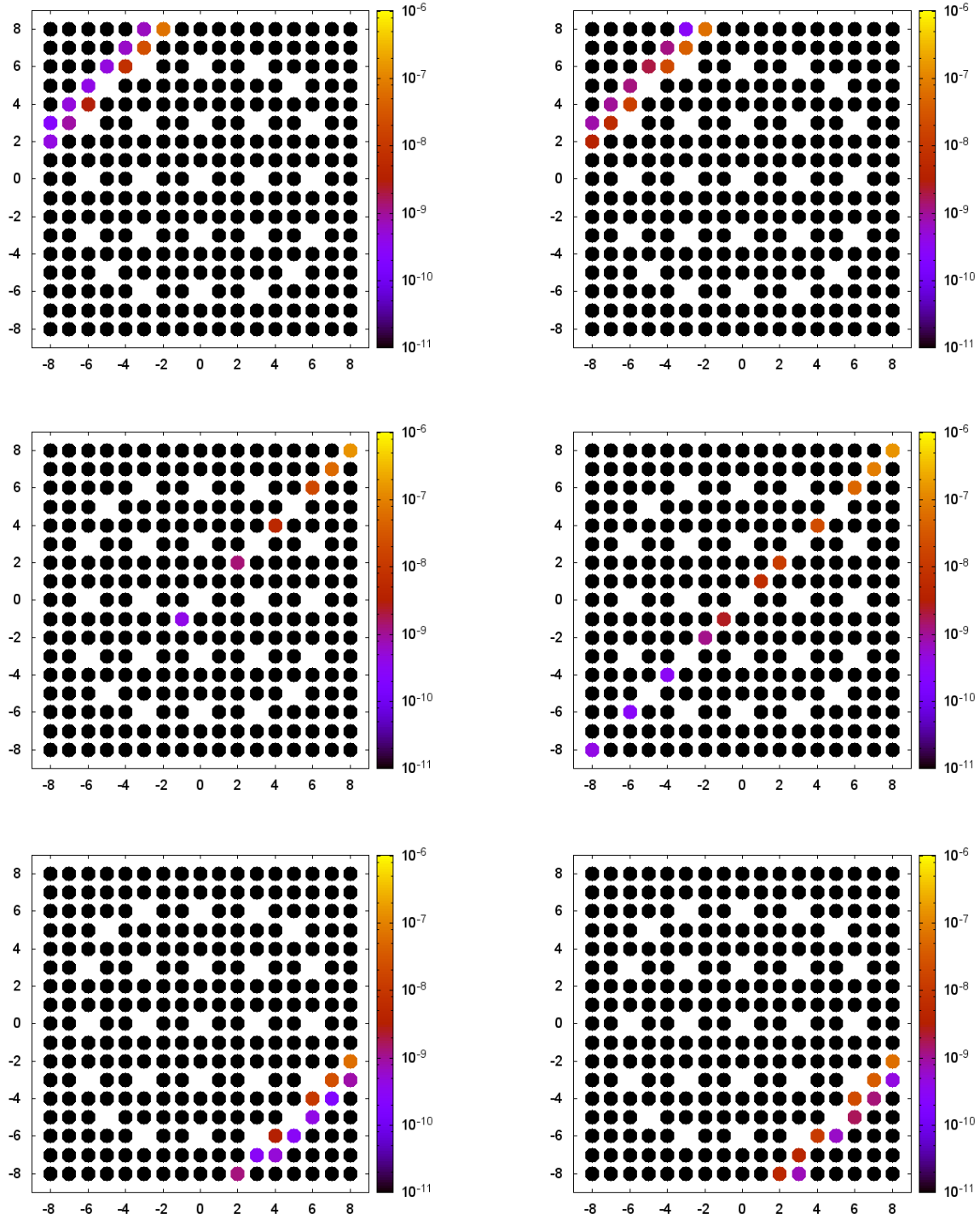


**Figure 30.** The number of counts in the full energy peak, per emitted source photon for the energies 662 keV (left column) and 1274 keV (right column), for detector numbers 3 (bottom), 5 and 7 (top) in the 45-degree rotation of case 1.



#### 8.5.4.4 Comparison Between Simulation Results

Variations of Case 1 were used to compare calculated contributions to the full energy detector response for each fuel pin. Variations of Case 2 were used to compare calculated projections.

##### Comparison of Pin Contributions, Case 1

The results of the Geant4 and the MCNP modeling of case 1, with a complete 17x17 PWR fuel assembly, were used to compare calculated full energy response for each fuel pin. The results are shown in Figure 31. The correlation coefficient between the MCNP and Geant4 models indicate a linear dependence between the models, indicating that either of the two models can be used to predict the contribution to the detector count, per fuel pin. No conversion between flux and energy deposition was performed for the MCNP case, but since only the full-energy peak of one gamma-ray energy is studied, the conversion factor would be constant implying no change in linearity. About  $10^{12}$  source particles were emitted in each Geant4 run and due to the lack of variance reduction, the Geant4 results have relatively large error bars (horizontal direction) compared to MCNP.

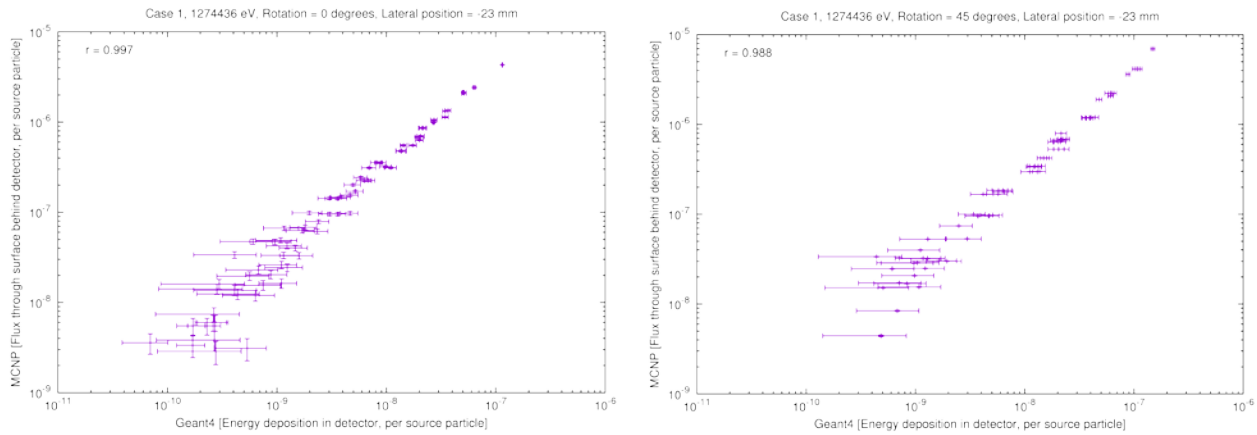


**Figure 31.** Comparison between Geant4 and MCNP calculations of the 1274-keV source in case 1. The left pane shows the 0-degree rotation and the right pane shows the 45-degree rotation. The correlation coefficient for a linear model is given by the parameter  $r$ , where a value close to 1 indicates linearity.

##### Comparison of Calculated Projections, Case 2

The results of the Geant4 and the MCNP modeling of case 2, with a 17x17 PWR fuel assembly with 11 missing pins, were used to compare calculated projections. Figure 32 shows this comparison, specifically with a source distributed homogeneously over the rods in the fuel assembly. In Figure 32, a horizontal line is plotted that indicates an arbitrary select threshold used for quantitative analysis. The threshold was here set at 10 percent of the maximum value in the projection, a setting that may be used also in a measurement situation where background counts from position between fuel rods or outside the assembly field of view will be discarded from analysis.

A quantitative analysis of the difference between the MCNP and Geant4 calculations were performed. Figure 33 shows the relative difference as a function of MCNP calculated full energy peak count. The threshold in Figure 32 is repeated in Figure 33, illustrating the fact that background counts are associated with large uncertainties. The frequency distribution of the relative differences between MCNP and Geant for responses above the threshold, are illustrated in Figure 34.



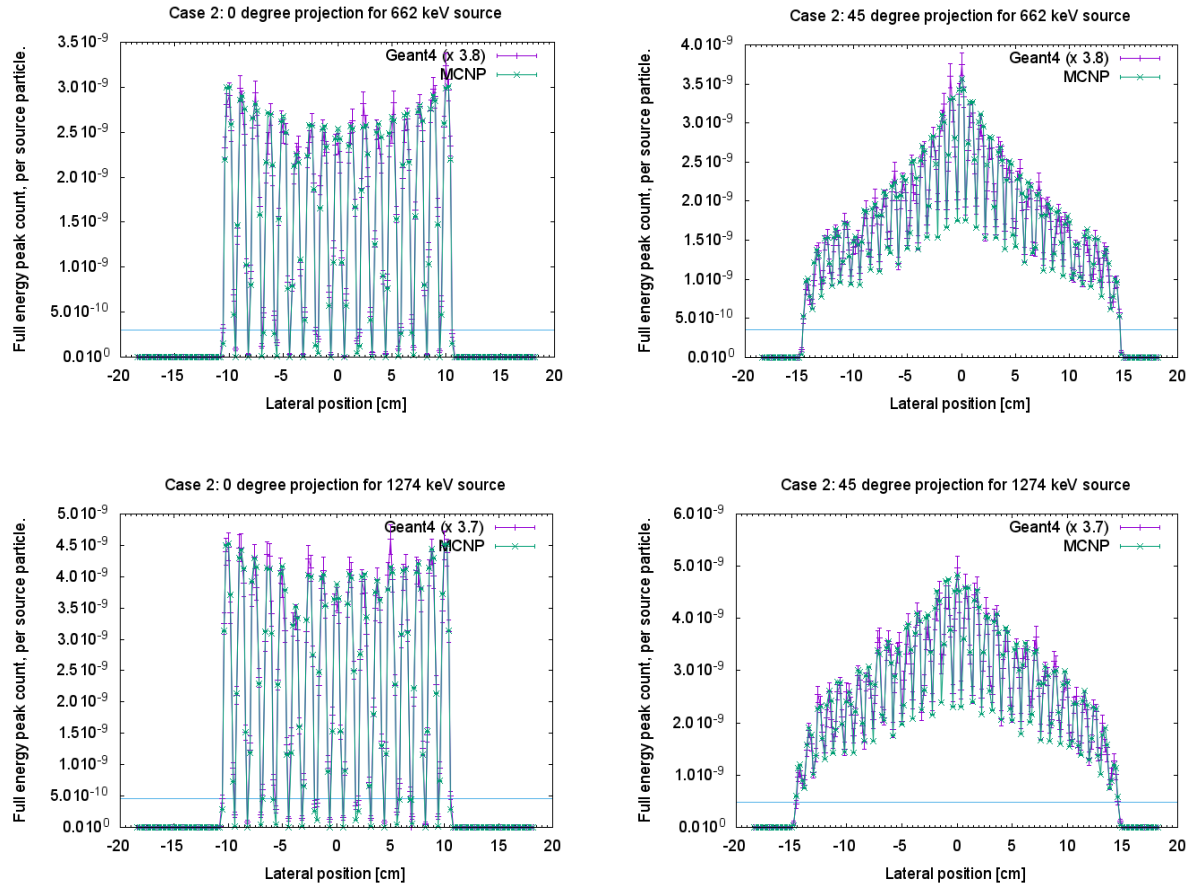


**Figure 32.** The projections for 0-degree (top) and 45-degree (bottom) rotation using a 1274-keV source distributed homogenously over the fuel rods, calculated with the MCNP and Geant4 models. The horizontal line indicates an arbitrarily selected threshold for removing counts originating outside the field of view.

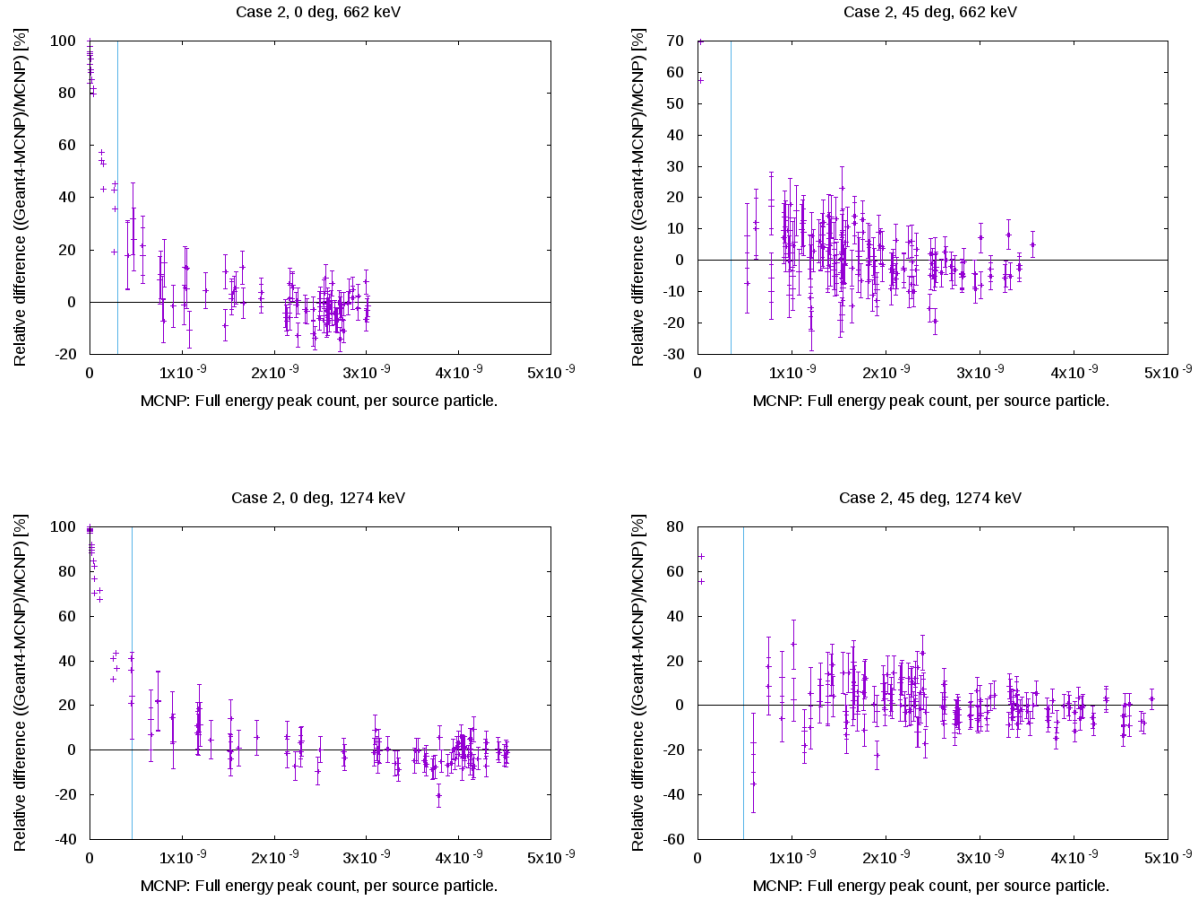


**Figure 33.** The relative difference between MCNP and Geant4 calculations as a function of MCNP calculated full energy peak counts. The vertical lines indicate the position of the threshold set in Figure 32.

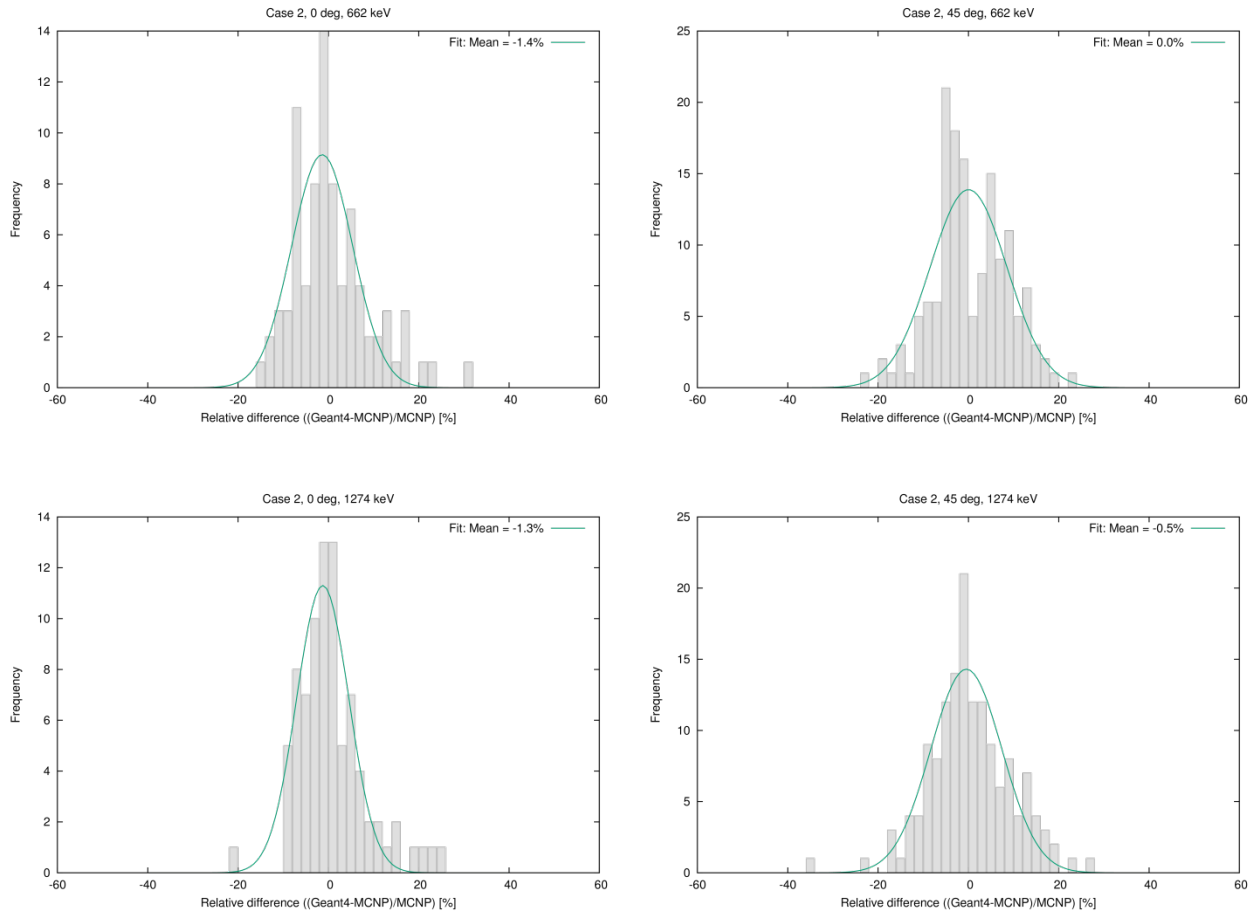


**Figure 34.** The frequency distribution of the relative differences between MCNP and Geant4 calculations, where all calculations are above the threshold set in Figure 34. The solid lines indicate a Gaussian fit to the calculated data.

The results in Figure 32 show that there is good qualitative agreement between the projections calculated with MCNP and Geant4. The more detailed analyses in Figure 33 indicate that low-count data points may be underestimated using the MCNP simulation framework in this benchmark, which may be expected because of the simplification of simulating a perfect collimator impenetrable for gamma-rays, for example. However, the frequency distributions in Figure 34 indicate that the relative difference between the two Monte Carlo frameworks is approaching Gaussian, which implies that both of the transport codes are producing physically reasonable results. There is small difference on the absolute scale (see normalization factor in Figure 32) between the two frameworks that remains unresolved. Some of the difference may be explained by differences in used cross-section libraries. In combination, this independent code-to-code verification provides confidence that the MCNP-based fuel libraries used in UGET simulations provide a sufficient level of fidelity for the JNT 1955 viability study.

## 9.0 Tomographic Reconstruction Algorithms

Using a tomographic reconstruction algorithm, sinogram data are mathematically inverted to form a representation of the cross-section of the fuel assembly. In this work, so-called emission tomography is applied, where the object itself (the fuel assembly) is radioactive, and the sinogram data consist of measured intensities of the gamma rays that have been emitted from the object, collected in a large number of positions relative to the object. Consequently, the reconstructed cross-sectional data represent the source distribution within the object.

There are a variety of algorithms available for emission tomography, which over the years have been developed and applied mainly for medical applications. However, a nuclear fuel assembly, with its highly inhomogeneous mix of strongly gamma-ray attenuating materials (such as uranium dioxide) and less attenuating materials (such as water or air), is a challenging object for tomographic measurement and reconstruction. If not taken into account in the reconstructions, gamma-ray attenuation will strongly influence the resulting representation of the source distribution. As accounted for below, one may directly analyze basic reconstructed images, being aware of the influence from gamma-ray attenuation, but there are also a variety of ways to include gamma-ray attenuation in the models. As a support to the reconstructions and analyses, image analysis tools also provide a useful means to extract information from reconstructed images, both in terms of geometry and of quantitative measures of pin-wise isotopic contents.

This section begins with an overview of available reconstruction and analysis methods. It then describes in greater detail the algorithms used in this work to evaluate GET performance for Verification Objectives 1 and 2.

### 9.1 Overview of Available Reconstruction and Analysis Methods

In general, one may divide tomographic reconstruction algorithms into two main classes: analytic and algebraic (Kak and Slaney 1988). In this work, options from both these classes have been explored and applied to experimental as well as simulated data. Furthermore, image analysis methods have been applied for extracting quantitative measures from reconstructed images.

Both the purely analytic methods, such as filtered backprojection (FBP), and the algebraic methods, also called model-based methods, may be applied using no *a priori* information about the object, thus being suitable for Verification Objective 1. The algebraic methods also allow more detailed information about the imaging system and object to be incorporated in the inversion, making them well suited also for Verification Objective 2. As part of this work, the applicability of a set of algorithms for quantitative reconstruction and analysis of nuclear fuel assemblies have been studied (Jacobsson Svård et al. 2015a), investigating the quantitative capabilities of different analysis methods for both verification objectives, based on data for previously used experimental devices. In addition, a variety of algorithms and analysis methods have been applied to simulated data from the suggested UGET design (defined in Section 7.0). This subsection gives a general overview of the methods available, while the specific algorithms used for analyzing data in the current project are presented in Subsections 9.2 and 9.3.

#### 9.1.1 Analytic Reconstruction Algorithms

Analytic reconstruction algorithms are based on the Radon transform, a technique originally developed in the beginning of the 20th century. The Radon transform describes a series of line integrals of an object function along lines at some distance ( $s$ ) from the origin and at some offset angle ( $\theta$ ) from a defined

object axis. In this work, covering emission tomography, the line integrals comprise the sum of activities along the measured line through the object, and the Radon transform can be used to reconstruct an internal image of the source distribution in the object (Kak and Slaney 1988).

The Radon transform is closely related to the Fourier transform (FT) via the Fourier slice theorem, or Central slice theorem, relating the FT of the object function to the FT of the projection, which means that an object can be estimated by performing two-dimensional inverse Fourier transforms (IFT). Hence, the Fourier transform,  $A(w_x, w_y)$ , of an activity distribution  $a(x, y)$  is related to the Fourier transform,  $P(w, \theta)$ , of its projections, or measured intensities,  $p(s, \theta)$ , as schematically shown in Figure 35.

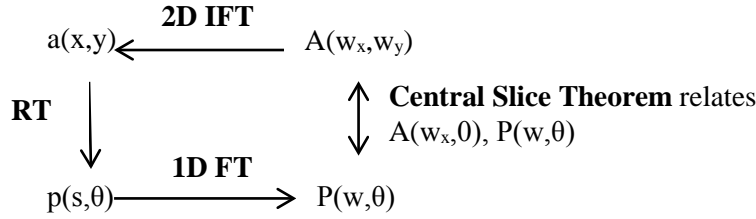


**Figure 35.** Schematic relations in Fourier reconstructions.

An alternative to deduce the source distribution  $a(x, y)$  based on the measured projections  $p(s, \theta)$  is to use the filtered back projection (FBP) technique, as illustrated in Figure 36, and applied in this work.

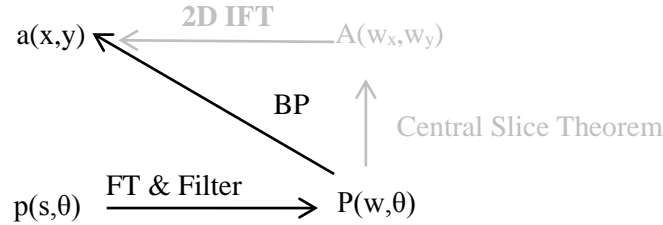


**Figure 36.** Schematic illustration of the filtered backprojection technique (BP=backprojection).

If scattering of gamma radiation into the detectors is excluded, and if absorption inside the object is not considered, the FBP technique can be directly applied. However, for a more accurate description of objects containing highly attenuating materials (such as nuclear fuel assemblies), attenuation in the objects should be included, and the imaging problem then concerns inverting the so-called attenuated Radon transform (Tretiak and Metz 1980). However, the practical applicability of the attenuated Radon transform may be questioned and its implementation lies beyond the scope of this work. When it comes to taking attenuation into account, this work focused on algebraic algorithms instead. Still, one means of taking attenuation into account in analytic algorithms is also available in terms of post-reconstruction corrections, as discussed in Jacobsson Svärd et al. 2015a.

Some pros and cons of the FBP algorithms, applied in this work, are summarized in Table 11.

**Table 11.** Pros and cons of analytic FBP reconstruction techniques for use on nuclear fuel assemblies.

Pros	Cons
<ul style="list-style-type: none"> <li>Established technique: algorithms and software are readily available</li> <li>Offer fast, online reconstructions</li> </ul>	<ul style="list-style-type: none"> <li>Poor capability to produce quantitative data, in particular due to not taking gamma-ray attenuation in the fuel assemblies into account</li> <li>Do not take measurement system's response function into account, neither with respect to finite field of view nor with respect to solid angle of detector as seen from the object</li> <li>Filtering must be responsively selected. The norm of the reconstruction may be lost and negative activity values may be reconstructed (i.e. making quantification of activities difficult)</li> </ul>

### 9.1.2 Algebraic Reconstruction Algorithms

A nuclear fuel assembly comprises a highly inhomogeneous mix of differently attenuating materials, which severely complicates the task of using measured gamma-ray intensities to reconstruct the internal source distribution quantitatively. However, since a fuel assembly is a well-known object with respect to geometry and composition, its impact on the measured gamma-ray intensities can be taken into account. For Verification Objective 2, it has been assumed that algebraic algorithms may be used to model the fuel geometry and composition in detail to calculate how gamma rays transport through the fuel, and thereby improve the precision in reconstructions of conclusive rod-by-rod activities. On the other hand, for Verification Objective 1, it has been assumed in this work that no detailed information on the fuel is available. In this case, images may be reconstructed while making use only of knowledge of the general material composition of nuclear fuel. For both verification objectives, inclusion of the detector system's response function can be implemented in the code to improve the reconstructions.

In the algebraic approach, the sought activity distribution is represented by the activities in  $N$  picture elements (pixels) in an axial cross-section of the fuel assembly. The gamma-ray intensity measured in a detector position  $m$  can then be mathematically defined as:

$$I_m = \sum_{n=1}^N \omega_{mn} A_n \quad (9.1)$$

Here,  $I_m$  is the measured intensity,  $A_n$  is the sought quantity, i.e. the activity in each pixel element  $n$ , and  $\omega_{mn}$  is the probability that gamma radiation emitted from pixel  $n$  will be detected in detector position  $m$ .  $\omega_{mn}$  are here called *contribution coefficients* and these can be calculated or estimated using available information of the objects and measurement setup.

For measured intensities in a large number of positions,  $m \in 1, M$ , an equation system is obtained:

$$\begin{aligned} I_1 &= \omega_{11}A_1 + \omega_{12}A_2 + \dots + \omega_{1N}A_N \\ I_2 &= \omega_{21}A_1 + \omega_{22}A_2 + \dots + \omega_{2N}A_N \\ &\vdots \\ I_M &= \omega_{M1}A_1 + \omega_{M2}A_2 + \dots + \omega_{MN}A_N \end{aligned} \quad (9.2 \text{ a})$$

or equivalently

$$\bar{I} = \overline{\overline{W}} \bullet \bar{A} \quad (9.2 \text{ b})$$

Accordingly, after calculating the contribution coefficients and measuring the gamma-ray intensities, the activity distribution can be reconstructed. There are many alternative ways to solve Eq. (9.2b) for  $\bar{A}$  (Yokoi et al. 2000). One example is the iterative solution technique called Additive Simultaneous Iterative Reconstruction Technique (ASIRT), which has been adopted by SWESP. The algorithm updates the activities from an iterative step,  $k$ , to the next, as shown in Eq. (9.3).

$$A_n^{k+1} = A_n^k + \frac{1}{\sum_{m=1}^M \omega_{mn}} \sum_{m=1}^M \frac{\left( I_m - \sum_{n=1}^N \omega_{mn} A_n^k \right) \omega_{mn}}{\sum_{n=1}^N \omega_{mn}} \quad (9.3)$$

The USSP employed a non-negative least squares (NNLS) method that solves the Karush-Kuhn-Tucker conditions for the non-negative least squares problem (Lawson and Hanson 1987). NNLS solves for the minimum squared difference between  $\overline{\overline{W}} \bullet \bar{A}$  and  $\bar{I}$  subject to the constraint that the activity at each location is non-negative:

$$\arg \min_A \left\| \overline{\overline{W}} \bullet \bar{A} \right\|_2 \text{ subject to } \bar{A} \geq 0 \text{ for each element of } \bar{A}.$$

Regardless of the iterative solution method employed, the most sensitive part in reconstruction is the calculation of the system matrix  $\overline{\overline{W}}$ . Defining a system matrix that accurately represents the physics prescribed in either simulated tomographer responses (the primary data source in this study) or actual field measurements is crucial to getting a useful reconstruction result.

A large degree of freedom exists in the definition of the matrix equation (9.2). First, the pixel pattern can be selected in a variety of ways. Second, the system matrix,  $\overline{\overline{W}}$ , may involve modeling in more or less detail. The efficiency of the reconstruction is predominantly governed by the definition of a representative system matrix, which should be adapted to the particular detection system used to collect the intensities,  $\bar{I}$ , and to the fuel assembly geometry under study. In this context, the position of the fuel assembly in the measuring device can be deduced by deploying image analysis tools on basic reconstructed images, as presented in Section 9.1.3, which enables detailed modeling of the gamma-ray transport through the fuel assemblies.

A list of pros and cons for algebraic reconstruction techniques for application on tomographic data from nuclear fuel assemblies is presented in Table 12.

**Table 12.** Pros and cons of algebraic reconstruction techniques for use on nuclear fuel assemblies.

Pros	Cons
<ul style="list-style-type: none"> <li>Has been demonstrated on experimental data from nuclear fuel assemblies, giving high precision in quantitative rod-by-rod data (Jacobsson Svärd et al., 2005)</li> <li>Allows for user-selected level of detail to be included in the reconstructions (i.e., applicable for both verification objectives)</li> <li>The response function of the detection system can be taken into account for both verification objectives</li> <li>The pixel pattern can be adapted to the current object and its position in the measuring device, provided that this information is known from the image analysis, for example</li> </ul>	<ul style="list-style-type: none"> <li>The system matrix, <math>W</math>, may be very large, in particular if high pixel resolution is requested, thus involving large memory requirements on the computing system used</li> <li>Depending on method used for modeling the system matrix <math>W</math>, computation time may be long, and accordingly, available time may govern the level of detail used in the reconstructions.</li> </ul>

### 9.1.3 Image Analysis Methods

Once a tomographic image has been reconstructed, either using analytic reconstruction (Section 9.1.1) or algebraic reconstruction (Section 9.1.2), image analysis routines can be applied to deduce information on the measured fuel assembly.

As an example, image analysis can determine the measured fuel assembly's current position in the measuring device. This capability may be of importance to perform adequate analyses, not the least since previously performed experiments (see Section 2.0) have shown that assembly misalignments of several mm to a few cm may occur in practice. In previous work, a set of image interpolation and mask matching routines have been applied for deducing the position of a BWR assembly based on tomographic images (Troeng 2004). These methods have been demonstrated to result in positioning with a precision within  $0.1^\circ$  in angle and 0.1 mm in lateral position. This level of detail in positioning enables modeling of the gamma-ray transport from the fuel rods to the detection system with high level of detail, supporting the more detailed algebraic reconstruction methods.

Images may also be analyzed to identify fuel rods in the image and deduce quantitative data for the identified rods. This capability was explored as part of the current project, and the results were published in (Davour et al. 2016). As discussed in (Davour et al. 2016) and demonstrated for Verification Objective 1 in Section 10.2, mask-matching tools can be used to identify and locate individual fuel rods in the images, without requiring any beforehand information of the fuel geometry. In this context, identification of fuel rods in the images will also enable identification of the fuel type of the measured assembly, although such routines have not been demonstrated in this work. Furthermore, accurate quantification of relative rod activities requires a reconstruction that preserves the relative activity level in different regions of the fuel.

In the absence of more advanced image analysis tools, one may also deduce scores for individual fuel rods directly by summing the reconstructed values of a number of pixels, said to represent a certain fuel rod. Such analyses require beforehand knowledge of the fuel geometry and the position of the assembly in the measuring device, which, on the other hand, may be obtained using image analysis.



## 9.2 Reconstruction and Analysis Methods used for Verification Objective 1

For Verification Objective 1, no *a priori* information on the fuel is to be assumed. The route taken in this case is to use the collected data of a fuel assembly (a sinogram) in a tomographic image reconstruction and thus to create an image of the axial cross section of fuel, which is further analyzed to deduce pin-wise data. USSP and SWESP methods used to transform the sinogram data into an image of reconstructed emission intensities (illustrated in Figure 37) are described below. In addition, the routines used for analyzing the images to extract pin-wise data from the images are presented.

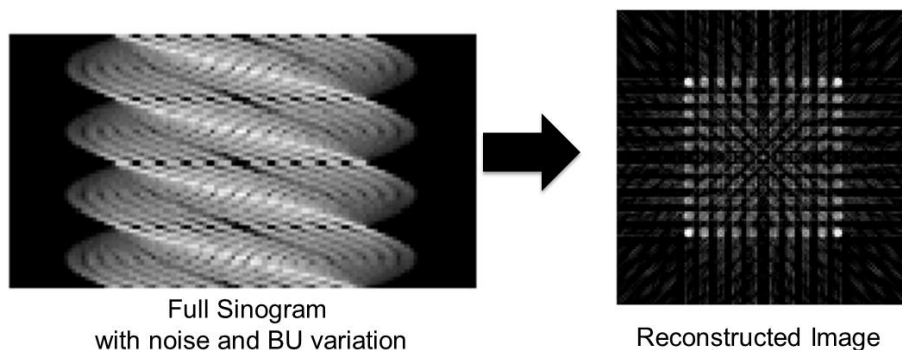


**Figure 37.** Tomographic reconstruction methods for Objective 1 transform sinogram data into images of gamma-ray emission intensity. These images are further analyzed to deduce pin-wise data.

### 9.2.1 Methods Used by USSP

An FBP algorithm with a simple ramp filter and without any form of attenuation correction is used as the reconstruction algorithm for the USSP's analysis of Objective 1 (Kak and Slaney 1988). USSP analysis assumed that the assembly location and orientation can be readily and accurately determined—no analysis tools were developed or applied to perform those tasks on the simulated data used in this study. For each image corresponding to a virtual fuel assembly, image intensity data were reconstructed on a regular pixel grid and the aggregated intensity of multiple pixels in a “neighborhood” centered on a number of pin location was calculated (Figure 38). These aggregated pin-region intensity values are referred to as the pin scores.

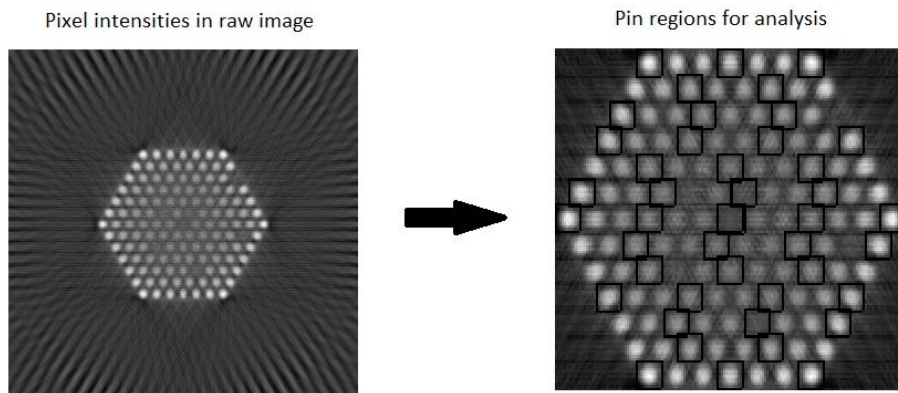


**Figure 38.** Example reconstructed image of a VVER-440 assembly from a virtual assembly population (left), pin-region average intensity values for that virtual assembly (right).

The variability of these pin scores for a population of virtual fuel assemblies can be visualized by examination of the score as a function of the pin position from the center of the assembly to the edge. An example pin-score summary for 100 VVER assemblies is shown in Figure 39. In this plot, the pins are indexed by their distance from the center of the assembly (abscissa) and the score is plotted on the ordinate. Pins that are present in the assembly (same initial enrichment, average burnup and cooling time, but with variations in pin-to-pin burnup and statistical noise) are shown in green, and scores from regions with missing pins are shown in red stars. The scores for missing pins near the periphery of the assembly (right side of the plot) are well separated from scores of pins that are present, but toward the center of the assembly the distribution of scores for missing and present pins begin to overlap.

These illustrative results reinforce intuition that it is generally easier to detect a missing pin in the outer part of the assembly than the inner part because the flux from inner pins is lower due to attenuation by the rest of the assembly. Note that missing pins in the innermost ring are more easily detected than pins in the next outer ring, presumably because of the proximity of the water channel near the innermost ring.

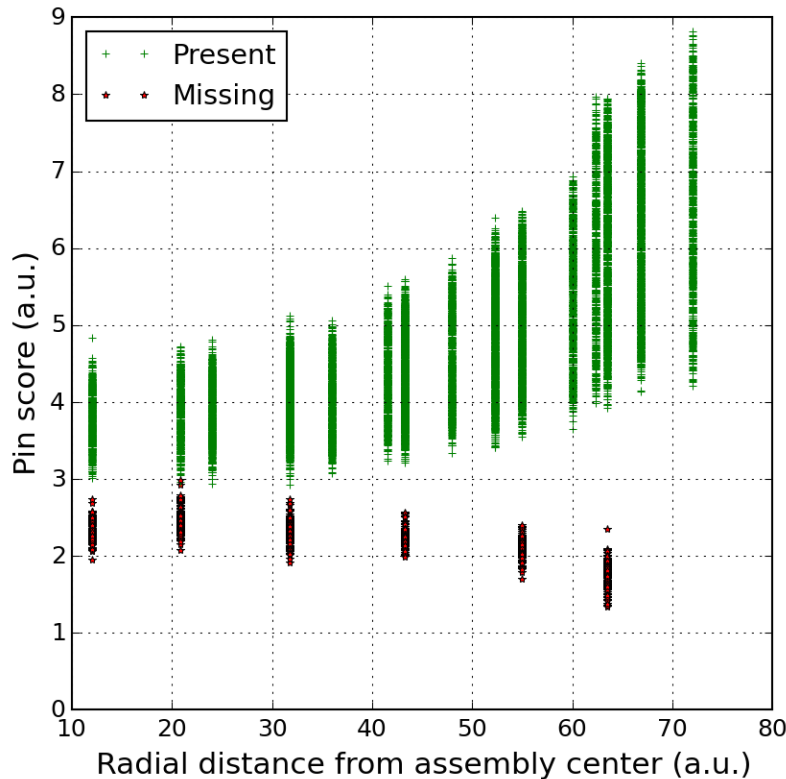


**Figure 39.** Pin scores from 100 VVER-440 assemblies assayed by the PGET, instrument assuming a total assay time of less than 10 minutes and an energy window of  $>700$  keV. The assembly population has a nominal burnup of 20 GWd/MTU, cooling time of 5 years and pin-wise activity variation of  $\pm 20$  percent.

## 9.2.2 Methods Used by SWESP

The SWESP studies of applicable image reconstruction methods for Verification Objective 1 comprise analytic as well as algebraic reconstructions methods. For the analytic methods, basic FBP reconstructions (without attenuation) were complemented with the introduction of gross corrections for gamma-ray attenuation. For the algebraic methods, the system matrix was introduced to enable the

inclusion of the intrinsic response function of the detection system, and reconstructions were performed without any attenuation corrections respectively by modeling a homogeneous mix of fuel materials, and thus uniform attenuation, in the image area. In all cases, image analysis methods were used to extract pin-wise data. Tomographic algorithms and results obtained in analyses of simulated data for the PLUTO device were published as part of the current project (Jacobsson Svård et al. 2015a), and brief descriptions are presented below.

### 9.2.2.1 Analytic Image Reconstruction and Post-correction for Attenuation

A typical feature of basic FBP reconstruction is the reconstruction of lower activities in the assembly center due to the strong gamma-ray attenuation in fuel material, as seen in the example image in Figure 38. This feature hinders the direct comparison between activity contents in different parts of reconstructed images, and thus complicates the counting of fuel rods. In order to enable analyses independent from *a priori* assumptions of expected reconstructed activity levels in different regions of the image, a post-correction method has been suggested, based on the simulated response of a homogeneous distribution of fuel material in the image area. An example of a correction image used to perform such correction for uniform attenuation is presented in Figure 40. The correction is applied by multiplying each reconstructed image pixel with its corresponding correction image pixel.

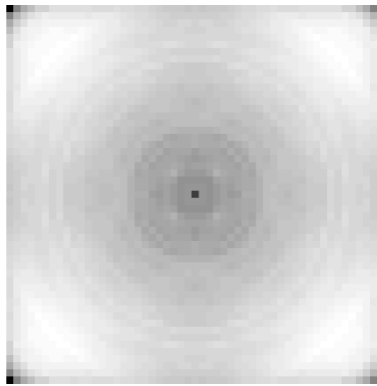


**Figure 40.** An example of an attenuation correction image obtained by simulating the response of a homogeneous distribution of fuel materials in the image area. The correction image is given by the inverse of the reconstruction results from these simulations, normalized to an average of one. Here, dark areas correspond to large correction factors and bright areas to small. For a homogeneous object of BWR fuel size, the ratio between the highest and lowest correction factor was 2.16. As expected, the correction matrix is rotationally symmetric. In this case, the corners are given high correction factors, which is a result of limitations in the width of each projection in the simulated data set used here.

The correction matrix is dependent on the simulated geometry, e.g. in terms of the size of the object, the number of projection angles, the width of each projection and the number of lateral positions used. Accordingly, the correction matrix should be determined using a simulated data set with similar properties as the experimental (or simulated) data set that it will be applied to.

Some results obtained in analyses of simulated data for the PLUTO device, with and without post-correction for attenuation, are presented in Section 9.2.2.4.

### 9.2.2.2 Algebraic Image Reconstruction

As mentioned above, algebraic reconstruction enables to take into account the device's intrinsic response function, not offered in the basic analytic reconstructions. In the algebraic reconstructions performed by SWESP in this work, the actual properties of the measurement system, in terms of finite collimator slit dimensions, solid-angle effects, and gamma-ray transmission through the collimator material, are introduced in a model of the system matrix  $W$  in Eq. 9.2. An example of the response function for the UGET device is presented in Figure 41. In this context the corresponding response function implicitly used in FBP reconstruction is an ideal, horizontal line at  $Y=0$  (i.e., non-realistically assuming a constant value over all  $X$  values at  $Y=0$  and value of 0 outside  $Y=0$ ).

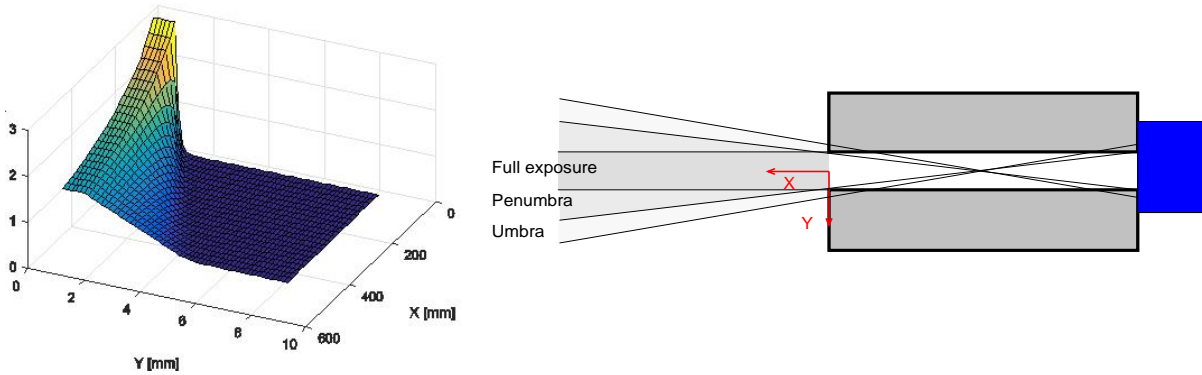


**Figure 41.** The modeled response function (a.u. on the z axis) of the UGET device for 1274 keV gamma rays (left figure), taking into account the physical properties of the measurement system (e.g., in terms of finite collimator slit width and gamma-ray transmission through the collimator material). These effects give rise to significant contributions from penumbra and umbra regions. The origin ( $X,Y=0$ ) of the response function is centered at the front of the slit opening, and only positive  $Y$ s are presented (right figure).

As a result of the modeling of the system's response function, it was concluded that as much as about 15% of the 1274 keV gamma rays from  $^{154}\text{Eu}$  that hit the detector in UGET will have transmitted unscattered with preserved energy some distance through the collimator material (predominantly short distances through its corners), showing the importance of this contribution. Accordingly, one may conclude that modeling the collimator material as opaque to gamma rays when defining the system matrix  $W$  would be a relatively poor approximation. The corresponding number for 662 keV gamma rays from  $^{137}\text{Cs}$  is about 10%.

Algebraic reconstruction also allows gamma-ray attenuation through the object to be explicitly taken into account in the modeling of the system matrix, thus offering an alternative to the post-corrections proposed for FBP reconstructions in section 9.2.2.1 while also including the system's response function illustrated in Figure 41. For Verification Objective 1, where no *a priori* information in the fuel geometry is to be assumed, SWESP used a gross "black-box" model that includes a homogeneous mix of fuel material, providing uniform attenuation in the image area. This model is illustrated in Figure 42 together with the pixel pattern used when performing algebraic reconstructions of BWR fuel.

In the SWESP algebraic reconstructions of PWR fuel, a quadratic pixel pattern with  $85 \times 85$  pixels has been used, and the image area has been adapted to the size of this object. In this case, the simulations were done with the assembly centered in the measuring device, and thus the image area was also centered. For experimental data, one must anticipate that the fuel may not be centered and thus adapt the image area

to the current position of the fuel. (Identifying the image area and centering the image over the object is easily done using the image analysis techniques presented in Section 9.2.2.3. One may also consider directly analyzing the collected sinograms to determine the assembly's position, albeit such techniques are not covered in this report.)

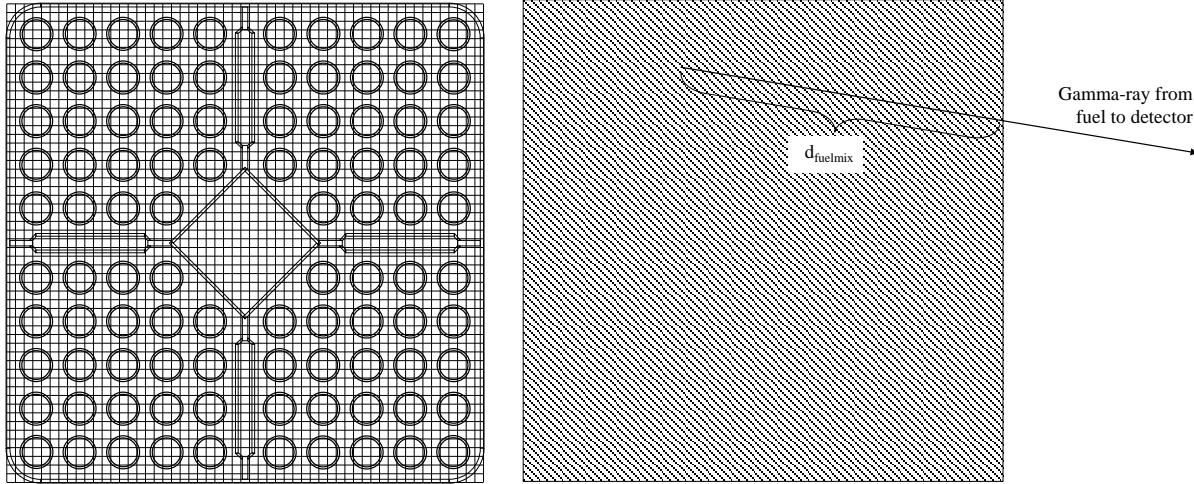


**Figure 42.** The 55x55 quadratic pixel pattern used for SWESP reconstructions of BWR fuel, overlaid over the SVEA-96 fuel geometry (left); an illustration of the gamma-ray attenuation model used in SWESP algebraic image reconstructions for Verification Objective 1 (right) (Jacobsson Svård et al. 2015a).

### 9.2.2.3 Image Analysis Methods

A set of established image analysis routines have been adopted by SWESP, when analyzing the reconstructed images in this work. First, bicubic image interpolation is applied to increase the number of pixels. Second, mask matching techniques are used to identify objects in the images and analyze their properties. In this work, the masks are user-defined and are either set based on *a priori* information of the complete fuel assembly geometry or set corresponding to a standard-size single fuel rod. Examples of the use of these image analysis techniques are presented below, and the techniques are more elaborately described in Davour et al. (2015) and Davour (2016). (These publications were presented as part of the current project.)

Masks corresponding to complete assembly geometries are used for determining the position of the fuel in the image, and thus in the measuring device. The mask applied for positioning of SVEA-96 fuel is illustrated in Figure 43, together with a drawing of the cross section of the fuel and an example of an interpolated reconstructed image. The original reconstruction was made on a 55x55 pixel grid (see Figure 42), and it has here been interpolated to a 1024x1024 pixel pattern (from Jacobsson Svård et al. 2005).



**Figure 43.** The cross section of the SVEA-96 fuel assembly (left), an example of a reconstructed image (middle), and the mask applied on the reconstructed images for deducing the position of the assembly in the measuring device (right).

In previous work (Troeng 2004), analyses of experimental data from PLUTO have demonstrated a capability to position a BWR fuel assembly with an accuracy within 0.1 mm laterally and  $0.1^\circ$  in angle using this technique. In this work, the same technique, albeit with a mask corresponding to VVER-440 fuel, has been applied on experimental PGET images of VVER-440 fuel, as described in section 10.2.1.

Masks corresponding to individual fuel rods are used for identifying individual fuel rods in the images. An example of such a mask is presented in Figure 44. Previous studies (Troeng 2004) have confirmed the intuitive conclusion that a mask size that corresponds to the actual rod size is most functional. In this work, *a priori* information has been used to set a mask size corresponding to the actual rod size in the fuel under study. However, most modern fuels have similar-sized fuel rods, and one may also envisage routines where mask size is adapted to the typical object size found in the image.



**Figure 44.** The reconstructed image from Figure 44 (left); a mask applied for identifying individual fuel rods in the image (right) (from Troeng 2004).

As a result of the identification of rod objects in the image, one can also extract a quantitative measure of the reconstructed activity in that rod. (Depending on image reconstruction method, the measure may be more or less accurately corresponding to the actual activity in the rod, and, in general, image reconstruction and analysis are limited to relative rod-activity estimates.) In the rod-search routine used in this work to count the number of fuel rods for Verification Objective 1, the image is scanned using the



mask shown in Figure 44 until the mask-sized region with the highest activity is found. Once it is found, the region of the image with the next highest activity is sought, and this is repeated until a pre-defined number of rod candidates have been found or until there is no more room in the image for more rods. Rods are not allowed to overlap. Using this routine, no *a priori* information is required to count the number of fuel rods in the measured assembly. However, two properties must be taken into account: 1) a standard rod size has to be assumed in the rod-search routine, and 2) an activity threshold has to be defined for discriminating between rods and background. Examples of results obtained using the rod-search routines on experimental and simulated data are given in Sections 10 and 11.

#### 9.2.2.4 Selection of SWESP Reconstruction Method for Verification Objective 1 Analyses of the UGET Design

Evaluations of the quantitative capability of the methods described above to determine rod-wise activity contents and discriminate them from background have been performed using simulated data for the PLUTO device. These effort were made within the current project, and the results were presented in Jacobsson Svård et al. (2015a) as part of this project. In the simulations, all fuel rods contained equal activities of  $^{137}\text{Cs}$ . Resulting histograms of activities are presented in Figure 45, where activities in fuel rods are presented in blue, and activities in background regions are presented in red.

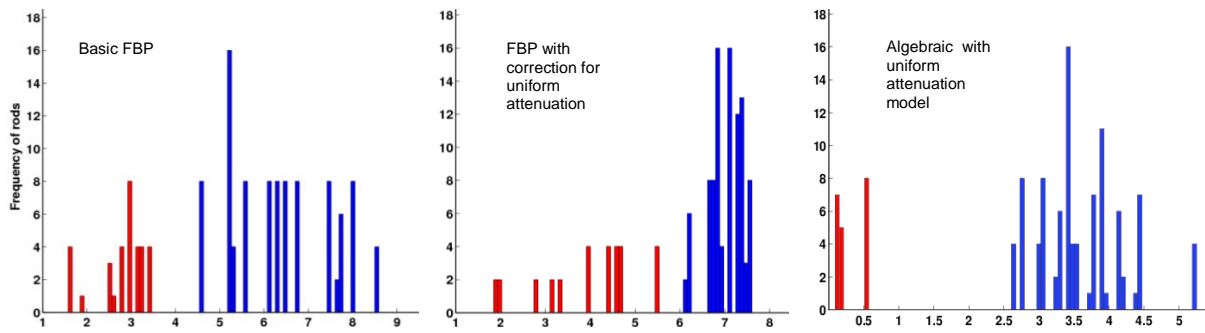


**Figure 45.** Histograms of rod activities (horizontal axes), deduced using image analysis routines applied on images reconstructed from simulated  $^{137}\text{Cs}$  data (662 keV) of a BWR assembly with equal activity contents in all fuel rods. Activities are presented in arbitrary units on the x axis and the frequency of fuel rods on the y axis. The search for fuel rods have continued until the whole image was filled. Identified objects corresponding to fuel rods are marked in blue, whereas regions in the background are marked in red.

As seen in Figure 45, the fuel rods can be discriminated from background in all images. However, the separation between fuel rods and background is largest for the algebraic reconstruction with the uniform attenuation model. Accordingly, this reconstruction method has been used in the SWESP Verification Objective 1 analyses of simulated data for the UGET device, presented in Section 10.1.

### 9.3 Reconstruction Methods Used for Verification Objective 2

As described in section 3.1.2, a basic assumption used in the studies of Verification Objective 2 is that information on the fuel geometry is available. (The nominal geometry may be available from operator declarations, or, alternatively, image analysis methods may be applied to basic tomographic images to deduce the fuel geometry, using the methods described in section 9.1.3.) This opens a possibility to apply detailed modeling of the fuel configuration when using the algebraic methods presented in Section 9.1.2, enabling a level of detail in the reconstructions not accessible using analytic methods. The choice of

algebraic methods for determining rod-wise fuel parameters is also supported by the fact that algebraic reconstruction previously has been applied on experimental data from BWR fuel (Jacobsson Svård et al. 2005), demonstrating a capability to produce reconstructed rod-wise data with percent-level precision.

Because of their demonstrated capability to produce conclusive pin-wise data, the route of using algebraic reconstruction methods has been taken by both SWESP and USSP in the studies of Verification Objective 2. A generic description of the algebraic reconstruction process is given in section 9.1.2, and its application for Verification Objective 2 is depicted in Figure 46 below. For algebraic methods in general in, the inverse problem is phrased as a matrix equation  $A = W^{-1}I$ . Here  $I$  is the measured data sinogram consisting of the intensity of each detector pixel at each angle, but re-formed into a vector (Figure 46). The object to reconstruct,  $A$ , is a vector of isotopic activities at each image pixel, and for Verification Objective 2, the image pixel geometry may be defined using the given *a priori* information of the fuel geometry. (Figure 46 illustrates  $A$  in terms of individual fuel pins, but one pin may also be covered by a set of pixels, adapted to the size and position of the pin, as illustrated in Figure 47 below.)  $W$  is the matrix that maps sinograms to isotopic activities in individual image pixels. In Figure 46, we consider image pixels corresponding to pins, so that each column of  $W$  is a single-pin sinogram. Representing  $A$  with single pins, or 5 image pixels per pin as in Figure 47, can be seen to greatly reduce the dimensionality of the problem—instead of mapping a sinogram of perhaps 20,000 elements onto a grid of up to 20,000 standard image pixels, the data are mapped to a much smaller list of image pixels adapted to the fuel geometry (for example, 126 for a VVER-440 assembly in the one-pixel-per-rod case, or 630 in the five-pixels-per-rod case).

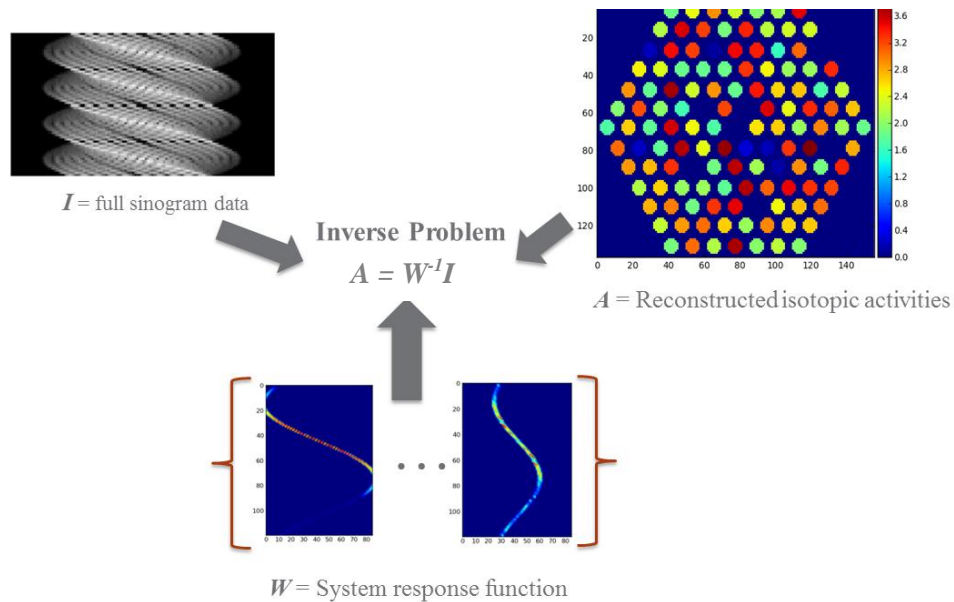


**Figure 46.** Graphical depiction of the Objective 2 reconstruction process.

Though the basic algebraic reconstruction process used by the SWESP and USSP is essentially the same, the methods for calculating the system matrix  $W$  presented in Eq.(9.2), differ somewhat, as described in Sections 9.3.1 and 9.3.2.

### 9.3.1 Methods Used by SWESP

The reconstruction methods used by SWESP for Verification Objective 2 have their origin in the deterministic ray-tracing methods developed for analysis of data from the PLUTO device, used in



Forsmark in 2002, and the PLUTO measurements provided an experimental benchmark. The methods are implemented in a software package called TOMOPACK, which is described more in detail in Appendix C. Methods and software were developed for the PLUTO measurement system, which included detectors and data-acquisition system that allowed the identification and analysis of individual full-energy peaks in the gamma spectrum (Jansson et al. 2006). Considering that the nominal UGETv1 design also offers these capabilities, these methods were considered directly applicable also for analyses of UGET data. In addition, the TOMOPACK software found use also within the Halden Reactor Project, where it is used for analyzing data from research reactor fuel collected using the novel GET device in Halden (Holcombe et al. 2015).

For algebraic methods to produce conclusive data, the system matrix  $\mathbf{W}$  must be representative for the measurement system. In the development of TOMOPACK, used by SWESP in this work, efforts had been made to introduce detailed modeling when defining the system matrix, mainly in terms of:

1. The intrinsic response function of the instrument to axially symmetric 3D objects, such as nuclear fuel rods
2. The gamma-ray transport (and attenuation) through the fuel matrix
3. Adaption of the pixel pattern to fit the object.

The intrinsic response function (1) for the UGET device design has been described in Section 9.2.2 and is illustrated in Figure 41. Together with the model of gamma-ray transport (2), it forms a complete framework for defining the system matrix  $\mathbf{W}$ . The mathematics behind these calculations is more thoroughly presented by Jacobsson Svärd (2004) and in (Jacobsson Svärd et al. 2015a), where it is shown that the coefficients  $\omega_{mn}$  can be given by the expressions in Eqs. (9.4a) and (9.4b).

$$\omega_{mn} = \frac{1}{S_n} \left( \frac{h_c^2}{4\pi l_c} \right) \cdot \iint_{x,y \in n} \frac{1}{R(x,y)} \left[ \frac{l_c}{h_c^2 \cdot R(x,y)} \cdot \omega_{coll}(x,y) + b(x,y) \right] e^{-\sum_i \mu_i d_i(x,y)} \cdot dy dx \quad (9.4a)$$

where

$$\omega_{coll}(x,y) = \int_z \left( \iint_{\substack{x_{det} \\ y_{det} \\ d_{coll} \neq 0}} e^{-\mu_{coll} \cdot d_{coll}(x,y,z,x_{det},y_{det})} dx_{det} dy_{det} \right) \cdot dz \quad (9.4b)$$

where

$S_n$  = the area of pixel  $n$

$h_c$  = height of collimator slit

$l_c$  = length of collimator slit

$R(x,y)$  = the distance from point  $(x,y)$  in the fuel to the detector in position  $m$

$b(x,y)$  = exposed width of the detector in position  $m$  from position  $(x,y)$  in the fuel

$\mu_i$  = the attenuation coefficient for material  $i$

$d_i(x,y)$  = the gamma-ray distance in material  $i$  from point  $(x,y)$  in the fuel to the detector in position  $m$

$\mu_{coll}$  = attenuation coefficient of the collimator material

Eq. (9.4b) can be calculated separately as it does not include any properties of the measured object. Setting it to zero implies that Eq. (9.4a) returns the ideal line-spread function (LSF), without any gamma-ray transmission through the collimator material. However, calculations have shown that between 10% and 15% of the undisturbed flux of gamma rays hitting the detectors in the UGET design will have traveled some distance through the collimator material, depending on the gamma-ray energy.

Because Verification Objective 2 is defined such that geometric information is available, detailed modeling of the current fuel geometry can be incorporated into the calculation of the system matrix using Eq. (9.4). Accordingly, the gamma-ray transport through the fuel can be modeled in detail, as illustrated in the right part of Figure 47.

In addition, one can make use of the *a priori* knowledge to assign pixels only to regions in the fuel that may contain gamma-ray-emitting materials, such as the fuel rods in the case of solid fission products in intact fuel rods (see point 3 in the list above). This assignment is equivalent to forcing the background in the image to be zero, which is justified if the background in measured data is negligible. This prerequisite was considered valid for the measurements in Jacobsson Svård et al. (2005) and it can be expected to be valid also for the UGET design, which comprises detectors with high full-energy peak efficiency and spectroscopic peak analysis with subtraction of background. (If, on the contrary, the detector and data acquisition system does not reject events occurring from gamma rays that have scattered in the water surrounding the fuel, and includes such events in the data together with the unscattered full-energy events, the algorithms will fail in assigning such events to the correct source pixel.)

Here, a pixel pattern with five pixels covering each fuel rod has been used, as illustrated for a SVEA 96 fuel assembly in the left part of Figure 47. The selection of one central and four peripheral pixels per rod helps in adapting to a possible radial distribution of fission products in the rods (Holcombe et al. 2015), and it also reduces the sensitivity to possible dislocations of individual fuel rods.

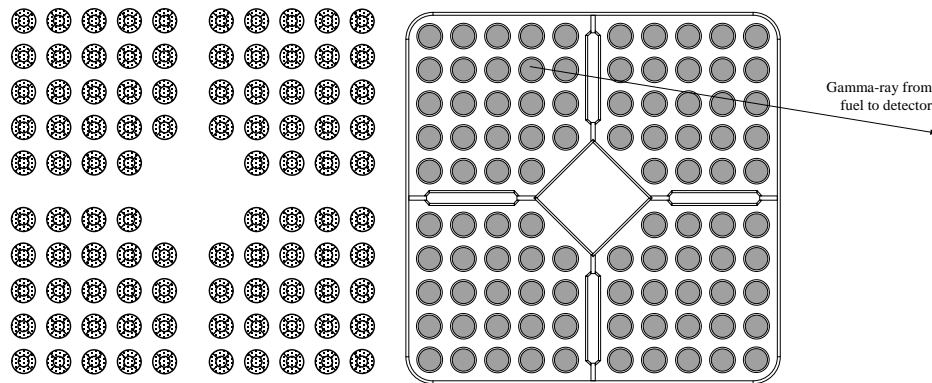


**Figure 47.** For Verification Objective 2, one may use *a priori* information to improve the algebraic reconstructions. Left: The pixel pattern can be adapted to fit the regions containing gamma-ray emitting materials. In the SWESP reconstructions in this work, a pattern with 5 pixels covering each fuel rod has been used, here illustrated for a SVEA-96 assembly. No pixels are assigned to other regions in the assembly. Right: The gamma ray attenuation in the fuel area is taken into account in detail by introducing exact estimates of the travel distances  $d_i$  through different materials in the fuel. In particular, the uranium dioxide of the fuel pellets, illustrated in grey shade, attenuates the gamma rays significantly.

Apart from the fuel geometry, the current position of the fuel assembly in the equipment is required for this detailed modeling to be performed. Troeng (2004) and Davour et al. (2015) have shown that the position can be provided by means of image analysis on a tomographic image, which can be reconstructed using either algebraic or analytic methods. Furthermore, using the rod mask matching technique described in Section 9.2.2, even the positions of individual fuel rods can be deduced, so that possible rod dislocations may be taken into account.

Finally, it may be noted that gamma-ray scattering is not included in the definition of the system matrix  $W$ , presented in Eq. (9.4). Accordingly, this method is well adapted to the analysis of data from detection systems such as PLUTO or UGET v1, where full-energy gamma peaks are analyzed, including

spectroscopic background subtraction. Its performance on data including also relatively large scattered components remains to be evaluated.

### **9.3.2 Methods Used by USSP**

PNNL employed two different methods for the calculation of a system matrix ( $W$ ) for Objective 2 analysis. The first was based on the same MCNP-generated data used to predict the full sinogram data set and the second used a completely independent transport method based primarily on a deterministic transport approach RADSAT, which was developed by PNNL previously.

#### **9.3.2.1 MCNP-based System Matrix**

The MCNP-based  $W$  was deemed a useful approach because it is “perfect” in the sense that there should be no systematic biases (e.g., in the predicted in-object scatter contributions) between the system matrix and simulated tomographer response produced using the same MCNP modeling approach. Therefore, the uncertainty in performance predictions based on the MCNP  $W$  should be due entirely to statistical noise introduced in the forward-projected sinogram data during the creation of the virtual assembly populations.

The contribution coefficients of the MCNP  $W$  are calculated using the single-pin detector response sinogram data for a given fuel type, without the addition of statistical noise. The assembly geometry is incorporated into the reconstruction method, similar to the description in Section 9.3.1, by using the pins themselves rather than pixels as the basis set. This assumes that the alignment of the system is known, such as via an initial FBP reconstruction and alignment, and provides a “best case” bound on incorporating the system geometry into the reconstruction. Choosing whole pins for the basis set also neglects activity variations within the pin, but for the purposes of detecting pin diversion this level of detail is not required.

It is important to note that the MCNP-based methodology used to calculate single pin sinograms is computationally tractable without the inclusion of object scatter (as applied to UGET) or with an assembly-averaged object scatter (as applied for PGET), but is not for calculating object scatter on a pin-by-pin basis. For the latter, PNNL used a RADSAT-based transport method, as discussed below.

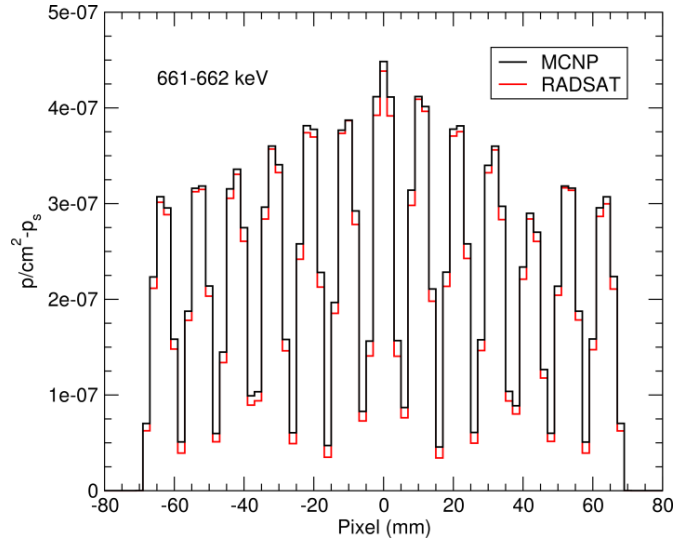
#### **9.3.2.2 RADSAT-based System Matrix**

The radiation detection community has traditionally relied on Monte Carlo modeling methods because of their geometric flexibility, well-tested cross-section libraries, and high accuracy through the direct simulation of fundamental physics processes. Because pulse-height tallies are inherently stochastic, simulation of gamma-ray spectrometer response is straightforward. However, a major drawback of Monte Carlo methods is the extremely long run times required to achieve good statistical precision, particularly for problems with deep penetration, high degree of scatter and self-attenuation, large physical scale, or those where low-probability effects (e.g., coherent scattering) may be important. Also, Monte Carlo solutions are not global—the fluxes, reaction rates, and other characteristics of the radiation field are only obtained in volumes and on surfaces that are selected prior to a simulation.

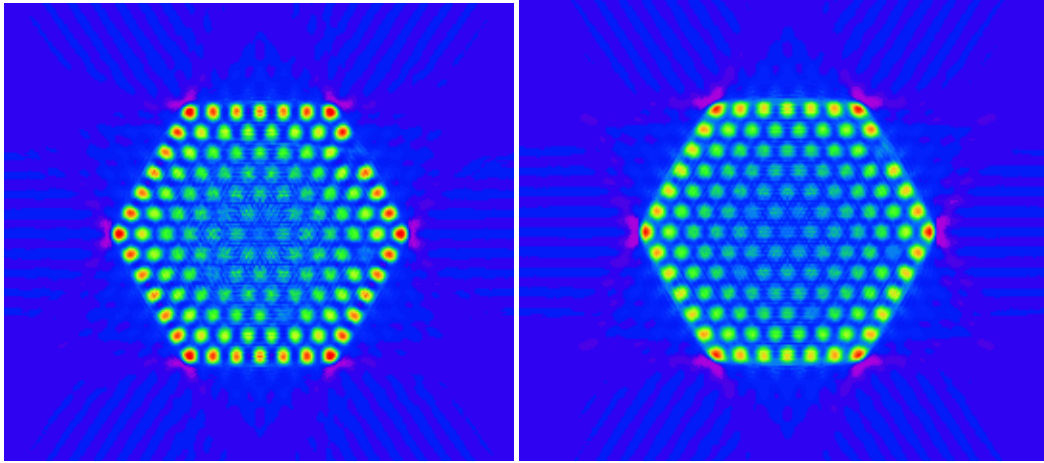
An alternative to Monte Carlo is to directly solve the Boltzmann transport equation using deterministic methods. Attractive advantages for deterministic methods are that they can be significantly faster than Monte Carlo methods for shielded and self-attenuating scenarios, they provide a solution everywhere in the computational domain, and the solution has no statistical noise. However, most deterministic codes rely on uniform Cartesian meshes, making them intractable for geometrically complex radiation detection scenarios. In addition, discretization errors such as ray effects can be problematic in detection scenarios



Figure 49 shows a comparison between MCNP and RADSAT for a full assembly projection at 0 degrees, for a 1-keV energy bin around the 662 keV emission from  $^{137}\text{Cs}$ . The differences between MCNP and RADSAT near the peaks of the response are approximately 3% and the total responses summed over all single-pin sinograms agree to within 3%. Figure 50 shows that reconstructed images based on the two methods are, at least visually, very similar (including some reconstruction artifacts in the corners).



**Figure 49.** Zero angle flux projections for RADSAT (red) and MCNP (black) for the flux in a 1-keV energy bin covering the 662-keV emission from  $^{137}\text{Cs}$ .



**Figure 50.** Reconstructions for 1-keV sinogram data (see Figure 50) generated by MCNP (left) and RADSAT (right) radiation transport.

The high degree of agreement for RADSAT and MCNP data in narrow peak energy regions is important and encouraging, but the true value-added of RADSAT for tomography is the ability to faithfully determine the object-scatter contributions on a pin-by-pin basis, in a reasonable amount of computational time. This capability is critical to analysis of tomographic data from the PGET device and is illustrated in Figure 51 where a single-pin, energy-dependent projection is shown for a pin emitting 662 keV gamma rays.

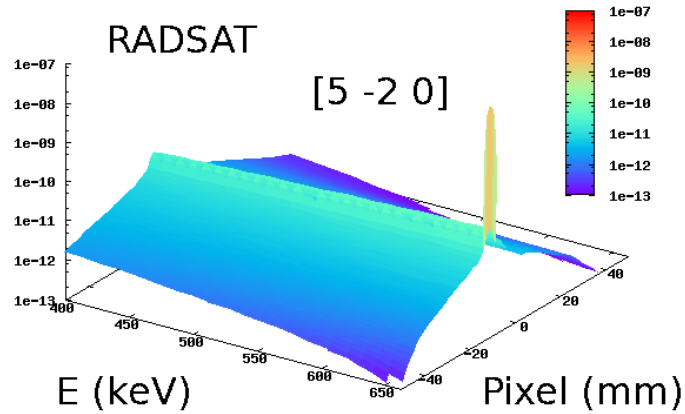


**Figure 51.** Un-normalized RADSAT single-pin projection data, illustrating the object-scatter contributions below the peak energy of 662 keV. Projection data is tallied against detector pixel location in the Ideal PGET design.

Because it is not reasonable to generate single-pin projection data inclusive of object scatter using MCNP, it is not possible to compare RADSAT and MCNP on that basis. However, a full-assembly projection comparison can be made, as in Figure 52 where the calculated down-scatter for MCNP and RADSAT over energy and pixel for a single (0 degrees) projection are depicted. Note that the MCNP data have large spikes due to statistical uncertainty and lack of convergence in these lower-intensity scattered energy regions. RADSAT, as a deterministic transport method, does not exhibit any statistical uncertainties. Note that the MCNP data required many times more computational time than RADSAT to generate.

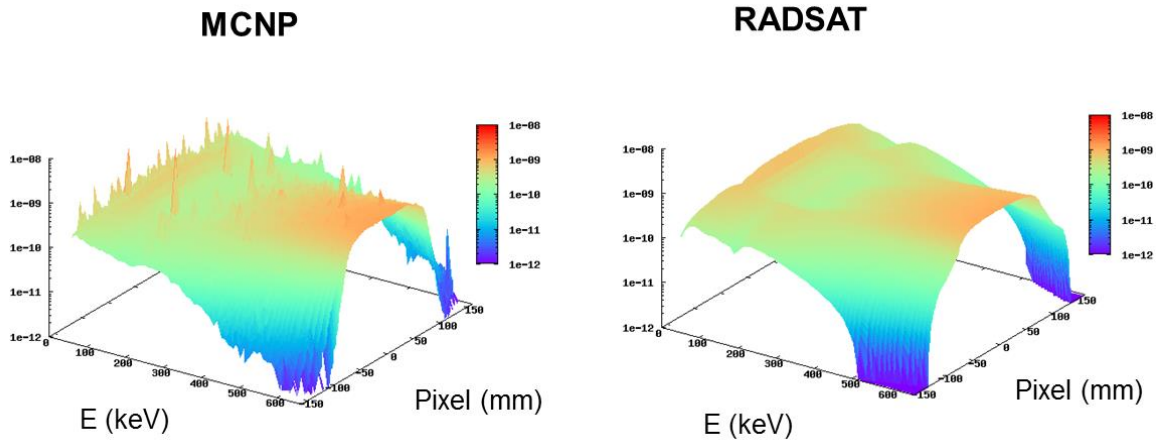


**Figure 52.** Un-normalized full-assembly down-scatter as a function of energy and detector pixel, assuming an Ideal PGET design, for a projection angle of 0 degrees: MCNP (left) and RADSAT (right).

## 9.4 Conclusions for Reconstruction and Analysis Methods

In general, one may argue that the higher level of detail introduced in the models used in tomographic reconstructions, the better the capability to obtain high-quality data and extract conclusive rod-wise information to support fuel inspections. However, there may also be limitations in applicability because of lack of information for the modeling (like for Verification Objective 1) or due to excessive needs for computational resources and/or computation time (which may be encountered for the most advanced models for Verification Objective 2).

The following are reflections on the approaches taken in this study:

- A tomographic measurement and analysis system can comprise a variety of available reconstruction and analysis tools. These tools may be applied to a dataset iteratively, without the need for additional collection of data. For example, one may consider an analysis sequence where an initial image reconstruction is performed with a low level of modeling detail and then a more detailed model is applied, based on the analyses of the initial images.
- An approach where subsequent, more detailed modeling is based on extracted data from initial reconstructions (“Verification Objective 1.5”) has not been explored in this work, but may be a subject for future studies.
- In some cases, the initial analyses may give information enough to support fuel verification, and thus subsequent, more detailed analyses may be required only in cases where the initial analyses do not allow for solid conclusions to be drawn.
- One may assume that time requirements put on measurements and/or analyses may differ between different types of analyses. Bulk analyses may be subject to strong time constraints while resolution of anomalies may allow for longer time consumption.

The image reconstruction and analysis methods presented for Verification Objective 1 in Section 9.2 are generally relatively fast and directly applicable to measurement data. The algebraic methods offer higher degree of flexibility as compared to FBP methods when it comes to disturbances such as incomplete data collection (e.g., non-functioning detector elements or limited angular coverage) or irregular measurement geometries, which may occur in practical data collection. The algebraic methods also allow for modeling of a device’s response function for a collimator with finite slit width, including realistic contributions from penumbra and umbra regions, whereas FBP methods implicitly assume an ideal line response from the object. Both techniques may take uniform attenuation into account to regularize the response from different parts of the fuel. Studies on a set of tomographic algorithms for reconstruction of gamma-ray emission data from nuclear fuel assemblies have indicated that algebraic image reconstruction methods offer better separation between fuel rods and non-rod regions than analytic ones (Jacobsson Svård et al. 2015a). However, one cannot rule out that there may be alternative image reconstruction methods that may offer similar or better performance for Verification Objective 1, other than the algorithms covered in that study. Finally, one may assume that image analysis methods will be an integral part of the analysis tools for Verification Objective 1, to perform automated analysis independent of assembly misalignment in the measuring device and similar geometric disturbances.

When it comes to reconstruction and analysis methods for Verification Objective 2, both SWESP and USSP have considered algebraic methods to be most useful because of their capability to enhance precision by including detailed modeling. Three alternatives for calculating the system matrix ( $W$ , see Eq. 9.3) have been presented:

- The SWESP Deterministic approach using UU’s Ray-Tracing toolbox
- The USSP Monte Carlo approach using MCNP
- The USSP Hybrid Deterministic-Stochastic approach using PNNL’s RADSAT

Some pros and cons for these alternatives are presented in Table 13, together with the role identified for each approach in this work.

**Table 13.** The alternative approaches taken in this work in the modeling of the system matrix  $W$  used in algebraic reconstructions for Verification Objective 2.

	<b>UU Ray-Tracing</b>	<b>USSP MCNP</b>	<b>PNNL RADSAT</b>
<b>Pros</b>	<ul style="list-style-type: none"> <li>• Fast</li> <li>• Independent</li> <li>• Relatively simple</li> <li>• Mature alternative for spectroscopic GET</li> <li>• Adaptable to geometry variations such as misalignment of assembly in device</li> <li>• Accessibility: source code can be purchased from UU researchers</li> </ul>	<ul style="list-style-type: none"> <li>• At hand for simulated cases, where it provides the “perfect” response function (simulation and reconstruction are done using same function)</li> <li>• Medium fidelity for “new” measured cases (object-scatter contributions are approximated)</li> <li>• Accessibility: requires MCNP license</li> </ul>	<ul style="list-style-type: none"> <li>• Relatively fast</li> <li>• High fidelity (object-scatter contributions are simulated explicitly)</li> <li>• Independent</li> <li>• Accessibility: requires purchase of commercial transport software, and open-source software from PNNL</li> </ul>
<b>Cons</b>	<ul style="list-style-type: none"> <li>• No gamma scattering into the detector included <math>\Rightarrow</math> currently not adapted to data with large contributions from scattering, such as unrefurbished PGET.</li> <li>• No user-friendly interface currently available</li> </ul>	<ul style="list-style-type: none"> <li>• Not independent for simulated cases.</li> <li>• Excessively slow for “new” measured cases</li> <li>• Medium user-friendliness (requires MCNP experience)</li> </ul>	<ul style="list-style-type: none"> <li>• Low user-friendliness (requires experienced transport analyst)</li> </ul>
<b>Role in this work</b>	Demonstration of the capabilities of an available analysis tool on simulated UGET v1 data	Illustrates absolute (upper) limits of GET performance if a “perfect model” is used	Illustration of potential, currently the only option for analyses that include high-fidelity object scatter



## 10.0 Objective 1: Performance Metrics and Results

As described previously, Objective 1 analysis is performed in a manner completely independent of operator-declared information (e.g., fuel assembly type, initial enrichment, burnup, and cooling time). The assembly is treated as an unknown sample and emitted gamma rays at one or more energies are used to directly calculate the spatial distribution of the emitting material. This spatial distribution is then used to determine the geometric pattern of the pins (e.g., sparse and rectangular for BWR, dense and hexagonal for VVER) and to count the number of pins composing that array. While two types of partial defects are possible—missing or substituted pins—the focus in this study has been on missing pins because it was shown to be the more difficult case for Objective 1.

The difficulty of the missing-pin detection task is expected to vary across the assembly. For example, the absence of an outer pin is expected to be easier to detect than the absence of an inner pin. Ideally, the probability of detection would be independently calculated for each pin in the assembly by running an ensemble of cases, each with a single pin removed. However, this would require changing not only the emission properties of each pin, but the attenuating effect of that pin on all other pins in the assembly, such that the full assembly must be recalculated. A more computationally tractable approach is to remove a few pins from a defined set of locations in the assembly, and take those locations to be representative of all pin locations with similar radial distance from the center of the assembly. Accordingly, pin positions are divided into “rings” of similar radial distance—four “rings” (quadratic) for the BWR, six “rings” (hexagonal) for the VVER-440, and eight “rings” (quadratic) for the PWR. At least one single pin is removed from each ring, placed such that no two missing pins are directly next to each other. Missing pin locations for each assembly are shown in Figure 53.

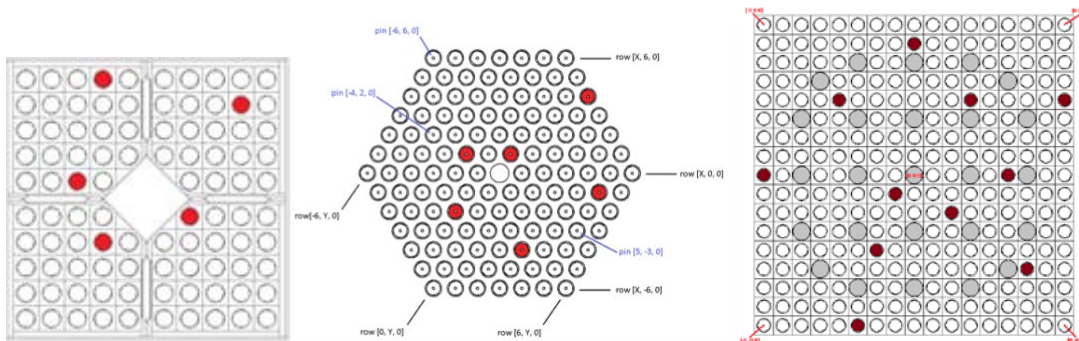


**Figure 53.** Map of the missing pin locations (in red) in the three assembly types: five for BWR (left), six for VVER (middle) and 11 for PWR (right).

In the comparative performance analyses of UGET and PGET in this section and throughout the rest of the report, it is assumed that both instruments have perfect efficiency and energy calibration. It should be noted that perfect efficiency and energy calibration cannot be achieved using the pulse processing electronics in the PGET device field-tested through 2015. The IAEA is refurbishing the PGET instrument to improve its capabilities in this regard, and the performance predictions in this report assume full success in that undertaking. To reflect the difference between the as-fielded instrument of the past, and the potential of the future analyzed here, the simulated device is often labeled “Ideal PGET.” Where that labeling is not present, it should be assumed. No such labelling is used with UGETv1 because it is a notional (not actual) instrument design.

The USSP and SWESP approaches to Objective 1 analysis, and results from those respective efforts, are described in the sections that follow.

## 10.1 USSP Analyses

Analysis of the virtual fuel assemblies in Objective 1 includes all of the tasks associated with finding the assembly in the image, finding the pin locations in the assembly, calculating the average gray level for each reconstructed pin, and reporting these averages in a pin-score rubric appropriate for subsequent processing with a performance evaluation metric. In actual field use, the exact location and orientation of the fuel assembly are not known, but for the simulation-based study, the USSP analysis assumed that the assembly location and orientation can be readily and accurately determined—no analysis tools were developed or applied to perform those tasks on the simulated data. The SWESP analysis did not make such an assumption (see Section 10.2).

### 10.1.1 Performance Metrics

A test statistic is needed that uses the location-specific pin-score distributions to determine the absolute performance of each candidate instrument design, and to compare the relative performance of proposed systems. The receiver operator characteristic (ROC) curve is a performance metric that can be used to understand the trade-off between probability of detection (PD) and probability of false alarm (PFA) in a classification task. ROC analysis is used in many fields; a standard reference from imaging sciences relevant to this work can be found in Metz (1978).

The pin scores (calculated as described in Section 9.2.1) for each pin location can be plotted as histograms, one histogram for the pins present and another for a missing pin. If these two histograms do not overlap, then threshold values between the distributions will result in perfect detection of missing pins without any false positives, for that pin location. If the histograms overlap then false alarms will be realized, depending on the threshold. By varying the threshold, the tradeoff between detection and false alarm can be quantified. An example of how the pin-score distributions for missing and present pins, in a particular pin location, can be used to generate a location-specific ROC curve is given in Figure 54.

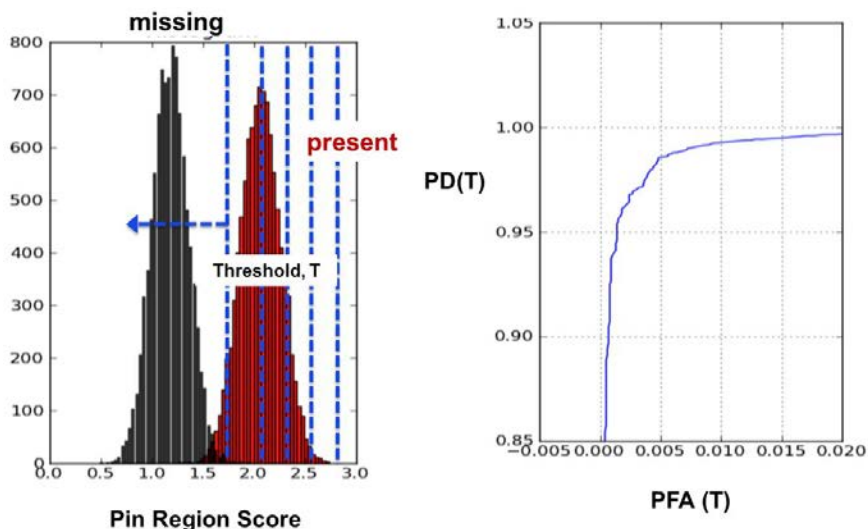


**Figure 54.** Illustrative example of how pin-score distributions for missing and present pins (left pane) can be used to calculate the probability of detection (PD) and probability of false alarm (PFA) as a function of threshold,  $T$ . The result is a ROC curve for a specific pin location (right pane).

This process is repeated for each pin location in the assembly or more practically, by groups of pins with similar radial distance from the center of the assembly. In this study, that grouping is named a “ring.” Examples of ROC curves generated for rings in a PWR assembly are given in Figure 55.

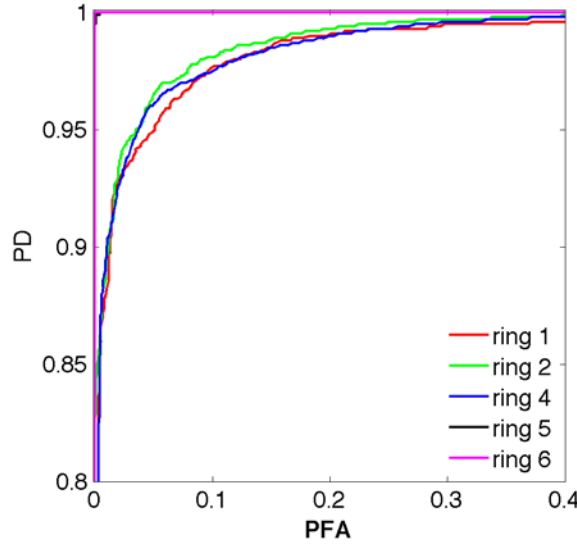


**Figure 55.** Example ROC curves as a function of pin location in a population of PWR assemblies with nominal burnup of 20 GWd/MTU, cooling time of 5 years and pin-wise burnup variation of +/-20%, and assay using the PGET device and an energy window >700 keV. Ring 1 is composed of the 8 pins that form a square closest to the center of the assembly, Ring 2 is formed from the pins in the next square region, and the rest of the rings are located similarly. Scores from the water channels are not included in the ROC analysis. Rings 6-8 have identical performance; only Ring 6 is shown.

Once the ring-specific PD and PFA values have been calculated, they need to be translated to an assembly-level PD and PFA that reflects how the IAEA is expected to make verification decisions in the field. In this study, the assembly-level performance predictions were formulated based on the following question: For given PD value at any missing-pin location, what is the assembly-level PFA? An assembly-level false alarm is defined as when at least one pin has a false alarm (i.e., the algorithm reports a missing pin when then pin is present). The sum of the probabilities for each configuration, where at least one pin alarms, can then be calculated. A simpler expression of the same quantity can be expressed in the negative: What is the probability that no pin alarms? The difference of this number from one indicates the assembly-level PFA:

$$PFA_{assembly} = 1 - \prod_{pin\_i} (1 - PFA(pin\_i)) = 1 - \prod_{ring\_j} (1 - PFA(ring\_j))^{n_{pins\_j}}$$

where  $PFA(ring\_j)$  indicates the false alarm probability for any pin in ring  $j$ , and the exponent is the number of pins in ring  $j$ . In the limit where the PFA is much less than one, the assembly PFA approaches the average number of false alarms per assembly.

### 10.1.2 Results

The USSP’s analysis assumptions for Objective 1 are given here:

- Total assay time: 60 minutes for UGET, less than 10 minutes for PGET

- Assembly populations: 1000 virtual assemblies with  $\pm 20\%$  pin-wise burnup variation
- Image analysis: fuel geometry, composition, and water-channel locations assumed known
- PGET ROIs: 400-700 keV for  $^{137}\text{Cs}$ ;  $>700$  keV for  $^{154}\text{Eu}$
- UGET ROIs: peak regions of interest at 662 keV ( $^{137}\text{Cs}$ ) and 1275 keV ( $^{154}\text{Eu}$ )

USSP's results for Objective 1 are summarized in Figure 56, Figure 57, and Figure 58, where performance of UGET and PGET are compared for different fuel types (BWR, VVER, and PWR), assuming fuel characteristics consistent with the three implementation scenarios and representative nominal burnup levels described in Section 3.2:

- 40 GWd/MTU, 1 yr cooling, anomaly resolution of short-cooled assemblies
- 20 GWd/MTU, 5 yr cooling, routine verification of fuel being transferred to dry storage
- 10 GWd/MTU, 40 yr cooling, routine verification of old fuel transferred to a repository

These figures portray performance as quantified with the assembly-level PD and PFA calculations described above.

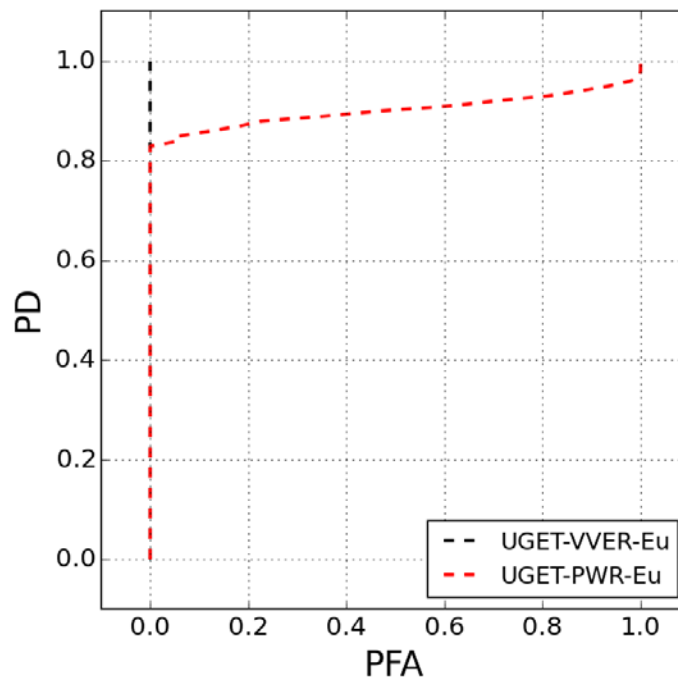


**Figure 56.** Predicted sensitivity for detection of a single missing pin (i.e., bias defect) for UGET, assuming VVER and PWR fuel with nominal burnup of 40 GWd/MTU and 1 year cooling time. BWR performance is even higher than for VVER and therefore, not shown. No results are shown for PGET because the count rates for this high-burnup, short-cooled fuel are too high for that instrument.

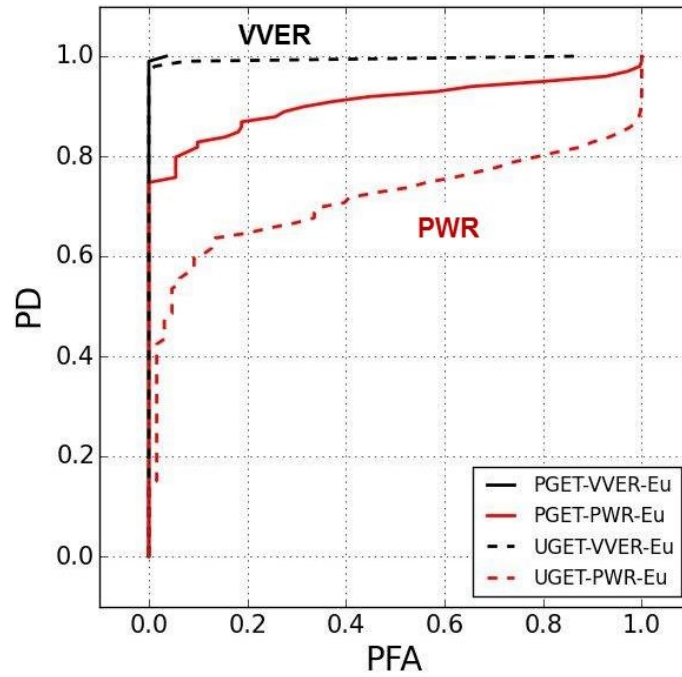


**Figure 57.** Predicted sensitivity for detection of a single missing pin (i.e., bias defect) for PGET and UGET, assuming VVER and PWR fuel with nominal burnup of 20 GWd/MTU and 5-year cooling time. BWR performance is even higher than for VVER and therefore, not shown.

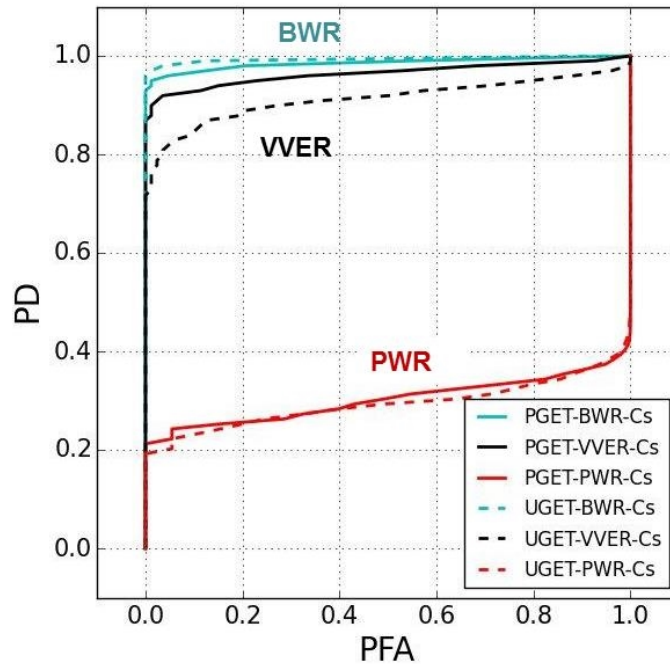


**Figure 58.** Predicted sensitivity for detection of a single missing pin (i.e., bias defect) for PGET and UGET, assuming BWR, VVER, and PWR fuel with nominal burnup of 10 GWd/MTU and 40-year cooling time.

Figure 58 illustrates that the single-missing-pin performance for PGET and UGET is low for PWR fuel due to its large physical dimension and relatively tight fuel-pin spacing. The summary results in Figure 58, assuming a very conservative assembly-level PFA formulation, are an aggregation of the sensitivities at all radial distances. Under the formula for assembly-level PFA described earlier, it is the inner rings that dominate the assembly-level PFA, but as Figure 59 shows, single missing pins are quite detectable for the outer rings of the assembly. Additional ROC curves, calculated on a ring-wise basis for all fuel types, are provided in Appendix E.

It is important to note that if the performance metric were defined for higher defect levels (e.g., 5% or 10% of the pins) instead of the <0.5% bias defect (1 missing pin out of 253 pins in a PWR) the ROC curves are expected to look considerably better for PWR fuels. This is an area for future work.

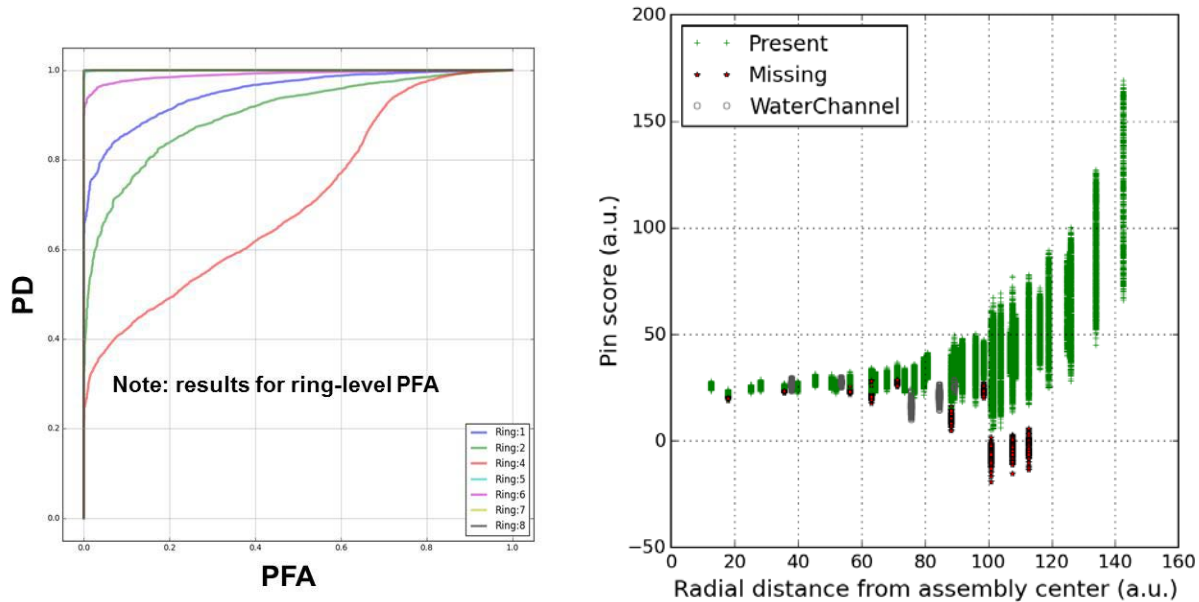


**Figure 59.** Ring-level ROC curves (left) and pin-score summary (right) for PWR fuel with nominal burnup of 10 GWd/MTU and 40-year cooling time. Note the overlap in pin scores between present and missing pins (and water channels) for much of the inner portion of the assemblies.

## 10.2 SWESP Analyses

The main purposes of the SWESP work within Verification Objective 1 were to

1. Complement USSP efforts:
  - Use a variety of tomographic reconstruction methods to investigate alternatives to basic analytic (FBP) reconstruction.
  - Investigate image analysis methods to extract information from reconstructed images.
2. Suggest in-field applicable procedures and tools:
  - Based on previous experience from experimental measurements bring forward and demonstrate robust tools that can handle in-field issues such as misalignment of assemblies, bowing of individual fuel rods, non-functioning detector elements, and irregular measurement positions etc.
  - Suggest procedures that may support in-field fuel inspections.

Accordingly, SWESP efforts included analyses of experimental as well as simulated data, where the former were performed to demonstrate the applicability of the studied reconstruction and analysis methods and to form a basis for suggested procedures on experimental data. Analyses were performed on data from SVEA-96 fuel measured with the PLUTO device at the Forsmark nuclear power plant in 2002, on data from BWR 8x8 fuel measured with the PGET device at Olkiluoto in 2014 and on data from VVER-440 fuel measured with the PGET device at Loviisa in 2014.

When it comes to analyses of simulated data for the UGET device, the analyses performed by SWESP within Verification Objective 1 have been limited to PWR fuels.

As described in Section 9.2.2, a number of alternative tomographic reconstruction methods have been covered, and a simulation study that was presented in Jacobsson Svård et al. (2015a) as part of this work, showed that the best performance in terms of quantification for Verification Objective 1 was obtained when using an algebraic reconstruction method including modeling of the system's response function and uniform "black-box" attenuation in the image area. Accordingly, the reconstructed images presented in this section were all obtained using this type of tomographic reconstruction.

### **10.2.1 Demonstration of Analysis Methods Using Experimental Data**

SWESP analyses of experimental data were performed in the following sequence of steps.

1. A simple image reconstruction was performed to produce an image for positioning of the fuel.
2. Automated image analysis was performed on the reconstructed image from step #1 to determine the position of the fuel in measuring device and confirm its size relative to the reconstructed image area.
3. A new image reconstruction was performed, where the image area was centered on the fuel's position in the device.
4. Automated image analysis was performed to identify fuel rods in the image using individual rod mask matching. The rod search routine was instructed to search for fuel rods until the image was filled.
5. Activities in the found regions in the image were extracted and displayed.

In step 1 above, a relatively simple image reconstruction routine is adequate to allow the image analysis in step 2, which also may be relatively simple. (Sinogram data may even be used directly to deduce the size and position of the measured assembly.) In steps 3-5, the selected reconstruction method and consecutive image analysis, as presented in Section 9.2.2 were applied. This complete procedure may be automated. Only steps 3-5 had to be applied in the analyses of simulated data in Section 10.2.2, because the simulations did not comprise any geometric irregularities.

Analyzing the  $^{140}\text{Ba}/\text{La}$  data (1596 keV) from PLUTO measurements on SVEA-96 fuel using this procedure gave the results presented in Figure 60.





**Figure 60.** Reconstructed image of the  $^{140}\text{Ba/La}$  distribution in the SVEA-96 fuel assembly that was measured using the PLUTO device in the Forsmark NPP in 2002 (left)(Jacobsson Svärd et al. 2005). The results of automated rod search in the reconstructed image, continuing until the whole image area is filled. Identified positions are overlaid in red over the reconstructed image (middle). A histogram of the rod activities extracted in the automated image analysis (right). The positions that correspond to actual fuel rods are marked with blue bars and non-rod positions are marked with red bars in the histogram.

Similar analyses were performed on experimental data from the PGET measurements on BWR 8x8 fuel in Olkiluoto, giving the results presented in Figure 61. Here, the initial reconstruction (step 1 above) is presented together with rod search results (step 4) and a rod-activity histogram (step 5).

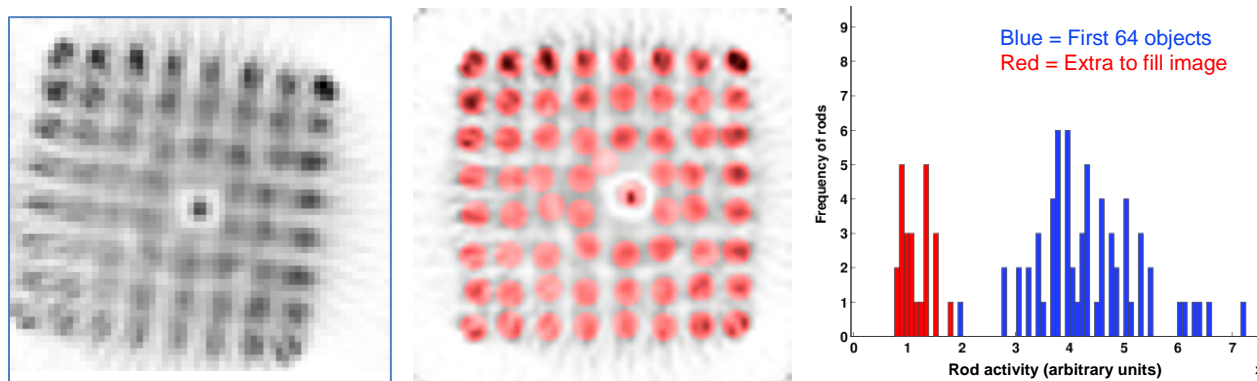


**Figure 61.** Initial reconstructed image based on PGET data collected on a BWR 8x8 assembly in Olkiluoto, showing assembly misalignment and a severe artifact in the device's center due to poor energy calibration of the detector elements (left). The frame illustrates the nominal fuel position in the device. The results of assembly positioning, a new image reconstruction and automated rod search in the new image (steps 2-4 above). Here, the 64 identified highest-activity positions are overlaid in red over the reconstructed image (middle). (NB: This fuel type contains 63 rods and one central water channel, but the central artifact destroys the possibility to analyze the fuel's centre.) A histogram of the rod activities obtained in the automated image analysis, when continuing to search for possible rods until the whole image area is filled (left). The 64 positions illustrated in the middle image are marked with blue bars in the histogram and the additional regions are marked with red bars.

In spite of a number of nonfunctioning detector elements and poor efficiency calibration of the remaining detector elements in the Olkiluoto measurements, which gave rise to a severe artifact in the center of the device that is evident in the reconstructed images in Figure 61, the deduced rod-wise data are promising in terms of partial defect detection capabilities on the single rod level. The analysis tools proved to



function robustly in spite of the encountered misalignment of the fuel assembly and the number of non-functioning detector elements. The results give some indication that the PGET device in combination with the presented analysis tools may be adequate for single-pin assessment of BWR fuel, provided that a data acquisition system upgrade is performed to allow for more robust methods for energy and efficiency calibration of the detector elements.

Furthermore, analyses of experimental PGET data from measurements on VVER-440 fuel in Loviisa have also been executed. The dataset under study included several flaws in terms of malfunctioning detectors, loss of one complete detector array and questionable angular information for the measured projections. Still, the results could be used to demonstrate the positioning capabilities of the image reconstruction and analysis routines, as presented in Figure 62.

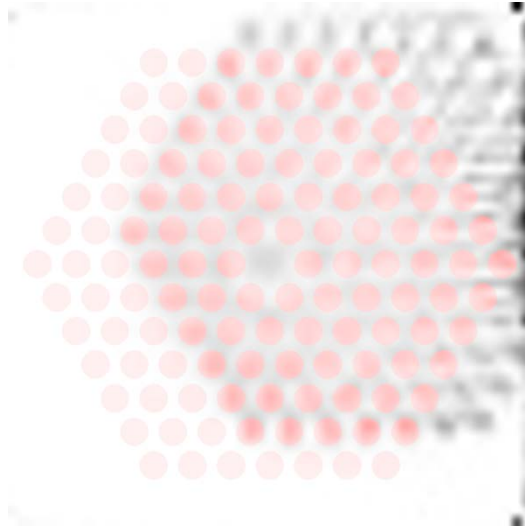


**Figure 62.** A reconstructed grey-scale image of a VVER-440 assembly in the PGET Loviisa measurements, including a representation (red) of a nominal VVER assembly geometry, centered in the device. (Figure from Davour et al. 2016.) Image analysis shows that the fuel assembly (in grey-scale) is dislocated by as much as +29.9 mm in x (horizontal in this image) and +10.2 mm in y (vertical in this image).

From the studies presented above, one can conclude that the routines presented may be used for automated analyses of experimental tomographic data.

### 10.2.2 Analyses of UGET Device Performance

Simulated data for the UGET device have been analyzed using the SWESP toolbox in a study covering only PWR 17x17 fuel. The cases under study are presented in Table 14.

**Table 14.** The set of fuel parameters and total assay times analyzed using the SWESP reconstruction and analysis toolbox. All cases were simulated for PWR 17x17 fuel, and each case comprised a set of 10 sinograms. The simulated data were provided by USSP. The total assay times given include time for positioning of the detectors as well as time for data collection, as were estimated by USSP.

CT	BU	Total assay time	Gamma-ray energies
1 y	40 GWd/tU	4.75 h 40 min 26 min	604 keV ( $^{134}\text{Cs}$ ) 662 keV ( $^{137}\text{Cs}$ ) 723 keV ( $^{154}\text{Eu}$ ) 796 keV ( $^{134}\text{Cs}$ ) 1274 keV ( $^{154}\text{Eu}$ )
40 y	10 GWd/tU	2.18 h 24 min 18 min	662 keV ( $^{137}\text{Cs}$ )

The simulations were performed by USSP using MCNP, as described in Section 8.0. The simulated configuration of fuel rods is presented in Figure 53, comprising 253 fuel rods, 11 empty fuel-rod positions and 25 water channels (corresponding to the 24 control-rod guide tubes and 1 instrumentation channel normally present in this fuel type). In the empty fuel-rod positions water had replaced the fuel rods. Accordingly, there were in total 35 positions in the fuel that could be used for analyzing the capability to discriminate fuel rods from non-fuel positions.

One may also note the following features of the analyzed data obtained from USSP:

- No variations in pin burnup existed.
- Data cover the full-energy component of selected peaks (i.e. assuming peak analysis with background subtraction enabled by the suggested use of LaBr<sub>3</sub>-detectors and spectrum collection in the UGET design).
- Each case under study included a set of 10 sinograms.
- The sinograms for each case were based on one long MCNP simulation, to which statistic noise was added corresponding to different collect times at each detector position.

The following conclusions could be drawn:

- For isotopes that emit gamma rays at more than one measurable energy, it is beneficial to use the higher energy for the analyses, because of its higher penetration from the inner sections of the fuel. Accordingly, the 604 keV energy from  $^{134}\text{Cs}$  and the 723 keV energy from  $^{154}\text{Eu}$  were not used for further analyses in this work. (Combined analyses of multiple peaks from one isotope may give additional information, and may be the subject for future studies.)
- Counting statistics affect results considerably, in particular for the precision obtained in the inner sections of the fuel.
- At the longer cooling time (40 years), only  $^{137}\text{Cs}$  is abundant enough to allow for analysis.
- At the shorter cooling time (1 year), gamma rays at higher energies are available, and higher count rates allows for better counting statistics at a certain measurement time, leading to better conditions for assay at short cooling times.

According to these conclusions, of the simulated cases in Table 14, the best opportunities for detection of partial defects on the single-rod level would be offered when using the 1274-keV gamma rays from  $^{154}\text{Eu}$  in 1-year-cooled fuel at the longest measurement time, 4.75 hours. The results from image reconstruction and automated image analysis for this case are presented in Figure 64.

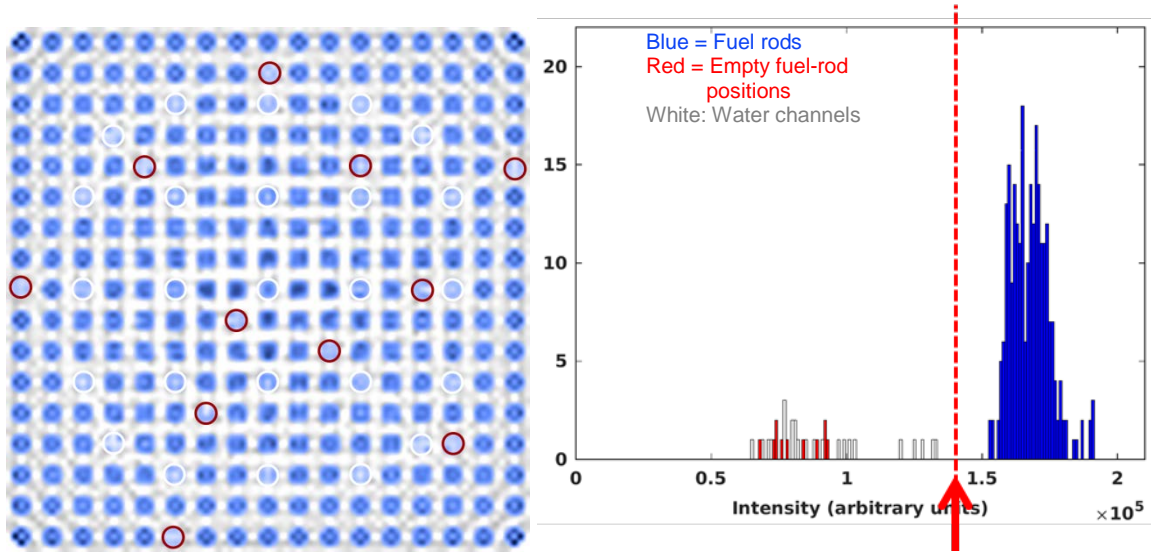


**Figure 63.** A reconstructed image (left), obtained in algebraic reconstruction including modeling of the UGET device's response function and uniform attenuation in the image area. Results of automated image analysis for identifying possible fuel rods in the image and quantifying their activity contents (right). A discriminator level is indicated in the figure, offering complete separation of fuel rods (blue) from water channels (white) and empty fuel-rod positions (red), indicating a perfect ROC curve.

As seen in the figure, this case offers complete separation of fuel rods (blue) from water channels (white) and empty fuel-rod positions (red). However, five of the water channels end up relatively close to the distribution of fuel rods, indicating that it may be difficult to separate them from fuel rods in more difficult cases. A closer analysis reveals that these five water channels are the most central ones in the fuel. Somewhat surprising, the most central removed-fuel-rod positions are more easily detected. An alternative way of presenting the results is shown in Figure 64, comprising the rod-wise data from all 10 sinograms simulated for this case.

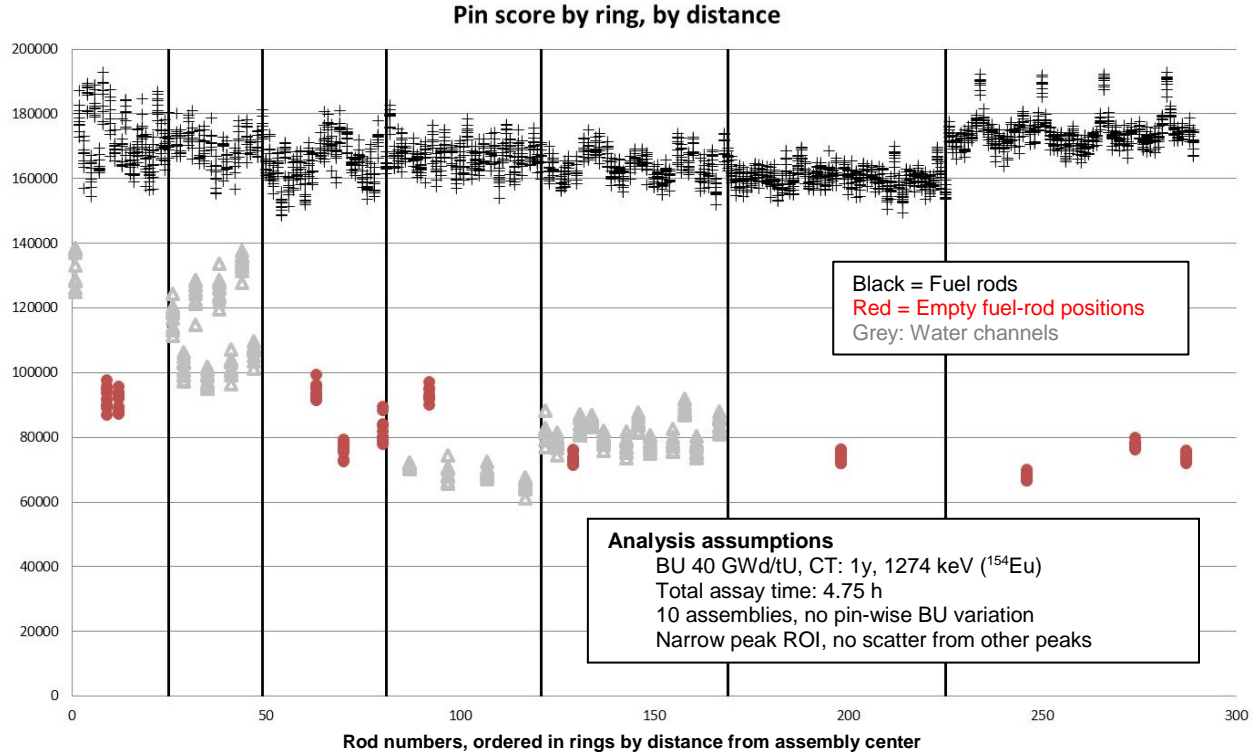


**Figure 64.** Rod scores obtained when analyzing a set of 10 sinograms from 1-year cooled PWR 17x17 fuel using algebraic image reconstruction and automated image analysis to extract reconstructed rod-by-rod activities. Rods are ordered in “rings” (quadratic) according to radial distance from the assembly center. The two innermost rings are not separated here. All empty fuel-rod positions are clearly separated from the distribution of fuel rods. However, for as yet unknown reasons, the five most central water channels do not offer the same level of separation, albeit still scoring lower than all fuel rod positions in all 10 simulations.

When going to the more realistically acceptable total assay time of 40 minutes, statistical noise implies that there is an overlap between the scores for the most central water channels and the fuel rods, as seen in Figure 65. However, all empty fuel-rod positions are still separated from the fuel rods.

Similar analyses have also been performed for the 796-keV energy of  $^{134}\text{Cs}$  and 662 keV from  $^{137}\text{Cs}$ . However, the lower gamma-ray energies imply somewhat worse capabilities to separate fuel rods from non-rod positions in the inner sections due to the higher gamma-ray attenuation.

When going to the long-cooled, low-burnup fuel (CT 40 years and BU 10 GWd/tU), only the 662 keV gamma rays from  $^{137}\text{Cs}$  are available for analysis. The rod scores for this case are presented in Figure 66.

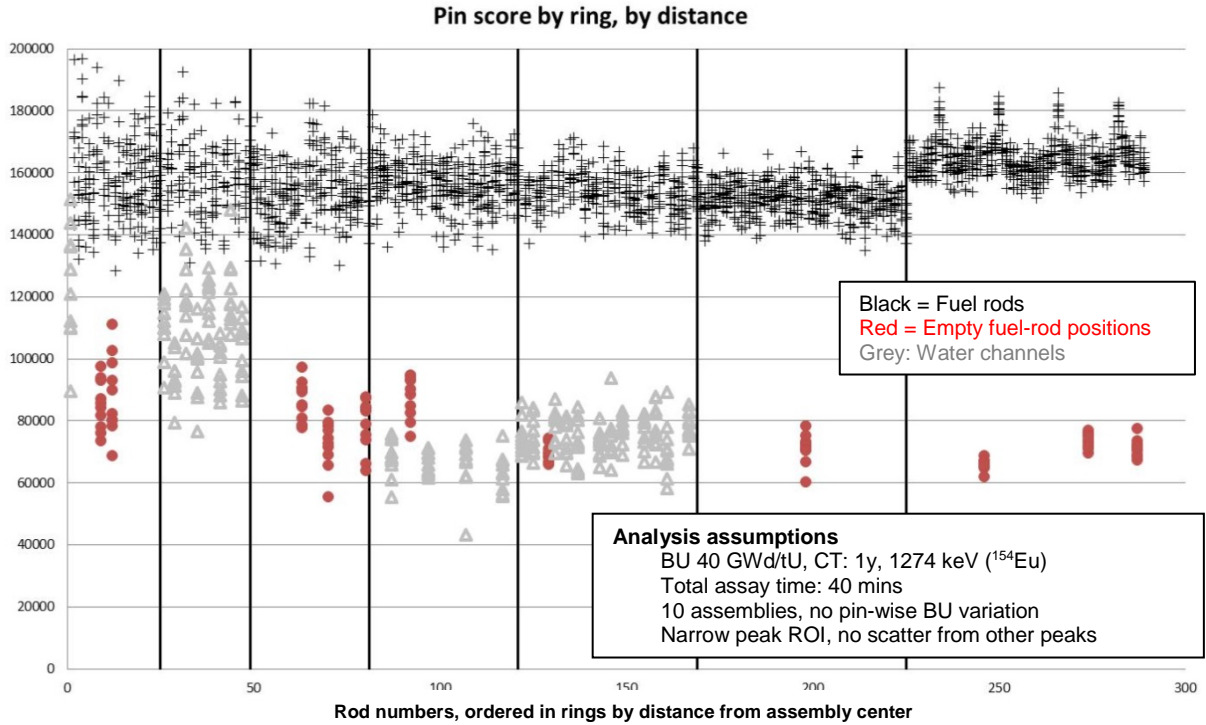


**Figure 65.** Similar analysis as in Figure 65, but for data at a total assay time of 40 mins. All empty fuel-rod positions are still clearly separated from the distribution of fuel rods. However, the five most central water channels overlap somewhat with the distribution of fuel rods.

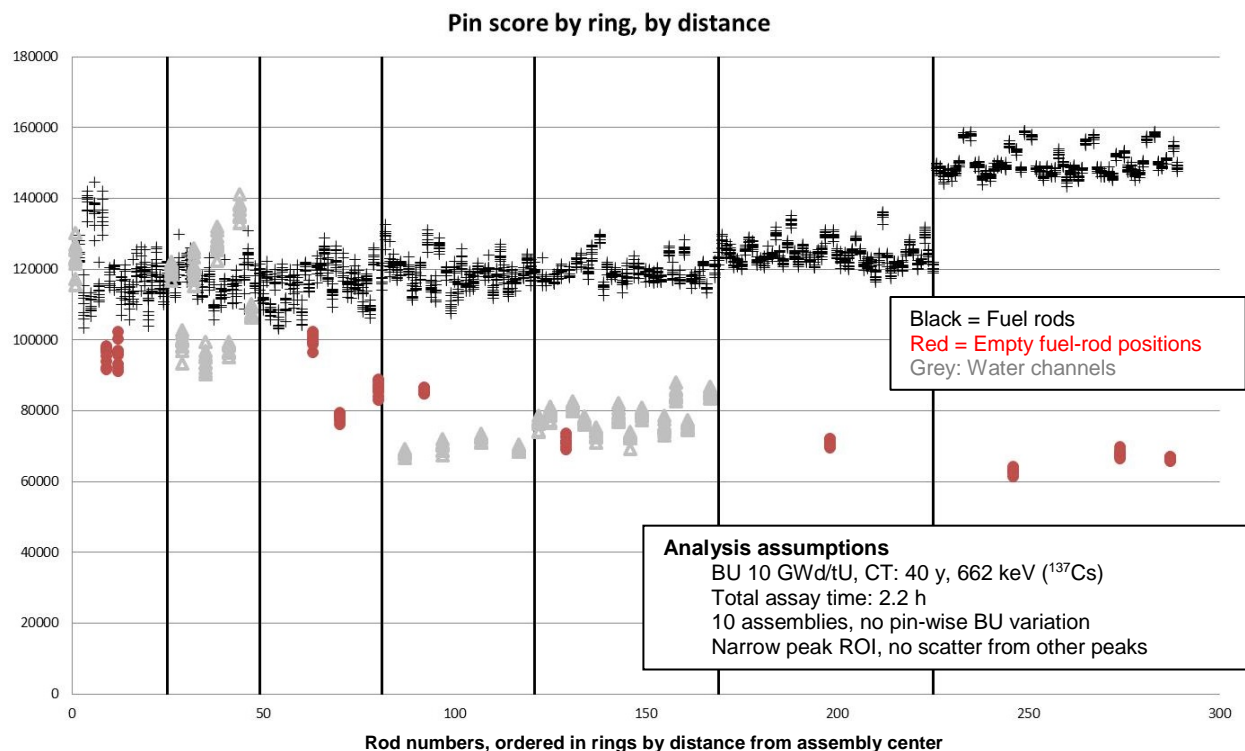


**Figure 66.** Rod scores obtained when analyzing a set of 10 sinograms from long-cooled, low-burnup PWR 17x17 fuel using algebraic image reconstruction and automated image analysis to extract reconstructed rod-by-rod activities. There are some overlaps between fuel rods and non-rod positions in the inner sections. However, for the dominant part of the fuel (the >70 percent that are situated in the four outermost rings), non-rod positions can be easily separated from fuel rods.

In a comparison of the SWESP PWR analysis results on fuel with a burnup of 10 GWd/tU and 40 years cooling time in Figure 66 to the corresponding results obtained in the USSP PWR analyses, presented in Figure 59, one can conclude that there are similarities as well as differences in the results. Among the similarities is a capability to separate fuel rods from all non-fuel positions in the outer sections of the fuel, whereas one cannot separate water channels from fuel rods in the inner sections. The results in Figure 66 indicate that the ability to identify empty positions in the central section may be better than the ability to identify water channels with this analysis, but the reason for this is yet unknown. Among the differences is a more level distribution of rod scores in this analysis, mainly because of the introduction of a uniform attenuation to the algebraic model used here. One may also interpret a slightly better capability in this analysis to separate fuel rods from non-rod positions in the intermediate sections of the assembly, however, one should also bear in mind that the results presented in Figure 59 incorporate a  $\pm 20\%$  distribution of fuel-rod burnups, not included in the simulated data set analyzed in Figure 66. Additional investigations would be needed to establish ROC curves for this type of analysis, similar to what is presented in Figure 59.

### 10.2.3 Conclusions and Suggested Inspection Procedure

The analyses of experimental data have demonstrated that the suggested methods for tomographic image analysis and image analysis are applicable to experimental data. In all datasets, large deviations from the nominal assembly position in the devices were detected and quantified. The image analysis tools have proven capable of determining the position of the fuel as well as to identify individual fuel rods in the

images and give quantitative estimates of their contents in the form of pin scores. For the PLUTO measurements on BWR fuel, the capability to separate fuel rods from background was demonstrated.

The analyses of simulated data were focused on PWR 17x17 fuel in the UGET device. Similar to PLUTO, this device is designed for spectroscopic data collection and full-energy peak analysis using detectors with relatively high full-energy detection efficiency. It was found that the availability of 1274-keV gamma rays from  $^{154}\text{Eu}$  (half-life of 8.6 years) at relatively short cooling times has the potential to provide partial-defect verification on the individual fuel rod level. However, one should note that the dataset analyzed by SWESP did not include any burnup variations among the fuel rods, which would likely degrade the results from those presented here. Still, the separation between fuel rods and non-rod regions was significant for the dominant part of the fuel, only the innermost sections may be challenging to assess. For long-cooled fuel (cooling time 40 years), only 662-keV gamma rays from  $^{137}\text{Cs}$  may be available for measurement, and the lower gamma ray energy implies that a smaller fraction of the gamma rays can escape the innermost parts of the fuel. The analyses for this case indicate that a larger region in the PWR assembly center may be inaccessible for partial-defect verification on the single rod level. However, there was significant separation between fuel rods and non-rod positions in the four outermost rings, comprising more than 70% of the rods. Additional investigations are needed to determine how large a fraction of the rods in the four innermost rings that may be removed before confident detection of the defect is allowed.

The conclusions may be summarized as follows.

- Procedures and tools that are adapted to in-field conditions have been demonstrated on experimental and simulated tomographic data.
- Algebraic reconstruction including modeling of system's intrinsic response function and uniform "black-box" attenuation gave the most promising results in terms of separation between fuel rods and background.
- Analyses of experimental data demonstrate that the presented image analysis and algebraic reconstruction tools offer robustness to experimental issues such as misalignment of assemblies, nonfunctioning detector elements and irregular measurement positions.
- For BWR fuel, partial-defect verification can be performed on the individual fuel rod level using any available gamma line at 662 keV ( $^{137}\text{Cs}$ ) or higher.
- For short-cooled PWR fuel, 1274 keV ( $^{154}\text{Eu}$ ) may offer partial-defect verification on the individual fuel rod level, even in the central sections of the assembly.
- For long-cooled PWR fuel, at 662 keV ( $^{137}\text{Cs}$ ) 70% of the fuel rods can be verified, whereas individual missing rods in the most central 30% are more difficult to assess.

The envisioned inspection procedure, identified and refined as part of this project can be expressed according as follows.

- Baseline inspection procedure:
  1. Tomographic measurement
  2. Online image reconstruction
  3. Online image analysis
  4. On-site initial integrity statement

If undeclared removal/replacement is suspected:

5. Detailed rod-activity reconstruction based on current fuel type and position in device. (No additional measurement is required.)

The last step may be considered as connected to Verification Objective 2, at least if operator-declared information is used for the detailed modeling. However, one may also envisage a “Verification Objective 1.5”, where geometric information is extracted directly from the reconstructed images, albeit such analyses was beyond the scope of this work.





## 11.0 Objective 2: Performance Metrics and Results

As discussed in Section 9.0, algebraic reconstruction algorithms use a system matrix,  $W$ , to solve for the activity distribution in each pin based on the sinogram projection data recorded by the tomographer. Based on reconstructed pin-wise isotopic data, the inspector may identify anomalies, e.g. in terms of unexpectedly large variations in burnup and/or cooling time among the population of fuel rods in the assembly. In the assumptions for Verification Objective 2 in this work, availability operator-declared data for verification was considered.

The analysis procedure used for Verification Objective 2 is illustrated in Figure 67.

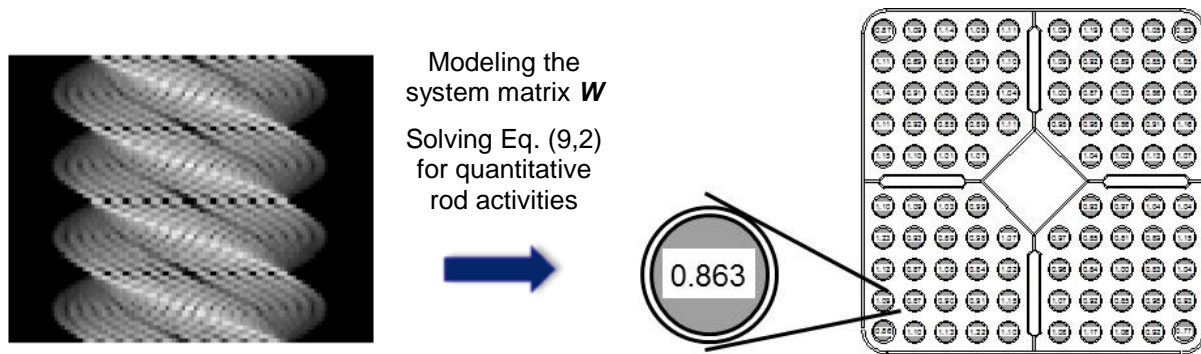


**Figure 67.** Illustration of the Objective 2 analysis approach. The comparison of reconstructed rod-wise isotopic activities to a known ground truth is the key performance metric for this objective.

In the simulation-based studies, the ground-truth isotopic concentrations are known exactly. Note that in practice, the availability and accuracy of pin-wise isotopic activities produced by operators using burnup codes may vary widely.

SWESP and USSP evaluation results for Objective 2 are described in this section. The analyses are complementary in that SWESP focused on PWR fuels while USSP focused on VVER fuels. SWESP also included a limited evaluation of the performance for BWR fuel.

### 11.1 SWESP Analyses and Results

The purposes and goals of the SWESP work within Verification Objective 2 were to:

1. Identify robust methods and tools, which offer conclusive pin assessment, even when encountering in-field issues such as misalignment of assemblies, bowing of individual fuel rods, non-functioning detector elements, irregular measurement positions, etc., and
  - Demonstrate these methods and tools on experimental data and on benchmarked simulated data
  - Suggest procedures that may support in-field fuel inspections.
2. Perform evaluations of the identified tools:
  - Assess pin-wise relative isotopic contents and investigate methods to determine fuel parameters such as burnup and cooling time based on these data
  - Estimate achievable precision in these assessments.

Here, the analysis tools and methods described in Section 9.3.1 have been applied to experimental and simulated BWR data for the PLUTO device, described previously, and to simulated PWR data for the UGETv1 device design. The methodology to deduce pin-wise burnup and cooling time from tomographic data was previously presented in Jacobsson Svärd et al. (2015b) and is further elaborated in Section 11.1.2.

### **11.1.1 Assessing Rod-wise Isotopic Distributions**

The analysis tools and methods described in Section 9.3.1 and Appendix C have previously been used on experimental data from the PLUTO device, demonstrating a capability to determine isotopic contents of  $^{140}\text{Ba}/\text{La}$  in BWR fuel with percent-level precision (Jacobsson Svärd et al. 2005). Because the performance of these tools already had been demonstrated for high-energy gamma rays (1596 keV) in BWR fuel, the route taken by SWESP in this work was to apply these tools also to BWR data for lower-energy gamma rays and to data for larger fuel geometries, such as PWR, to evaluate their performance for more difficult cases, where gamma rays escape the central section of the fuel to a smaller extent.

One may note that the analyses presented in Jacobsson Svärd et al. (2005) required knowledge of the positions of the fuel in the measuring device, which was originally obtained in separate positioning measurements. However, it was later shown that image reconstruction in combination with image analysis can be used to deduce accurate geometric information from the tomographic data, implying that separate positioning measurements can be omitted (see Davour 2016).

#### **11.1.1.1 $^{137}\text{Cs}$ in BWR fuel**

Simulations were performed for 662 keV gamma rays from  $^{137}\text{Cs}$  in BWR fuel using the Monte Carlo simulation code MCNP, modeling a SVEA-96 fuel assembly in the PLUTO equipment and a similar measurement scheme as for the experimental data collected using PLUTO. (It was not possible to extract any  $^{137}\text{Cs}$  data from the experimental PLUTO data due to the low energy resolution of the detectors and the presence of other strong peaks near the 662 keV peak at the short cooling time of the fuel in these measurements.) Details on the simulations can be found in Jacobsson Svärd et al. (2015a). The level of statistics in the simulated data was relatively low, with a precision in the highest intensity data points of about 3%, as estimated by the MCNP code. To facilitate the analysis, all rods were simulated with equal  $^{137}\text{Cs}$  content. The results of the tomographic reconstructions are presented in Figure 68.

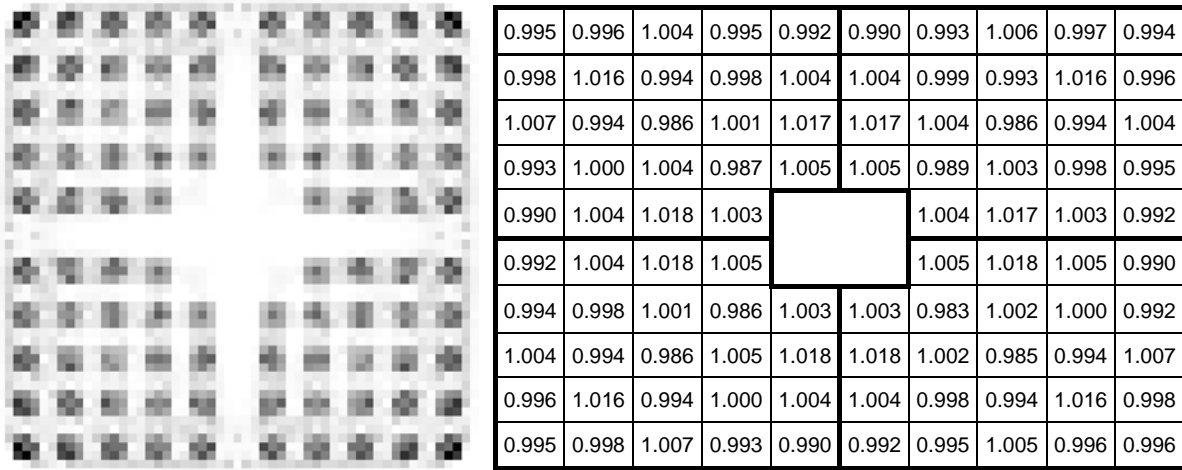


**Figure 68.** Results obtained in tomographic reconstructions of simulated  $^{137}\text{Cs}$  data from a SVEA-96 fuel assembly in the PLUTO device (data from Jacobsson Svård et al. 2015a). All rods were assigned equal  $^{137}\text{Cs}$  contents in the simulations. A gray-scale 55x55-pixel tomographic image of the  $^{137}\text{Cs}$  distribution in the assembly cross section (left). Relative pin-wise contents of  $^{137}\text{Cs}$  obtained in a reconstruction using the methods described in Section 9.3.1 (right). The precision obtained was 0.87 percent ( $1\sigma$ ), indicating that relative pin-by-pin  $^{137}\text{Cs}$  contents can be measured at the 1% level for this fuel type.

In conclusion, the results presented in Figure 68 show that high-precision tomographic measurements of rod-wise isotopic contents in BWR fuel can be performed also at the lower gamma-ray energy of  $^{137}\text{Cs}$  (662 keV), in addition to the previously experimentally demonstrated 1596 keV energy.

#### 11.1.1.2 PWR Fuel

The studies of the capability to measure pin-wise isotopic contents in PWR fuel using the UGET device design are based on the same USSP simulated data that was analyzed for Verification Objective 1, as presented in Section 10.2.2. The simulated configuration of fuel rods was presented in Figure 53 (right). The assembly comprised 253 fuel rods and 36 non-rod positions, which contained mostly water because these were either removed fuel rods or water channels. The fuel parameters and total assay times covered in the analyzed cases were previously presented in Table 14, and each case comprised 10 datasets (sinograms) to allow for a limited statistical analysis of the results.

In the tomographic reconstructions, the fuel configuration was assumed to be known *a priori*, based on the prerequisites for Verification Objective 2. Knowledge of the current assembly position in the measuring device was also assumed—an assumption that is supported by the results from image analysis presented in Section 10.2.2. The algebraic reconstruction methods presented in Section 9.3.1 were applied to each dataset, and rod-by-rod relative isotopic contents were extracted from the reconstructions.

Based on the reconstruction results, some general conclusions could be drawn, which were all according to expectations:

1. Longer total assay time leads to higher precision.
2. Precision for pins in the assembly periphery is higher than for pins in its center.
3. Higher gamma-ray energy generally gives better results for the center pins:
  - For  $^{134}\text{Cs}$ , 796 keV is more useful than 604 keV
  - For  $^{154}\text{Eu}$ , 1274 keV is more useful than 723 keV.

Results for the short-cooled, high-burnup fuel are presented in Figure 69 in terms of relative rod-by-rod activities for fuel rods ordered ring-by-ring from the fuel assembly center to the periphery. In the presented cases, the level of statistics in the analyzed data sets corresponds to 40 minutes total assay time. Since a prerequisite for Verification Objective 2 was that the fuel geometry was known *a priori*, activities are only reconstructed in fuel rods and not in water channels or positions of missing rods.

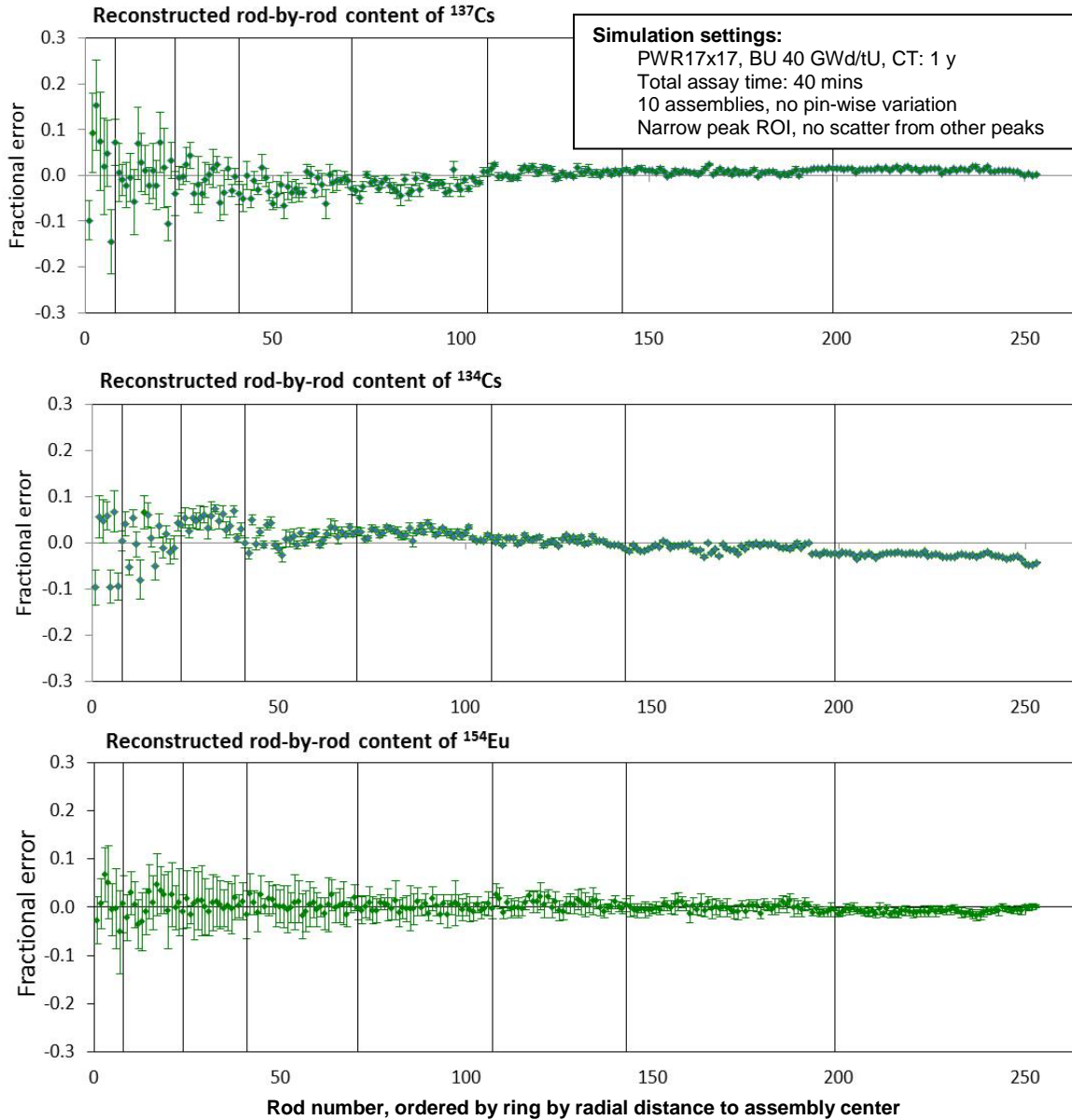


**Figure 69.** Results obtained in tomographic reconstructions of simulated sinograms for a short-cooled, high-burnup PWR 17x17 fuel assembly in the suggested UGET device design, presented as mean values of fractional error in reconstructed rod-by-rod isotopic contents obtained in analyses of 10 datasets, including error bars corresponding to  $\pm 1 \sigma$  confidence intervals. All rods were assigned equal isotopic contents in the simulations. The analyses were made based on full-energy gamma peaks at 662 keV ( $^{137}\text{Cs}$ ), 796 keV ( $^{134}\text{Cs}$ ) respectively 1274 keV ( $^{154}\text{Eu}$ ).

The results illustrated in Figure 69 are also presented in Table 15 to further account for the varying precision for fuel rods from the assembly center to the periphery.

**Table 15.** Ring-by-ring precision and systematic deviations of reconstructed isotopic contents from true values, obtained in analyses of simulated sinograms for a 1-year-cooled high-burnup PWR 17x17 assembly in the UGET device design. The statistics in the simulated data corresponds to a total assay time of 40 minutes.

Ring	<sup>137</sup> Cs (662 keV)		<sup>134</sup> Cs (796 keV)		<sup>154</sup> Eu (1274 keV)	
	Precision (1 $\sigma$ )	Average deviation	Precision (1 $\sigma$ )	Average deviation	Precision (1 $\sigma$ )	Average deviation
8 (periphery)	0.5%	1.2%	0.7%	-2.7%	0.9%	-0.8%
7	0.6%	0.8%	0.8%	-0.9%	1.5%	0.0%
6	1.2%	0.5%	0.8%	0.6%	2.1%	0.5%
5	1.8%	-2.1%	1.1%	2.3%	2.7%	0.0%
4	3.0%	-2.5%	2.2%	1.2%	3.9%	0.4%
3	4.5%	-0.6%	2.3%	4.9%	5.3%	0.4%
2	7.3%	0.3%	4.9%	0.4%	5.8%	0.7%
1 (center)	12.9%	2.1%	8.5%	-0.8%	7.5%	0.5%

Results for the pin-wise assessment of isotopic contents of <sup>137</sup>Cs in the long-cooled, low-burnup assembly are presented in Figure 70. For the presented case, the level of statistics in the simulated data corresponds to a total assay time of 2.2 h.

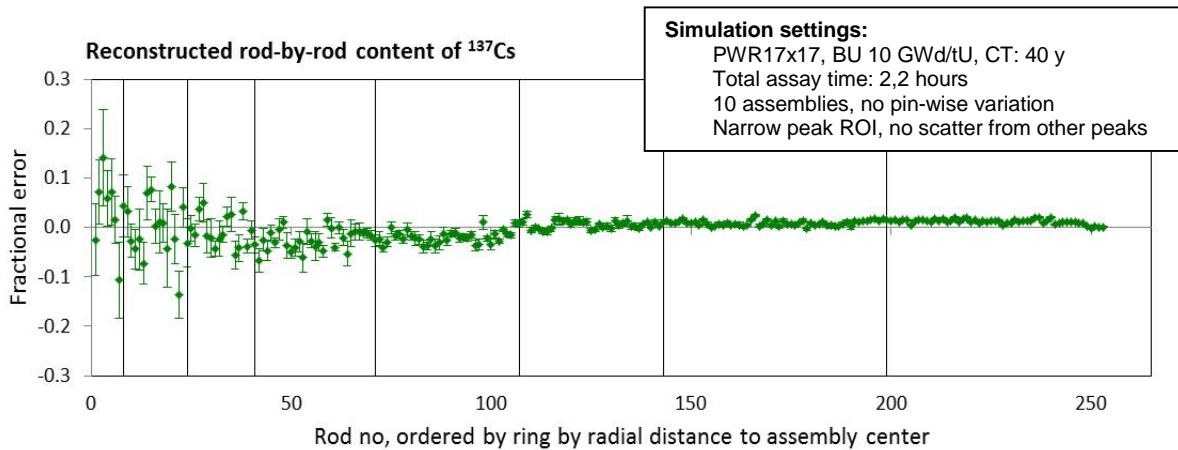


**Figure 70.** Results obtained in tomographic reconstructions of simulated sinograms for a long-cooled, low-burnup PWR 17x17 fuel assembly in the suggested UGET device design, presented as mean values of fractional error in reconstructed rod-by-rod isotopic contents of <sup>137</sup>Cs obtained in analyses of 10 datasets, including error bars corresponding to  $\pm 1 \sigma$  confidence intervals. All rods were assigned equal isotopic contents in the simulations.

The dependence of precision on total assay time for pin-wise assessment of <sup>137</sup>Cs in long-cooled low-burnup PWR 17x17 fuel is also presented in Table 16.

**Table 16.** Ring-by-ring precision and systematic deviations of reconstructed  $^{137}\text{Cs}$  contents from true values, obtained in analyses of simulated sinograms for a 40-year-cooled low-burnup PWR 17x17 assembly in the suggested UGET device design. The statistics in the data corresponds to varying total assay times, as accounted for in the table.

Ring	2.2 h total assay time		24 min. total assay time		18 min. total assay time	
	Precision (1 $\sigma$ )	Average deviation	Precision (1 $\sigma$ )	Average deviation	Precision (1 $\sigma$ )	Average deviation
8 (periphery)	0.5%	1.2%	0.7%	1.4%	0.9%	1.2%
7	0.6%	0.8%	1.1%	0.9%	1.5%	0.9%
6	1.1%	0.4%	2.3%	0.6%	2.6%	0.5%
5	1.5%	-2.1%	3.8%	-2.1%	4.6%	-2.0%
4	2.8%	-2.6%	5.8%	-2.1%	9.4%	-2.8%
3	4.4%	-0.3%	9.5%	0.2%	13.9%	-1.0%
2	7.6%	-0.3%	15.8%	0.1%	22.3%	1.3%
1 (center)	10.1%	3.3%	24.4%	-3.4%	35.0%	1.2%

It is clearly seen in Table 15 and Table 16 that the isotopic contents in the fuel rods in the assembly periphery can be determined with high precision, whereas uncertainties are larger for fuel rods near the assembly center. Still, the detailed modeling of the fuel performed in this type of tomographic reconstructions enables the assessment of rod-wise isotopic contents with precision down to the 10% level (1  $\sigma$ ) even for the 662 keV gamma rays from  $^{137}\text{Cs}$ .

In general, higher gamma-ray energies give higher precision, but counting statistics also has strong influence on the uncertainty, as illustrated in Table 16. When comparing the full set of data displayed in Table 15 and Table 16, no evident systematics can be noted between fuel rods in different rings, and for the central fuel rods, counting statistics dominates the uncertainties.

### 11.1.2 Determining Pin-wise Burnup and Cooling Time

Gamma-ray spectroscopy is an established technique to characterize nuclear fuel, and several studies have been made to establish correlations between full-energy peak intensities of gamma rays from  $^{137}\text{Cs}$ ,  $^{134}\text{Cs}$  and  $^{154}\text{Eu}$ , recorded in gamma-scanning measurements of nuclear fuel assemblies, to fuel parameters such as burnup and cooling time (Jansson 2002). The use of gamma-ray signatures from these isotopes have also been proposed for verification of operator-declared irradiation history (Willman et al. 2006).

Typically, two isotopes are used for determining burnup and cooling time from gamma scanning data, as accounted for in Table 17. However, one may also consider other combinations of isotopes with established fuel parameter dependences.

**Table 17.** Isotopes typically used for determining fuel burnup and cooling time in gamma-scanning measurements, given with half-lives ( $T_{1/2} = \ln(2)/\lambda$ ), gamma-ray energies ( $E_\gamma$ ) and burnup dependence  $\kappa$  (from Jansson 2002).

Isotope 1	$T_{1/2}$ [years]	$E_\gamma$ [keV]	$\kappa$	Isotope 2	$T_{1/2}$ [years]	$E_\gamma$ [keV]	$\kappa$
$^{137}\text{Cs}$	30.1	662	1.0	$^{134}\text{Cs}$	2.1	605, 796	2.0
				$^{154}\text{Eu}$	8.6	1274	1.6

The following equations for determining burnup (BU) and cooling time (CT) based on two gamma-ray intensities  $I_1$  and  $I_2$ , measured by means of gamma scanning, are given in Jansson (2002):

$$BU = \exp \left[ \frac{\ln \left( \left( \frac{k_2}{I_2} \right)^{\lambda_1} \cdot \left( \frac{I_1}{k_1} \right)^{\lambda_2} \right)}{\lambda_2 \kappa_1 - \lambda_1 \kappa_2} \right] \quad (10.1)$$

$$CT = \frac{\ln \left\{ \left( \frac{k_2}{I_2} \right)^{\kappa_1} \cdot \left( \frac{I_1}{k_1} \right)^{\kappa_2} \right\}}{\lambda_2 \kappa_1 - \lambda_1 \kappa_2} \quad (10.2)$$

where  $k_1$  and  $k_2$  are calibration constants, which need to be set for the gamma scanning equipment used.

Because tomographic measurement and analysis can return pin-wise contents of these isotopes, this technique also enables assessment of pin-wise fuel parameters, which can be used to verify the consistency of operator-declared data and reveal possible manipulation of the fuel. Provided that a proper calibration has been done, Eq. (10.1) and (10.2) may then be applied to tomographic pin data by using the reconstructed pin-activity contents instead of intensities for  $I_1$  and  $I_2$ .

Error propagation of uncertainties in pin-activity contents gives uncertainties in determined fuel parameters values according to the following:

$$\frac{\Delta BU}{BU} = \frac{1}{|\lambda_2 \kappa_1 - \lambda_1 \kappa_2|} \cdot \sqrt{\lambda_2^2 \left( \frac{\Delta I_1}{I_1} \right)^2 + \lambda_1^2 \left( \frac{\Delta I_2}{I_2} \right)^2} \quad (10.3)$$

$$\Delta CT = \frac{\sqrt{(\kappa_2 \Delta I_1 / I_1)^2 + (\kappa_1 \Delta I_2 / I_2)^2}}{|\lambda_2 \kappa_1 - \lambda_1 \kappa_2|} \quad (10.4)$$

Because one may consider establishing of pin-wise calibration factors  $k_1$  and  $k_2$ , eventual systematic deviations—due to possibly incomplete modeling in the reconstruction codes for example—might be taken into account in this type of analysis. Accordingly, the evaluation of achievable precision in the tomographic determination of pin-wise burnup and cooling time, according to Eqs (10.1)-(10.4) has here been based solely on counting statistics. The results for short-cooled PWR 17x17 are given in Table 18.



**Table 18.** Estimation of achievable uncertainties in the tomographic determination of pin-wise burnup and cooling time for 1-year cooled high-burnup PWR17x17 fuel based on the effect from counting statistics, given for fuel rods at various distances from the assembly center. The estimations for each combination of isotopes were deduced from the analyses of 10 simulated datasets (sinograms) for the suggested UGET device design, with counting statistics corresponding to a total assay time of 40 minutes.

	<sup>154</sup> Eu and <sup>137</sup> Cs	<sup>134</sup> Cs and <sup>137</sup> Cs	<sup>154</sup> Eu and <sup>134</sup> Cs			
Ring	ΔBU/BU	ΔCT [y]	ΔBU/BU	ΔCT [y]	ΔBU/BU	ΔCT [y]
8 (periphery)	0.56%	0.20	0.22%	0.01	0.74%	0.04
7	0.99%	0.34	0.43%	0.03	1.2%	0.07
6	1.6%	0.50	0.80%	0.05	1.7%	0.11
5	2.5%	0.71	1.3%	0.08	2.3%	0.14
4	4.4%	1.2	2.5%	0.16	3.4%	0.21
3	6.8%	1.7	3.9%	0.25	4.8%	0.30
2	11.0%	2.4	6.7%	0.42	4.9%	0.32
1 (center)	15.1%	3.4	9.7%	0.60	5.9%	0.39

In this context, one may note that there is an irradiation-history dependence for short-lived nuclides rather than a cooling-time dependence, which complicates the use of Eqs (10.1) and (10.2), in particular when <sup>134</sup>Cs is used. However, the equations may still be used for control of consistency of the population of fuel rods. In addition, one may also select to apply verification of irradiation history according to [Willman 2006].

For long-cooled fuel, such as the simulated 40-year cooled PWR17x17 fuel analyzed in this work, only <sup>137</sup>Cs may be available for measurement. In such cases, <sup>137</sup>Cs can still give a direct measure of the fuel burnup, provided that all fuel rods have the same cooling time. Accordingly, the precision obtained according to Table 16 gives a direct measure of the best-case precision in pin-wise burnup determination.

### 11.1.3 Concluding Remarks on the SWESP Analyses for Verification Objective 2

The SWESP analysis for Verification Objective 2 may be summarized as follows.

- Procedures and tools that are adapted to in-field conditions have been identified, comprising image analysis of basic (Verification Objective 1-type) reconstructions to determine the position of the fuel assembly in the measuring device, thereby enabling detailed modeling of gamma-ray transport through the fuel configuration in algebraic reconstructions to produce conclusive pin-wise data. As discussed in Section 10.2, algebraic reconstruction methods also offer robustness to issues such as non-functioning detector elements, irregular measurement positions, etc.
- These procedures and tools have previously been used on experimentally recorded <sup>140</sup>Ba/La tomographic data from short-cooled BWR fuel, demonstrating the capability to perform %-level assessment of pin-wise isotopic contents. In this work, similar performance has been presented for <sup>137</sup>Cs in long-cooled BWR fuel, based on simulated data.
- Simulation studies of the UGETv1 device design indicate that for short-cooled PWR fuel, <sup>137</sup>Cs, <sup>134</sup>Cs, and <sup>154</sup>Eu isotopic contents in peripheral fuel pins can be assessed with percent-level precision, and center pins with about 10% precision or below ( $1\sigma$ ).
- For long-cooled PWR fuel, <sup>137</sup>Cs isotopic contents in peripheral fuel pins can be assessed with percent-level precision and center pins with 10-20% precision ( $1\sigma$ ).

- Precision is highly dependent on assay time. (The estimates in the two previous bullets are given for total assay times of 30-60 minutes, by interpolating results presented for total assay times of between 18 minutes and 4.75 hours.)
- According to these results, manipulated fuel pins with burnup deviations larger than about 20 % and about 40% from expected may be detected in short-cooled and long-cooled PWR fuel, respectively, at total assay times less than 1 hour.

Finally, one should note that the performance of algebraic reconstructions is highly dependent on the fidelity of the system matrix,  $\mathbf{W}$ , as pointed out in section 9.1.2. Accordingly, accurate modeling of the properties of the measurement system is essential for the performance of this type of reconstruction.

## 11.2 USSP Analyses and Results

While SWESP's Objective 2 analysis included determination of isotopic activity as well as calculation of burnup and cooling time on a pin-wise basis in PWR fuels, the USSP analysis focused only on isotopic activity determination in VVER fuels. USSP's analysis included substituted, tampered pins with a burnup lower than the average burnup of the assembly, and considered the effects of pin-wise burnup variation. The USSP's analysis assumptions for Objective 2 are summarized as follows.

- Total assay time - 60 minutes maximum
- Assembly populations - 100 virtual assemblies with  $\pm 20\%$  pin-wise burnup variation
- Image analysis - fuel geometry, composition, and water-channel locations assumed known
- Tampered pins - six locations, one in each VVER radial ring, burnup is 50% of assembly value

The primary performance metric for the USSP analyses is fractional error, relative to the known isotopic activity in each pin of an assembly, for the calculated activity. The fractional error has two components: systematic bias and statistical uncertainty. The bias can be assessed from the mean fractional error for each pin location, over the 100-assembly population; the statistical uncertainty is quantified using the one-sigma error bars associated with those mean values. The statistical uncertainty has two primary components for USSP's Objective 2 analysis: counting-statistics uncertainty associated with the collection efficiency of the tomographer and the total assay time, and uncertainty associated with pin-wise burnup variation, for example the signal cross-talk produced by a high-burnup pin located adjacent to a low-burnup pin that leads to misassignment of activity in the reconstruction process.

The USSP's results for Objective 2 are summarized in the next sections. Predicted performance for PGET and UGET is quantified using VVER fuels with characteristics corresponding to the three implementation scenarios described previously (similar to USSP's Objective 1 analysis).

### 11.2.1 Results: MCNP-based System Matrix for Methods Confirmation

As discussed previously, the USSP's implementation of an MCNP-based system matrix, in the analysis of projection data also simulated by MCNP, had two primary objectives:

- Verify the correctness of the data reduction, analysis and reporting methods
- Illustrate the best-possible performance for a given verification scenario, by analyzing the scenario for which there are no systematic differences between the forward transport calculations (used to generate sinogram data from the true isotopic activity concentrations) and the system matrix (used to translate the sinogram data back into the calculated isotopic activity concentrations).

Note that the application of the MCNP-based system matrix to MCNP-based projection data is used here only for methods confirmation internal consistency checks in the USSP analysis algorithms. As such, the results presented here should not be interpreted as realistic estimates of predicted performance.

Example results for pin-by-pin quantification of  $^{137}\text{Cs}$  and  $^{154}\text{Eu}$  concentration in VVER fuel assemblies, using UGET and an MCNP-based system matrix, are shown in Figure 71. For both isotopes, the mean fractional error for every present- and tampered-in location is 0, aside from minor statistical variation. There is no obvious bias trend from outer to inner pins. As discussed previously, this lack of systematic bias is verification of the analysis mechanics used by PNNL for Objective 2 analysis. The fact that the size of the error bars increases as the radial position of the pin decreases, and that this trend is most notable for the lower-energy 662-keV emission, and is consistent with intuition that self-attenuation reduces the tomographic signal for interior pins versus exterior pins.

PGET was not analyzed using the MCNP-based system matrix because, as described earlier, simulation of pin-by-pin object scatter contributions was not tractable using Monte Carlo methods.

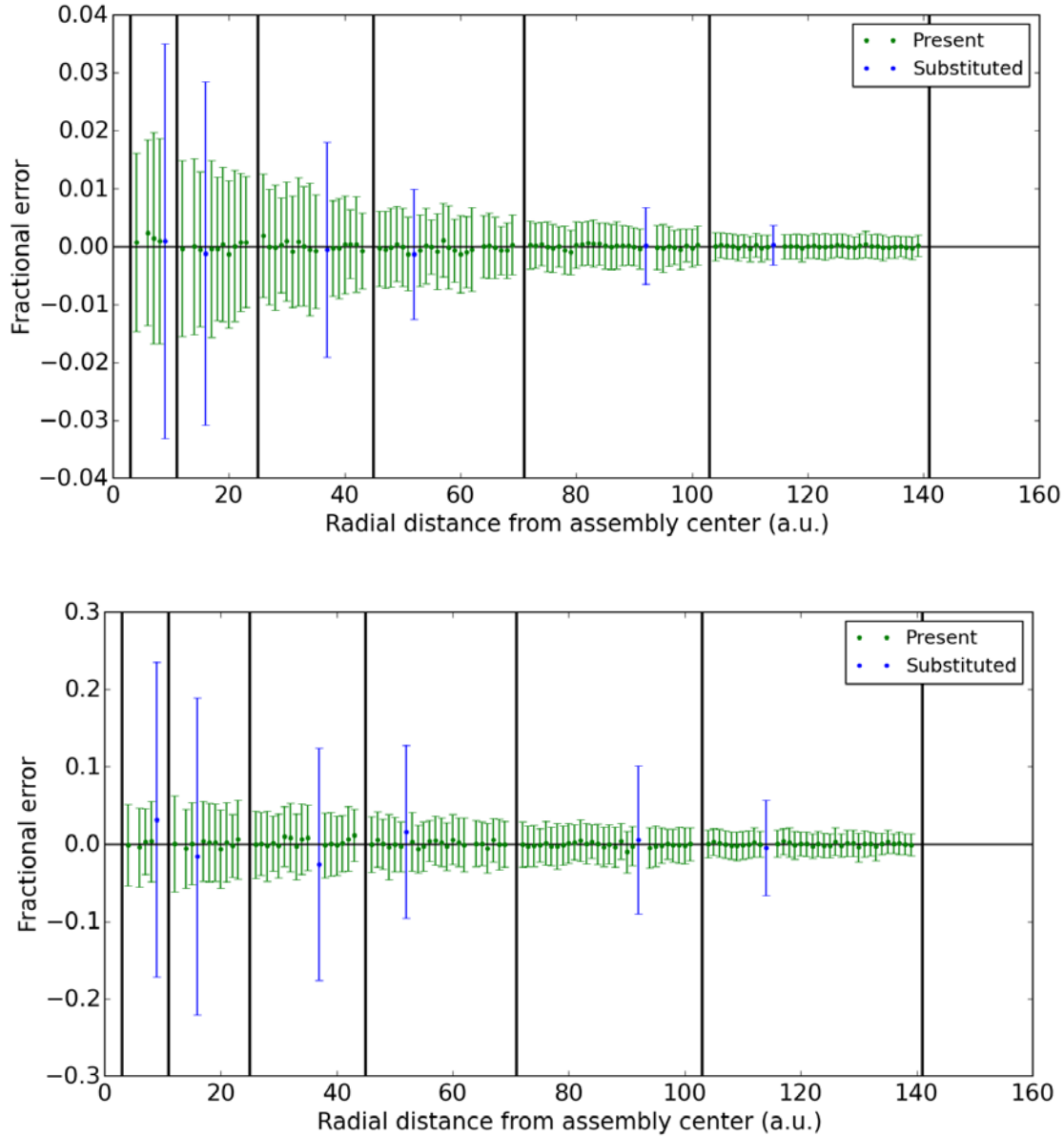


**Figure 71.** Fractional error, relative to true values, for pin-by-pin isotopic activity determination using UGET, PNNL’s algebraic reconstruction method, and MCNP-based system response function. The top pane shows results for  $^{137}\text{Cs}$ , and the bottom pane shows results for  $^{154}\text{Eu}$ . The 100-assembly population assumed VVER fuel with nominal burnup of 20 GWd/MTU, 5-year cooling time, and  $\pm 20$  percent pin-wise burnup variation. Tampered pins (blue), have a nominal activity half that of the present pins (green).

### 11.2.2 Results: RADSAT-based System Matrix

Objective 2 results for pin-by-pin quantification of  $^{137}\text{Cs}$  and  $^{154}\text{Eu}$  concentration, using a RADSAT-based system matrix, for three VVER fuel variants, are shown in Figure 71, Figure 72, and Figure 73. Supporting information for the UGET and PGET results is provided here.

The UGET Objective 2 analysis was based on single-pin sinograms produced from MCNP simulations that approximated the full fuel length using a 2.5-cm active fuel length. As discussed previously, this

active fuel length was selected as a balance between computational time and reduction in the fidelity of the single-pin sinogram data. Because UGET is assumed to be a peak-based spectroscopic device, the effects of object scatter in the sinograms were assumed to be negligible. Therefore, no object scatter was included in the forward MCNP transport calculations—only the uncollided full-energy flux from the key emission lines was simulated. The degree to which coherent scatter effects are included in the MCNP transport, which uses several variance reduction techniques, is not fully understood. The RADSAT system matrix for UGET was calculated from single-pin sinograms produced from deterministic transport calculation of a 50-cm active fuel length (while the MCNP-based forward projections were based on 1.0cm (PGET) or 2.5 cm (UGET), which likely introduces some systematic bias—see Conclusions section). All coherent scatter cross-sections were included in the RADSAT calculations, but the angular distribution on the coherent scatter may be of questionable fidelity (coherent scatter is highly forward peaked) since a relatively low-order quadrature set was employed for coherent reactions. Septal penetration (i.e., gamma rays that enter through the septum for one detector and pass unattenuated through the septum wall into the adjacent detector) was explicitly modeled, for adjacent detector pixels. Consistent with the forward MCNP calculations, only the full-energy gamma-ray flux (i.e., uncollided plus coherent scatter) was used in the definition of the system matrix. For  $^{154}\text{Eu}$ , only the 1275-keV line was incorporated in the system matrix.

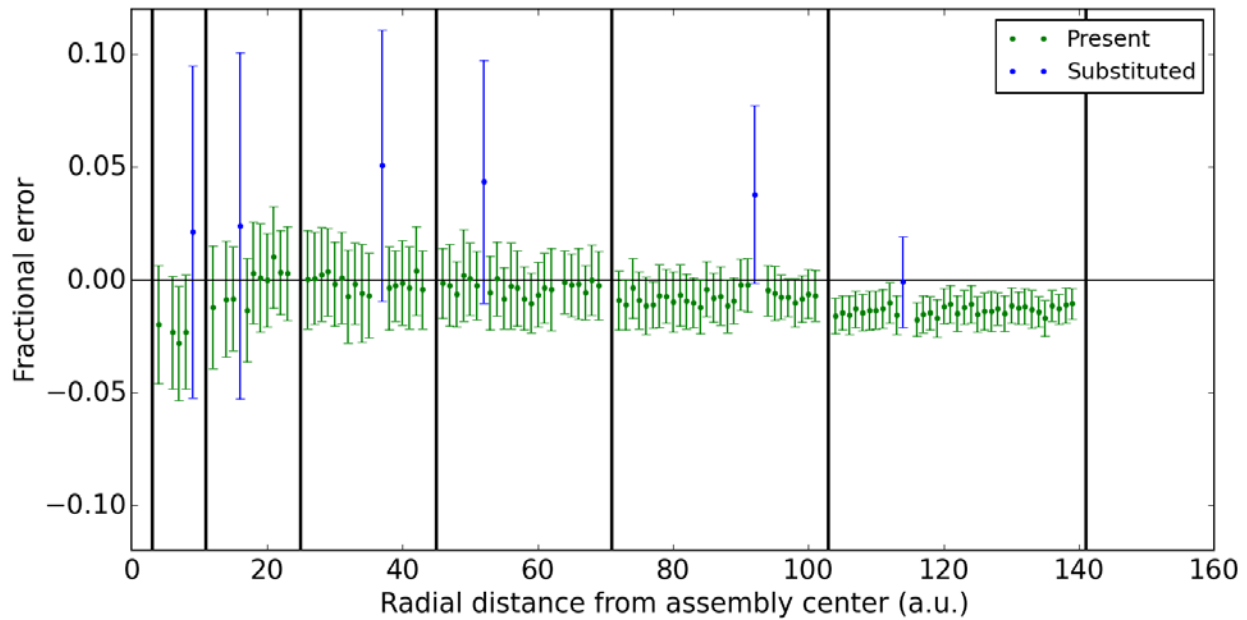


**Figure 72.** Fractional error, relative to true values, for pin-by-pin  $^{154}\text{Eu}$  activity determination using UGET, PNNL’s algebraic reconstruction method, and RADSAT-based system response function. The 100-assembly population assumed VVER fuel with nominal burnup of 40 GWd/MTU, 1-year cooling time, and  $\pm 20$  percent pin-wise burnup variation. Tampered (substituted) pins (blue), have a nominal activity half that of the present pins (green). No results are shown for PGET because the count rates for this high-burnup, short-cooled fuel are too high for that instrument.

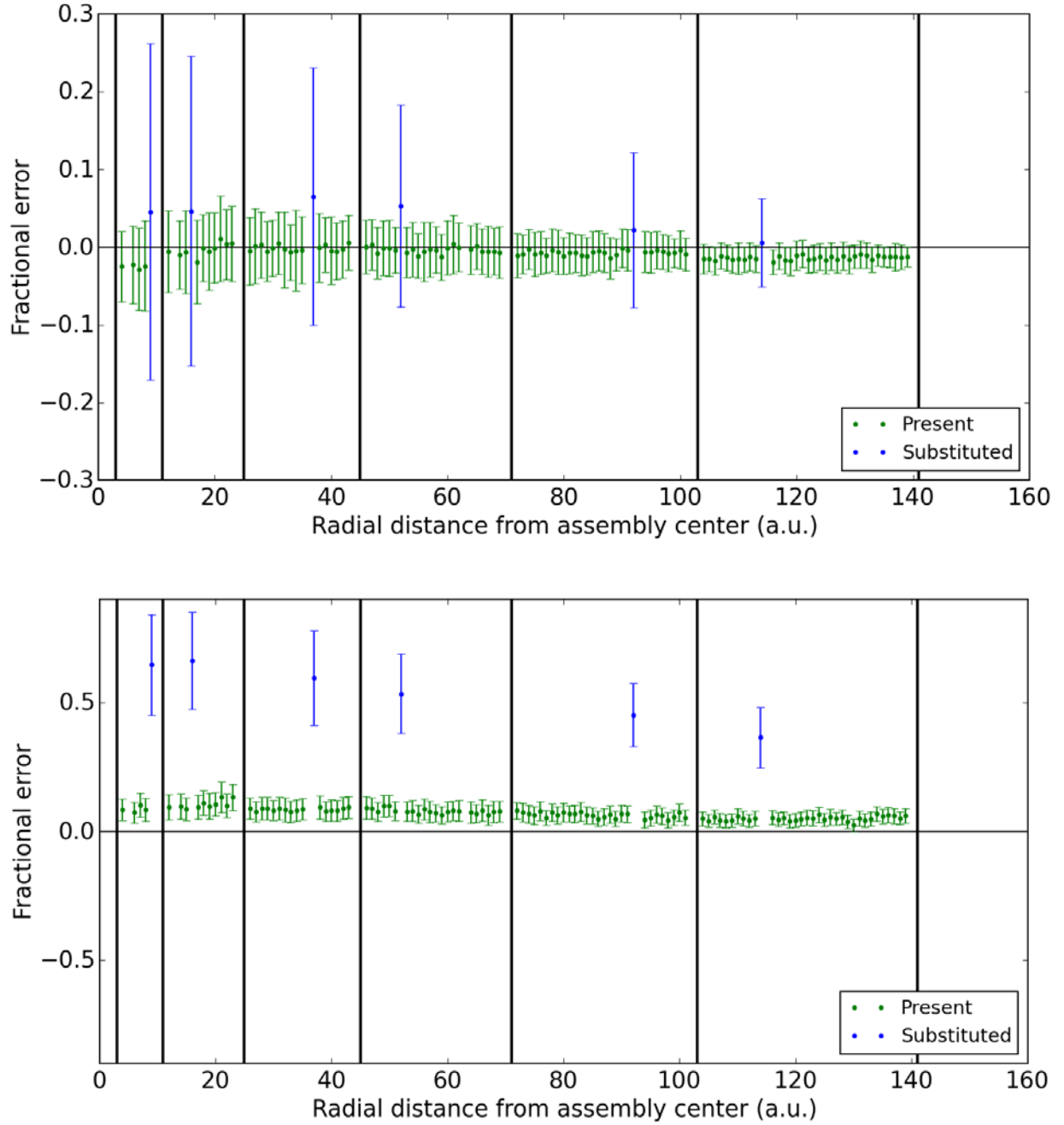


**Figure 73.** Fractional error, relative to true values, for pin-by-pin  $^{154}\text{Eu}$  activity determination using UGET (top panel) and PGET (bottom panel) using PNNL's algebraic reconstruction method and RADSAT-based system response function. The 100-assembly population assumed VVER fuel with nominal burnup of 20 GWd/MTU, 5-year cooling time, and  $\pm 20$  percent pin-wise burnup variation. Tampered pins (blue), have a nominal activity half that of the present pins (green).

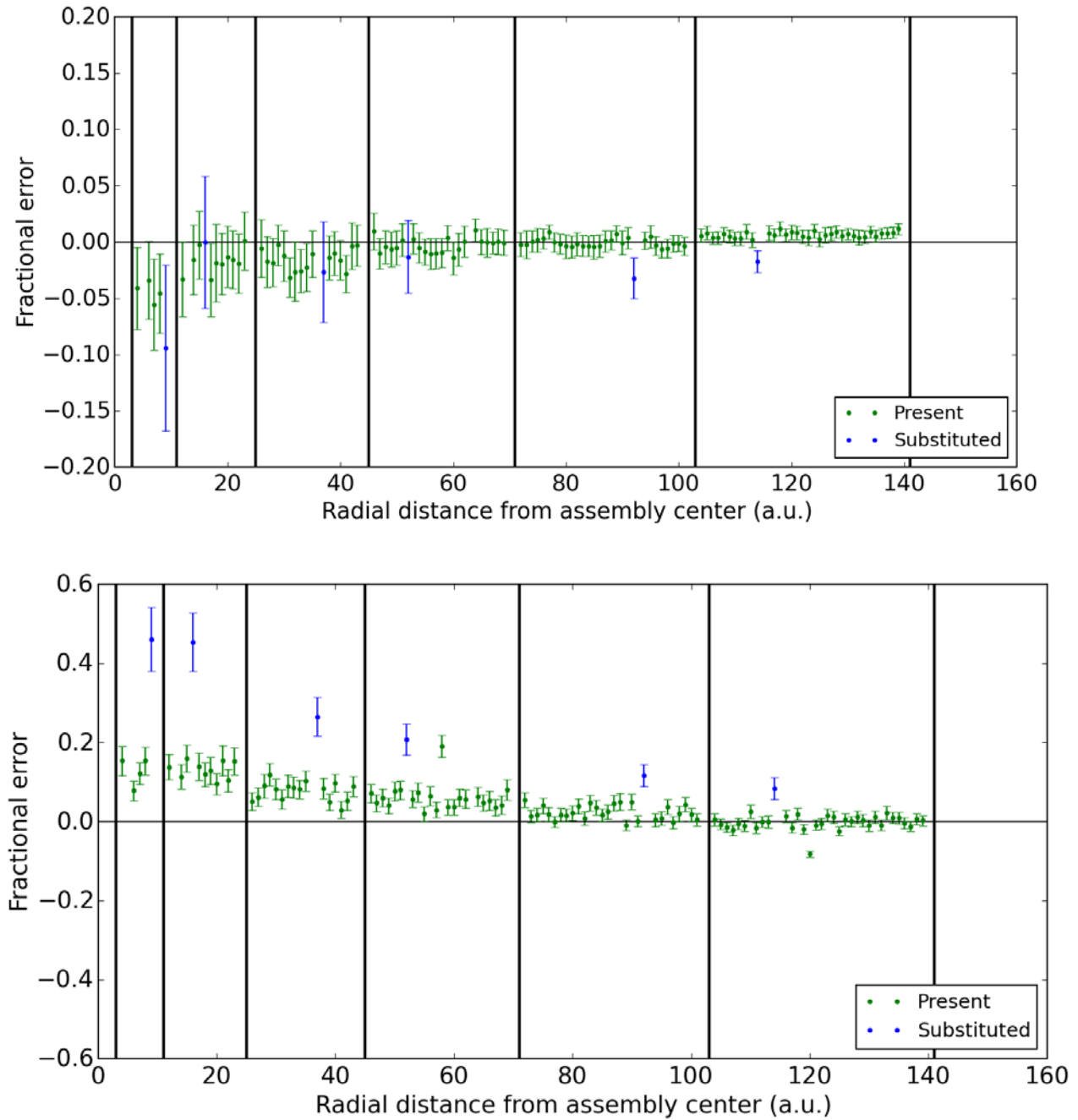


**Figure 74.** Fractional error, relative to true values, for pin-by-pin  $^{137}\text{Cs}$  activity determination using UGET (top panel) and PGET (bottom panel) using PNNL's algebraic reconstruction method and RADSAT-based system response function. The 100-assembly population assumed VVER fuel with nominal burnup of 10 GWd/MTU, 40-year cooling time, and  $\pm 20$  percent pin-wise burnup variation. Tampered pins (blue), have a nominal activity half that of the present pins (green).

The PGET analysis was based on single-pin sinograms produced from MCNP simulations that approximated the full fuel length using a 1.0-cm active fuel length; some questions about potential degrading effects of this relatively short active section remain (see below). Because PGET is generally operated as a broad-ROI, integrating device rather than a peak-based spectroscopic, it was critical to include object scatter in both the forward transport and inverse-problem solution. MCNP single-pin sinograms were based on a combination of the full-energy flux from the key emission lines (as for UGET) and a nominal, assembly-level object-scatter flux. (It was not tractable to simulate single-pin object-scatter contributions, as discussed previously.) As with the UGET MCNP simulations, the degree to which coherent scatter effects are included in the variance reduction techniques, is not fully understood. The RADSAT system matrix was calculated from single-pin sinograms produced from deterministic transport calculation of a 1-cm active fuel length. All coherent scatter cross-sections were included in the RADSAT calculations of the full-energy peak flux, but as discussed above, the angular distribution on the coherent scatter may be of questionable fidelity. No coherent scatter treatment was included in the object-scatter flux. Septal penetration was explicitly modeled but in the name of computational efficiency, by using different approaches for the full-energy uncollided flux and the object-scatter flux. For the former, cross-talk between the nearest five detector pixels on each side of a given detector was calculated. For the latter, only nearest-neighbor effects were included and consequently, the fidelity of the coherent scatter effects in the object-scatter flux may be suspect. For both MCNP and RADSAT, all of the major emission lines were included in the calculations. For  $^{154}\text{Eu}$ , all five prominent lines were explicitly incorporated.

Observations and interpretation for the UGET results on the VVER-440 fuel follow.

- The UGET systematic bias for isotopic activity in present pins is less than 2%, except for the inner-most pin locations where a somewhat larger negative bias arises. PNNL hypothesizes that this inner-pin trend may be an artifact of the different active lengths used in the MCNP and RADSAT calculations. The 2.5-cm active length of the MCNP model may produce an artificially low simulated response, particularly for inner pins where the collimator field of view may be slightly longer. Outer-pin responses tend to be dominated by the nearest-detector response in the weighted least-squares reconstruction process and therefore, the effect is less pronounced.
- The UGET statistical uncertainty for present pins is typically less than 5% (assuming a 60-minute collection time), for both  $^{154}\text{Eu}$  and  $^{137}\text{Cs}$  quantification. Uncertainties increase from outer to inner pins, consistent with expectations based on self-attenuation and nearest-neighbor effects.
- For tampered pins, the UGET performance is marginally degraded from the present pins. The larger systematic bias is likely due to cross-talk where the adjacent present pins produce “shadowing” effects in the lower-activity tampered pins. The shadowing effects may also be the source of significantly higher statistical uncertainty (i.e., larger error bars) for the tampered pins, for example when neighboring present pins have burnup values at the extremes of the pin-wise burnup distribution (e.g., +20% from the nominal burnup value in one neighbor, -20% in another). More investigation of object-scatter effects is needed.

Observations and interpretation for PGET results on the VVER-440 fuel follow.

- The PGET systematic bias for isotopic activity in present pins can exceed 10%, particularly for inner pins. For the  $^{154}\text{Eu}$ , a probable explanation for the relatively high and flat bias across pin locations is a deficient septal penetration model in the system matrix that under-predicts the impact of the object-scatter contributions to neighboring detector pixels. Septal penetration effects are less likely to be a factor for the lower-energy  $^{137}\text{Cs}$  emission at 662 keV, and consistent with that intuition, there is no constant positive bias. However, the steady upward trend in bias from outer to inner pins for 662 keV does indicate a cross-section discrepancy that compounds as the number of attenuation lengths traversed by escaping gamma rays increases. PNNL believes that differences in the coherent scatter treatments in MCNP and RADSAT may be to blame, an effect that will be considerably more



pronounced at 662 keV than at 1275 keV because the coherent scatter cross-section drops steeply with increasing energy.

- The PGET statistical uncertainty for present pins is typically less than 5%, for both  $^{154}\text{Eu}$  and  $^{137}\text{Cs}$  quantification. Uncertainties increase from outer to inner pins, consistent with expectations based on self-attenuation and nearest-neighbor effects.
- For tampered pins, PGET performance is significantly degraded compared to the present pins. The positive bias, as for UGET but somewhat larger, is likely due to shadowing effects from neighboring pins, but the effects are substantially compounded by the broad PGET energy windows—even photons scattering at significant angles can contribute to the shadow effect. Significantly higher statistical uncertainty for the tampered pins is also observed, consistent with the results for UGET. Smaller energy windows, for example 630-680 keV instead of 400-700 keV for  $^{137}\text{Cs}$  may help to reduce the systematic bias in the application of PGET to Objective 2, and also to reduce the statistical uncertainties associated with pin cross-talk, but the counting-statistics contributions would increase when using smaller ROIs. More investigation of object-scatter effects, as a function of energy-window width in PGET, is needed.

## 12.0 Conclusions

As documented in this report, a team comprised of multiple Member State Support Programs, the IAEA and Euratom Safeguards has successfully completed JNT 1955 Phase I, a viability analysis of gamma-ray tomography for spent-fuel verification applications. Tasks undertaken in the project include:

- Definition of high-priority IAEA fuel verification objectives and implementation scenarios to guide the scope and evaluation metrics of the viability analysis.
- Definition of a nominal universal GET design (UGETv1) capable of spanning all of the verification objectives and implementation scenarios assumed in this study, and based on commercially available hardware. The design is intended to be adaptable to both attended and unattended applications.
- Monte Carlo modeling of GET responses over a wide range of fuel types and fuel properties encountered in IAEA applications, and verification of these modeled responses using code-to-code comparisons and available field measurements.
- Implementation and preliminary evaluation of candidate tomographic reconstruction algorithms capable of incorporating a range of *a priori* information about the object model used in the reconstruction. Emphasis was placed on non-proprietary algorithms and codes that facilitate long-term maintenance and enhancement by the IAEA.
- Quantitative assessment of predicted performance for Objective 1, independent pin counting for verification of item integrity. Predicted performance for the UGETv1 and Ideal PGET designs was compared.
- Preliminary viability assessment of gamma-ray tomography for Objective 2, verification of pin-by-pin characteristics, and detection of anomalies. Potential UGETv1 and Ideal PGET performance was explored using various assumptions and analysis methods.

### *Key Findings and Messages*

- GET has the potential to provide bias-defect sensitivity in most fuel verification scenarios, a significant improvement over IAEA's current partial-defect capabilities using a Fork-based system or digital Cerenkov viewing device.
- A Universal GET design is capable of supporting the full range of fuel characteristics considered in this study, but that versatility comes at a price in terms of both assay time and instrument lifecycle cost. The lifecycle cost of the first four-head UGETv1 analyzed in this study is estimated at about 800k€ of which ~380k€ is for purchase of components, ~220k€ is for engineering and fabrication, and 200k€ is for software development. Subsequent units are estimated to cost approximately 550k€ due to reduced engineering and software development costs. A UGET variant design only for longer-cooled (i.e., greater than a few years) fuel could be significantly lighter and lower cost.
- Ideal PGET and UGETv1 provide similar performance for Objective 1, the detection of single missing pins, but PGET achieves that sensitivity in shorter total assay times. However, PGET is not viable for short-lived fuels due to high count rates that are well beyond the limits of even the most capable pulse-processing electronics for room-temperature semiconductors.
- Predicted performance for Ideal PGET is lower than for UGETv1 for Objective 2, pin-by-pin isotopic quantification, primarily because large scatter contributions in PGET's wide energy windows perturb a relatively small full-energy peak signal. Modifications to the data acquisition parameters for PGET

(e.g., narrower energy windows) could offer improvements in Objective 2 performance for PGET, but more study is needed to quantify this potential.

- Efforts were made to assess the performance of various reconstruction techniques for the UGETv1 design. Among the conclusions drawn for Verification Objective 1 were that algebraic reconstruction, including modeling of a system's intrinsic response function and uniform "black-box" attenuation, gave the most promising results in terms of separation between fuel rods and background for detection of missing pins. In terms of methodology, this approach may be viewed as between the baseline Objective 1 and Objective 2 methodologies. Further exploration of this and other potential "Objective 1.5" approaches that focus on missing-pin detection is recommended.
- Procedures and tools have also been presented for Verification Objective 2, where the *a priori* known fuel geometry is used to perform detailed algebraic modeling of the gamma-ray transport through the fuel and thus to enable conclusive analysis of its pin-wise contents of gamma emitters. The position of the fuel assembly in the measuring device is required, which may be determined by means of image analysis using a basic tomographic image and the *a priori* known fuel geometry. Such tools have previously been experimentally demonstrated to produce percent-level precision for BWR fuel, and their predicted capacity for determining pin-wise fuel properties also in other fuel types has been investigated in this work. (One may also consider that the fuel geometry could be determined by identifying individual fuel rods in basic tomographic images, by means of image analysis without using any *a priori* information on the fuel geometry, and building a model on this geometry. In terms of methodology, this approach may be viewed as between the baseline Objective 1 and Objective 2 methodologies. Further exploration of this and other potential "Objective 1.5" approaches that focus on missing-pin detection is recommended as a potential next step.)
- The modeling and analysis framework developed for Phase I provides end-to-end capability to assess tomographer performance for nuclear fuel assay, and could be considered a new, standing capability for the international safeguards community. The library of simulated and measured projection data for a variety of fuel types could be a resource for continuing GET study. Because much of the framework was developed in a modular fashion, portions of it (e.g., specific image analysis and image reconstruction algorithms) can be extracted for specific purposes. It should be noted, however, that there has been no effort to integrate, harden, and interface the software components. Additional development work would be needed to support field application by safeguards inspectors.
- Informed by prior work and the findings of this study, possible inspection procedure for GET-based verification of spent fuel was developed. The first set of analyses would include a baseline measurement and analysis of the assembly assuming no *a priori* information about the fuel, and would provide an initial finding about the integrity of the assembly (i.e., evidence of missing pins), as well as an assertion about the fuel assembly geometry (based on the tomographic image). If undeclared removal or substitution is suspected, a second analysis, focused on calculating the pin-by-pin characteristics (e.g., isotopic activity or cooling time) and utilizing fuel assembly geometry information (inferred or declared) could be performed—with no additional measurement required.

#### *Important Assumptions and Caveats*

- The Ideal PGET analyzed in this study assumes perfect collection efficiency and energy calibration across all 208 CdTe detectors. The current design of the PGET pulse processing electronics cannot support this kind of high-fidelity calibration, but an ongoing project to refurbish and improve PGET's data acquisition system is expected to close the gap between the actual instrument and the idealized response simulated in this study. Further study, using measured responses from the refurbished PGET, could illuminate on the realistic performance of the device.

- The UGETv1 collimator design is likely overly conservative, based on recent analysis and additional inquiry into the count rates that can be accurately managed by commercially available pulse-processing electronics. A UGET collimator design with a larger field of view (e.g., in vertical direction) would increase sensitivity and produce incremental improvement to the performance reported here for both Objective 1 and Objective 2. As with the Ideal PGET analysis, the UGETv1 analysis assumes perfect absolute efficiency and energy calibration across all detectors. It is presumed that a system based on relatively few spectrometers with relatively high peak efficiency and energy resolution, each with a dedicated multi-channel analyzer, could provide high-fidelity energy and efficiency calibrations, but the degree to which an actual UGETv1 could approach the assumption of perfection in this study is not known.
- The MCNP simulations at the heart of this study, in order to make the computational times tractable, included approximations and variance reduction techniques. While it is expected that the effects of these approximations on the high-level conclusions are negligible, they are noted here for completeness and transparency. First, the scaling of response from short active fuel lengths (1.0 cm and 2.5 cm were for PGET and UGET, respectively) to approximate response in the full field of view likely creates systematic bias for some projection angles and pin positions. Second, object scatter was completely ignored in UGET analysis due to the very tight degree of collimation and peak-based spectroscopic analysis methods. Third, coherent scatter (most prominent for energies below 1 MeV) was not fully accounted for in the transport calculations. The effects of these approximations are most likely to be important for Objective 2 analysis.
- The level of fidelity of the simulation-based performance predictions from this study is not fully understood, due to a relatively limited set of empirical data on which to validate, the significant effects of algorithm performance on overall performance, and the complexity of the tomographic analysis process. It is expected that real-world effects may degrade actual field performance from the values presented here but it is also possible that algorithms tailored to the IAEA verification needs can realize performance improvements.

### *Potential Next Steps*

The modeling and analysis framework, and the findings presented in this report, provide a solid foundation on which to base continued exploration of GET for IAEA verification needs. Clear to the JNT 1955 team is that additional development, both on hardware and software, will be needed to realize the potential of tomography for safeguards verification challenges. Recommendations for further study and development include:

- Additional study of the so-called Objective 1.5 approach with the following characteristics: focused on missing-pin detection; requires no declared information about the assembly; incorporates knowledge about the GET design and uniform attenuation characteristics in the fuel region to produce an initial reconstructed image; executes image analysis on the initial image to determine the current fuel geometry; uses the derived fuel geometry to model the gamma-ray transport in detail in conclusive rod-activity reconstructions; and identifies possible anomalies based on measured rod-wise contents of one or several gamma-ray emitters.
- Further study of how different reconstruction and analysis algorithms perform is needed, to inform decisions about the potential of GET for various verification scenarios.
- Refinement of the MCNP-based modeling approach and some of the variance-reduction assumptions, particularly the choice of active-fuel lengths used in the forward transport of projection data.
- Continued study of UGET performance for a design with a less-restrictive collimator and that takes full advantage of filters and high-rate pulse-processing electronics to manage count rate. It is expected

that assay times could be significantly reduced from those presented for UGETv1 in this report, under these revised assumptions. It is also possible that UGETv1 performance could be improved via methods that were outside the scope of this project, for example alternative data collection geometries (i.e., irregular angular sampling) intended to extract more information from interior pins.

- Continued study of deterministic transport approaches that can efficiently and accurately capture both primary and object-scatter contributions to the system response function—key attributes for high-fidelity algebraic reconstruction. This challenge is particularly acute when broad energy windows are used in the data collection (e.g., with current PGET device). The potential benefits of using narrower energy windows could also be considered using advanced transport methods.
- Improve the fidelity of the burnup variation distributions for each fuel type (in this work, uniform  $\pm 20\%$  for all fuel types), including possible outliers related to, for example, burnable poisons, and assess the potential impact of those new assumptions on analysis for Objectives 1, 1.5 and 2.
- Continue to evolve image registration, pin scoring and analysis algorithms toward the actual needs of GET-based field verification by the IAEA, and in a software form suitable for inclusion in the IAEA's evolving GET toolbox.

## 13.0 References

- Agostinelli A. et al. 2003. "Geant4-a simulation toolkit." *Nuclear Instruments and Methods in Physics Research Section A*, 506:250–303. DOI: [10.1016/S0168-9002\(03\)01368-8](https://doi.org/10.1016/S0168-9002(03)01368-8)
- Baird B. 2013. "Quantitative analysis of the fission product distribution in a damaged fuel assembly using gamma-spectrometry and computed tomography for the Phebus FPT3 test." *Nuclear Engineering and Design*, 262:469-483.
- Berndt R, C Rovei, T Honkamaa, A Turunen, F Levai, L DiCesare, P Timossi, and R Covini. 2012. "Passive gamma emission tomography for spent nuclear fuel. Test in the ESSOR spent fuel pond at JRC, Ispra," JRC Scientific and Policy Reports, Joint Research Centre, Ispra, Italy.
- Caruso S and F. Jatuff. 2014. "Design, development and utilization of a tomography station for  $\gamma$ -ray emission and transmission analysis of light water reactor spent fuel rods." *Progress in Nuclear Energy*, 72:49-54.
- Caruso S. 2007. "Characterization of High-Burnup LWR Fuel Rods through Gamma Tomography," doctoral thesis from the Polytechnical University of Lausanne, France.
- Davour A, S Jacobsson Svärd, P Andersson, S Grape, S Holcombe, P Jansson and M Troeng. 2016. "Applying image analysis techniques to tomographic images of irradiated nuclear fuel assemblies." *Annals of Nuclear Energy* DOI: [10.1016/j.anucene.2016.05.024](https://doi.org/10.1016/j.anucene.2016.05.024)
- Davour A, S Jacobsson Svärd, and S. Grape. 2015. "Image analysis methods for partial defect detection using tomographic images on nuclear fuel assemblies." 2015 ESARDA Symposium, Manchester, UK.
- Galloway JD, HR Trellue, ML Fensin, and BL Broadhead. 2012. "Design and Description of the NGSI Spent Fuel Library with an Emphasis on Passive Gamma Signal." *Journal of Nuclear Materials Management*, 40(3): 25.
- Hakimabad HM, H Panjeh, and A Vejdani-Noghreian. 2007. "Response Function of a 3×3 in. NaI Scintillation Detector in the range of 0.081 to 4.438 MeV." *Asian Journal of Experimental Sciences*, 21(2): 233-237.
- Holcombe S, S Jacobsson Svärd, and L Hallstadius. 2015. "A novel gamma emission tomography instrument for enhanced fuel characterization capabilities within the OECD Halden Reactor Project." *Annals of Nuclear Energy*, (85):837–845.
- Holcombe S, K Eitrheim, and S Jacobsson Svärd. 2012. "Advanced fuel assembly characterization capabilities based on gamma tomography at the Halden Boiling Water Reactor." International Conference on the Physics of Reactors (PHYSOR), Knoxville, Tennessee, USA, April 15-19, 2012.
- Honkamaa T, F Levai, A Turunen, R Berndt, S Vaccaro, and P Schwalbach. 2014. "A Prototype for passive gamma emission tomography." 2014 IAEA Safeguards Symposium.

- Hu J, I Gauld, V Mozin, S Tobin, S Vaccaro, U Backstrom, A Sjöland, A Worrall. 2016. “High-Fidelity Modeling of Spent Fuel Assemblies for Advanced NDA Instrument Testings.” *Nuclear Instruments and Methods in Physics Research Section A* (accepted for print).
- Humphrey MA, SJ Tobin, and KD Veal. 2012. “The Next Generation Safeguards Initiative’s Spent Fuel Nondestructive Assay Project.” *Journal of Nuclear Materials Management*, 40(3):6.
- IAEA - International Atomic Energy Agency. 2013. *IAEA Department of Safeguards Long-Term R&D Plan, 2012-2023*. STR-375. International Atomic Energy Agency, Vienna, Austria.
- IAEA - International Atomic Energy Agency. 2010. *Model Integrated Safeguards Approach for a Spent Fuel Encapsulation Plant*. SG-PR-1305. International Atomic Energy Agency, Vienna, Austria.
- IAEA - International Atomic Energy Agency. 2009. *Special Criteria for Difficult-to-Access Fuel Items*. SG-GC-Annex-04. International Atomic Energy Agency, Vienna, Austria.
- IAEA - International Atomic Energy Agency. 2006. *International Atomic Energy Agency, Integrated Safeguards for Spent Fuel Transfers to Dry Storage*. SG-OP-GRNL-PL-0019. International Atomic Energy Agency, Vienna, Austria.
- Jacobsson S, C Andersson, A Håkansson, and A Bäcklin. 2001a. “A Tomographic Method for Verification of the Integrity of Spent Nuclear Fuel Assemblies - I: Simulation Studies.” *Nuclear Technology*, 135(2):131-145.
- Jacobsson S, A. Håkansson, P. Jansson, and A. Bäcklin. 2001b. “A Tomographic Method for Verification of the Integrity of Spent Nuclear Fuel Assemblies - II: Experimental Investigation.” *Nuclear Technology*, 135(2):146-153.
- Jacobsson S, A Bäcklin, A Håkansson, and P. Jansson. 2000. “A tomographic method for experimental verification of the integrity of spent nuclear fuel.” *Applied Radiation and Isotopes*, 53(4-5):681-689.
- Jacobsson S, A Håkansson, C Andersson, P Jansson and A Bäcklin. 1998. *A Tomographic Method for Verification of the Integrity of Spent Nuclear Fuel*. Report 98:17, ISSN 1104-1374, ISRN SKI-R-98/17-SE, Swedish Nuclear Power Inspectorate, Stockholm, Sweden.  
[http://www.iaea.org/inis/collection/NCLCollectionStore/\\_Public/29/032/29032968.pdf](http://www.iaea.org/inis/collection/NCLCollectionStore/_Public/29/032/29032968.pdf)
- Jacobsson S. 1996. “Theoretical Investigations of Tomographic Methods used for Determination of the Integrity of Spent Nuclear Fuel.” MSc Thesis, Uppsala University.
- Jacobsson Svärd S, S Holcombe, and S Grape. 2015a. “Applicability of a set of tomographic reconstruction algorithms for quantitative SPECT on irradiated nuclear fuel assemblies.” *Nuclear Instruments and Methods in Physics Research Section A*, 783:128–141.
- Jacobsson Svärd S, P Andersson, A Davour, S Grape, S Holcombe, and P Jansson. 2015b. “Tomographic determination of spent fuel assembly pin-wise burnup and cooling time for detection of anomalies.” 2015 ESARDA Symposium, Manchester, UK,
- Jacobsson Svärd S, A Håkansson, A Bäcklin, P Jansson, O Osifo, and C Willman. 2006. “Tomography for partial-defect verification - experiences from measurements using different devices.” *ESARDA Bulletin*, 33:15-25.

- Jacobsson Svärd S, A Håkansson, A Bäcklin, O Osifo, C Willman, and P Jansson. 2005. "Non-destructive Experimental Determination of the Pin-power Distribution in Nuclear Fuel Assemblies." *Nuclear Technology*, 151(1):70-76.
- Jacobsson Svärd S. 2004. "A Tomographic Measurement Technique for Irradiated Nuclear Fuel Assemblies." PhD thesis, Uppsala University, Sweden. Retrieable at <http://urn.kb.se/resolve?urn=urn:nbn:se:uu:diva-4227>.
- Jansson P, S Grape, S Tobin, and H Liljenfeldt. 2014. "Experimental Comparison between High Purity Germanium and Scintillator Detectors for Determining Burnup, Cooling Time and Decay Heat of Used Nuclear Fuel." In *Proceedings of the 40<sup>th</sup> annual Waste Management (WM) Conference, Phoenix, Arizona, USA, March 2014*. <http://urn.kb.se/resolve?urn=urn:nbn:se:uu:diva-220908>
- Jansson P, S Jacobsson Svärd, S Grape, and A. Håkansson. 2013. "A laboratory device for developing analysis tools and methods for gamma emission tomography of nuclear fuel." 2013 ESARDA Symposium, Bruges, Belgium.
- Jansson P, S Jacobsson Svärd, A Håkansson, A Bäcklin. 2006. "A Device for Non-destructive Experimental Determination of the Power Distribution in Nuclear Fuel Assemblies." *Nuclear Science and Engineering*, 152(1):76 86.
- Jansson P. 2002. "Studies of Nuclear Fuel by Means of Nuclear Spectroscopic Methods." PhD thesis, Uppsala University, Sweden. Retrieable at <http://urn.kb.se/resolve?urn=urn:nbn:se:uu:diva-2057>.
- JNT 1955. 2013. UGET Collaboration, "JNT 1955 Work Plan", May 2013.
- Kak AC and M Slaney. 1988. *Principles of Computerized Tomographic Imaging*, IEEE Press, ISBN 0-85274-349-1, Piscataway, NJ.
- Lawson C and RJ Hanson R.J. 1987. *Solving Least Squares Problems*. Society for Industrial and Applied Mathematics, Philadelphia, PA.
- Lévai F, T Honkamaa, M Moring, M Mayorov, S Vaccaro, V Kondratjev, V Kruglov . 2014. *Evaluation of an exercise on testing the Prototype Tomographic system at the VVER NPP Lovisa*. Interim report, Hungarioan Support Program.
- Lévai F, M Tarvainen, T Honkamaa, J Saarinen, S Jacobson, A Rialhe, and R Arlt. 2002. *Feasibility of gamma emission tomography for partial defect verification of spent LWR fuel assemblies*. STUK-YTO-TR-189, Task JNT A1201, Säteilyturvakeskus (Radiation and Nuclear Safety Authority [STUK]), Helsinki, Finland.
- Lévai F, S Dési, M Tarvainen, and R Arlt. 1993. Use of high energy gamma emission tomography for partial defect verification of spent fuel assemblies. Final report on Task FIN A98 of the Finnish Support Programme to IAEA Safeguards. STUK-YTO-TR 56. Säteilyturvakeskus (Radiation and Nuclear Safety Authority [STUK]), Helsinki, Finland.
- Lundqvist T, S Jacobsson Svärd, A Håkansson, and A Bäcklin. 2010. "Recent Progress in the Design of a Tomographic Device for Measurements of the Three-Dimensional Pin-Power Distribution in Irradiated Nuclear Fuel Assemblies." *Nuclear Science and Engineering*, 165(2):232-239.



- Lundqvist T, S Jacobsson Svärd, and A Håkansson. 2007. "SPECT imaging as a tool to prevent proliferation of nuclear weapons," *Nuclear Instruments and Methods in Physics Research A*, 580(2):843-847.
- Metz CE. 1978. "Basic Principles of ROC Analysis." *Seminars in Nuclear Medicine*, 8(4):283-298.
- Mozin V, A. Hunt, B. Ludewigt, L. Campbell. 2012. *Delayed Gamma-Ray Spectroscopy for Spent Nuclear Fuel Assay*, Journal of Nuclear Materials Management 40, 78.
- Mozin V and S Tobin. 2010. *DGSDEF: Discrete Gamma-ray Source DEFINition code*. LA-CC-10-083. Los Alamos National Laboratory, Los Alamos, New Mexico.
- Niculae C and T Craciunescu. 1996. "On the reconstruction of the fission product distribution in nuclear fuel rods." *International Journal of Energy Research*, 20:999-1002.
- Quarati F, AJJ Bos, S Brandenburg, C Dathy, P Dorenbos, S Kraft, RW Ostendorf, V Ouspenski, and A Owens. 2007. "X-ray and gamma-ray response of a 2"×2" LaBr<sub>3</sub>:Ce scintillation detector." *Nuc. Inst. & Meth.* A574:115–120.
- Pelowitz DB. 2008. *MCNPXTM User's Manual. Version 2.6.0*. NM LA-CP-07-1473 Los Alamos National Laboratory, Los Alamos, New Mexico.
- Richter M and P Siffert. 1992. "High resolution gamma ray spectroscopy with CdTe detector systems." *Nuc. Inst. & Meth.* A322:529–537.
- Sawicka BD and BJF Palmer. 1988. "Density gradients in ceramic pellets measured by computed tomography." *Nuclear Instruments and Methods in Physics Research Section A*, 263:525-528.
- SCALE. 2009. *SCALE: A Modular Code System for Performing Standardized Computer Analyses for Licensing Evaluation, Version 6, Vols. I–III*, TN ORNL/TM-2005/39. Oak Ridge National Laboratory, Oak Ridge, Tennessee.
- Shaver MW, LE Smith, RT Pagh, EA Miller, and RS Wittman. 2009. "The Coupling of a Deterministic Transport Field Solution to a Monte Carlo Boundary Condition for the Simulation of Large Gamma-Ray Spectrometers." *Nuclear Technology* 168(1):95-100.
- Smith LE, list other authors. 2008. "Deterministic Transport Methods for the Simulation of Gamma-Ray Spectroscopy Scenarios," In *2006 IEEE Nuclear Science Symposium Conference Record*, vol. 1, pp. 588-592. IEEE, 2006.
- Sokolov A, V Kondratjev, V Kourlov, F Levai, and T Honkamaa. 2008. "CdTe Linear Arrays with Integrated Electronics for Passive Gamma Emission Tomography System." *2008 IEE Nuclear Science Symposium Conference Record*. N02-221, pp. 999-1002.
- Trellue HR, ML Fensin, JR Richard, J Galloway, and JL Conlin. 2011. Description of the Spent Nuclear Fuel Used in the Next Generation Safeguards Initiative to Determine Plutonium Mass in Spent Fuel. LA-UR 11-00300, Los Alamos National Laboratory, Los Alamos, New Mexico.
- Tretiak OJ and C Metz. 1980. "The exponential Radon transform". *SIAM J. Appl. Math.* 39:341–354.

- Troeng M. 2004. *Positioning of Nuclear Fuel Assemblies by Means of Image Analysis on Tomographic Data*, MSc Thesis, ISSN 1401-5749, Uppsala University, Uppsala, Sweden.
- Vaccaro S, S Tobin, A Favalli, B Grogan, P Jansson, H Liljenfeldt, V Mozin, J Hu, P Schwalbach, A Sjöland, H Trellue and D Vo. “PWR and BWR spent fuel assembly gamma spectra measurements,” *Nuclear Instruments and Methods in Physics Research Section A*, 833: 208-225.
- White TA, S Jacobsson-Svard, LE Smith, VV Mozin, P Jansson, A Davour, S Grape, H Trellue, NS Deshmukh, RS Wittman, T Honkamaa, S Vaccaro, and JH Ely. 2015. “Passive Tomography for Spent Fuel Verification: Analysis Framework and Instrument Design Study.” ESARDA Symposium, Manchester, UK.
- White, T, LE Smith, V Mozin, N Deshmukh, R Wittman. 2014. “Gamma-Ray Emission Tomography for Spent Fuel Assay: Modeling and Performance Evaluation Methods.” In *Proceedings of the INMM 55th Annual Meeting*, Atlanta, Georgia.
- Willman C, A Håkansson, O Osifo, A Bäcklin and S Jacobsson Svärd. 2006. “Nondestructive assay of spent nuclear fuel with gamma-ray spectroscopy,” *Annals of Nuclear Energy*, 33(5):427–438.
- Wilson WB, ST Cowell, TR England, AC Hayes, and P Moller. 2008. *A Manual for CINDER’90 Version 07.4 Codes and Data*. Manual LA-UR-07-8412. Los Alamos National Laboratory, Los Alamos, New Mexico.
- Yokoi T, H Shinohara, T Hashimoto, T Yamamoto and Y Niio. 2000. “Implementation and Performance Evaluation of Iterative Reconstruction Algorithms in SPECT: A Simulation Study Using EGS4,” In *Proceedings of the Second International Workshop on EGS, Tsukuba, Japan*, KEK Proceedings 200 20:224-234.

## Appendix A

### Tabular Overview of Modeling and Analysis Framework

A tabular overview of data and products from the modeling and analysis framework, including fuel type, tomographer design, forward transport method, reconstruction technique and analysis technique, is provided here.

**Table APX A.1.** Overview of Modeling and Analysis Framework.

<b>OBJECTIVE 1</b>					
	<b>BU/CT</b>	<b>Tomographer Design</b>	<b>Forward Modeling</b>	<b>Reconstruction Technique</b>	<b>Analysis Technique</b>
<b>USSP</b>					
BWR 10x10	40 / 1	UGET	Single-pin MCNP sinograms  +  Full- assembly MCNP scatter sinogram (PGET only)  (USSP)	Filtered back-projection	ROC
	20 / 5	PGET / UGET			
	10 / 40	PGET / UGET			
VVER-440	40 / 1	UGET			
	20 / 5	PGET / UGET			
	10 / 40	PGET / UGET			
PWR 17x17	40 / 1	UGET			
	20 / 5	PGET / UGET			
	10 / 40	PGET / UGET			
BWR 10x10 (SVEA-96)	<1 yr CT	PLUTO <sup>1</sup>	real <sup>140</sup> Ba/La data  +  Full assembly calculated <sup>140</sup> Ba/La	Filtered back-projection	Benchmark

<b>OBJECTIVE 1</b>					
	<b>BU/CT</b>	<b>Tomographer Design</b>	<b>Forward Modeling</b>	<b>Reconstruction Technique</b>	<b>Analysis Technique</b>
			projection data		
VVER-440 (Loviisa NPP)	43.5 / 44	PGET <sup>1</sup>	real data + Full assembly calculated <sup>140</sup> Ba/La projection data	Filtered back- projection	Benchmark
<b>SWESP</b>					
BWR 10x10 (SVEA-96)		PLUTO	Full assembly MCNP with uniform pin-to-pin <sup>137</sup> Cs (SWESP)	Pixel-based algebraic reconstruction with uniform attenuation	Automated pin location and intensity calculation
	<1 yr CT	PLUTO <sup>1</sup>	(real <sup>140</sup> Ba/La data)	Pixel-based algebraic reconstruction with uniform attenuation	
BWR 8x8	35 / 32	PGET <sup>1</sup>	(real data)	Pixel-based algebraic reconstruction with uniform attenuation	Automated determination of fuel displacement from center
VVER-440 (Loviisa NPP)		PGET <sup>1</sup>			
PWR 17x17	40 / 1	UGET	Single-pin MCNP sinograms  (USSP)	Pixel-based algebraic reconstruction with uniform attenuation	Automated pin location and intensity calculation

<sup>1</sup> Analysis of measured data set

OBJECTIVE 2					
	BU/CT	Tomographer Design	Forward Model	Inverse Model	Analysis
USSP					
VVER-440	20 / 5	UGET	Single-pin MCNP sinograms (USSP)		Demonstrate reconstruction when forward and inverse models are consistent
	40 / 1	UGET	Single-pin MCNP sinograms  +  Full- assembly MCNP scatter sinogram (PGET only) (USSP)	Pin-wise deterministic transport for both primary and object-scatter fluxes (USSP)	Relative pin activity
	20 / 5	UGET / PGET			
	10 / 40	UGET / PGET			
PWR 17x17		UGET	Single-pin MCNP sinograms  +  Full- assembly MCNP scatter sinogram (USSP)		
SWESP					
BWR 10x10 (SVEA-96)	<sup>137</sup> Cs, uniform activity	PLUTO	Full assembly MCNP (SWESP)	Pin-based deterministic model for primary flux (SWESP)	Relative pin activity
PWR 17x17	40 / 1	UGET	Single-pin MCNP sinograms (uniform BU) (USSP)		Relative pin activity for 10 assemblies x 3 isotopes  +  BU / CT calculations
	10 / 40	UGET			Relative <sup>137</sup> Cs activity for 3 assay times

Notes on simulations and methods:

1. MCNP-based single-pin sinograms (USSP)
  - a. Basis for comparative evaluations for Ideal PGET and UGETv1, Objectives 1 and 2
  - b. 1-cm axial extent of gamma-ray source in fuel simulated for PGET with a scaling factor to account for the actual field of view. Subset of calculations completed for the 28-cm axial source extent.
  - c. 2.5-cm axial source extent for UGET
  - d. Object-scatter included in transport runs, but data only reported for a narrow energy bin corresponding to primary gamma-ray energy
  - e. Used to create variable-BU sinograms for spectroscopic GET systems (for which it is assumed that a photopeak can be extracted from the continuum) and to create the scatter-free component of sinograms to which a scatter model is added for non-spectroscopic systems (PGET)
2. MCNP-based full-assembly sinograms (uniform activity) (USSP)
  - a. Used for Ideal PGET analysis only
  - b. 1-cm axial source extent, subset of calculations with 28-cm source extent.
  - c. Full object-scatter terms, reported in variable-width energy bins across the spectrum
  - d. Uses for PGET analysis:
    - i. Create full sinogram data for specific burn-ups or to match measurements
    - ii. Couple, as an approximation of the scatter component in PGET systems (scaled by nominal assembly burnup) to single-pin sinograms: Note: This method does not capture the variations due to pin-wise burnup variations
    - iii. Create variable-BU sinograms to match specific measurements
3. RADSAT-based single-pin sinograms (USSP)
  - a. Used to generate pin-wise system response functions for tomographic data inversion in support of USSP analysis of both Ideal PGET and UGETv1 performance
  - b. Deterministic transport method
  - c. Includes primary and object-scatter photons
  - d. Mimics MCNP (USSP) geometry
4. Geant4-based full-assembly sinograms (SWESP)
  - a. Used only for modeling validation of PLUTO response to the  $^{140}\text{Ba}/\text{La}$  gamma-ray energy in BWR fuel (based on  $^{140}\text{Ba}/\text{La}$  experimental data)
  - b. Not used for comparative analysis of UGETv1 and PGET
  - c. Fuel length longer than collimator opening
  - d. Variance reduction tools not used

## Appendix B

### Emission Intensity Values for Characteristic Gamma-ray Lines from GET Fuel Library

The GET “lookup tables” provide exact values for absolute emission intensity normalization for nine characteristic gamma-ray lines emitted from four primary fission products:  $^{137}\text{Cs}$  (30-year half-life),  $^{154}\text{Eu}$  (8.6-year half-life),  $^{134}\text{Cs}$  (2-year half-life), and  $^{144}\text{Pr}$  (284-day half-life). These nine gamma-ray lines define the energy structure and are proportional to the total rate of gamma-ray emissions in the energy region between 0.4 and 2.5 MeV, important for tomographic measurement.

The relative emission intensity for the four isotopes are calculated for specific burnup values from fuel inventory calculations performed with the Monteburns code coupled with the MCNP transport code. Atom densities of fission products were folded with isotope-specific half-life and gamma-ray emission branching ratios to determine the number of emissions at an arbitrary cooling time.

Gamma-ray emission intensity results in the tables below are provided in absolute units reflecting the number of emissions in 1 cm of fuel pin axial extent per second. Examples are given for 1, 5, and 40 years of cooling time.

**Table APX B.1.** Characteristic Gamma-ray Emission Intensities for GET Assemblies at 1 Year Cooling Time.

Assembly type: BWR, ~ 2 wt% initial enrichment, 1 year cooling time													
Burnup (MWd/ MTU)	Atom density (atoms/barn-cm <sup>3</sup> )				Characteristic Gamma-ray Emission Intensity (1/cm of fuel pin axial length/sec.)								
	Cs-134	Cs-137	Pr-144	Eu-154	Cs-134	Cs-137	Pr-144		Eu-154				
					0.6047 MeV	0.6617 MeV	0.7959 MeV	2.1857 MeV	1.2744 MeV	0.7233 MeV	1.0048 MeV	0.8732 MeV	0.9963 MeV
5222.82	2.56E-07	7.73E-06	2.16E-10	4.01E-08	1.00E+09	8.76E+08	2.46E+09	9.16E+03	1.74E+07	1.00E+07	8.98E+06	6.02E+06	5.23E+06
6924.43	4.19E-07	1.02E-05	2.61E-10	6.55E-08	1.64E+09	1.44E+09	3.27E+09	1.10E+04	2.84E+07	1.63E+07	1.47E+07	9.83E+06	8.53E+06
8625.98	5.94E-07	1.27E-05	2.99E-10	9.34E-08	2.33E+09	2.04E+09	4.06E+09	1.27E+04	4.04E+07	2.33E+07	2.09E+07	1.40E+07	1.22E+07
10327.55	7.75E-07	1.52E-05	3.31E-10	1.23E-07	3.03E+09	2.65E+09	4.86E+09	1.40E+04	5.32E+07	3.07E+07	2.75E+07	1.85E+07	1.60E+07
12000.93	9.53E-07	1.77E-05	3.58E-10	1.53E-07	3.73E+09	3.27E+09	5.63E+09	1.52E+04	6.63E+07	3.82E+07	3.43E+07	2.30E+07	1.99E+07
12014.02	9.29E-07	1.76E-05	3.29E-10	1.52E-07	3.63E+09	3.18E+09	5.63E+09	1.39E+04	6.59E+07	3.80E+07	3.41E+07	2.29E+07	1.98E+07
12118.75	9.39E-07	1.78E-05	3.32E-10	1.54E-07	3.67E+09	3.22E+09	5.68E+09	1.41E+04	6.67E+07	3.84E+07	3.45E+07	2.31E+07	2.01E+07
13820.32	1.11E-06	2.03E-05	3.63E-10	1.85E-07	4.35E+09	3.81E+09	6.46E+09	1.54E+04	8.00E+07	4.61E+07	4.13E+07	2.77E+07	2.41E+07
15522.16	1.36E-06	2.27E-05	3.80E-10	2.25E-07	5.31E+09	4.64E+09	7.24E+09	1.61E+04	9.73E+07	5.60E+07	5.03E+07	3.37E+07	2.93E+07
17224.16	1.65E-06	2.52E-05	3.92E-10	2.7E-07	6.44E+09	5.64E+09	8.03E+09	1.66E+04	1.17E+08	6.73E+07	6.04E+07	4.05E+07	3.52E+07
18926.16	1.91E-06	2.76E-05	4.05E-10	3.11E-07	7.49E+09	6.56E+09	8.79E+09	1.71E+04	1.34E+08	7.75E+07	6.95E+07	4.66E+07	4.05E+07
20628	2.24E-06	3E-05	4.14E-10	3.57E-07	8.77E+09	7.68E+09	9.56E+09	1.75E+04	1.54E+08	8.89E+07	7.98E+07	5.35E+07	4.64E+07



**Assembly type: BWR, ~ 2 wt% initial enrichment, 1 year cooling time**

Burnup (MWd/ MTU)	Atom density (atoms/barn-cm <sup>3</sup> )				Characteristic Gamma-ray Emission Intensity (1/cm of fuel pin axial length/sec.)								
	Cs-134	Cs-137	Pr-144	Eu-154	Cs-134	Cs-137	Pr-144		Eu-154				
					0.6047 MeV	0.6617 MeV	0.7959 MeV	2.1857 MeV	1.2744 MeV	0.7233 MeV	1.0048 MeV	0.8732 MeV	0.9963 MeV
22329.8	2.60E-06	3.24E-05	4.19E-10	4.07E-07	1.02E+10	8.92E+09	1.03E+10	1.77E+04	1.76E+08	1.01E+08	9.11E+07	6.11E+07	5.30E+07
24003.65	2.98E-06	3.47E-05	4.24E-10	4.57E-07	1.17E+10	1.02E+10	1.11E+10	1.79E+04	1.98E+08	1.14E+08	1.02E+08	6.86E+07	5.95E+07
24016.74	2.90E-06	3.47E-05	3.91E-10	4.55E-07	1.14E+10	9.94E+09	1.11E+10	1.65E+04	1.97E+08	1.13E+08	1.02E+08	6.82E+07	5.92E+07
24121.48	2.93E-06	3.49E-05	3.92E-10	4.58E-07	1.15E+10	1.00E+10	1.11E+10	1.66E+04	1.98E+08	1.14E+08	1.02E+08	6.88E+07	5.97E+07
25823.76	3.34E-06	3.73E-05	4.01E-10	5.1E-07	1.31E+10	1.14E+10	1.19E+10	1.70E+04	2.21E+08	1.27E+08	1.14E+08	7.65E+07	6.64E+07
27526.14	3.75E-06	3.96E-05	4.07E-10	5.59E-07	1.47E+10	1.29E+10	1.26E+10	1.72E+04	2.42E+08	1.39E+08	1.25E+08	8.40E+07	7.28E+07
29228.26	4.18E-06	4.2E-05	4.10E-10	6.07E-07	1.64E+10	1.43E+10	1.34E+10	1.74E+04	2.63E+08	1.51E+08	1.36E+08	9.12E+07	7.91E+07
30930.13	4.62E-06	4.44E-05	4.12E-10	6.54E-07	1.81E+10	1.58E+10	1.42E+10	1.74E+04	2.83E+08	1.63E+08	1.46E+08	9.82E+07	8.52E+07
32632.6	5.07E-06	4.67E-05	4.13E-10	7E-07	1.99E+10	1.74E+10	1.49E+10	1.75E+04	3.03E+08	1.74E+08	1.57E+08	1.05E+08	9.11E+07
34334.28	5.53E-06	4.91E-05	4.14E-10	7.43E-07	2.16E+10	1.89E+10	1.57E+10	1.75E+04	3.22E+08	1.85E+08	1.66E+08	1.12E+08	9.68E+07
36008.22	5.97E-06	5.14E-05	4.14E-10	7.85E-07	2.34E+10	2.05E+10	1.64E+10	1.75E+04	3.40E+08	1.96E+08	1.76E+08	1.18E+08	1.02E+08
36021.3	5.81E-06	5.13E-05	3.81E-10	7.79E-07	2.27E+10	1.99E+10	1.64E+10	1.61E+04	3.37E+08	1.94E+08	1.74E+08	1.17E+08	1.01E+08
36126.02	5.81E-06	5.13E-05	3.82E-10	7.8E-07	2.28E+10	1.99E+10	1.64E+10	1.62E+04	3.37E+08	1.94E+08	1.74E+08	1.17E+08	1.02E+08

**Assembly type: BWR, ~ 2 wt% initial enrichment, 1 year cooling time**

Burnup (MWd/ MTU)	Atom density (atoms/barn-cm <sup>3</sup> )				Characteristic Gamma-ray Emission Intensity (1/cm of fuel pin axial length/sec.)								
	Cs-134	Cs-137	Pr-144	Eu-154	Cs-134	Cs-137	Pr-144		Eu-154				
					0.6047 MeV	0.6617 MeV	0.7959 MeV	2.1857 MeV	1.2744 MeV	0.7233 MeV	1.0048 MeV	0.8732 MeV	0.9963 MeV
37827.87	5.84E-06	5.14E-05	3.84E-10	7.83E-07	2.29E+10	2.00E+10	1.64E+10	1.62E+04	3.39E+08	1.95E+08	1.75E+08	1.17E+08	1.02E+08
39529.93	6.32E-06	5.38E-05	3.89E-10	8.25E-07	2.47E+10	2.17E+10	1.71E+10	1.65E+04	3.57E+08	2.06E+08	1.85E+08	1.24E+08	1.07E+08
41231.8	6.77E-06	5.6E-05	3.92E-10	8.63E-07	2.65E+10	2.32E+10	1.79E+10	1.66E+04	3.73E+08	2.15E+08	1.93E+08	1.29E+08	1.12E+08
5392.57	1.31E-07	7.46E-06	2.30E-10	1.86E-08	6.78E+08	5.94E+08	1.21E+10	1.83E+00	1.63E+08	9.36E+07	8.41E+07	5.64E+07	4.89E+07
7136.52	2.34E-07	9.86E-06	2.84E-10	3.33E-08	7.55E+08	6.61E+08	2.60E+09	9.93E+03	1.19E+07	6.85E+06	6.15E+06	4.12E+06	3.58E+06
8881.42	3.63E-07	1.23E-05	3.31E-10	5.25E-08	1.17E+09	1.03E+09	3.23E+09	1.16E+04	1.88E+07	1.08E+07	9.70E+06	6.51E+06	5.64E+06
10623.1	5.18E-07	1.46E-05	3.71E-10	7.64E-08	1.67E+09	1.46E+09	3.85E+09	1.30E+04	2.73E+07	1.57E+07	1.41E+07	9.46E+06	8.21E+06
12364.61	6.97E-07	1.70E-05	4.06E-10	1.05E-07	2.25E+09	1.97E+09	4.48E+09	1.42E+04	3.75E+07	2.16E+07	1.94E+07	1.30E+07	1.13E+07
14108.4	9.00E-07	1.94E-05	4.36E-10	1.38E-07	2.91E+09	2.54E+09	5.10E+09	1.52E+04	4.92E+07	2.84E+07	2.55E+07	1.71E+07	1.48E+07
15852.43	1.13E-06	2.18E-05	4.62E-10	1.75E-07	3.64E+09	3.19E+09	5.73E+09	1.61E+04	6.26E+07	3.61E+07	3.24E+07	2.17E+07	1.88E+07
17597.72	1.37E-06	2.41E-05	4.84E-10	2.17E-07	4.44E+09	3.89E+09	6.35E+09	1.69E+04	7.74E+07	4.46E+07	4.00E+07	2.69E+07	2.33E+07
19339.26	1.64E-06	2.65E-05	5.03E-10	2.62E-07	5.31E+09	4.65E+09	6.97E+09	1.76E+04	9.36E+07	5.39E+07	4.84E+07	3.25E+07	2.82E+07
21082.02	1.93E-06	2.88E-05	5.19E-10	3.11E-07	6.24E+09	5.46E+09	7.58E+09	1.81E+04	1.11E+08	6.39E+07	5.74E+07	3.85E+07	3.34E+07

**Assembly type: BWR, ~ 2 wt% initial enrichment, 1 year cooling time**

Burnup (MWd/ MTU)	Atom density (atoms/barn-cm <sup>3</sup> )				Characteristic Gamma-ray Emission Intensity (1/cm of fuel pin axial length/sec.)								
	Cs-134	Cs-137	Pr-144	Eu-154	Cs-134	Cs-137	Pr-144		Eu-154				
					0.6047 MeV	0.6617 MeV	0.7959 MeV	2.1857 MeV	1.2744 MeV	0.7233 MeV	1.0048 MeV	0.8732 MeV	0.9963 MeV
22025.1	2.24E-06	3.11E-05	5.33E-10	3.62E-07	7.22E+09	6.32E+09	8.20E+09	1.86E+04	1.29E+08	7.45E+07	6.69E+07	4.49E+07	3.89E+07
24569.55	2.56E-06	3.35E-05	5.44E-10	4.16E-07	8.27E+09	7.24E+09	8.81E+09	1.90E+04	1.49E+08	8.56E+07	7.69E+07	5.16E+07	4.47E+07
26314.67	2.90E-06	3.58E-05	5.53E-10	4.73E-07	9.37E+09	8.20E+09	9.42E+09	1.93E+04	1.69E+08	9.72E+07	8.73E+07	5.85E+07	5.08E+07
28059.21	3.26E-06	3.81E-05	5.61E-10	5.31E-07	1.05E+10	9.21E+09	1.00E+10	1.96E+04	1.89E+08	1.09E+08	9.80E+07	6.57E+07	5.70E+07
29800.46	3.63E-06	4.04E-05	5.67E-10	5.90E-07	1.17E+10	1.03E+10	1.06E+10	1.98E+04	2.11E+08	1.21E+08	1.09E+08	7.30E+07	6.33E+07
31544.85	4.02E-06	4.27E-05	5.72E-10	6.49E-07	1.30E+10	1.14E+10	1.12E+10	2.00E+04	2.32E+08	1.34E+08	1.20E+08	8.04E+07	6.97E+07
33288.38	4.42E-06	4.50E-05	5.75E-10	7.10E-07	1.43E+10	1.25E+10	1.19E+10	2.01E+04	2.53E+08	1.46E+08	1.31E+08	8.79E+07	7.62E+07
35032.8	4.84E-06	4.73E-05	5.78E-10	7.70E-07	1.56E+10	1.37E+10	1.25E+10	2.02E+04	2.75E+08	1.58E+08	1.42E+08	9.53E+07	8.27E+07
36778.14	5.27E-06	4.96E-05	5.80E-10	8.29E-07	1.70E+10	1.49E+10	1.31E+10	2.02E+04	2.96E+08	1.71E+08	1.53E+08	1.03E+08	8.91E+07
38524.84	5.71E-06	5.19E-05	5.81E-10	8.88E-07	1.84E+10	1.61E+10	1.37E+10	2.03E+04	3.17E+08	1.83E+08	1.64E+08	1.10E+08	9.55E+07
40268.75	6.15E-06	5.41E-05	5.81E-10	9.47E-07	1.99E+10	1.74E+10	1.42E+10	2.03E+04	3.38E+08	1.95E+08	1.75E+08	1.17E+08	1.02E+08
4425.52	7.24E-08	6.51E-06	2.86E-10	1.25E-08	2.83E+08	2.48E+08	2.08E+09	1.21E+04	5.41E+06	3.11E+06	2.79E+06	1.87E+06	1.63E+06
9119.28	3.95E-07	1.34E-05	4.92E-10	6.01E-08	1.55E+09	1.36E+09	4.27E+09	2.08E+04	2.60E+07	1.50E+07	1.34E+07	9.02E+06	7.83E+06

**Assembly type: BWR, ~ 2 wt% initial enrichment, 1 year cooling time**

Burnup (MWd/ MTU)	Atom density (atoms/barn-cm <sup>3</sup> )				Characteristic Gamma-ray Emission Intensity (1/cm of fuel pin axial length/sec.)								
	Cs-134	Cs-137	Pr-144	Eu-154	Cs-134	Cs-137	Pr-144		Eu-154				
					0.6047 MeV	0.6617 MeV	0.7959 MeV	2.1857 MeV	1.2744 MeV	0.7233 MeV	1.0048 MeV	0.8732 MeV	0.9963 MeV
13423.99	9.14E-07	1.96E-05	6.44E-10	1.38E-07	3.58E+09	3.13E+09	6.27E+09	2.73E+04	5.99E+07	3.45E+07	3.10E+07	2.08E+07	1.80E+07
17475.18	1.58E-06	2.55E-05	7.67E-10	2.42E-07	6.20E+09	5.43E+09	8.15E+09	3.25E+04	1.05E+08	6.04E+07	5.42E+07	3.64E+07	3.16E+07
21315.45	2.37E-06	3.11E-05	8.67E-10	3.64E-07	9.27E+09	8.11E+09	9.93E+09	3.67E+04	1.58E+08	9.08E+07	8.15E+07	5.47E+07	4.75E+07
24996.51	3.24E-06	3.64E-05	9.48E-10	4.99E-07	1.27E+10	1.11E+10	1.16E+10	4.01E+04	2.16E+08	1.24E+08	1.12E+08	7.49E+07	6.50E+07
24996.51	3.16E-06	3.64E-05	8.49E-10	4.95E-07	1.24E+10	1.08E+10	1.16E+10	3.59E+04	2.14E+08	1.24E+08	1.11E+08	7.44E+07	6.45E+07
25041.79	3.18E-06	3.66E-05	8.62E-10	4.99E-07	1.24E+10	1.09E+10	1.17E+10	3.65E+04	2.16E+08	1.24E+08	1.12E+08	7.49E+07	6.50E+07
25403.02	3.27E-06	3.71E-05	8.75E-10	5.13E-07	1.28E+10	1.12E+10	1.18E+10	3.70E+04	2.22E+08	1.28E+08	1.15E+08	7.70E+07	6.68E+07
27978.28	3.96E-06	4.09E-05	9.46E-10	6.14E-07	1.55E+10	1.36E+10	1.31E+10	4.00E+04	2.66E+08	1.53E+08	1.37E+08	9.22E+07	8.00E+07
31220.67	4.91E-06	4.57E-05	1.00E-09	7.49E-07	1.92E+10	1.68E+10	1.46E+10	4.24E+04	3.24E+08	1.87E+08	1.68E+08	1.12E+08	9.75E+07
34196.97	5.83E-06	5.00E-05	1.03E-09	8.77E-07	2.28E+10	2.00E+10	1.60E+10	4.38E+04	3.80E+08	2.19E+08	1.96E+08	1.32E+08	1.14E+08
37130.12	6.80E-06	5.43E-05	1.06E-09	1.00E-06	2.66E+10	2.33E+10	1.73E+10	4.50E+04	4.35E+08	2.51E+08	2.25E+08	1.51E+08	1.31E+08
39895.07	7.74E-06	5.83E-05	1.08E-09	1.13E-06	3.03E+10	2.65E+10	1.86E+10	4.57E+04	4.87E+08	2.81E+08	2.52E+08	1.69E+08	1.47E+08

**Table APX B.2.** Characteristic Gamma-ray Emission Intensities for GET Assemblies at 5 Years Cooling Time.

Assembly type: BWR, ~ 2 wt% initial enrichment, 5 years cooling time														
Burnup (MWd/ MTU)	Atom density (atoms/barn-cm <sup>3</sup> )					Characteristic Gamma-ray Emission Intensity (1/cm of fuel pin axial length/sec.)								
	Cs-134	Cs-137	Pr-144	Eu-154		Cs-134		Cs-137	Pr-144	Eu-154				
					0.6047 MeV	0.7959 MeV	0.6617 MeV	2.1857 MeV	1.2744 MeV	0.7233 MeV	1.0048 MeV	0.8732 MeV	0.9963 MeV	
5222.82	2.56E-07	7.73E-06	2.16E-10	4.01E-08		2.61E+08	2.28E+08	2.25E+09	2.62E+02	1.26E+07	7.24E+06	6.50E+06	4.36E+06	3.78E+06
6924.43	4.19E-07	1.02E-05	2.61E-10	6.55E-08		4.27E+08	3.74E+08	2.98E+09	3.16E+02	2.05E+07	1.18E+07	1.06E+07	7.12E+06	6.18E+06
8625.98	5.94E-07	1.27E-05	2.99E-10	9.34E-08		6.06E+08	5.31E+08	3.71E+09	3.62E+02	2.93E+07	1.69E+07	1.51E+07	1.01E+07	8.80E+06
10327.55	7.75E-07	1.52E-05	3.31E-10	1.23E-07		7.90E+08	6.92E+08	4.43E+09	4.01E+02	3.85E+07	2.22E+07	1.99E+07	1.34E+07	1.16E+07
12000.93	9.53E-07	1.77E-05	3.58E-10	1.53E-07		9.72E+08	8.51E+08	5.14E+09	4.34E+02	4.80E+07	2.76E+07	2.48E+07	1.66E+07	1.44E+07
12014.02	9.29E-07	1.76E-05	3.29E-10	1.52E-07		9.47E+08	8.29E+08	5.13E+09	3.98E+02	4.78E+07	2.75E+07	2.47E+07	1.66E+07	1.44E+07
12118.75	9.39E-07	1.78E-05	3.32E-10	1.54E-07		9.57E+08	8.38E+08	5.18E+09	4.02E+02	4.83E+07	2.78E+07	2.50E+07	1.68E+07	1.45E+07
13820.32	1.11E-06	2.03E-05	3.63E-10	1.85E-07		1.13E+09	9.92E+08	5.89E+09	4.39E+02	5.79E+07	3.34E+07	2.99E+07	2.01E+07	1.74E+07
15522.16	1.36E-06	2.27E-05	3.80E-10	2.25E-07		1.38E+09	1.21E+09	6.60E+09	4.60E+02	7.05E+07	4.06E+07	3.64E+07	2.44E+07	2.12E+07
17224.16	1.65E-06	2.52E-05	3.92E-10	2.70E-07		1.68E+09	1.47E+09	7.32E+09	4.74E+02	8.46E+07	4.87E+07	4.37E+07	2.93E+07	2.55E+07
18926.16	1.91E-06	2.76E-05	4.05E-10	3.11E-07		1.95E+09	1.71E+09	8.02E+09	4.90E+02	9.74E+07	5.61E+07	5.04E+07	3.38E+07	2.93E+07
20628	2.24E-06	3.00E-05	4.14E-10	3.57E-07		2.29E+09	2.00E+09	8.72E+09	5.01E+02	1.12E+08	6.44E+07	5.78E+07	3.87E+07	3.36E+07

**Assembly type: BWR, ~ 2 wt% initial enrichment, 5 years cooling time**

Burnup (MWd/ MTU)	Atom density (atoms/barn-cm³)					Characteristic Gamma-ray Emission Intensity (1/cm of fuel pin axial length/sec.)								
	Cs-134	Cs-137	Pr-144	Eu-154		Cs-134		Cs-137	Pr-144	Eu-154				
						0.6047 MeV	0.7959 MeV	0.6617 MeV	2.1857 MeV	1.2744 MeV	0.7233 MeV	1.0048 MeV	0.8732 MeV	0.9963 MeV
22329.8	2.60E-06	3.24E-05	4.19E-10	4.07E-07		2.66E+09	2.32E+09	9.43E+09	5.07E+02	1.28E+08	7.35E+07	6.60E+07	4.42E+07	3.84E+07
24003.65	2.98E-06	3.47E-05	4.24E-10	4.57E-07		3.04E+09	2.66E+09	1.01E+10	5.13E+02	1.43E+08	8.26E+07	7.41E+07	4.97E+07	4.31E+07
24016.74	2.90E-06	3.47E-05	3.91E-10	4.55E-07		2.96E+09	2.59E+09	1.01E+10	4.73E+02	1.43E+08	8.21E+07	7.37E+07	4.94E+07	4.29E+07
24121.48	2.93E-06	3.49E-05	3.92E-10	4.58E-07		2.99E+09	2.61E+09	1.01E+10	4.75E+02	1.44E+08	8.27E+07	7.42E+07	4.98E+07	4.32E+07
25823.76	3.34E-06	3.73E-05	4.01E-10	5.10E-07		3.40E+09	2.98E+09	1.08E+10	4.86E+02	1.60E+08	9.21E+07	8.26E+07	5.54E+07	4.81E+07
27526.14	3.75E-06	3.96E-05	4.07E-10	5.59E-07		3.83E+09	3.35E+09	1.15E+10	4.92E+02	1.75E+08	1.01E+08	9.06E+07	6.08E+07	5.28E+07
29228.26	4.18E-06	4.20E-05	4.10E-10	6.07E-07		4.27E+09	3.74E+09	1.22E+10	4.96E+02	1.90E+08	1.10E+08	9.84E+07	6.60E+07	5.73E+07
30930.13	4.62E-06	4.44E-05	4.12E-10	6.54E-07		4.72E+09	4.13E+09	1.29E+10	4.99E+02	2.05E+08	1.18E+08	1.06E+08	7.11E+07	6.17E+07
32632.6	5.07E-06	4.67E-05	4.13E-10	7.00E-07		5.18E+09	4.53E+09	1.36E+10	5.00E+02	2.19E+08	1.26E+08	1.13E+08	7.61E+07	6.60E+07
34334.28	5.53E-06	4.91E-05	4.14E-10	7.43E-07		5.64E+09	4.94E+09	1.43E+10	5.01E+02	2.33E+08	1.34E+08	1.20E+08	8.08E+07	7.01E+07
36008.22	5.97E-06	5.14E-05	4.14E-10	7.85E-07		6.09E+09	5.34E+09	1.49E+10	5.01E+02	2.46E+08	1.42E+08	1.27E+08	8.53E+07	7.40E+07
36021.3	5.81E-06	5.13E-05	3.81E-10	7.79E-07		5.93E+09	5.19E+09	1.49E+10	4.61E+02	2.44E+08	1.41E+08	1.26E+08	8.47E+07	7.35E+07
36126.02	5.81E-06	5.13E-05	3.82E-10	7.80E-07		5.93E+09	5.19E+09	1.49E+10	4.63E+02	2.44E+08	1.41E+08	1.26E+08	8.47E+07	7.35E+07

**Assembly type: BWR, ~ 2 wt% initial enrichment, 5 years cooling time**

Burnup (MWd/ MTU)	Atom density (atoms/barn-cm³)					Characteristic Gamma-ray Emission Intensity (1/cm of fuel pin axial length/sec.)								
	Cs-134	Cs-137	Pr-144	Eu-154		Cs-134		Cs-137	Pr-144	Eu-154				
						0.6047 MeV	0.7959 MeV	0.6617 MeV	2.1857 MeV	1.2744 MeV	0.7233 MeV	1.0048 MeV	0.8732 MeV	0.9963 MeV
37827.87	5.84E-06	5.14E-05	3.84E-10	7.83E-07		5.96E+09	5.22E+09	1.50E+10	4.65E+02	2.45E+08	1.41E+08	1.27E+08	8.51E+07	7.38E+07
39529.93	6.32E-06	5.38E-05	3.89E-10	8.25E-07		6.45E+09	5.64E+09	1.56E+10	4.71E+02	2.59E+08	1.49E+08	1.34E+08	8.97E+07	7.78E+07
41231.8	6.77E-06	5.60E-05	3.92E-10	8.63E-07		6.90E+09	6.04E+09	1.63E+10	4.75E+02	2.70E+08	1.56E+08	1.40E+08	9.38E+07	8.14E+07
5392.57	1.31E-07	7.46E-06	2.30E-10	1.86E-08		6.78E+08	5.94E+08	1.21E+10	1.83E+00	1.63E+08	9.36E+07	8.41E+07	5.64E+07	4.89E+07
7136.52	2.34E-07	9.86E-06	2.84E-10	3.33E-08		1.97E+08	1.72E+08	2.37E+09	2.84E+02	8.61E+06	4.96E+06	4.45E+06	2.99E+06	2.59E+06
8881.42	3.63E-07	1.23E-05	3.31E-10	5.25E-08		3.06E+08	2.67E+08	2.94E+09	3.31E+02	1.36E+07	7.83E+06	7.02E+06	4.71E+06	4.09E+06
10623.1	5.18E-07	1.46E-05	3.71E-10	7.64E-08		4.36E+08	3.81E+08	3.51E+09	3.71E+02	1.98E+07	1.14E+07	1.02E+07	6.85E+06	5.95E+06
12364.61	6.97E-07	1.70E-05	4.06E-10	1.05E-07		5.87E+08	5.14E+08	4.09E+09	4.06E+02	2.71E+07	1.56E+07	1.40E+07	9.41E+06	8.16E+06
14108.4	9.00E-07	1.94E-05	4.36E-10	1.38E-07		7.58E+08	6.63E+08	4.66E+09	4.36E+02	3.57E+07	2.05E+07	1.84E+07	1.24E+07	1.07E+07
15852.43	1.13E-06	2.18E-05	4.62E-10	1.75E-07		9.49E+08	8.30E+08	5.22E+09	4.62E+02	4.53E+07	2.61E+07	2.34E+07	1.57E+07	1.36E+07
17597.72	1.37E-06	2.41E-05	4.84E-10	2.17E-07		1.16E+09	1.01E+09	5.79E+09	4.84E+02	5.61E+07	3.23E+07	2.90E+07	1.94E+07	1.69E+07
19339.26	1.64E-06	2.65E-05	5.03E-10	2.62E-07		1.38E+09	1.21E+09	6.35E+09	5.03E+02	6.78E+07	3.90E+07	3.50E+07	2.35E+07	2.04E+07
21082.02	1.93E-06	2.88E-05	5.19E-10	3.11E-07		1.63E+09	1.42E+09	6.92E+09	5.18E+02	8.03E+07	4.63E+07	4.15E+07	2.79E+07	2.42E+07

**Assembly type: BWR, ~ 2 wt% initial enrichment, 5 years cooling time**

Burnup (MWd/ MTU)	Atom density (atoms/barn-cm <sup>3</sup> )					Characteristic Gamma-ray Emission Intensity (1/cm of fuel pin axial length/sec.)								
	Cs-134	Cs-137	Pr-144	Eu-154		Cs-134		Cs-137	Pr-144	Eu-154				
						0.6047 MeV	0.7959 MeV	0.6617 MeV	2.1857 MeV	1.2744 MeV	0.7233 MeV	1.0048 MeV	0.8732 MeV	0.9963 MeV
22025.1	2.24E-06	3.11E-05	5.33E-10	3.62E-07		1.88E+09	1.65E+09	7.48E+09	5.32E+02	9.37E+07	5.40E+07	4.84E+07	3.25E+07	2.82E+07
24569.55	2.56E-06	3.35E-05	5.44E-10	4.16E-07		2.16E+09	1.89E+09	8.04E+09	5.43E+02	1.08E+08	6.20E+07	5.57E+07	3.73E+07	3.24E+07
26314.67	2.90E-06	3.58E-05	5.53E-10	4.73E-07		2.44E+09	2.14E+09	8.60E+09	5.52E+02	1.22E+08	7.04E+07	6.32E+07	4.24E+07	3.68E+07
28059.21	3.26E-06	3.81E-05	5.61E-10	5.31E-07		2.74E+09	2.40E+09	9.15E+09	5.60E+02	1.37E+08	7.90E+07	7.09E+07	4.76E+07	4.13E+07
29800.46	3.63E-06	4.04E-05	5.67E-10	5.90E-07		3.06E+09	2.68E+09	9.71E+09	5.66E+02	1.52E+08	8.78E+07	7.88E+07	5.29E+07	4.59E+07
31544.85	4.02E-06	4.27E-05	5.72E-10	6.49E-07		3.38E+09	2.96E+09	1.03E+10	5.71E+02	1.68E+08	9.67E+07	8.68E+07	5.82E+07	5.05E+07
33288.38	4.42E-06	4.50E-05	5.75E-10	7.10E-07		3.72E+09	3.26E+09	1.08E+10	5.74E+02	1.83E+08	1.06E+08	9.49E+07	6.36E+07	5.52E+07
35032.8	4.84E-06	4.73E-05	5.78E-10	7.70E-07		4.07E+09	3.56E+09	1.14E+10	5.77E+02	1.99E+08	1.15E+08	1.03E+08	6.90E+07	5.99E+07
36778.14	5.27E-06	4.96E-05	5.80E-10	8.29E-07		4.43E+09	3.88E+09	1.19E+10	5.79E+02	2.14E+08	1.24E+08	1.11E+08	7.44E+07	6.45E+07
38524.84	5.71E-06	5.19E-05	5.81E-10	8.88E-07		4.80E+09	4.21E+09	1.25E+10	5.80E+02	2.30E+08	1.32E+08	1.19E+08	7.97E+07	6.91E+07
40268.75	6.15E-06	5.41E-05	5.81E-10	9.47E-07		5.18E+09	4.53E+09	1.30E+10	5.80E+02	2.45E+08	1.41E+08	1.27E+08	8.49E+07	7.37E+07
4425.52	7.24E-08	6.51E-06	2.86E-10	1.25E-08		7.39E+07	6.47E+07	1.90E+09	3.47E+02	3.91E+06	2.25E+06	2.02E+06	1.36E+06	1.18E+06
9119.28	3.95E-07	1.34E-05	4.92E-10	6.01E-08		4.03E+08	3.53E+08	3.89E+09	5.95E+02	1.88E+07	1.09E+07	9.74E+06	6.53E+06	5.67E+06



**Assembly type: BWR, ~ 2 wt% initial enrichment, 5 years cooling time**

Burnup (MWd/ MTU)	Atom density (atoms/barn-cm³)					Characteristic Gamma-ray Emission Intensity (1/cm of fuel pin axial length/sec.)								
	Cs-134	Cs-137	Pr-144	Eu-154		Cs-134		Cs-137	Pr-144	Eu-154				
						0.6047 MeV	0.7959 MeV	0.6617 MeV	2.1857 MeV	1.2744 MeV	0.7233 MeV	1.0048 MeV	0.8732 MeV	0.9963 MeV
13423.99	9.14E-07	1.96E-05	6.44E-10	1.38E-07		9.33E+08	8.17E+08	5.72E+09	7.79E+02	4.34E+07	2.50E+07	2.24E+07	1.51E+07	1.31E+07
17475.18	1.58E-06	2.55E-05	7.67E-10	2.42E-07		1.62E+09	1.41E+09	7.43E+09	9.29E+02	7.60E+07	4.38E+07	3.93E+07	2.63E+07	2.29E+07
21315.45	2.37E-06	3.11E-05	8.67E-10	3.64E-07		2.41E+09	2.11E+09	9.06E+09	1.05E+03	1.14E+08	6.58E+07	5.90E+07	3.96E+07	3.44E+07
24996.51	3.24E-06	3.64E-05	9.48E-10	4.99E-07		3.31E+09	2.90E+09	1.06E+10	1.15E+03	1.56E+08	9.01E+07	8.08E+07	5.42E+07	4.70E+07
24996.51	3.16E-06	3.64E-05	8.49E-10	4.95E-07		3.22E+09	2.82E+09	1.06E+10	1.03E+03	1.55E+08	8.95E+07	8.03E+07	5.39E+07	4.67E+07
25041.79	3.18E-06	3.66E-05	8.62E-10	4.99E-07		3.24E+09	2.84E+09	1.06E+10	1.04E+03	1.56E+08	9.01E+07	8.08E+07	5.42E+07	4.70E+07
25403.02	3.27E-06	3.71E-05	8.75E-10	5.13E-07		3.34E+09	2.92E+09	1.08E+10	1.06E+03	1.61E+08	9.26E+07	8.31E+07	5.58E+07	4.84E+07
27978.28	3.96E-06	4.09E-05	9.46E-10	6.14E-07		4.04E+09	3.54E+09	1.19E+10	1.15E+03	1.93E+08	1.11E+08	9.95E+07	6.68E+07	5.79E+07
31220.67	4.91E-06	4.57E-05	1.00E-09	7.49E-07		5.01E+09	4.38E+09	1.33E+10	1.21E+03	2.35E+08	1.35E+08	1.21E+08	8.14E+07	7.06E+07
34196.97	5.83E-06	5.00E-05	1.03E-09	8.77E-07		5.95E+09	5.21E+09	1.46E+10	1.25E+03	2.75E+08	1.58E+08	1.42E+08	9.54E+07	8.28E+07
37130.12	6.80E-06	5.43E-05	1.06E-09	1.00E-06		6.94E+09	6.07E+09	1.58E+10	1.29E+03	3.15E+08	1.81E+08	1.63E+08	1.09E+08	9.48E+07
39895.07	7.74E-06	5.83E-05	1.08E-09	1.13E-06		7.90E+09	6.92E+09	1.70E+10	1.31E+03	3.53E+08	2.03E+08	1.82E+08	1.22E+08	1.06E+08

**Table APX B.3.** Characteristic Gamma-ray Emission Intensities for GET Assemblies at 40 Yrs. Cooling Time.

Assembly type: BWR, ~ 2 wt% initial enrichment, 40 years cooling time														
Burnup (MWd/ MTU)	Atom density (atoms/barn-cm <sup>3</sup> )					Characteristic Gamma-ray Emission Intensity (1/cm of fuel pin axial length/sec.)								
	Cs-134	Cs-137	Pr-144	Eu-154		Cs-134		Cs-137	Pr-144	Eu-154				
						0.6047 MeV	0.7959 MeV	0.6617 MeV	2.1857 MeV	1.2744 MeV	0.7233 MeV	1.0048 MeV	0.8732 MeV	0.9963 MeV
5222.82	2.56E-07	7.73E-06	2.16E-10	4.01E-08		2.02E+03	1.77E+03	1.01E+09	8.14E-12	7.47E+05	4.30E+05	3.86E+05	2.59E+05	2.25E+05
6924.43	4.19E-07	1.02E-05	2.61E-10	6.55E-08		3.32E+03	2.91E+03	1.33E+09	9.82E-12	1.22E+06	7.02E+05	6.30E+05	4.23E+05	3.67E+05
8625.98	5.94E-07	1.27E-05	2.99E-10	9.34E-08		4.71E+03	4.12E+03	1.66E+09	1.13E-11	1.74E+06	1.00E+06	8.98E+05	6.03E+05	5.23E+05
10327.55	7.75E-07	1.52E-05	3.31E-10	1.23E-07		6.14E+03	5.37E+03	1.98E+09	1.25E-11	2.29E+06	1.32E+06	1.18E+06	7.94E+05	6.89E+05
12000.93	9.53E-07	1.77E-05	3.58E-10	1.53E-07		7.55E+03	6.61E+03	2.30E+09	1.35E-11	2.85E+06	1.64E+06	1.47E+06	9.89E+05	8.58E+05
12014.02	9.29E-07	1.76E-05	3.29E-10	1.52E-07		7.36E+03	6.44E+03	2.30E+09	1.24E-11	2.84E+06	1.63E+06	1.47E+06	9.84E+05	8.53E+05
12118.75	9.39E-07	1.78E-05	3.32E-10	1.54E-07		7.44E+03	6.51E+03	2.32E+09	1.25E-11	2.87E+06	1.65E+06	1.48E+06	9.95E+05	8.63E+05
13820.32	1.11E-06	2.03E-05	3.63E-10	1.85E-07		8.80E+03	7.70E+03	2.64E+09	1.37E-11	3.44E+06	1.98E+06	1.78E+06	1.19E+06	1.03E+06
15522.16	1.36E-06	2.27E-05	3.80E-10	2.25E-07		1.07E+04	9.40E+03	2.96E+09	1.43E-11	4.18E+06	2.41E+06	2.16E+06	1.45E+06	1.26E+06
17224.16	1.65E-06	2.52E-05	3.92E-10	2.70E-07		1.30E+04	1.14E+04	3.28E+09	1.48E-11	5.03E+06	2.89E+06	2.60E+06	1.74E+06	1.51E+06
18926.16	1.91E-06	2.76E-05	4.05E-10	3.11E-07		1.52E+04	1.33E+04	3.59E+09	1.52E-11	5.78E+06	3.33E+06	2.99E+06	2.01E+06	1.74E+06
20628	2.24E-06	3.00E-05	4.14E-10	3.57E-07		1.78E+04	1.55E+04	3.90E+09	1.56E-11	6.64E+06	3.82E+06	3.43E+06	2.30E+06	2.00E+06

**Assembly type: BWR, ~ 2 wt% initial enrichment, 40 years cooling time**

Burnup (MWd/ MTU)	Atom density (atoms/barn-cm <sup>3</sup> )					Characteristic Gamma-ray Emission Intensity (1/cm of fuel pin axial length/sec.)								
	Cs-134	Cs-137	Pr-144	Eu-154		Cs-134		Cs-137	Pr-144	Eu-154				
						0.6047 MeV	0.7959 MeV	0.6617 MeV	2.1857 MeV	1.2744 MeV	0.7233 MeV	1.0048 MeV	0.8732 MeV	0.9963 MeV
22329.8	2.60E-06	3.24E-05	4.19E-10	4.07E-07		2.06E+04	1.81E+04	4.22E+09	1.58E-11	7.58E+06	4.36E+06	3.92E+06	2.63E+06	2.28E+06
24003.65	2.98E-06	3.47E-05	4.24E-10	4.57E-07		2.36E+04	2.07E+04	4.52E+09	1.60E-11	8.51E+06	4.90E+06	4.40E+06	2.95E+06	2.56E+06
24016.74	2.90E-06	3.47E-05	3.91E-10	4.55E-07		2.30E+04	2.01E+04	4.52E+09	1.47E-11	8.46E+06	4.88E+06	4.38E+06	2.94E+06	2.55E+06
24121.48	2.93E-06	3.49E-05	3.92E-10	4.58E-07		2.32E+04	2.03E+04	4.54E+09	1.48E-11	8.53E+06	4.91E+06	4.41E+06	2.96E+06	2.57E+06
25823.76	3.34E-06	3.73E-05	4.01E-10	5.10E-07		2.64E+04	2.31E+04	4.85E+09	1.51E-11	9.49E+06	5.47E+06	4.91E+06	3.29E+06	2.86E+06
27526.14	3.75E-06	3.96E-05	4.07E-10	5.59E-07		2.97E+04	2.60E+04	5.16E+09	1.53E-11	1.04E+07	6.00E+06	5.38E+06	3.61E+06	3.13E+06
29228.26	4.18E-06	4.20E-05	4.10E-10	6.07E-07		3.31E+04	2.90E+04	5.47E+09	1.54E-11	1.13E+07	6.51E+06	5.84E+06	3.92E+06	3.40E+06
30930.13	4.62E-06	4.44E-05	4.12E-10	6.54E-07		3.66E+04	3.21E+04	5.78E+09	1.55E-11	1.22E+07	7.02E+06	6.30E+06	4.22E+06	3.66E+06
32632.6	5.07E-06	4.67E-05	4.13E-10	7.00E-07		4.02E+04	3.52E+04	6.09E+09	1.56E-11	1.30E+07	7.50E+06	6.73E+06	4.52E+06	3.92E+06
34334.28	5.53E-06	4.91E-05	4.14E-10	7.43E-07		4.38E+04	3.83E+04	6.39E+09	1.56E-11	1.38E+07	7.97E+06	7.15E+06	4.80E+06	4.16E+06
36008.22	5.97E-06	5.14E-05	4.14E-10	7.85E-07		4.73E+04	4.14E+04	6.69E+09	1.56E-11	1.46E+07	8.41E+06	7.55E+06	5.06E+06	4.39E+06
36021.3	5.81E-06	5.13E-05	3.81E-10	7.79E-07		4.60E+04	4.03E+04	6.68E+09	1.43E-11	1.45E+07	8.36E+06	7.50E+06	5.03E+06	4.37E+06
36126.02	5.81E-06	5.13E-05	3.82E-10	7.80E-07		4.61E+04	4.03E+04	6.68E+09	1.44E-11	1.45E+07	8.36E+06	7.50E+06	5.03E+06	4.37E+06

**Assembly type: BWR, ~ 2 wt% initial enrichment, 40 years cooling time**

Burnup (MWd/ MTU)	Atom density (atoms/barn-cm <sup>3</sup> )				Characteristic Gamma-ray Emission Intensity (1/cm of fuel pin axial length/sec.)									
	Cs-134	Cs-137	Pr-144	Eu-154	Cs-134		Cs-137	Pr-144	Eu-154					
					0.6047 MeV	0.7959 MeV	0.6617 MeV	2.1857 MeV	1.2744 MeV	0.7233 MeV	1.0048 MeV	0.8732 MeV	0.9963 MeV	
37827.87	5.84E-06	5.14E-05	3.84E-10	7.83E-07		4.63E+04	4.05E+04	6.70E+09	1.44E-11	1.46E+07	8.39E+06	7.53E+06	5.05E+06	4.38E+06
39529.93	6.32E-06	5.38E-05	3.89E-10	8.25E-07		5.01E+04	4.38E+04	7.00E+09	1.46E-11	1.54E+07	8.85E+06	7.94E+06	5.33E+06	4.62E+06
41231.8	6.77E-06	5.60E-05	3.92E-10	8.63E-07		5.36E+04	4.69E+04	7.29E+09	1.48E-11	1.61E+07	9.25E+06	8.30E+06	5.57E+06	4.83E+06
5392.57	1.31E-07	7.46E-06	2.30E-10	1.86E-08		6.78E+08	5.94E+08	1.21E+10	1.83E+00	1.63E+08	9.36E+07	8.41E+07	5.64E+07	4.89E+07
7136.52	2.34E-07	9.86E-06	2.84E-10	3.33E-08		1.53E+03	1.34E+03	1.06E+09	8.83E-12	5.11E+05	2.95E+05	2.64E+05	1.77E+05	1.54E+05
8881.42	3.63E-07	1.23E-05	3.31E-10	5.25E-08		2.37E+03	2.08E+03	1.32E+09	1.03E-11	8.07E+05	4.65E+05	4.17E+05	2.80E+05	2.43E+05
10623.1	5.18E-07	1.46E-05	3.71E-10	7.64E-08		3.38E+03	2.96E+03	1.57E+09	1.15E-11	1.17E+06	6.76E+05	6.07E+05	4.07E+05	3.53E+05
12364.61	6.97E-07	1.70E-05	4.06E-10	1.05E-07		4.56E+03	3.99E+03	1.83E+09	1.26E-11	1.61E+06	9.28E+05	8.33E+05	5.59E+05	4.85E+05
14108.4	9.00E-07	1.94E-05	4.36E-10	1.38E-07		5.88E+03	5.15E+03	2.08E+09	1.36E-11	2.12E+06	1.22E+06	1.09E+06	7.34E+05	6.37E+05
15852.43	1.13E-06	2.18E-05	4.62E-10	1.75E-07		7.37E+03	6.45E+03	2.34E+09	1.44E-11	2.69E+06	1.55E+06	1.39E+06	9.34E+05	8.10E+05
17597.72	1.37E-06	2.41E-05	4.84E-10	2.17E-07		8.99E+03	7.87E+03	2.59E+09	1.50E-11	3.33E+06	1.92E+06	1.72E+06	1.16E+06	1.00E+06
19339.26	1.64E-06	2.65E-05	5.03E-10	2.62E-07		1.07E+04	9.40E+03	2.84E+09	1.56E-11	4.02E+06	2.32E+06	2.08E+06	1.40E+06	1.21E+06
21082.02	1.93E-06	2.88E-05	5.19E-10	3.11E-07		1.26E+04	1.11E+04	3.10E+09	1.61E-11	4.77E+06	2.75E+06	2.47E+06	1.65E+06	1.44E+06

**Assembly type: BWR, ~ 2 wt% initial enrichment, 40 years cooling time**

Burnup (MWd/ MTU)	Atom density (atoms/barn-cm <sup>3</sup> )				Characteristic Gamma-ray Emission Intensity (1/cm of fuel pin axial length/sec.)									
	Cs-134	Cs-137	Pr-144	Eu-154	Cs-134		Cs-137	Pr-144	Eu-154					
					0.6047 MeV	0.7959 MeV	0.6617 MeV	2.1857 MeV	1.2744 MeV	0.7233 MeV	1.0048 MeV	0.8732 MeV	0.9963 MeV	
22025.1	2.24E-06	3.11E-05	5.33E-10	3.62E-07	1.46E+04	1.28E+04	3.35E+09	1.65E-11	5.57E+06	3.21E+06	2.88E+06	1.93E+06	1.67E+06	
24569.55	2.56E-06	3.35E-05	5.44E-10	4.16E-07	1.67E+04	1.47E+04	3.60E+09	1.69E-11	6.39E+06	3.68E+06	3.31E+06	2.22E+06	1.92E+06	
26314.67	2.90E-06	3.58E-05	5.53E-10	4.73E-07	1.90E+04	1.66E+04	3.85E+09	1.72E-11	7.26E+06	4.18E+06	3.75E+06	2.52E+06	2.18E+06	
28059.21	3.26E-06	3.81E-05	5.61E-10	5.31E-07	2.13E+04	1.86E+04	4.10E+09	1.74E-11	8.15E+06	4.69E+06	4.21E+06	2.83E+06	2.45E+06	
29800.46	3.63E-06	4.04E-05	5.67E-10	5.90E-07	2.37E+04	2.08E+04	4.34E+09	1.76E-11	9.05E+06	5.22E+06	4.68E+06	3.14E+06	2.72E+06	
31544.85	4.02E-06	4.27E-05	5.72E-10	6.49E-07	2.63E+04	2.30E+04	4.59E+09	1.78E-11	9.97E+06	5.74E+06	5.15E+06	3.46E+06	3.00E+06	
33288.38	4.42E-06	4.50E-05	5.75E-10	7.10E-07	2.89E+04	2.53E+04	4.84E+09	1.79E-11	1.09E+07	6.28E+06	5.63E+06	3.78E+06	3.28E+06	
35032.8	4.84E-06	4.73E-05	5.78E-10	7.70E-07	3.16E+04	2.77E+04	5.08E+09	1.79E-11	1.18E+07	6.81E+06	6.11E+06	4.10E+06	3.56E+06	
36778.14	5.27E-06	4.96E-05	5.80E-10	8.29E-07	3.44E+04	3.01E+04	5.33E+09	1.80E-11	1.27E+07	7.34E+06	6.58E+06	4.42E+06	3.83E+06	
38524.84	5.71E-06	5.19E-05	5.81E-10	8.88E-07	3.73E+04	3.27E+04	5.57E+09	1.80E-11	1.36E+07	7.86E+06	7.05E+06	4.73E+06	4.11E+06	
40268.75	6.15E-06	5.41E-05	5.81E-10	9.47E-07	4.02E+04	3.52E+04	5.82E+09	1.80E-11	1.45E+07	8.38E+06	7.52E+06	5.04E+06	4.38E+06	
4425.52	7.24E-08	6.51E-06	2.86E-10	1.25E-08	5.74E+02	5.02E+02	8.48E+08	1.08E-11	2.33E+05	1.34E+05	1.20E+05	8.06E+04	7.00E+04	
9119.28	3.95E-07	1.34E-05	4.92E-10	6.01E-08	3.13E+03	2.74E+03	1.74E+09	1.85E-11	1.12E+06	6.45E+05	5.78E+05	3.88E+05	3.37E+05	

Assembly type: BWR, ~ 2 wt% initial enrichment, 40 years cooling time														
Burnup (MWd/ MTU)	Atom density (atoms/barn-cm <sup>3</sup> )					Characteristic Gamma-ray Emission Intensity (1/cm of fuel pin axial length/sec.)								
	Cs-134	Cs-137	Pr-144	Eu-154		Cs-134		Cs-137	Pr-144	Eu-154				
						0.6047 MeV	0.7959 MeV	0.6617 MeV	2.1857 MeV	1.2744 MeV	0.7233 MeV	1.0048 MeV	0.8732 MeV	0.9963 MeV
13423.99	9.14E-07	1.96E-05	6.44E-10	1.38E-07		7.25E+03	6.35E+03	2.56E+09	2.42E-11	2.58E+06	1.49E+06	1.33E+06	8.94E+05	7.76E+05
17475.18	1.58E-06	2.55E-05	7.67E-10	2.42E-07		1.25E+04	1.10E+04	3.33E+09	2.89E-11	4.51E+06	2.60E+06	2.33E+06	1.56E+06	1.36E+06
21315.45	2.37E-06	3.11E-05	8.67E-10	3.64E-07		1.88E+04	1.64E+04	4.05E+09	3.26E-11	6.78E+06	3.91E+06	3.51E+06	2.35E+06	2.04E+06
24996.51	3.24E-06	3.64E-05	9.48E-10	4.99E-07		2.57E+04	2.25E+04	4.75E+09	3.57E-11	9.29E+06	5.35E+06	4.80E+06	3.22E+06	2.79E+06
24996.51	3.16E-06	3.64E-05	8.49E-10	4.95E-07		2.50E+04	2.19E+04	4.74E+09	3.20E-11	9.23E+06	5.31E+06	4.77E+06	3.20E+06	2.78E+06
25041.79	3.18E-06	3.66E-05	8.62E-10	4.99E-07		2.52E+04	2.20E+04	4.76E+09	3.25E-11	9.29E+06	5.35E+06	4.80E+06	3.22E+06	2.79E+06
25403.02	3.27E-06	3.71E-05	8.75E-10	5.13E-07		2.59E+04	2.27E+04	4.83E+09	3.29E-11	9.55E+06	5.50E+06	4.94E+06	3.31E+06	2.87E+06
27978.28	3.96E-06	4.09E-05	9.46E-10	6.14E-07		3.14E+04	2.75E+04	5.33E+09	3.56E-11	1.14E+07	6.59E+06	5.91E+06	3.97E+06	3.44E+06
31220.67	4.91E-06	4.57E-05	1.00E-09	7.49E-07		3.89E+04	3.40E+04	5.95E+09	3.77E-11	1.39E+07	8.03E+06	7.21E+06	4.83E+06	4.19E+06
34196.97	5.83E-06	5.00E-05	1.03E-09	8.77E-07		4.62E+04	4.04E+04	6.51E+09	3.90E-11	1.63E+07	9.41E+06	8.44E+06	5.66E+06	4.91E+06
37130.12	6.80E-06	5.43E-05	1.06E-09	1.00E-06		5.39E+04	4.72E+04	7.07E+09	4.00E-11	1.87E+07	1.08E+07	9.67E+06	6.49E+06	5.63E+06
39895.07	7.74E-06	5.83E-05	1.08E-09	1.13E-06		6.14E+04	5.37E+04	7.59E+09	4.06E-11	2.10E+07	1.21E+07	1.08E+07	7.27E+06	6.30E+06

## Appendix C

### **TOMOPACK software for Objective 2 System Matrices**

A deterministic methodology for fast and efficient calculation of system response functions and execution of algebraic pin-activity reconstruction of nuclear fuel assemblies is implemented in the TOMOPACK software package. TOMOPACK was developed in the early 2000's by researchers at Uppsala University for the purpose of tomographic pin-power measurements on commercial nuclear fuel assemblies. The applicability of the software was demonstrated in measurements on a laboratory fuel mockup respectively on commercial BWR fuel at the Forsmark NPP. A copy of the software was sold to the Institute for Energy Technology (IFE, Norway) in 2012 to be used within the OECD Halden Reactor Project, where its applicability has been further demonstrated on fuel assemblies from the HBWR research reactor. In all cases studied, a capability has been demonstrated to reconstruct pin-by-pin data from irradiated nuclear fuel assemblies with a precision in the order of one to a few percent.

In the UGET project, TOMOPACK has been used in the SWESP reconstructions of simulated data from BWR and PWR fuel assemblies, as described in Section 11.1. The simulations, described in section 8.0, were executed by means of Monte Carlo calculations (using MCNP), and, accordingly, the models implemented in TOMOPACK are completely independent from the models used in the simulations, both in terms of geometric as well as physics modelling. The precision demonstrated in Section 11.1 for the simulated data of the UGET project was consistent with the precision previously demonstrated for experimental data, adding further confidence to the performance of the code.

An overview of the general properties of algebraic reconstruction methods is given in Section 9.1.2, while an overview of the analysis methodology implemented in TOMOPACK is presented in Appendix C. This appendix focuses primarily on the software implementation, but some notes are also given on the physics representation.

#### **The software's physics representation**

As described in Section 11.1, TOMOPACK is based on deterministic transport calculations of the unscattered gamma flux from a set of picture elements (pixels) through a geometry of fuel rods and assembly construction materials to a collimated gamma-ray detector setup. This calculation mode makes TOMOPACK adapted to a measurement situation where full-energy peaks are selected in recorded gamma-ray energy spectra and used for the analyses. If such a selection is provided, the data produced by TOMOPACK represents the distribution of the particular isotope that emits the selected gamma rays. Separate analyses can be performed of different energy peaks, giving the possibility to determine fuel parameters on the individual fuel rod level, according to Section 11.1.2.

There are two main features of the modelling implemented in TOMOPACK:

1. The instrument response is modelled for axially symmetric 3D objects, such as nuclear fuel rods,
2. The attenuation is modelled in detail for full-energy gamma rays that are emitted from the fuel through the measured object to the detector.

The modelling can be described by Eqs. (9.4a) and (9.4b), which are presented in Section 9.3.1. In this context, one may note a few items:

- The intrinsic response function for an instrument (not taking any attenuation in the measured object into account), may be calculated separately and stored for each gamma-ray energy analyzed, leaving only the attenuation part for the on-line reconstructions.
- In spite of being a function described in 2D, the intrinsic response function includes 3D effects like (i) solid angle of the detector as seen from the point of emission, (ii) visible height of the object at the 2D distance between the point of emission and the detector, and (iii) gamma-ray transmission through the collimator material.
- There is also a possibility to add contributions from coherent scattering in the collimator material to the intrinsic response function by adding a term similar to the collimator transmission term (Eq. (9.4b)).
- The attenuation coefficients for the materials involved have been obtained using the XCOM photon cross section data base.<sup>1</sup>
- The calculations of gamma-ray attenuation can be adapted to the current geometry of the fuel and measurement setup, including e.g. assembly torsion and/or lateral displacement as well as equipment offsets and/or irregular angular and/or lateral distances of the recorded data points,
- The attenuation part is implemented as a pure 2D function, enabling high-speed on-line computation of the system response matrix,  $W$ , while taking the current geometry into account.

Furthermore, the pixel pattern can be adapted to the size and position of each individual fuel rod, implying that numeric rod-by-rod data can be extracted directly from the reconstructions, without the need for additional analysis steps.

## Programming language and object-oriented structure

The TOMOPACK software was developed in standard Fortran90 (F90). It is thus applicable on any platform for which there is a F90 compiler available. So far, it has primarily been used in a standard Windows PC or laptop environment, but it has also been executed on a Linux computer cluster. TOMOPACK has primarily been intended as a research tool, which is operated by researchers who develop methods and tools for analyses of nuclear fuel and perform experimental characterization of nuclear fuel. Accordingly, it is currently implemented as a “console application”, meaning that the execution is completely defined directly in the F90 code. At present, there is thus no “window-based, user-friendly interface” developed for the software.

In order to allow for flexibility, both regarding the ability of treating various fuel configurations and various reconstruction strategies, the implementation is fully object-oriented. Accordingly, all attributes and functions defined for a certain object are collected in a separate module, specific for that object, and an object’s attributes are only available using the functions and subroutines defined in the module. Consequently, various parts of the code that involve a certain object can use the same modules, and improvements made in one module will immediately be valid for all parts of the code using it. Provided that calls to functions and subroutines remain unchanged, the module can be used continuously, without requiring any changes in other parts of the code, even if internal changes have been made to the module and its functions and subroutines. Furthermore, new modules and subroutines can be seamlessly added, without affecting other parts of the software, thus simplifying the evaluation of alternative analysis paths.

---

<sup>1</sup> The XCOM database is managed by The National Institute of Standards and Technology (NIST). It is available at <http://www.nist.gov/pml/data/xcom/>



Three main groups of objects and modules have been implemented in the software, which are further described below:

- Basic modules
- Geometry modules
- Tomography modules

In addition, three pieces of software span over the execution, namely a module specific for the data of a particular measurement setup (here: the UGET device design), the IO module and the main program. These are also described below.

## Basic modules

There are two basic modules:

- Data\_Kind\_mod.f90

This module contains the definitions of the data types and constants used in the calculations. Here, one may note that the code currently uses double precision for all float type values, defined as a data type named “dup”. Double precision generally requires longer execution than default precision, but allows for higher precision in the calculations. However, the precision can easily be changed in this module by redefining the “dup” data type.

- Attenuation\_mod.f90

This module contains attenuation coefficients for a number of pre-defined gamma-ray energies and materials, stored in arrays. The code is designed for using data from one specific gamma-ray energy, and the attenuation coefficients for the pre-defined materials are extracted using the subroutine:

```
“Attenuation_SelectEnergy(My_array,EnergyNum)”.
```

Enumerated names can be used when selecting values from the arrays. As an example, one can select the 662 keV gamma-ray energy of Cs-137 by calling the subroutine using `EnergyNum=Csl37_662`. The subroutine returns the attenuation coefficients of the material selected in the “My\_array”. Enumerated names can also be used when selecting the attenuation coefficient for a certain material. To use the coefficient for water, one may e.g. write: `My_array(H2O)`.

## Geometry modules (2-dimensional)

The geometry modules describe various 2-dimensional geometrical formations, i.e. POINT, LINE, CIRCLE, RING, CIRCLE PART, TRIANGLE and QUADRANGLE, and their properties. Subroutines describing the interaction between the different geometrical objects are implemented in a module called GEOMETRY\_2D. These modules are further described below.

- Point\_2D\_mod.f90

The attributes of the least complex item, POINT, are two float type numbers: [x] and [y]. To make use of this object easier, operators such as assignment(=), addition(+), subtraction(-) and multiplication(\*) have been implemented. There are also operators for retrieving common information, such as the POINT attributes, the distance between two points etc. Additional subroutines are available, e.g. for rotating a POINT object around another POINT object and for sorting an array of points by their x- or y-values.

- Line\_2D\_mod.f90

Two POINT type items can define a LINE, but a LINE can also be infinite, i.e. without endpoints, and it is then defined using the coefficients “k” and “m” as in  $y = kx + m$ . There are similar operators defined for the LINE object as for the POINT object, but some notable additions are e.g. the operators defined for checking whether two lines cross each other, for calculating the cutpoint between two

lines and the operators for calculating the nearest point and the nearest distance between a LINE and a POINT.

- **Triangle\_2D\_mod.f90**  
Three POINT type items can be used to define a TRIANGLE. As for the previous objects, there are several operators defined also for this object, but a notable addition is the operator for getting its area.
- **Quadrangle\_2D\_mod.f90**  
Four POINT type items can be used to define a QUADRANGLE. There are similar operators defined as for the TRIANGLE object.
- **Circle\_2D\_mod.f90**  
The CIRCLE type has a POINT and a radius (float type number) as its attributes. There are similar operators defined as for the objects above, but some additional routines may also be noted. In particular, routines to spread a number of points within the object's area respectively to get a random point within this area are useful when defining points of emission for gamma rays from the fuel to the detector.
- **Ring\_2D\_mod.f90**  
A RING object is defined using a POINT and two radii (inner and outer). Similar routines are available as for the CIRCLE object.
- **Circle\_part\_2D\_mod.f90**  
A CIRCLE\_PART object is defined using a POINT, two radii (inner and outer) and two angles (minimum and maximum). If the minimum and maximum angles selected imply that the whole 360-degrees are covered, the object will be similar to a Ring or a Circle, albeit defined differently in the code. A few alternatives of the CIRCLE\_PART object are illustrated in Figure APX C.1.

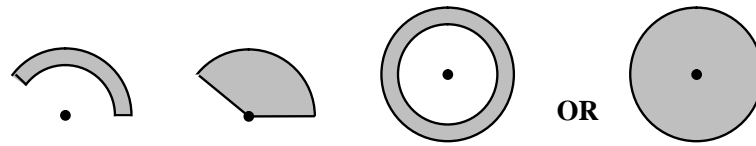


**Figure APX C.1.** Illustration of some possible geometries of the CIRCLE\_PART object.

Similar routines are available for the CIRCLE\_PART object as for the CIRCLE object. One important use of the CIRCLE\_PART object in TOMOPACK is in the definition of pixels that adapt to the size and position of fuel rods. These pixel objects are further described below.

- **Geometry\_2D\_mod.f90**  
This module does not describe any particular object but is rather used to describe the interaction between the geometry objects above. Some of the routines implemented in this module are operators for getting the distance between objects, getting a logical answer to whether a POINT lies within an object or not, getting the distance that a LINE travels through an object, etc. As further described below, these routines are e.g. used when calculating the travel lengths of a gamma ray through the various parts of a nuclear fuel assembly.

The software structure implemented for the geometry modules is illustrated in Figure APX C.2.

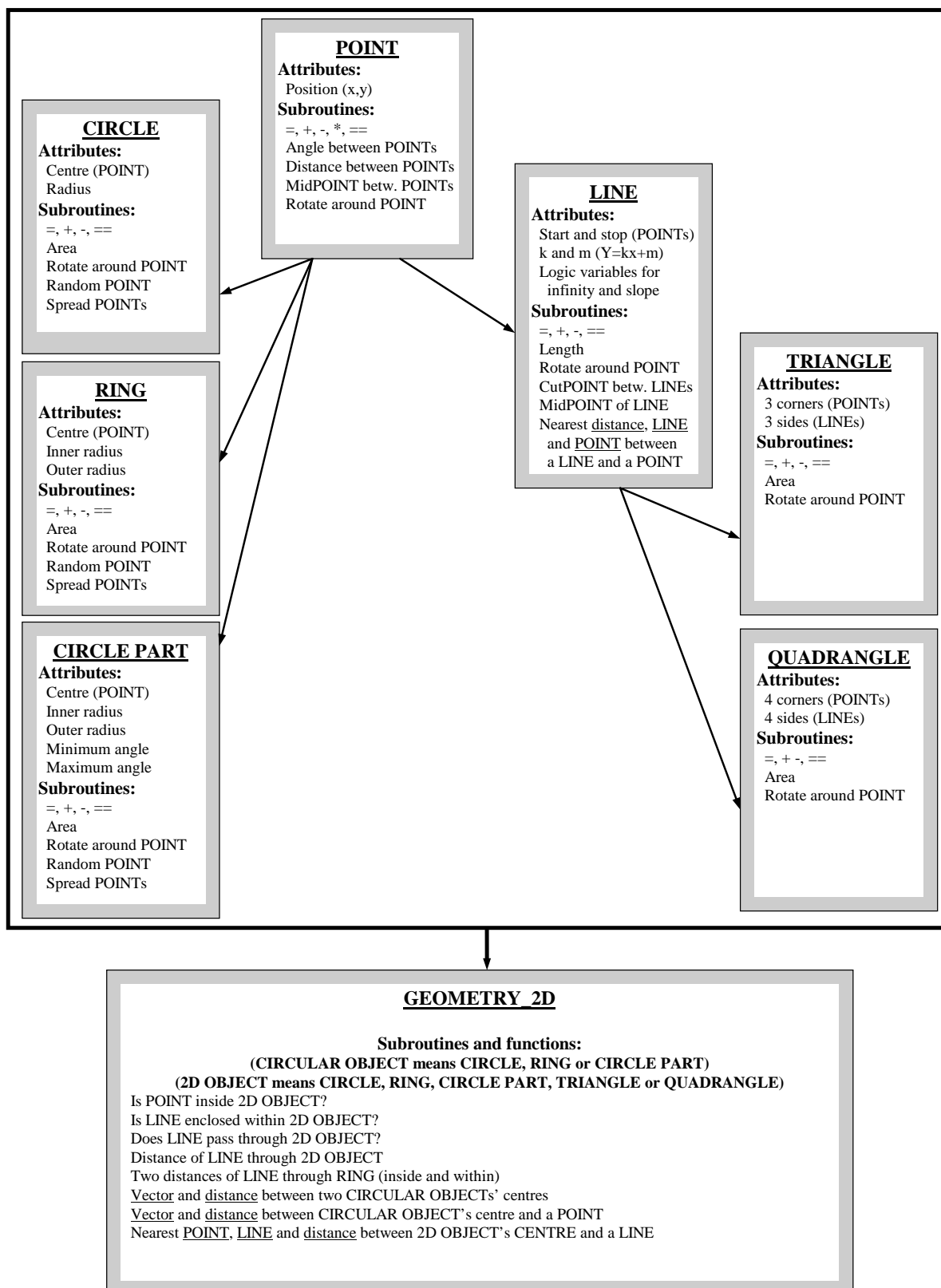


**Figure APX C.2.** Overview over the TOMOPACK software implementation of geometry modules.

## Tomography modules (2-dimensional).

The tomography modules are used to define nuclear fuel and other objects and operations involved when performing a tomographic measurement. The tomography objects make use of the geometry objects, described above. By defining a gamma-ray as a LINE and a fuel rod as a RING, the software may e.g. easily retrieve the travel distances of the gamma ray through the different materials of the fuel rod, and thus easily calculate the gamma-ray attenuation. Furthermore, various geometric configurations of the fuel and equipment can be easily implemented and various types of pixel patterns can be defined for the tomographic reconstructions. In addition, routines are implemented to facilitate changes to a nominal, pre-defined geometry, which has proven useful when analyzing data from experiments on irradiated fuel. (As described in Section 10.2.1, the current experimental geometry, including angular and lateral offsets of the measured assembly, can be identified using image analysis of FBP images. These offsets can easily be taken into account in rod-activity analyses using TOMOPACK, as demonstrated in previous measurements using the PLUTO device.)

- Measurement\_mod.f90

The MEASUREMENT object comprises three float-type attributes: Rotation, Translation and Intensity. It thus carries information of each gamma-ray intensity recorded and the position of the recording detector element and its related collimators relative to the object, when recording that intensity. Among the routines implemented, one may note the possibility to correct intensities with a selected factor, typically used for detector efficiency calibration, and to remove low-intensity data points. The latter is adequate due to the fact that low-intensity data points have poor relative uncertainty and zero-intensity data points do not even carry any information at all on rod activities (being the subject for analyses using TOMOPACK).

- Collimator\_2D\_mod.f90

A collimator is defined using four values: the width, height and length of the collimator slit and the distance from its front opening to the rotation centre of the measurement setup. These values are then used to set four POINTs in 2D, defining one LINE for the slit's front opening and one LINE for its back opening. The COLLIMATOR object is illustrated in Figure APX C.3.

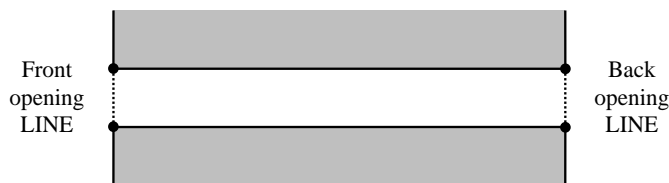


**Figure APX C.3.** Illustration of the COLLIMATOR object.

The angular and lateral position of the collimator is set for each data point according to the information in Measurement\_2D\_mod. All calculations of the extent to which the detector element can be exposed to gamma radiation from different parts of the fuel are based on the two opening LINES and the position relative to the point of emission according to Eq. (9.4a). Gamma-ray transmission through the corners of the collimator slit are added using pre-calculated data according to Eq. (9.4b). As an alternative, the complete intrinsic response function of the detector system can be pre-calculated and used. An example of the calculated intrinsic response function for the UGET device to axially symmetric objects (like nuclear fuel rods) is presented in Figure 41 in Section 9.2.2.

- Fuel\_box\_2D\_mod.f90

The box surrounding BWR fuel (a.k.a. “fuel channel”) is modelled using QUADRANGLE and CIRCLE\_PART objects. Nominal FUEL\_BOX geometries can be added to the software based on

available data sheets. Routines are e.g. implemented for positioning the FUEL\_BOX and for calculating the travel distance of a gamma ray (LINE) through its materials.

- Fuel\_2D\_mod.f90

The FUEL (assembly) object comprises an optional FUEL\_BOX object and a set of arrays of RING objects, representing e.g. fuel rods, water rods, homogeneous steel or zircaloy rods and gas-filled rods, respectively. (The latter may be used to take into account the fact that measurements may be performed at an axial level covering the gas plenum of some fuel rods.) An illustration of the FUEL object is presented in Figure APX C.4.

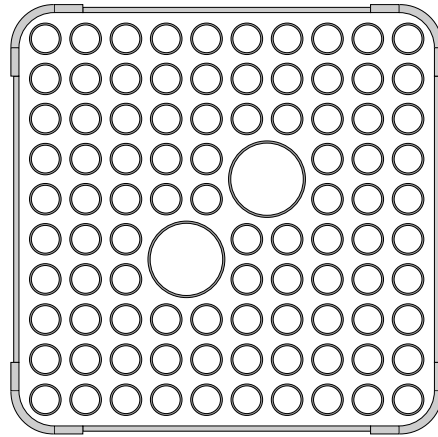


**Figure APX C.4.** Illustration of the FUEL object, here with data for a GE12S fuel assembly. In this case, small-diameter RINGS are fuel rods and large-diameter RINGS are water rods.

There is a large number of operators and subroutines for assigning a FUEL object, for retrieving its information, for moving or rotating it, for assigning positions of individual fuel rods etc, but the most important routines for tomography are the ones for calculating the travel distances of gamma rays (LINES) in different materials. In particular, the subroutine “FUEL\_2D\_LineTravelDists” is used in the Tomography\_2D module.

- Circlepart\_pixel\_mod.f90

The attributes of the PIXEL objects are a CIRCLE\_PART object (see Figure APX D.1), an activity and a pointer for storing the pixel’s contribution coefficients (i.e. the coefficients in the system matrix that represent the defined pixel). The subroutines and operators implemented mainly cover the defining, setting and retrieving of information to/from this object.

- Tomography\_2D\_mod.f90

Subroutines for executing tomographic reconstructions are collected in this module, which uses the objects accounted for above. The most important routines are the following:

- Calculate the system matrix,  $W$ , used in an algebraic reconstruction,
- Set initial activities in the pixels, based on measured intensities and calculated contribution coefficients,
- Solve the inverse problem (perform reconstructions) using e.g. the ASIRT method.

Furthermore, there are routines for deducing information of possible dislocations of a fuel rod based on the use of a symmetric pixel pattern over the rod.

An illustration of the interaction between the software modules can be found in Figure APX C.5

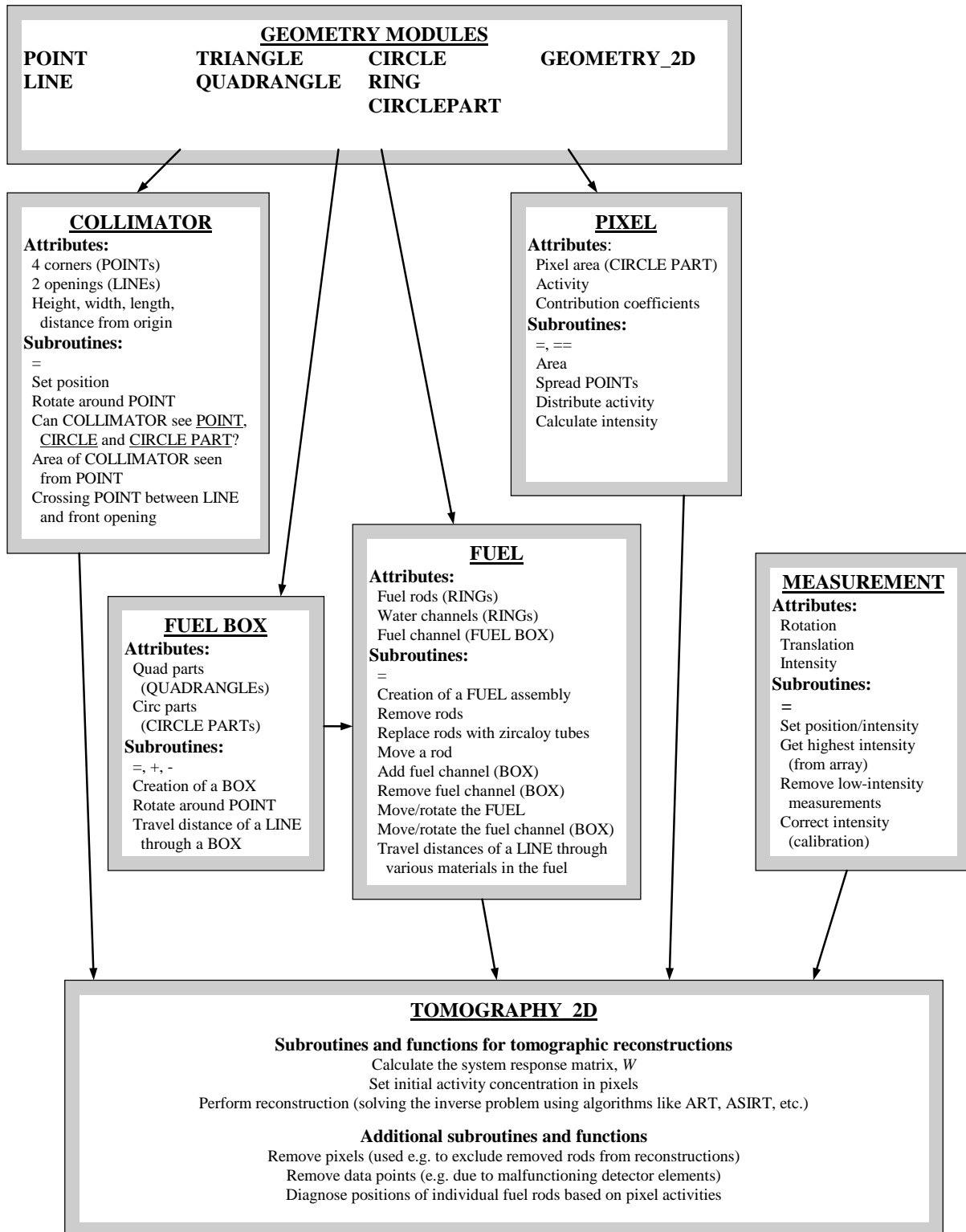


Figure APX C.5. Overview over the TOMOPACK software implementation of tomography modules.

## Other modules and main program

In order to perform reconstructions of the data obtained using a tomographic measurement device, some additional modules and a main program are implemented according to the following:

- **IO\_mod.f90**  
Input/output can be made manually/to screen or using files. All input/output is defined in the module IO\_mod.f90.
- **UGET\_mod.f90 (and other device-specific modules)**  
It has been found useful to implement a module for each specific measurement device for which data is analyzed using TOMOPACK. Accordingly, such a module has been created for the UGET device design in the JNT 1955 project. In particular, the device-specific modules comprise routines that read data from the device (in the UGET case: simulated data) and transfer it to the format defined for the MEASUREMENT object. It has also been found useful to implement e.g. routines for efficiency calibration of individual detector elements in the respective device-specific module.

### Reconstruction.f90 (main program)

In the main program, all the above modules are used to execute a tomographic reconstruction of the rod-wise activity content in the fuel assembly based on measured or simulated intensities. The assembly type is defined, the materials and the gamma-ray energy are defined, the pixel pattern is selected and details on the reconstruction are set.

In the main program, adjustments may also made to the assembly geometry (using the routines defined in the FUEL module), with details obtained e.g. using analysis of reconstructed FBP images. The routines allow the pixel pattern to be defined in accordance with the selected fuel geometry. Similarly, eventual corrections for detected offsets in the measurement setup are made in the main program. Furthermore, a discriminator level of the lowest intensities that are accepted is selected.

In the main program, the system matrix,  $W$ , is calculated, and using the measured (or simulated) intensities, the inverse problem is solved, returning a set of reconstructed pixel activities. Provided that the pixel pattern has been defined so that each rod is covered by a well-defined set of pixels, the program can return rod-by-rod activities without requiring any additional analyses of the data.

As pointed out above, one should note that although all items are defined using 2D geometry objects, calculations are performed taking the third (axial) dimension into account. This is enabled by the basic assumption that nuclear fuel is axially symmetric.

## Notes on time consumption and memory needs

The deterministic character of TOMOPACK, and its use of basic geometric functions, allows for fast execution of the tomographic reconstructions. As an example, the execution of reconstructions of experimental data from the PLUTO device was generally performed within a few minutes on a standard laptop. However, one should note that the execution time depends on the size of the problem, i.e. the number of data points recorded and the number of pixels selected for the reconstruction. There are two main calculation steps, for which execution time depend differently on problem size:

- The time required for calculating the system matrix depends linearly on the number of data points and it is also typically linearly dependent on the size of the fuel under study. (Since an axial cross section

of PWR fuel is about twice as large as that of BWR fuel, one should expect the execution time to double for PWR as compared to BWR due to image size.)

- The time required for solving the inverse problem depends to a higher order on problem size. The ASIRT solution method (see Eq. (9.3)) used in this work is iterative, and the time required for one iteration depends on both the number of data points and the image size (the number of pixels). Furthermore, the number of iterations required for the solution to converge also depends on the size of the problem.

In addition, one should note that storing the system matrix,  $W$ , in the computer memory may require relatively large memory usage. Experience from this project indicates that as long as the computer's cache memory can hold the problem, execution is generally performed within on the order of minutes. If data needs to be swapped to external memory, execution time grows.

Still, all pin-activity reconstructions performed in this work has been relatively fast; a standard laptop has been used even for the largest problems defined for the UGET device (PWR fuel recorded with more than 20,000 data points), and execution has been performed within about one hour per reconstruction. If faster execution time is required, one may e.g. implement parallel computing (for which the computations encountered in algebraic reconstruction are highly suitable) and thus use the multi-core capability available in most modern computers to allow for even shorter computation times.



## Appendix D

### RADSAT for Objective 2 System Matrices

To address the question of performing reconstructions with a model independent system response function, a deterministic Radiation Detection Scenario Analysis Toolbox (RADSAT) transport model of a 126-pin VVER-440 spent nuclear fuel assembly previously modeled with Monte Carlo N-Particle (MCNP), was considered. Six pins are assumed to be missing and 120 of the pins emit 662 keV gammas from decaying  $^{137}\text{Cs}/^{137}\text{Ba}$ . In general, both Monte Carlo and deterministic transport approaches require the definition of model geometry, materials and their cross sections, detector observables, and solution convergence parameters. Of course, the specifics of each method differ in the way they are implemented, but once all detector observables are calculated the tomographic reconstruction is calculated the same way in both approaches. The challenge for both approaches is to calculate efficiently the large number of detector projections for tomography; specifically, 159 detector responses for each of 128 angles. For Monte Carlo efficiency equates to tracking particle histories with the greatest influence on the observables. While a huge body of research exists on variance reduction methods to weight the most important particle histories, the problem becomes increasingly challenging when contributions from scattering become dominant. For deterministic transport efficiency equates to choosing the sparsest spatial, angular and energy quadratures that are still representative of the system geometry and transport physics.

The RADSAT model geometries used in this study were based on MCNP models of the water-water energetic reactor (VVER) and pressurized water reactor (PWR) fuel assemblies. Figure APX D.1 shows RADSAT model geometry and mesh for a VVER-440 fuel assembly: the outlines of a 2-mm horizontal mesh scale across pins with a 0.757 cm outer diameter (OD) and an increasing mesh scale on the order of centimeter in the water. The mesh scale in the axial direction was on the order of 50 cm to take advantage of the axial symmetry.

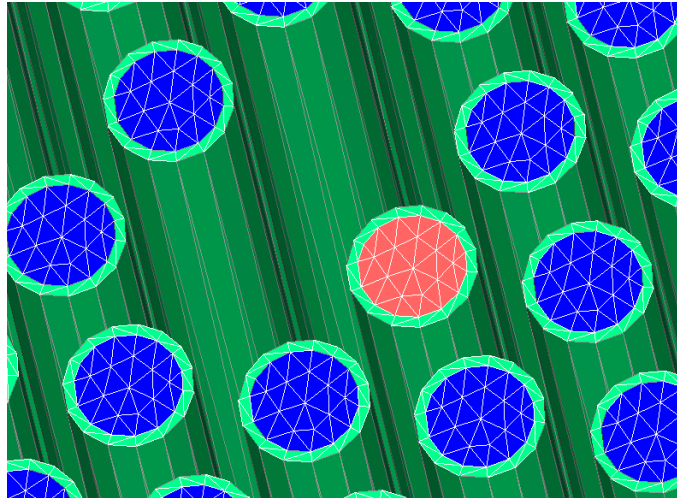


**Figure APX D.1.** Predefined tetrahedral mesh showing fuel and clad regions.

A 50-cm length segment of the assembly was assumed for RADSAT with gamma emission from the entire length for the universal gamma emission tomographer (UGET) simulations, but not for modeling

the passive gamma emission tomographer (PGET). Because the PGET MCNP model assumed the emitting source extended only 1 cm; the same assumption was made for RADSAT to avoid systematic field-of-view biases.

While the MCNP model accurately modeled the fuel pin, gap space, and cladding regions with the corresponding materials, the RADSAT model treated the fuel, gap as part of the cladding and did not include the central hole in the fuel. This simplification was assumed to make the number of mesh cells (126,000) computationally tractable while preserving the pin masses and the dimensions of the assigned source regions. Additionally, no attempt was made to model the 10-cm-thick JNT 1510 collimator in the RADSAT transport model. Instead, the angular flux solution was calculated at all detector positions for all collimator angles in a single RADSAT transport run using an  $S_{16}$  triangular Chebychev Legendre quadrature.

For PGET, down scatter energy groups were calculated with a subset of angles (257) of a last collided flux (LCF)  $S_{120}$  quadrature looking back from a detector position through a collimator opening are shown in Figure APX D.2 (left). Two user-defined square Chebychev Labatto quadratures (subsets of  $S_{120}$ ) with zeniths facing the detectors were used to calculate the scalar flux sinograms and to test collimator penetration. The calculated scalar flux showed no significant difference in the two quadrature sets and all reported results are calculated with the 257 angles shown on the left side of Figure APX D.2. For the angles that penetrate the collimator (Figure APX D.2 outside the rectangle), an attenuated flux was calculated from the transport angular flux and the known path length through tungsten for each of the energy groups. Of course no attenuation was assumed for the angles within the field of view (FOV) of the aperture. For the peak groups the 6614 angles (Figure APX D.2, center) were used for PGET to accurately resolve the 1-cm emitting region of the pins and avoid ray effects.

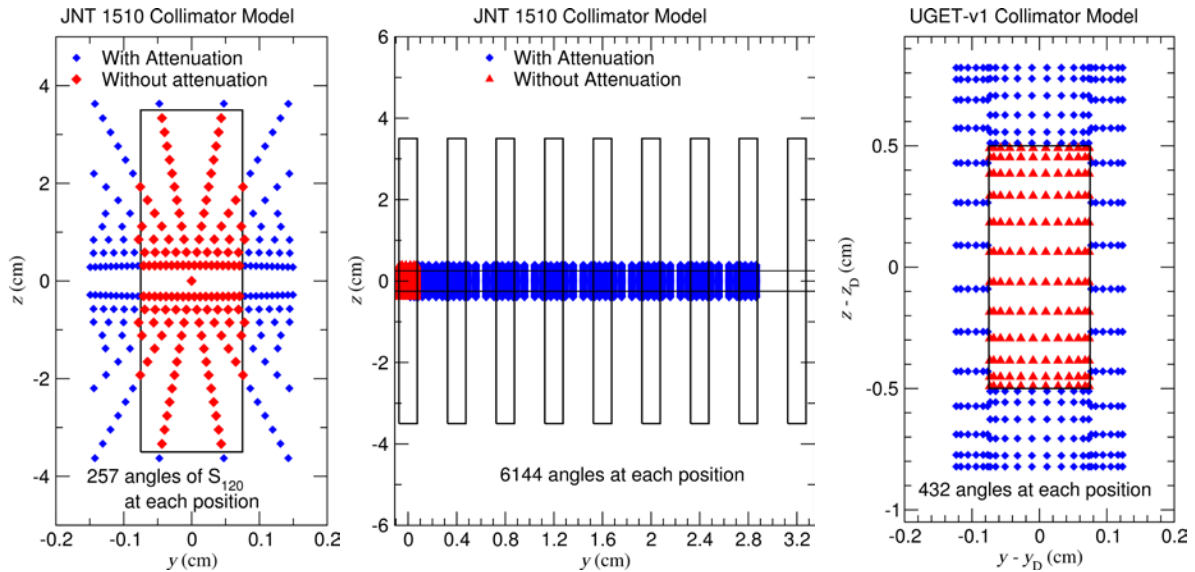


**Figure APX D.2.** Treatment of JNT 1510 collimator with two sets of angles showing aperture field of view angles (red) and penetrating angles (blue) for down-scatter energy groups (left) and peak energy groups (center); and (right) treatment of the UGET-v1 collimator with unattenuated aperture field of view angles (red) and penetrating angles (blue).

A program was written for performing the collimator calculations and converting the angular flux to sinograms. The average scalar flux over the detector was calculated from the angular flux according to:

$$\bar{\varphi} = \frac{1}{wh} \int_{-w/2}^{w/2} dy_D \int_{-h/2}^{h/2} dz_D \int_{-w/2}^{w/2} dy \int_{-h/2}^{h/2} dz \frac{D \exp[-\mu_w l(\hat{\Omega})]}{4\pi R^3} \psi(\hat{\Omega}) \quad (\text{E-1})$$

where

$w$  and  $h$  are the width and height of the collimator,

$l(\hat{\Omega})$  is the path length through the collimator in direction  $\hat{\Omega}$ ,

$\mu_w$  is the tungsten cross section

and the coordinate system is given in Figure APX D.3. The integral over the detector face was assumed to be  $wh$  with  $(y_D, z_D) = (0, 0)$ . For the ( $D = 10$  cm) PGET collimator it was necessary to consider septal penetration that could occur through adjacent neighboring apertures (Figure APX D.2, center) to accurately (<3 percent) reproduce the peak energy flux of MCNP. For the downscatter energies (Figure APX D.2, left) it is likely that the PGET collimator model did not include enough angles penetrating the collimator to accurately reproduce the MCNP scatter contribution for the higher energies ( $> 1000$  keV). For the longer ( $D = 20$  cm) UGET collimator, no attenuated paths through the tungsten were assumed for 662 keV and the angles shown in blue (Figure APX D.2, right) were assumed for 1274 keV. It was determined that the additional penetration flux for UGET was only a few percent for 662 keV, but could be 10-12 percent for 1274 keV.

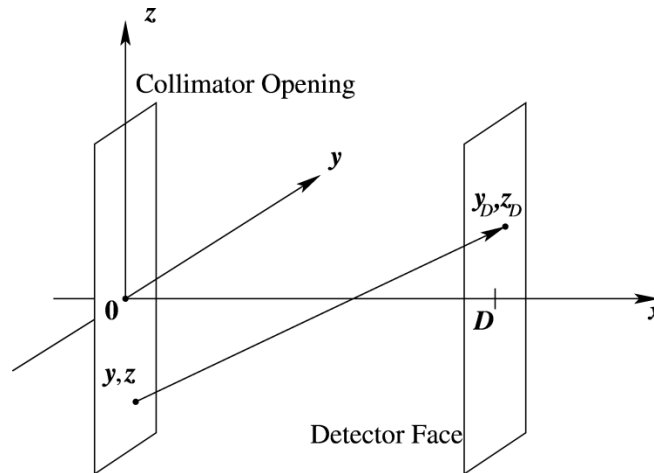


**Figure APX D.3.** Coordinate system to define angular quadrature for modeling the collimators.

For a “without penetration angle” comparison of both collimators, Equation E-1 gives the angular sensitivities shown in Figure APX D.4, where the integral over the aperture sensitivities gives the effective solid angle FOV for each collimator.

A comparison of the main features of the reconstruction is shown at the peak energy in Figure APX D.5 and Figure APX D.6 for VVER-440 and PWR assemblies respectively. Visually, there appears to be little difference between the reconstructions for the MCNP model and the RADSAT model (Figure APX D.7,

Figure APX D.8). A close comparison shows that RADSAT may give slightly less contrast for the outer pins and slightly more contrast for the inner pins. Further work is needed to determine if this is a consequence of the aperture effect or of some other model difference.

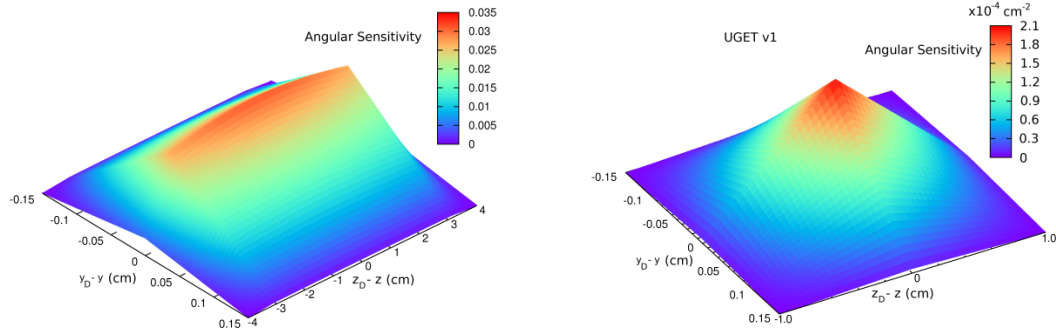


**Figure APX D.4.** Angular sensitivities of the PGET (left) and UGET (right) collimators.

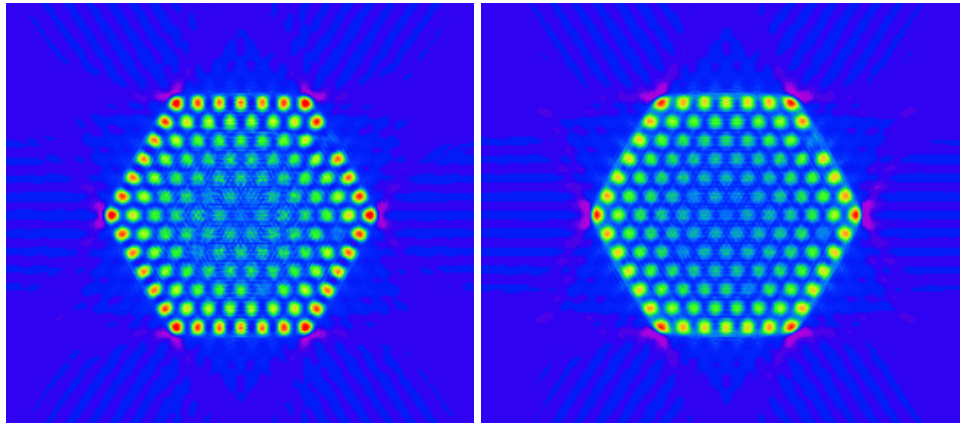


**Figure APX D.5.** Reconstructions from 661-662 keV sinograms from MCNP (left) and RADSAT (right) based models for a VVER-440 assembly.

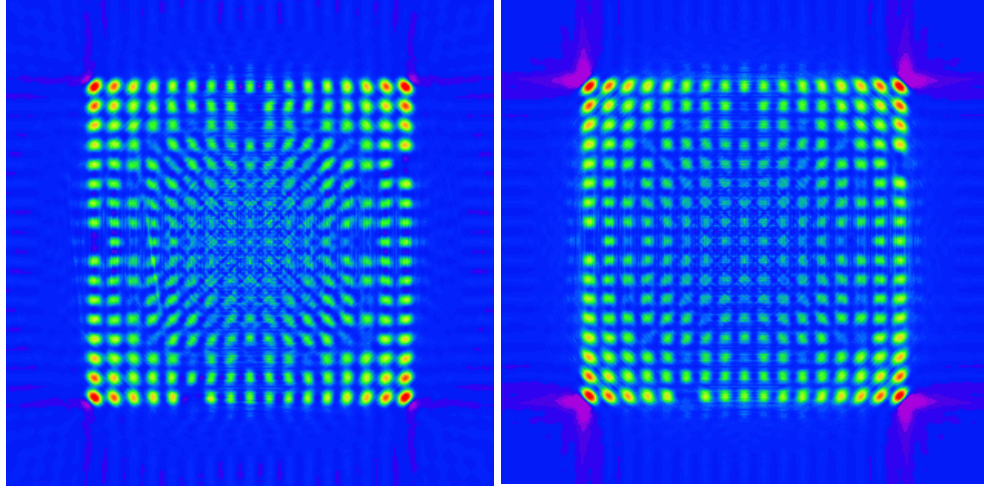


**Figure APX D.6.** Reconstructions from 661-662 keV sinograms from MCNP (left) and RADSAT (right) based models for a PWR assembly.

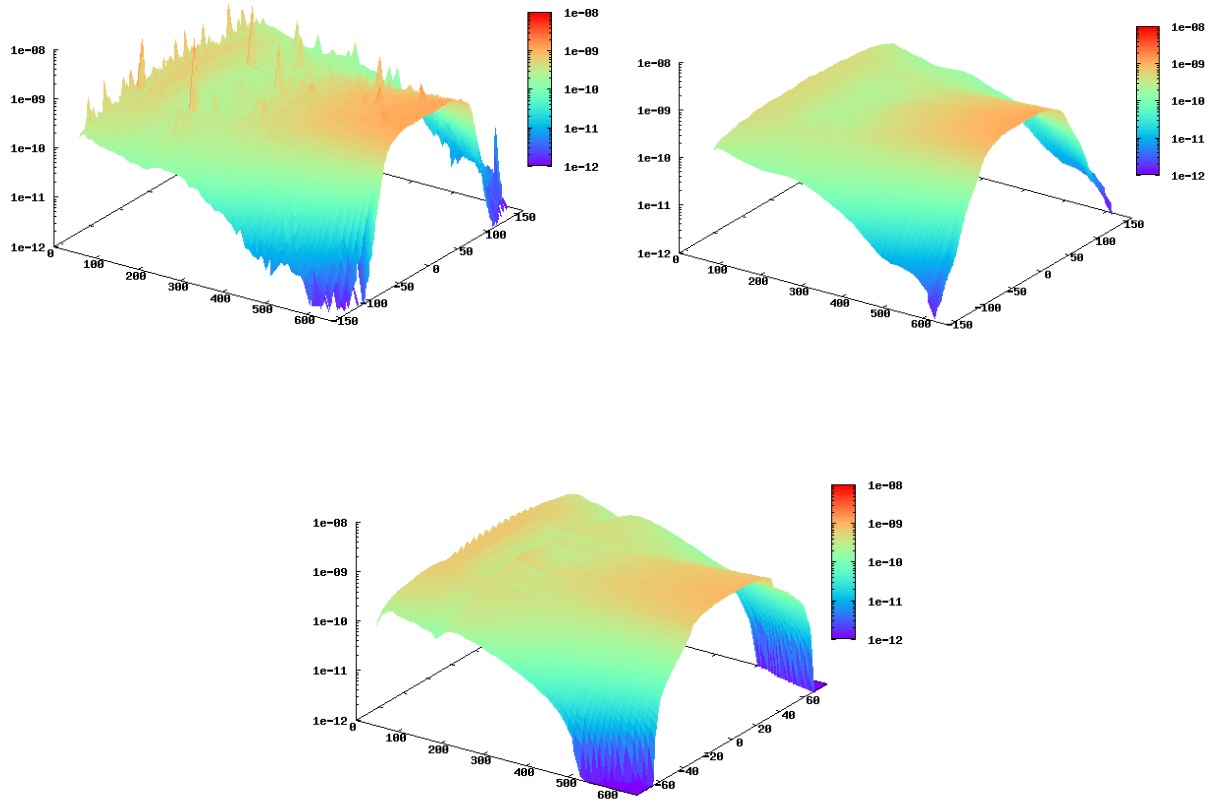


**Figure APX D.7.** Zero angle projections for all downscattered energy bins from (40-661 keV) from MCNP (upper-left), MCNP “smoothed” (upper-right) and RADSAT (lower) based models.

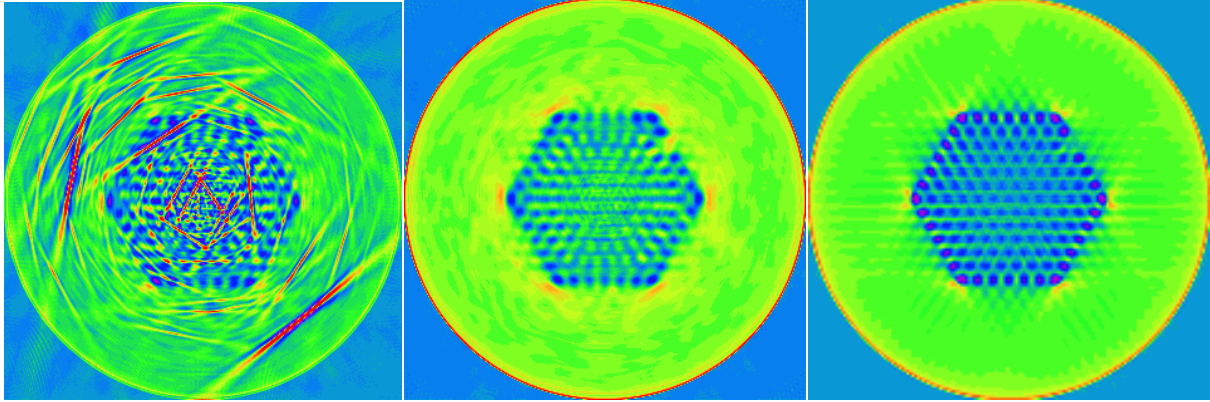


**Figure APX D.8.** Reconstructions from 200-210 keV sinograms from MCNP (left), MCNP “smoothed” (center) and RADSAT (right) based models.

For all runtime estimates of Table APX D.1, it was assumed that both the RADSAT and MCNP transport solutions had converged. Figure APX D.7 shows the zero-angle projections over the downscattered energies. While the RADSAT solution seemed to be stable, MCNP showed statistical fluctuations for projections at downscattered energies (Figure APX D.7, top left). The relative errors for the peak (661-662 keV) bin statistics was within 1 percent, but downscattered bins could vary by greater than 50 percent. Because of the correlated information between energies and pixels, it should be possible to “smooth” the MCNP projections by averaging neighboring pixels and energy bins.

As a simple example, the smoothed MCNP projections (Figure APX D.7, top-right) were obtained from a 7x7 grid average over energy bin and pixel and iterating the elimination of outliers greater than two times the previous average. Of course, more sophisticated averaging methods that would exploit the physics could be considered. Reconstructions from the Figure APX D.7 projections and corresponding sinograms are shown in Figure APX D.8 and Figure APX D.9.

**Table APX D.1.** Transport parameters and typical runtimes.

Model Run Case	Total Runtime	Runtime/processor/ pin	Notes
<b>MCNP</b> ( $5 \times 10^8$ histories)	58,368 h	463 h	Simultaneous calculation of all pins
<b>RADSAT</b> (transport, $S_{16}$ , $P_2$ )	43 min	43 min	Simultaneous calculation of all angles
<b>RADSAT</b> (LCF)*	3.0 h	3.0 h	Low efficiency with <16 of 32 cores active
* Additional time to generate scalar flux sinograms from the LCFs is < 2 min			



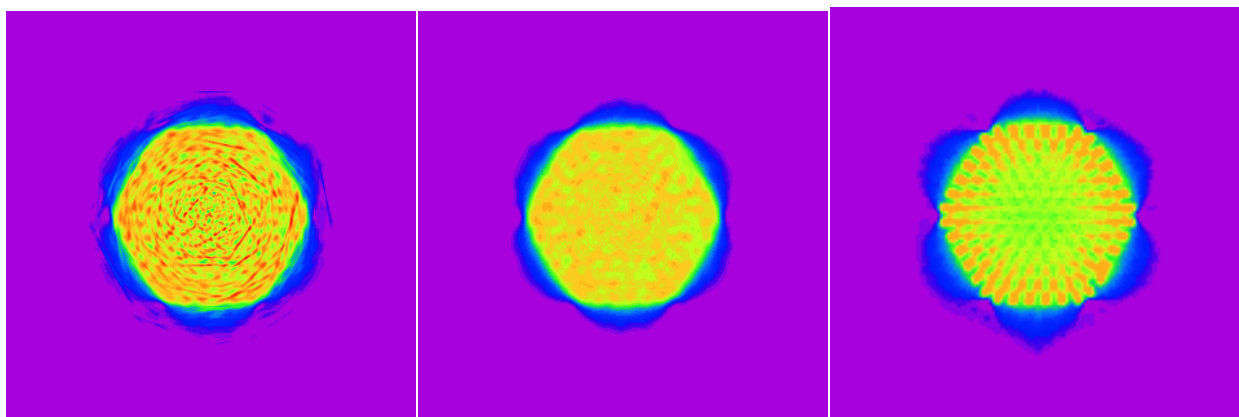


**Figure APX D.9.** Reconstructions from 400-661 keV sinograms from MCNP (left), MCNP “smoothed” (center) and RADSAT (right) based models.

At downscattered energies the pins appear as the darker regions and it is the scattered photons in the water that produce the lighter regions. For the non-smoothed MCNP reconstructions (left side of Figure APX D.8 and Figure APX D.9), streaking artifacts appear in the image from the randomly occurring nonconverged bins – the smoothing seems to eliminate the streaks, but introduces a loss in resolution. It may be possible that a physics-based smoothing can avoid loss of resolution, but the inherently smooth solution from the RADSAT approach could be an advantage for rapid tomographic modeling where downscattered photons contain the significant information. One example is the modeling of the potential for using downscattered photon energy data to independently estimate the attenuation properties of the materials. While the main interest in using RADSAT-calculated downscatter in this work is to include its effects in the system response function, this complementary information could increase the ability to correct or interpret the spatial and spectral content of primary interest in reconstructions.

While MCNP modeling of the tomographic systems served as the standard for understanding the physics of the designs, the application of deterministic transport (RADSAT) provided a truly complementary definition of the system response function for representing the reconstruction process independent of the data. Additionally, a deterministic approach allowed a tractable path to include the scatter contribution within the response function and give some insight into its effect on reconstruction accuracy. Work is in progress to model system scatter and collimators more accurately in a deterministic approach.

## Appendix E

### ROC Curves for Objective 1

A compilation of receiver-operator characteristic (ROC) curves from the U.S. Support Program to the IAEA (USSP) Objective 1 analysis are given here. Unlike the Objective 1 figures presented in the body of the report, based on an assembly-level probability of false alarm (PFA), these data assume a ring-level PFA. They allow a deeper inspection, for example, into which missing-pin locations (i.e., which ring in the assembly configuration) have low detection probabilities, and therefore, dominate the assembly-level summary curves. These ring-level data are the input to the assembly-level PFA calculation described in the body of the report, and are generated from the same analysis assumptions:

- Total assay time - 60 minutes for the universal gamma emission tomographer (UGET), less than 10 minutes for the passive gamma emission tomographer (PGET)
- Assembly populations - 1000 virtual assemblies with  $\pm 20\%$  pin-wise burnup variation
- Image analysis - fuel geometry, composition and water-channel locations assumed known
- PGET regions of interest (ROIs) - 400-700 keV for  $^{137}\text{Cs}$ ;  $>700$  keV for  $^{154}\text{Eu}$
- UGET ROIs - span peaks at 662 keV ( $^{137}\text{Cs}$ ) and 1275 keV ( $^{154}\text{Eu}$ )

UGET and PGET performance is compared for different fuel types (boiling water reactor [BWR], water-water energetic reactor [VVER], and pressurized water reactor [PWR]), assuming fuel characteristics consistent with three implementation scenarios (Figure APX E.1, Figure APX E.2, and Figure APX E.3):

- 40 GWd/MTU, 1-yr cooling, anomaly resolution of short-cooled assemblies
- 20 GWd/MTU, 5-yr cooling, routine verification of fuel being transferred to dry storage
- 10 GWd/MTU, 40-yr cooling, routine verification of old fuel transferred to a repository

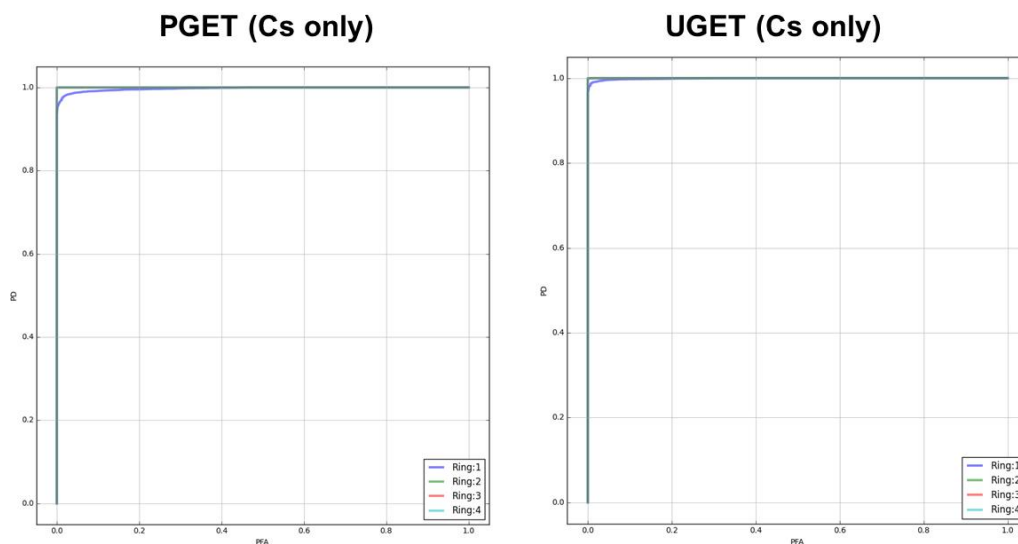
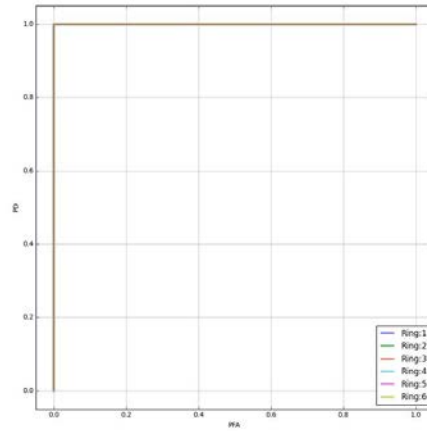


**Figure APX E.1.** Probability of detection (PD) for a single missing pin in each ring of an assembly, versus the ring-level PFA (i.e., not assembly-level PFA) for PGET (left) and UGET (right). Fuel is BWR nominal burnup of 10 GWd/MTU and 40-year cooling.

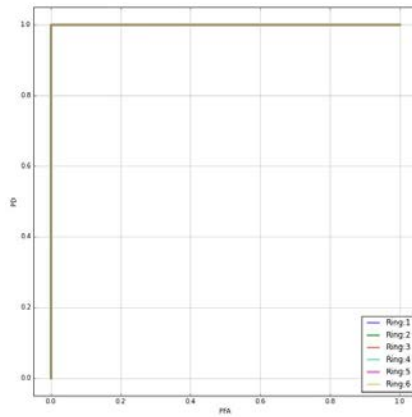


**No PGET results:  
Count rates too high**

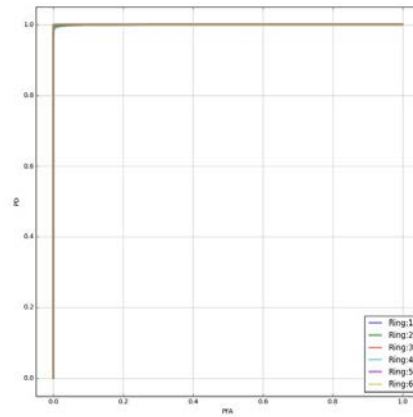
**UGET (Eu only)**



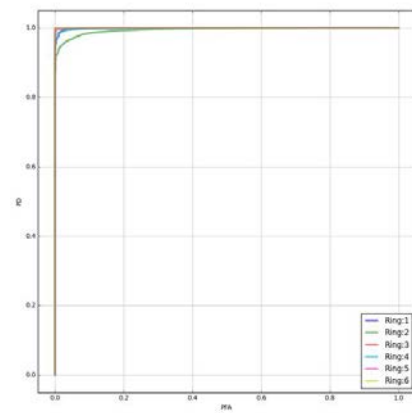
**PGET (Eu only)**



**UGET (Eu only)**



**PGET (Cs only)**



**UGET (Cs only)**

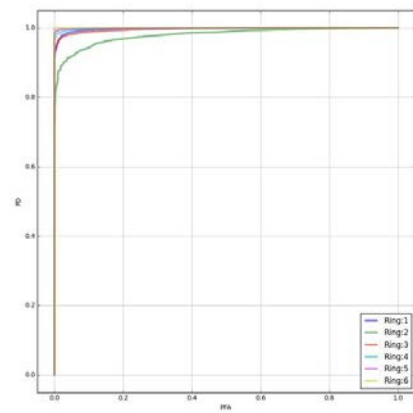


**Figure APX E.2.** PD for a single missing pin in each ring of an assembly, versus the ring-level PFA (i.e., not assembly-level PFA) for PGET and UGET, assuming VVER-440 fuels: 40 GWd/MTU, 1-year cooling (top); 20 GWd/MTU, 5-year cooling (middle); 10 GWd/MTU, 40-year cooling (middle).

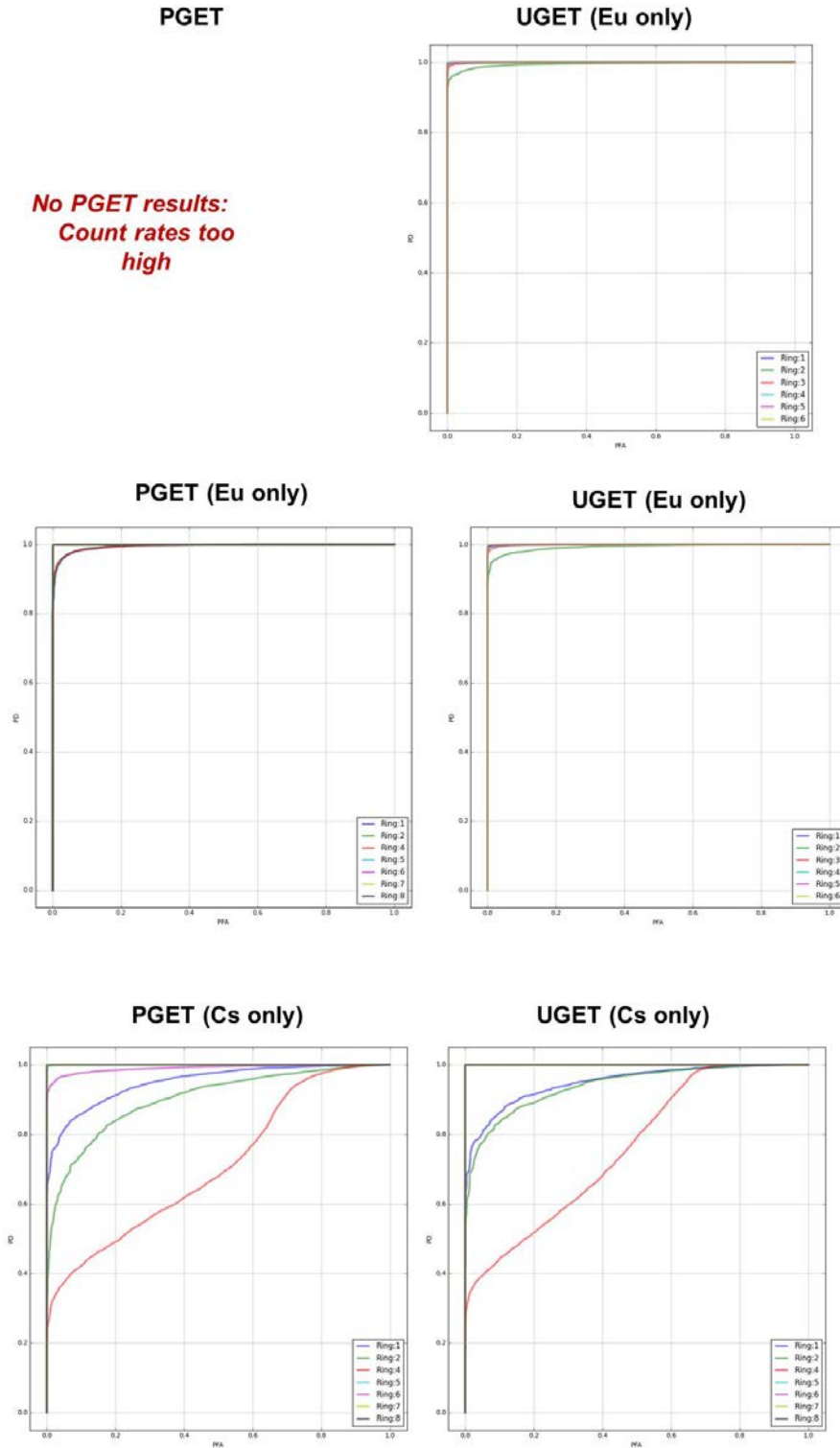


**Figure APX E.3.** PD for a single missing pin in each ring of an assembly, versus the ring-level PFA (i.e., not assembly-level PFA) for PGET and UGET, assuming PWR fuels: 40 GWd/MTU, 1-year cooling (top), 20 GWd/MTU, 5-year cooling (middle), 10 GWd/MTU, 40-year cooling (bottom).